Quantifying Radiation Belt Electron Precipitation through Bremsstrahlung X-ray Spectral Imaging

by

G. D. Berland

B.S., University of Illinois at Urbana-Champaign, 2018

M.S., University of Colorado Boulder, 2020

A thesis submitted to the

Faculty of the Graduate School of the

University of Colorado in partial fulfillment

of the requirements for the degree of

Doctor of Philosophy

Department of Aerospace Engineering Sciences

2023

Committee Members:

Robert A. Marshall, Chair

Lauren Blum

Xinlin Li

Zoltan Sternovsky

Christopher Cully

Berland, G. D. (Ph.D., Aerospace Engineering Science)

Quantifying Radiation Belt Electron Precipitation through Bremsstrahlung X-ray Spectral Imaging

Thesis directed by Prof. Robert A. Marshall

Energetic particle precipitation (EPP) is a phenomenon that couples planetary magnetospheres and atmospheres through high-energy charged particle transport into the atmosphere. Due to the large spatial scales over which this process occurs, it is difficult to observe directly and therefore the spatial and temporal scales of EPP are poorly constrained. Open questions of magnetosphere-atmosphere coupling relate to the driving mechanisms of EPP: how does EPP vary seasonally, temporally, and with magnetospheric conditions; and what are the spatial scales over which this process occurs? The study of EPP will improve current understanding of the behavior of the radiation belts and the atmosphere's response to EPP, and will lend a deeper understanding of the dynamic interactions of planetary magnetospheres and atmospheres. This work specifically focuses on electron precipitation involving the highest energy particles in the magnetosphere: the radiation belts.

Obtaining global measurements of EPP is difficult due to the spatial scale and height above Earth's surface at which this process occurs; the drivers interact with charged particles in the heart of the radiation belts at 4 – 7 Earth radii, and the effects at Earth cover the entire globe, from mid-latitudes to the poles, and at altitudes too high for in-situ balloon measurements, and too low for radar remote sensing. Measuring EPP's effects through remote sensing in the ionosphere is difficult due to high atmospheric density driving fast recombination such that the atmospheric effects of EPP dissipate quickly. Perturbations in atmospheric chemistry can be measured as a proxy to precipitation inputs, but the complicated reactions and transport dynamics makes the inversion to precipitation characteristics uncertain. On the other hand, direct in-situ measurements of charged particles from spacecraft cannot easily obtain the spatial and temporal coverage necessary to quantify EPP due to the limited nature of a single (or a few) spacecraft in orbit. Additionally,

charged particle instruments are often angular resolution-limited and are unable to resolve the loss cone at various points in the orbit, which is necessary to provide a global image of precipitation.

EPP can instead be inferred through remote measurements of X- and gamma-ray photons, which are a byproduct of relativistic electron precipitation. Once an electron has entered the atmosphere it interacts with neutrals and can spontaneously generate a high energy photon via the bremsstrahlung ("braking radiation") interaction. The resulting photon energy is correlated with the precipitating electron energy, such that statistical relationships can be formed between the two quantities. By measuring X- and gamma-ray photons that escape the atmosphere with a spacecraft-based imaging spectrometer, a global perspective of EPP can be obtained: the spatial scales of EPP can be directly measured by photon imaging of the upper atmosphere from low-Earth orbit, and by measuring in-situ electron spectra along with photon measurements, the photon flux and spectra can be inverted to estimate precipitating electron flux and spectra.

This thesis is split into three parts. First, the design, development, and testing of the Atmospheric X-ray Imaging Spectrometer (AXIS) instrument onboard the upcoming Atmospheric Effects of Precipitation through Energetic X-rays (AEPEX) CubeSat mission is described. The detectors, shielding design, and signal-to-noise ratio calculations are described in detail. Second, the novel X-ray optics and algorithmic reconstruction technique of the AXIS instrument are developed and described. The wide field-of-view imager implements a coded aperture mask in order to obtain spatial resolution of X-ray photons. Finally, EPP simulations are performed with a kinetic model of precipitation built using GEANT4 to determine the X-ray signal and atmospheric effects of EPP at Earth and Jupiter in support of the AEPEX mission and other studies of planetary magnetospheres. The development of the AXIS instrument and tools developed herein are extended for a NASA-funded concept study of a spacecraft mission to Jupiter, which aims to address open questions of Jupiter's radiation belts.

Dedication

For Carly

Acknowledgements

To my best friend, Carly, who has been with me for so long I couldn't imaging life without her, thank you for absolutely everything. I am forever grateful for your love and support for the last decade.

I simply would not have been able to get through grad school without the help of my wonderful friends and labmates, thank you so very much! You have all helped keep me feeling loved, supported, and happy for my time in Boulder and I will be forever grateful to you all.

I've had an incredible amount of mentorship from and collaboration with so many people through the last 5 years that I will be forever grateful for; Austin Sousa, Wei Xu, André Lucas Antunes de Sá, and Forrest Gasdia from the LAIR lab, and Chris Cully, Michael McCarthy, Lauren Blum, George Clark, and so many more, I cannot thank you all enough for the help and support, it has meant the world to me. The AEPEX engineering team, including professional engineers at LASP has been instrumental in supporting my research and the development of the AEPEX spacecraft.

I would lastly like to thank my advisor, Bob, who went out on a limb bringing me into the research group and has endlessly supported me throughout grad school, thank you.

Contents

Chapter

Tables

Table

Figures

Figure

Chapter 1

Introduction

1.1 Planetary Magnetospheres

A planetary body can be enveloped by a magnetic field that is either generated intrinsically through dynamo motion of a conducting fluid in that planet's interior, or induced from interactions with solar charged particle ejecta (Kivelson & Bagenal, 2014). The near-planetary region where the influence of the body's magnetic field dominates over the host star's magnetic field is referred to as its **magnetosphere**. A planet's magnetosphere determines how that planet will interact with its host star, and is vital in coupling the behavior near the planetary body with the behavior of the charged particles from the host star (Bagenal, 2013).

The study of magnetospheres, both in general and specifically at Earth, is scientifically interesting for investigating and understanding the coupling mechanisms between magnetized bodies and their host stars. This coupling influences the formation and behavior of planetary ionospheres and atmospheres, and if a body is lacking those systems, this coupling can directly affect planetary surfaces (Wolf, 1975; D. Baker, 1985; Strazzulla, Brucato, Cimino, Leto, & Spinella, 1995; Fujimoto et al., 2008). It is currently under debate whether magnetospheres prevent atmospheric escape to the point where the presence of a magnetosphere is necessary for the sustenance of a planetary atmosphere (Russell, 1993; Khodachenko et al., 2007; Jakosky et al., 2018). Magnetospheres and the subsequent **radiation belts**, which form from acceleration of trapped charged particles within the magnetosphere, have been discovered around low mass stars and brown dwarfs, pulsars, and extrasolar planetary bodies, making the study of radiation belt dynamics a universal process (Tverskoy,

1969; Kao, Mioduszewski, Villadsen, & Shkolnik, 2023; Luo & Melrose, 2007a).

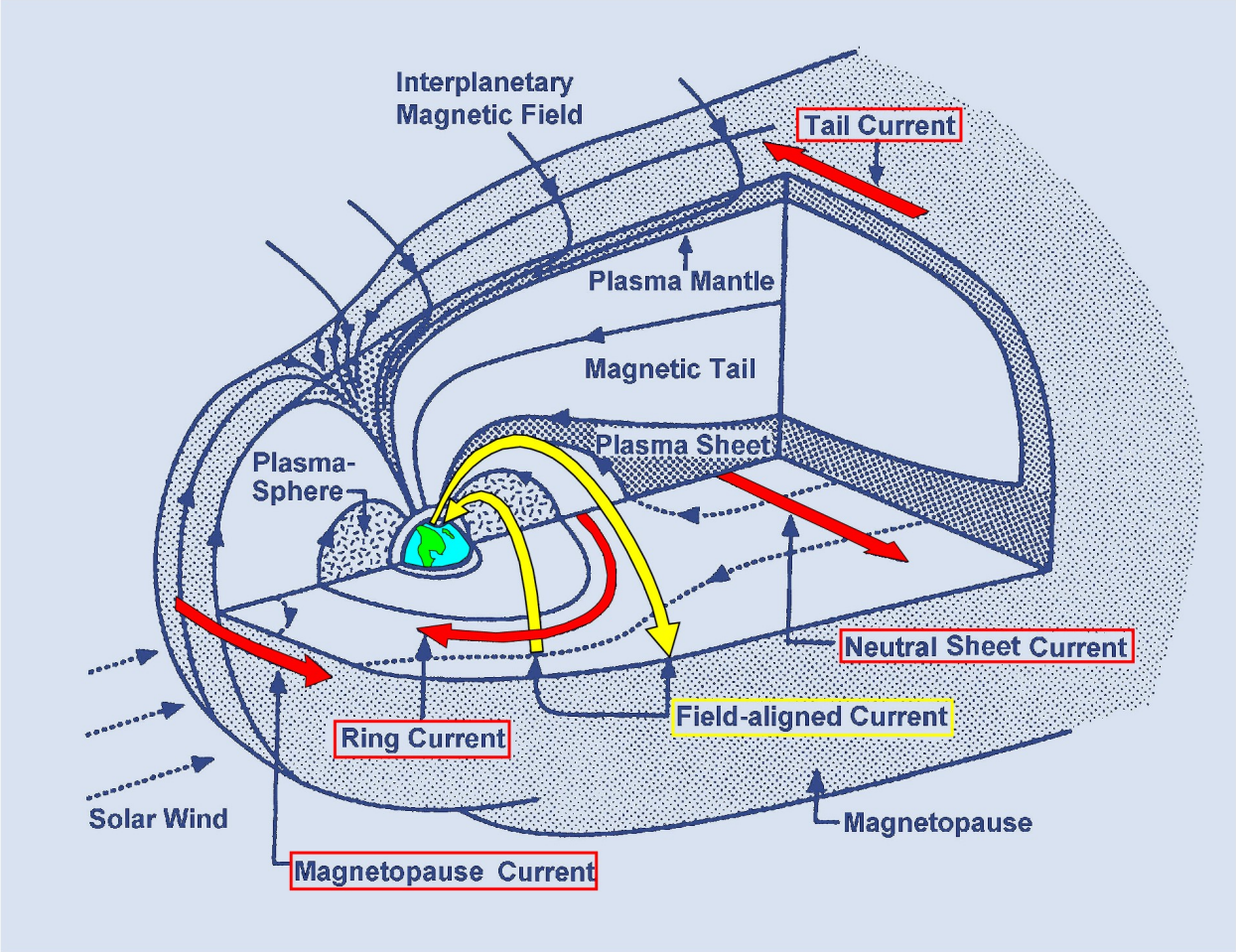

Figure 1.1: A diagram of Earth's magnetosphere, showing magnetic field structure and current systems which are caused by the flow of charged particle and are driven by magnetospheric convection in the Dungey cycle. Solar wind flow is from the left side of the diagram and is comprised of charged particles that enter the magnetosphere and join the magnetospheric population, and the current systems ultimately to Earth's atmosphere, closing the system. Figure from Kivelson and Russell (1995).

Within a magnetospheric system, there are complicated and interdependent processes of particle sourcing, acceleration, and loss: Figure 1.1 shows the current flow systems, magnetized regions, and solar wind flow that are mediated by the motion of charged particles in the magnetic field near Earth. At Earth these current systems are driven by the magnetized plasma ejected from the Sun, known as the solar wind, in the Dungey cycle convection process where magnetic

field-line structures are swept from the bow shock to the magnetotail (convecting from left to right in Figure 1.1). This convection subsequently drives magnetic flux and plasma flow back towards the night-side and around the dusk-side of Earth, forming the **ring current** (W. I. Axford & Hines, 1961; Dungey, 1963).

These current flows, as well as the open magnetic field lines near the North and South magnetic poles of Earth, enter Earth's atmosphere and exert a force on the embedded plasma in the upper atmosphere which couples the magnetosphere and atmosphere (W. Axford, 1964; Stern, 1983). In the other direction, the atmosphere and ionosphere also couple to the magnetosphere: atmospheric up-welling and outflow of neutral and charged particles become a part of the magnetospheric charged particle population and populate a region of cold (i.e., low energy), high-density plasma known as the **plasmasphere** (Yau, Peterson, & Shelley, 1988; Strangeway et al., 2000; N. M. Brice, 1967; Nishida, 1966; J. Lemaire, 1975). Further, charged particle-neutral collisions within the atmosphere add resistance to the magnetospheric current flows, a vital component that closes the circuit of the magnetosphere-**ionosphere** system (Robinson, Vondrak, Miller, Dabbs, & Hardy, 1987; Ridley, Gombosi, & DeZeeuw, 2004).

Far away from Earth where the magnetic field is weaker, the plasma population behaves mores like a fluid and is subjected to turbulence, collisional heating, and random thermal motion, whereas near the Earth the magnetic field is stronger and the plasma's motion is primarily along magnetic field lines. In this near-Earth region, particles can enter Earth's atmosphere and **precipitate** at different latitudes on Earth from the different magnetospheric populations (Frank & Ackerson, 1971; Foster, Holt, Musgrove, & Evans, 1986).

Through precipitation, the magnetospheric system ultimately couples with Earth's **ionosphere**, the portion of Earth's atmosphere that extends from approximately 60 km upwards that is a partially ionized gas embedded within the atmosphere and near-Earth magnetic field, and interacts directly through a number of coupling mechanisms to the magnetosphere (Chapman, 1956).

The discrete populations of charged particles that can precipitate into the atmosphere, in

order of increasing latitude, are the ring current, the current sheet, the **radiation belts**, and **auroral** electrons (i.e. the electron population responsible for the visible aurora). The radiation belts at Earth are two distinct torii of high energy charged particles that are spatially separated into the inner and outer belts. The inner belt is populated primarily by high energy protons and ions that are sourced from atmospheric outwelling of ionospheric particles and the cosmic ray albedo neutron decay (CRAND) process (Freden & White, 1960; R. Selesnick et al., 2014; X. Li et al., 2017). This inner belt is located between the **L-shells** of 1.5 – 3 (L-shell is equivalent to Earth radii at the equator) and is less affected by varying solar and geomagnetic conditions due to the momentum of these energetic protons and the strong background magnetic field at lower altitudes.

In contrast, the outer radiation belts are highly variable and dynamic; the study of **energetic particle precipitation (EPP)** at Earth is, both explicitly and implicitly, a study of the variability of the outer radiation belt. The charged particle population in the outer belt is primarily made of high-energy electron fluxes located between L = 4 – 8, where the electron flux of particles with kinetic energies greater than 0.1 MeV can reach 10^8 cm^{-2} s^{-1} and electron energies can reach up to 10s of MeV (Vette, 1991; R. Selesnick & Blake, 1997; X. Li & Temerin, 2001).

At mid-latitudes, ion precipitation into the atmosphere occurs from the ring current and inner radiation belts. At higher latitudes (>60° magnetic latitude, e.g.), outer radiation belt and current sheet scattering precipitation (Sergeev, Sazhina, Tsyganenko, Lundblad, & Søraas, 1983; Ni et al., 2016) become significant. Finally, at high latitudes is the auroral oval region, where lower-energy charged particles are accelerated by magnetic field-aligned electric fields at the poles and enter the atmosphere, causing the colorful optical emissions of the aurora borealis and aurora australis (Angot, 1897; Eather, 1967; Swift, 1981). Precipitation from higher energy populations also cause visible light emissions, but the energy flux is much lower than auroral precipitation so these emissions are relatively dim (e.g. Sivadas, Semeter, Nishimura, and Mrak (2019); R. A. Marshall, Newsome, Lehtinen, Lavassar, and Inan (2010)).

Earth's magnetosphere has been studied with satellites since its discovery in the late 1950s. The more recent Van Allen Probes mission drove an improved understanding of behavior of charged

particles and fields in the near-Earth space environment (Fox & Burch, 2014; Reeves et al., 2013; W. Li & Hudson, 2019). These advances are crucial to the scientific understanding of planetary and solar systems, atmospheric driving effects, and the myriad satellite engineering and anthropogenic interactions that occur as a results of **space weather** (D. Baker, 1998; D. N. Baker, 2000; P. Cannon et al., 2013; Gombosi et al., 2017).

Of particular interest, the charged particle populations in a magnetosphere can be extremely dynamic and can span energies of fractions of an eV (electron-volt, i.e. the kinetic energy gained by an electron when the electric potential in the vicinity of the electron is increased by one volt) up to 100s of MeV (10^8 eV) in Jupiter's radiation belts, for instance (H. J. Allison & Shprits, 2020; Horne et al., 2008; Kollmann et al., 2018). The inner magnetosphere is supplied by two sources of charged particles: the extension of the upper atmosphere in which neutral particles are ionized by solar UV and X-ray photons that provides the cold, dense plasma to the region referred to as the plasmasphere; and the solar wind plasma, which enters the inner magnetosphere through the open magnetic field lines in the polar regions, or through injections from further down the magnetotail, and provides the source of the ring current, plasma sheet, and radiation belt populations (J. F. Lemaire & Gringauz, 1998; O'Brien & McPherron, 2000; Borovsky, Thomsen, & Elphic, 1998). Day-side injection of plasma, especially during magnetic reconnection events, is also a source of energetic charged particles in the magnetosphere (Reiff, Hill, & Burch, 1977; Hill & Reiff, 1977).

The inner belt energy flux is primarily protons and is generated by the cosmic-ray albedo neutron decay (CRAND) process (X. Li et al., 2017) and acceleration of ionospheric plasma. The outer belt is primarily populated by electrons which are energized by inward radial diffusion and wave-particle interactions. Fluxes of electrons with energies greater than 0.1 MeV can reach 10^8 cm^{-2} s^{-1} and electron energies can reach 10s of MeV at Earth (Vette, 1991). Between the two belts lie a relative barren "slot region," with the exception of the serendipitous formation of a third belt of high energy electrons during times of enhanced geomagnetic conditions (D. Baker et al., 2013; I. R. Mann et al., 2016). These enhanced geomagnetic conditions, or "geomagnetic storms," are

driven by solar events, such as coronal mass ejections with a southward interplanetary magnetic field component, and are exacerbated by internal feedback mechanisms within the magnetosphere, such as energetic particle injections from the magnetotail. This third belt is then slowly depleted until the inner magnetosphere returns to its nominal state. Similarly, the inner and outer radiation belts undergo loss processes that play a role in the dynamic nature of the near-Earth space environment. This highlights the complexity of the radiation belts and their dynamics.

1.2 Energetic Particle Precipitation

1.2.1 EPP at Earth

The loss of charged particles from the outer belt occurs by two primary mechanisms: i) losses outwards into the region beyond the magnetosphere where particles are swept down-tail, and ii) losses inwards to the Earth's atmosphere through EPP. The first loss mechanism is referred to as **magnetopause shadowing**, and occurs due to compression of the magnetopause that causes charged particles to drift onto open magnetic field lines where they are subsequently lost to the region where the interplanetary magnetic field and the solar wind plasma flow dominates the forces exerted on a particle (West, Buck, & Walton, 1972; Millan & Thorne, 2007). Losses from the inner radiation belt are primarily due to EPP; the sources and loss of charged particles are approximately matched and maintain the relatively stable inner radiation belt (Farley & Walt, 1971; Rodger, McCormick, & Clilverd, 2004).

Charged particles undergo three primary types of motion within Earth's magnetosphere: a gyromotion about the magnetic field line with a small radius and fast period; a sinusoidal bounce motion along a magnetic field line between the Northern and Southern hemispheres; and a relatively slow drift in the equatorial direction that differs in direction based on particle charge. These motions are depicted in the left graphic of Figure 1.2. These three types of motion arises from **adiabatic invariants** that describe a charged particle's momentum and energy in the presence of a magnetic field, driven by the Lorentz force (Northrop, 1961, 1963).

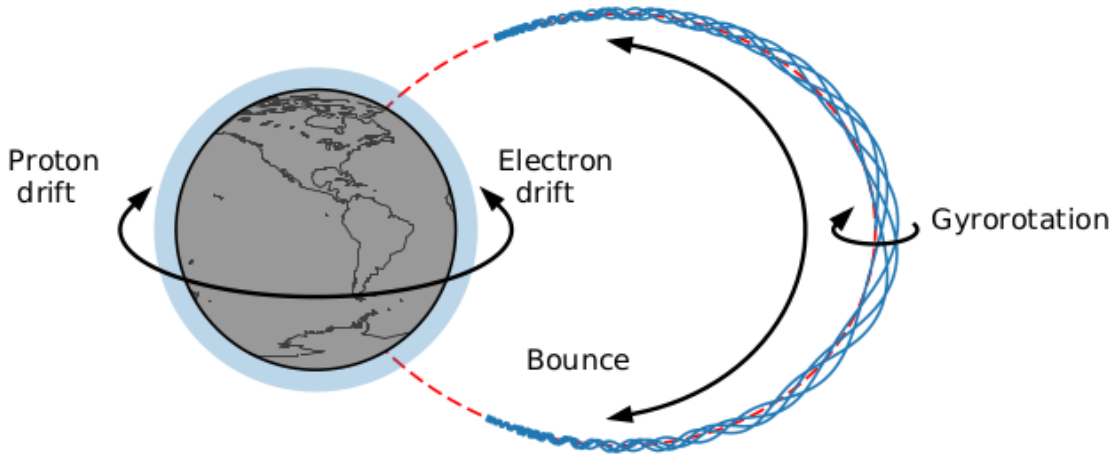

Figure 1.2: The three types of charged particle motion in a dipole magnetic field are shown: gyration around the field line which has a fast period, bounce motion between the mirror points in the Northern and Southern hemispheres, and the slow drift motion in the equatorial direction that is charge dependent. The charged particle trajectory is determined by adiabatic invariants of motion that conserve particle energy and momentum. Figure from Sousa (2018).

Precipitation is the process in which a particle's **mirror point**, or turn-around point in its bounce trajectory, is located within the atmosphere; altitudes at or below 100 km are taken as a reference location for where loss occurs via EPP (Kennel, 1969; L. Lyons, 1997). (See Chapter 2 for an explanation of the factors that lead to charged particle bounce motion within the magnetosphere) At these altitudes, Earth's atmospheric density has increased exponentially with decreasing altitude and the particle is much more likely (compared to altitudes above 100 km) to interact with a neutral particle through collisional interactions at rates faster than the charged particle's gyrofrequency. The charged particle loses energy through collisions until its kinetic energy is low enough that it cannot escape back up the magnetic field line; from here the particle has precipitated and is lost to the atmosphere. Once precipitated, the charge particle has lost enough energy to join the thermal ionospheric plasma population (Thorne, 1980; Reagan, Meyerott, Evans, Imhof, & Joiner, 1983; D. Baker, 2000).

Particle precipitation into the atmosphere is a persistent process and a natural consequence of magnetospheric convection (Southwood & Wolf, 1978). A portion of the auroral electron portion

(< 30 keV) of EPP can be driven by quasi-static electric fields parallel to the magnetic field in the polar regions, which is the cause of discrete aurora at high latitudes, and wave-particle interactions which scatter high energy electrons, and is associated with more diffuse aurora (Swift, 1981; Newell, Sotirelis, & Wing, 2009). All forms of EPP have strong correlations with enhanced plasma wave and geomagnetic activity (Rodger et al., 2007; Horne, Lam, & Green, 2009).

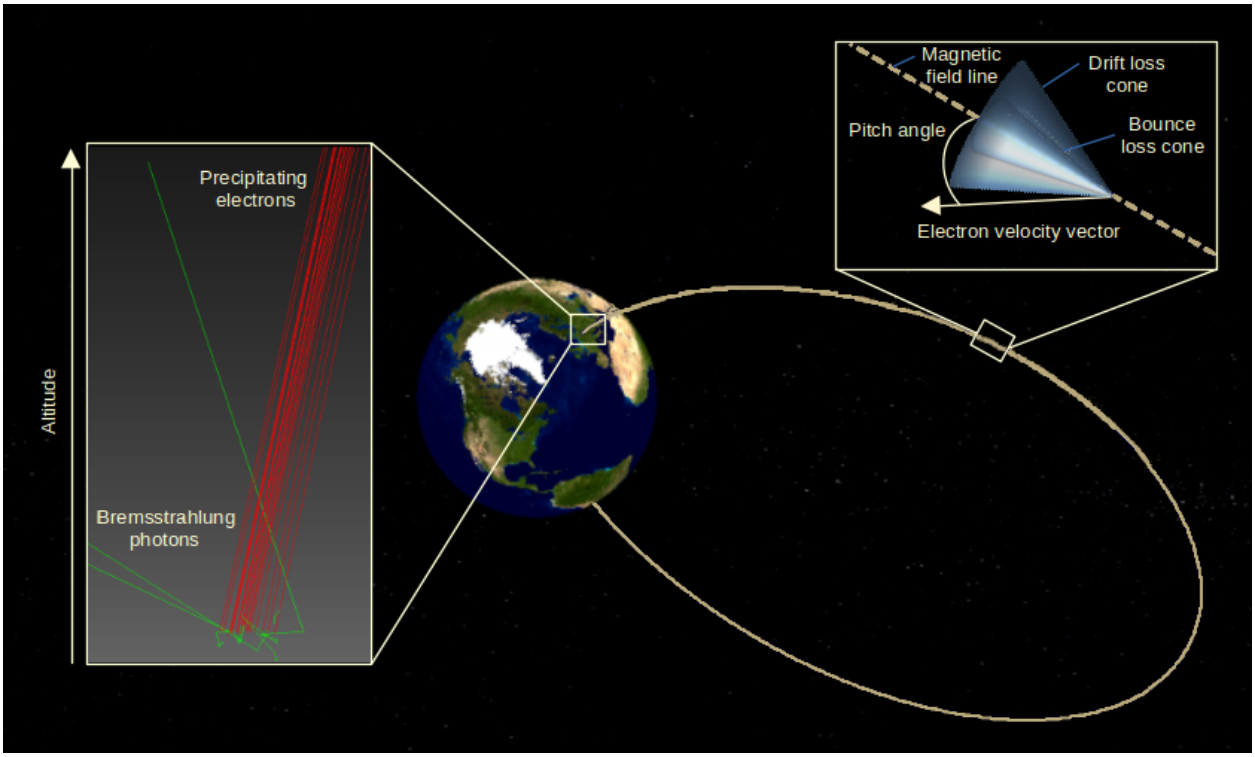

Figure 1.3: Wave-particle interactions can cause a portion of the electron population's pitch angle to diffuse towards lower angles which lowers their mirror point in altitude and allows them to enter the loss cone. Once that occurs, a column of electrons will reach altitudes where the atmosphere becomes dense enough for a sufficient number of electron-neutral interactions and the electrons may precipitate. Electrons can lose large amounts of energy impulsively to the atmosphere through bremsstrahlung interactions, which produce a high-energy photon. Geant4 simulations of precipitation are shown on the left with electrons in red and photons in green.

One of the main ways in which Earth's upper atmosphere couples with the magnetosphere is through precipitation. This work focuses on radiation belt electron precipitation, which we will refer to as EPP hereafter. EPP occurs when wave-particle interactions or other mechanisms cause electron **pitch angle** scattering or diffusion, which drives the electron mirror point closer to Earth

(Thorne, 2010; Turner et al., 2014). An electron's pitch angle is the angle formed between the electron momentum vector and the local magnetic field vector. When an electron has a lower pitch angle, i.e. its momentum is more field aligned, the particle dives deeper into Earth's atmosphere where precipitation can occur. There exists a critical angle that corresponds to mirror altitudes at or below 100 km where precipitation becomes very likely. The region of phase space that is formed by rotating the critical pitch angle around the magnetic field line is referred to as the "loss cone." See Figure 1.3 for a visualization of the geometry. More specifically, the region of phase space formed when electrons are lost along a magnetic field line at any longitude is known as the bounce loss cone (BLC) (L. R. Lyons & Thorne, 1973; Walt, 1996).

There exists another subtype of EPP driven by the drift motion of the electron in **magnetic local time** (MLT). Electrons in the drift loss cone (DLC) enter the atmosphere through EPP in a process that arises from a longitudinally-stationary weakening of Earth's magnetic field over the Southern Atlantic ocean and Brazil, referred to as the South Atlantic Anomaly (SAA) (Dessler, 1959). Charged particles precipitate from the DLC while they drift around the Earth equatorially in MLT and enter the atmosphere at the SAA (Abel & Thorne, 1999). This weakening is relevant at all magnetic **L-shells**, or fixed paths along magnetic field lines, since particles drifting in longitude, combined with the Earth's rotation, will inevitably cause precipitation for the quasi-trapped particles that are in the DLC but not the BLC (see Chapter 2 for an quantitative explanation of this phenomenon).

The Earth's outer radiation belt, which is primarily comprised of high energy electrons, maps to the Earth at mid-latitudes ($\sim 50^\circ$ – 70° magnetic latitude) where the outer radiation belt maps to Earth's surface. Precipitation of radiation belt electrons is sometimes specifically referred to energetic electron precipitation (EEP) or relativistic electron precipitation (REP), and describes electron populations with kinetic energies of 10s of keV to many MeV. Once a high energy electron enters the atmosphere, it interacts with the neutral population, causing excess ionization of atmospheric particles, and loses kinetic energy. The electron will eventually lose enough energy and slow to either join the thermal plasma population, or be captured by a positive ion and experience

recombination (R. A. Marshall & Cully, 2020). A trapped electron's energy and location in the magnetosphere will typically determine which acceleration mechanisms can affect the particle and determines the "type" of precipitation that it may experience.

Auroral precipitation is typically a lower energy, high-latitude phenomenon where charged particles are accelerated into the atmosphere by kV quasi-static electric fields that are generated from the solar-driven convection of Earth's magnetosphere (Newell et al., 2009). Auroral precipitation occurs for electrons with eV – 10s keV kinetic energies and is an important source for upper atmospheric ionization and heating (Hays, Jones, & Rees, 1973). There is also evidence that some forms of aurora, for example pulsating aurora, are a higher energy phenomenon generated by 10s of keV to over 1 MeV electrons (Nishimura et al., 2010; Shumko et al., 2021). These high energy electrons can go on to have radiative interactions with the neutral constituents of the atmosphere, including visible light emission in the various optical wavelengths of oxygen and nitrogen emissions.

One such radiative interaction that occurs during precipitation is bremsstrahlung ("braking-radiation") photon production (Koch & Motz, 1959). Electron-neutral bremsstrahlung has an energy-dependent cross section, or probability of occurrence per particle, and becomes likely to occur when energetic electrons (>10s keV) pass in the vicinity of an atomic nuclei. The likelihood of a bremsstrahlung interaction can be quantified by the electron radiation length of a material, which is defined as the distance at which an electron traveling through a material has a $1/e$ likelihood of a bremsstrahlung interaction (Baier & Katkov, 2005; Gupta, 2010). Equivalent radiation lengths can occur in different contexts: an electron traveling through a few millimeters of a dense material (e.g. tungsten) may have the same radiation length as kilometers of a sparse gas (e.g. the upper atmosphere).

Bremsstrahlung radiation typically results in X-ray or gamma ray radiation with photon energies of a few keV to many MeV, depending on the energy of the incident electron, the scattering material, and other factors. The differential cross section with respect to incident electron and generated photon angle is non-trivial to calculate and is described in Chapter 2. Figure 1.3 shows that photons can be produced at oblique angles relative to the incident electron and can also

undergo Compton scattering, allowing X-ray photons to escape the atmosphere. The photons that do not escape the atmosphere contribute to the transport of energy lower in altitude.

EPP represents an important boundary condition to Earth's atmosphere and **is a poorly-constrained source of energy and ionization for the upper atmosphere**. Examples of EPP's effects on the upper atmosphere are presented in the work of C. Randall et al. (2006) and J. Pettit et al. (2019), where the authors investigate discrepancies between modeled atmospheric response to EPP and measurements of trace chemicals that arise after strong EPP events, including NO_x and HO_x, odd nitrogen and hydrogen compounds. These trace chemicals go on to have myriad atmospheric effects after transport to lower altitudes, including destruction of ozone. EPP also creates a local enhancement of ionization, which can have indirect effects through atmospheric chemistry and transport (C. Randall et al., 2007). This enhancement in ionization changes the path length of very-low frequency (VLF) electromagnetic waves that are propagating through the Earth-ionosphere waveguide via lowering of the ionospheric reflection height (Clilverd et al., 2009). This enhanced ionization also attenuates high-frequency (HF) radio communication, which is relevant for many communication systems (Zawdie, Drob, Siskind, & Coker, 2017; Obayashi & Hakura, 1960a). For these reasons, it is of cross-disciplinary scientific interest to formulate a parameterization for EPP for input into other models.

The current state-of-the-art modeling efforts to characterize EPP's effects on the atmosphere, namely excess ionization of atmospheric neutrals, are through the work of Fang et al. (2008, 2010) and Xu, Marshall, Tyssøy, and Fang (2020). Inputs to these models include various geomagnetic parameters including the disturbance storm-time index (Dst) and the planetary K-index (K_p), and output an estimate of the ionization profile with altitude. These models effectively parameterize the energy deposition effects of EPP, but do not generalize globally. Since EPP is a localized and highly variable phenomenon, additional information, either in the form of high-coverage observations or an enhanced understanding of when and where EPP occurs, is needed to use these models in such a way that captures the true influence of EPP on both the radiation belts and the atmosphere. See Chapter 5 for more background and development of EPP modeling.

1.2.2 EPP at Jupiter

Despite a litany of satellite- and ground- based measurements of the magnetosphere at Earth, it offers only "one" data point in the field of planetary magnetospheres. Questions on the universality of particle dynamics, magnetic configuration, and interactions with a host star are unanswerable by observations of Earth's magnetosphere alone. These reasons motivate the study of planetary magnetospheres in general in order to assess the processes that may be unique or rare to Earth versus processes that are universal to magnetized bodies in the universe. The study of energetic particle precipitation at Jupiter is relevant in comparing and contrasting the highest energy portion of EPP at that occurs at Earth.

Jupiter's magnetosphere was, in part, discovered from electron synchrotron radiation from Earth-based radio wavelength observations in 1955 that suggested a trapped population at Jupiter with energies of at least 10s keV (de Pater, 2006; S. J. Bolton et al., 2001). In-situ measurements at Jupiter by the Pioneer and Voyager spacecraft confirmed the presence of an extremely strong magnetic field and high fluxes of ultra-relativistic charged particles that extend to electron kinetic energies of 10s to 100s of MeV and heavy ion kinetic energies of GeV per nucleon (Divine & Garrett, 1983). Jupiter has a magnetic dipole moment that is approximately 10^4 times stronger than Earth, which puts it on scale with other higher energy, magnetized, compact bodies in the universe (E. Smith et al., 1974; Treumann, Baumjohann, & Balogh, 2014). A comparison of the spatial scales of Jupiter's radiation belt to Earth's outer radiation belt is shown in Figure 1.4.

Jupiter's intense magnetosphere couples with the ionosphere to maintain megavolt (MV) electrostatic potentials connecting Jupiter's auroral region with the middle magnetosphere. This potential accelerates precipitating electrons and ions to MeV energies (B. H. Mauk et al., 2017; Clark et al., 2020). Wave-particle interactions also play an important role in driving precipitation at Jupiter. Waves are generated by Jupiter's Galilean moons through near-field interactions with the plasma and far-field interactions via wave generation along magnetic field lines – both of which lead to a complex relationship between Jupiter's magnetosphere and embedded moons (Horne et

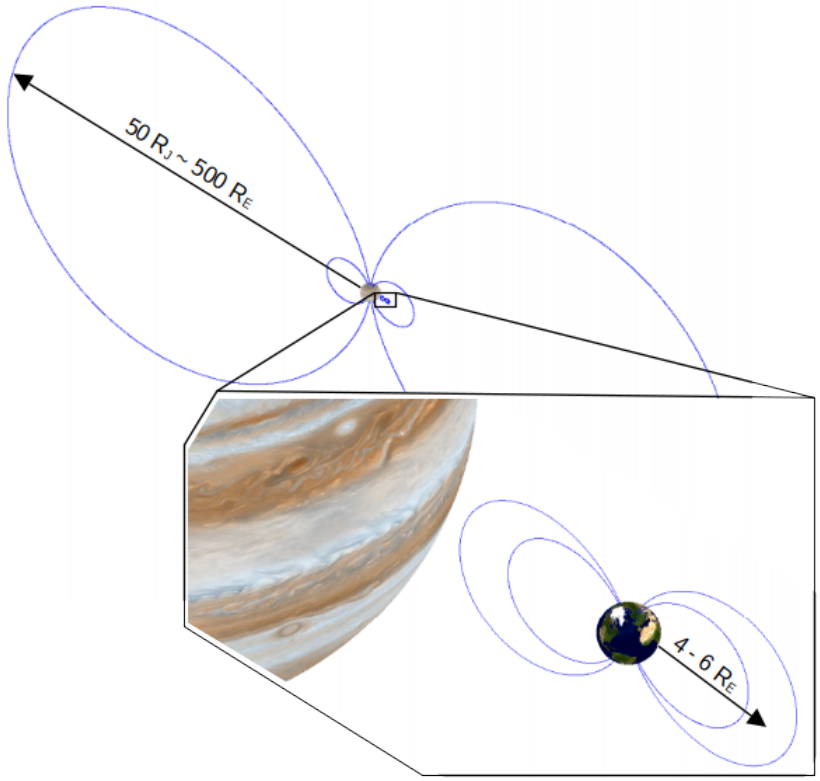

Figure 1.4: A spatial comparison of the inner and outer edges of Jupiter's radiation belt, which extend to nearly 50 Jupiter radii (R_J) and Earth's outer radiation belt, which extends to perhaps 7 to 8 Earth radii (R_E) during solar quiet times. For reference, one Earth radii is approximately 1/10 that of Jupiter.

al., 2008; Y. Y. Shprits et al., 2018).

At Jupiter, high energy precipitation is a near-continuous process and is the primary loss mechanism for charged particles due to the enormous size of the Jovian magnetosphere; magnetopause shadowing is infeasible because the magnetopause is far outside the most energetic parts of Jupiter's radiation belts, even during solar storm compression (N. Brice & Mcdonough, 1973; Horanyi, Cravens, & Waite Jr, 1988; Cravens, Howell, Waite Jr, & Gladstone, 1995). Particles can however be lost to collisions with Jupiter's Galilean moons or neutral particles in the vicinity of the Io plasma torus (W. Hess, Birmingham, & Mead, 1974; Nénon et al., 2018; Long et al., 2022). EPP at Jupiter occurs between an ultra-relativistic electron and a primarily hydrogen-helium atmosphere; as a result, the X-ray energies produced from EPP are lower than that at Earth (Divine

& Garrett, 1983; Seiff et al., 1996, 1998). Many of the wave modes that occur in Jupiter's magnetosphere also occur at Earth; one of the main differences between the terrestrial and Jovian systems is in Jupiter's moons which are embedded within the magnetosphere and causes near- and far-field effects on Jupiter's auroral regions (e.g. Tsurutani, Southwood, Smith, & Balogh, 1993; Hospodarsky et al., 2012; Y. Shprits, Menietti, Gu, Kim, & Horne, 2012; Roussos & Kollmann, 2021; Y. Y. Shprits et al., 2018). The relative influence of each of these loss mechanisms on the energetic plasma population is an open questions of Jupiter's magnetosphere.

Through the comparative study of Earth and Jupiter's magnetospheres, we can gain a deeper understanding of the acceleration and loss processes of magnetospheres in general. Jupiter provides a unique opportunity to study a moon-embedded magnetosphere, and also one of the most extreme environments in the solar system, where the highest energy component of Jupiter's radiation belt is comparable to the magnetized region around neutron stars and galactic nuclei.

1.3 Motivation

When modeling the radiation belts of Earth and of other planetary systems, the effects of the loss process of EPP must be modeled accurately to quantify its relative impact on the full system. Being able to accurately reproduce, and eventually predict, EPP quantities, such as magnitude, spatial and temporal scales, and energy input, is vital to the understanding of both magnetospheric systems as well as planetary atmospheres.

This thesis describes an approach to quantifying the amount of energy lost from the radiation belts and deposited into the atmosphere through the proxy measurement of X-ray photons generated from bremsstrahlung interactions during EPP. In order to constrain the spatial scales and climatology of EPP, a CubeSat mission has been designed and implemented to measure X-ray spectra from EPP from low Earth orbit (LEO). Onboard the CubeSat is a novel X-ray imaging spectrometer developed at CU Boulder.

The Atmospheric X-ray Imaging Spectrometer (AXIS) instrument is designed, built, and tested for the Atmospheric Effects of Precipitation through Energetic X-rays (AEPEX) CubeSat

mission, which will generate data that are scientifically useful to both the radiation belt and atmospheric modeling communities. Kinetic EPP modeling is performed alongside the construction of the AXIS instrument to improve the latest estimates of the impact EPP has on the atmosphere and to quantify the proxy quantities that can be used as indirect measurements of EPP. An inversion method based on Green's functions is developed that improves the inversion accuracy of X-ray measurements to EPP parameter estimates.

The open questions of EPP that can be answered from the AEPEX mission and EPP modeling are related to the spatial and temporal scales of EPP, as well as the variability of the drivers of EPP. By obtaining meso-scale to global coverage of the X-ray signatures that EPP causes through many orbits, we can make definitive statements about the variability of EPP with different driving processes, as well as linking those drivers to spatial scales and spectral hardness of precipitation.

1.4 Contributions

In order to constrain the electron flux lost from the outer radiation belt, and subsequently input into the upper atmosphere through EPP, high spatial measurements coverage is needed. These measurements are invaluable in supporting theoretical modeling of magnetospheric acceleration and loss processes, and in data-model fusion efforts that go towards now-casting and eventually predicting the impacts that EPP has on both the radiation belts and the atmosphere.

Remote photon measurements from above have not been performed with modern instrumentation and inversion methods to electron precipitation characteristics; the AEPEX mission with the novel AXIS instrument will be the first dedicated mission to performing terrestrial hard X-ray observations for the purpose of quantifying radiation belt electron precipitation. The AXIS instrument developed in this work use a novel, wide field-of-view coded aperture optical system in order to achieve spatial resolution within the CubeSat form factor. This instrument has been selected and proposed as the heritage instrument design for multiple other missions, including on full-sized spacecraft and in NASA-funded concept studies to other planets.

The precipitation model development and simulations performed in this work improves the

accuracy of ionization profiles versus altitude, a vital input into atmospheric models that require parameterizations of EPP, and the generation, transport, and attenuation of bremsstrahlung photons by using the high fidelity, validated physics models of GEANT4. Further, this new model is verified against older analytical and Monte Carlo models, and validated using a combination of in-situ and remotely sensed data in two case studies.

This model is extended to Jupiter for the purpose of contributing to the study of comparative magnetospheres. This study aims to answer the question: are magnetospheric acceleration and loss processes observed at Earth unique to our system, or are they universal processes of all magnetized bodies? This leads to the NASA-funded concept study of the COMPASS mission, an in-situ orbiter to the Jovian system to study Jupiter's magnetosphere. Selected for this study is the AXIS instrument as heritage for the X-ray Imager (XRI) instrument onboard COMPASS. In addition to auroral precipitation, a variety of other X-ray sources are analyzed in order to design the XRI instrument.

The key contributions this work offers to the field of space physics and aeronomy can be summarized with the following points:

- The development of the AXIS instrument; a novel, wide field-of-view hard X-ray imaging spectrometer on the upcoming AEPEX CubeSat mission to observe bremsstrahlung photons generated in the atmosphere from EPP.
- The development of the coded aperture X-ray optics design and combined pinhole-constrained imaging deconvolution algorithm.
- The implementation of a new EPP model based off of the GEANT4 radiation transport code and validated with case studies using remote and in-situ data, leading to the improvement of EPP parameterizations
- The extension of the validated EPP model to Jupiter, in addition to other Jovian X-ray modeling, in order to design the XRI instrument for the COMPASS concept study mission to study the Jovian magnetosphere.

1.5 Organization

This thesis is organized into seven chapters and four appendices: this section concludes Chapter 1, a general introduction to planetary magnetospheres, Earth's radiation belts, and the process of EPP, as well as the motivation for this work. Chapter 2 is a more thorough treatment of the background physics of electrons and photons that are relevant to this work, including charged particle motion in a magnetic field and the bremsstrahlung X-ray generation process. Appendix A describes the bremsstrahlung cross section and numerical implementations of the process in physics simulations in more detail. The drivers of EPP from within the radiation belts, and atmospheric effects of precipitating electrons are included in this chapter, as well as previous missions that use a variety of techniques to study outer radiation belt electron losses through EPP.

Chapter 3 describes the AEPEX CubeSat mission and the development of the AXIS instrument, which will image and perform spectroscopy of bremsstrahlung X-ray photons generated by EPP in order to answer some of the open questions in the study of EPP. Appendix B supports this chapter by describing in-depth a calculation that relates the results of a numerical simulation to the background noise counts induced on the detectors in order to calculate the signal-to-noise ratio. Chapter 4 details the novel coded aperture X-ray optics of the AXIS instrument, including detailing the of X-ray detection theory, coded aperture imaging, and the pinhole aperture-constrained image inversion algorithm developed in this work. Simulations and laboratory testing of coded aperture imaging is documented in this chapter. Appendix C documents a Python implementation of the image reconstruction algorithm.

Chapter 5 transitions to electron kinetic modeling of the process of EPP, both in support of the AEPEX mission's future measurements and to advance the fidelity of state-of-the-art high-energy electron precipitation modeling and photon transport. Myriad model results are described in this chapter and two case studies are performed with data from a variety of different measurements in order to validate the model results and an inversion method based off of Green's function described in this work. This work is extended to Jupiter in Chapter 6, where many of the results

described in Chapter 5 for precipitation at Earth are calculated for Jupiter. Other X-ray sources at Jupiter are described to provide context for the COMPASS concept study mission to Jupiter, which includes an X-ray imaging spectrometer instrument based on the AXIS design. Appendix D describes a re-calculation of inverse Compton scattering in the Jovian radiation belt for use in the COMPASS mission design and by the community at large.

Chapter 2

Background

2.1 Charged Particle Motion in a Magnetic Field

The motion of charged particles in a magnetic field under the influence of electromagnetic forces are responsible for the transport of energy and matter throughout a magnetospheric system. A thorough understanding of how a particle will behave when subjected to electric and magnetic forces is vital in understanding the mechanics of precipitation, and enables further study of wave-particle interactions. This section will introduce the fundamentals of charged particle motion in order to provide context for a large portion of this work.

For a collection of charged particles (e.g. electrons and protons in a plasma), each particle is exerting an electric force on one another that is the dominant force at very small scales, typically on the scale of the **Debye length**, λ_D

$$\lambda_D = \sqrt{\frac{k_B T}{n\ q^2}} \tag{2.1}$$

where k_B is the Boltzmann constant, T is the average temperature of the plasma, n is the electron density (we assume here the plasma is **quasi-neutral**, i.e. $q_e n_e \approx q_i n_i$, the total charge of the negative and positive components of the system are balanced), and q is the particle charge number. Typical Debye length values range from 0.1 centimeters in the ionosphere and up to 100 meters in the magnetosphere (Blandford & Thorne, 2008). This section will describe the bulk behavior of a plasma that occurs on scales much greater than λ_D.

Charged particle motion is tied to the magnetic structure in the immediate vicinity of the

particle, so the magnitude, direction, and spatial and temporal gradients of the magnetic field are vital in the description of charged particle dynamics. Earth's magnetic field, to first order, is well approximated by a **tilted dipole field**, which varies spatially and is constant in time. Earth's dipole magnetic field can be described at any location above the Earth's surface, i.e. $r > R_{Earth}$, by the vector

$$\mathbf{B}(r, \lambda) = \frac{M}{r^3}\left(-2\sin(\lambda)\ \hat{r} + \cos(\lambda)\ \hat{\phi}\right) \tag{2.2}$$

where M is Earth's dipole moment of $8.05{\times}10^6$ T-km^3, λ is the *geomagnetic* latitude (tilted approximately 11° from the geographical latitude), and the coordinate r is measured from the center of the Earth and can be written in terms of altitude h from the Earth's surface as $r = R_{Earth} + h$. The vector components are described in a spherical coordinate system where $\hat{r}$ is the radial direction, $\hat{\phi}$ is the elevation angle (latitudinal) direction, and a dipole model predicts no magnetic field component in the azimuthal (longitudinal) direction $\hat{\theta}$.

A charged particle's motion in a magnetic field is primarily the effect of electromagnetic forces. This includes motion due to the electric and magnetic forces, as well as the transient motion induced when a charged particle travels through a spatially or temporally varying field. The Lorentz force describes the instantaneous motion of a particle with charge q in electromagnetic fields:

$$\mathbf{F} = q(\mathbf{E} + \mathbf{v} \times \mathbf{B}) \tag{2.3}$$

where $\mathbf{E}$ and $\mathbf{B}$ are the electric and magnetic field vectors, respectively, and $\mathbf{v}$ is the particle velocity with respect to the fields. This force can be related to acceleration $d\mathbf{v}/dt = \dot{\mathbf{v}}$ for a particle with mass m operating in non-relativistic and non-quantum regimes, i.e. the particle's velocity is much less than the speed of light and interactions occur at sufficient distances between particles such that they can be treated as point charges.

We'll assume a charged particle is travelling through a region where the influence of the magnetic field is much greater than the electric field, which is the case for much of near-Earth geospace. For now, we'll let $|\mathbf{E}| = 0$ and from here we can relate the particle acceleration to its

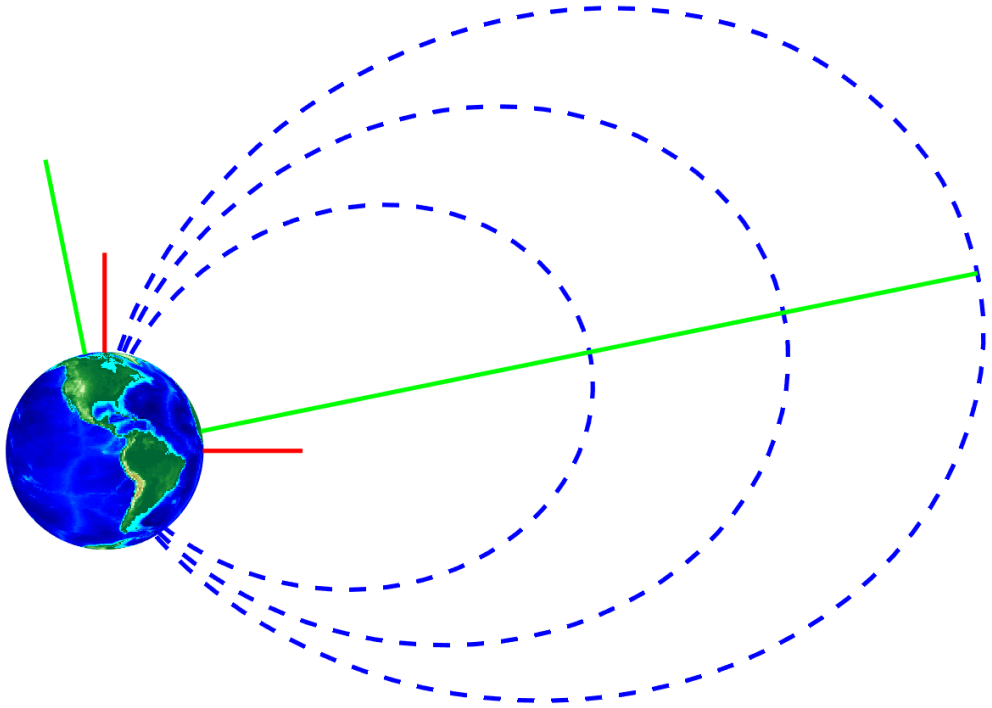

Figure 2.1: An example of magnetic field lines at L = 4, 6, and 8 in a tilted dipole model. The red lines show the geodetic axes and the green show the magnetic reference axes, drawn through the magnetic equator and magnetic north pole and tilted 11° with respect to the geometric axes that pass through the rotation North Pole and equator. Where the blue magnetic field lines cross the green magnetic equator axis is where L-shell number is equal to Earth radii.

velocity directly through the relationship

$$\dot{\mathbf{v}} = \frac{q}{m}(\mathbf{v} \times \mathbf{B}) \tag{2.4}$$

If we let the magnetic field be uniform in one direction, e.g. $\mathbf{B} = |\mathbf{B}|\hat{z}$, we can expand the cross product to write Equation 2.4 component-wise

$$\dot{v}_x = \frac{q|\mathbf{B}|}{m} v_y \tag{2.5}$$

$$\dot{v}_y = -\frac{q|\mathbf{B}|}{m} v_x \tag{2.6}$$

$$\dot{v}_z = 0 \tag{2.7}$$

Terms written in bars, e.g. $|\mathbf{B}|$, refer to the 2-norm or vector magnitude of a quantity. We can differentiate these equations again in time to find a useful relationship that directly relates the

velocity and its second time derivative:

$$\ddot{v}_x = \frac{q|\mathbf{B}|}{m}\dot{v}_y = -\left(\frac{q|\mathbf{B}|}{m}\right)^2 v_x \tag{2.8}$$

$$\ddot{v}_y = -\frac{q|\mathbf{B}|}{m}\dot{v}_x = -\left(\frac{q|\mathbf{B}|}{m}\right)^2 v_y \tag{2.9}$$

By writing Equations 2.8 and 2.9 in terms of Equations 2.5 and 2.6, we can decouple the cross-velocity dependencies and we now have independent equations in v_x and v_y. These equations can be solved with an ansatz of circular motion in the x-y plane of the form $v_x(t) = |\mathbf{v}|\cos(at)$, where the unknown coefficient a can be found by inspection:

$$v_x(t) = |\mathbf{v}|\ \cos\left(\frac{q|\mathbf{B}|}{m}\ t\right) \tag{2.10}$$

$$v_y(t) = -|\mathbf{v}|\ \sin\left(\frac{q|\mathbf{B}|}{m}\ t\right) \tag{2.11}$$

For simplicity, we neglect to include an initial velocity condition that makes this integration unique. The coefficient $q|\mathbf{B}|/m$ is the **gyrofrequency** of this motion and is denoted ω_c. In order to find the spatial dynamics of the charged particle, we can integrate in time and employ the geometric relationship between perpendicular velocity and angular rate at distance r through $v_\perp = \omega\ r$ to find the trajectory of the particle

$$x(t) = \frac{mv_\perp}{q|\mathbf{B}|}\sin(\omega_c t) \tag{2.12}$$

$$y(t) = \frac{mv_\perp}{q|\mathbf{B}|}\cos(\omega_c t) \tag{2.13}$$

where again some initial data are required that uniquely define this integrated form. From these equation we can define a related parameter, the **gyroradius** $r_g = mv_\perp/q|\mathbf{B}|$, which is the radius of the circular magnetized motion and is a function of the particle's momentum component $mv_\perp$ in the perpendicular direction with respect to the magnetic field vector. These quantities are derived under the special case where the magnetic field is uniform in the z-component, but hold for all $\mathbf{v}, \mathbf{B}$ if we specify that v is the velocity component perpendicular to the magnetic field $v_\perp$ in Equations 2.12 and 2.13. We'll define this component, and its complement the parallel, or field-aligned component, $v_\parallel$ as

$$v_\perp = |\mathbf{v}|\ \sin(\alpha) \tag{2.14}$$

$$v_{\parallel} = |\mathbf{v}| \ \cos(\alpha) \tag{2.15}$$

where α is the particle's **pitch angle** with respect to the background magnetic field. The pitch angle is a fundamental quantity in charged particle motion for trapped particles in Earth's magnetosphere and the pitch angle evolution of charged particles is the topic of extensive measurement and modeling efforts by the radiation belt community.

By combining the gyromotion and pitch angle motion, we can write the full kinematic equations for a charged particle in a uniform magnetic field as

$$\frac{\mathbf{v}(t)}{|\mathbf{v}|} = \begin{bmatrix} \cos(\omega_c t)\sin(\alpha) \\ -\sin(\omega_c t)\sin(\alpha) \\ \cos(\alpha) \end{bmatrix} \tag{2.16}$$

This vector describes both gyromotion about a magnetic field line as well as the spiraling pitch angle motion that is important in this work. Further, we can amend the gyroradius formulation for very high electron energies where mass and velocity become ambiguous where we can write the gyroradius instead with the perpendicular momentum component $r_g = p_{\perp}/q|\mathbf{B}|$. This formula is used to generate Figure 2.2 for a range of kinetic energies and pitch angles.

A variety of useful quantities can be found from this formulation. For instance, by reasoning that since a magnetic field does no net work on a particle, the amount of magnetic flux that passes through one complete circular gyrophase must be conserved, otherwise the particle would experience a net acceleration. By writing the current I through a loop of area A that's traced out by the electrons circular motion, we can calculate the dipole moment μ of the electron's motion, which is a conserved quantity of the magnetic motion:

$$\mu = I \times A = \text{constant} \tag{2.17}$$

An electron moving in a circle with perimeter C at velocity $v_{\perp}$ creates a current $qv_{\perp}/C$, where the perimeter is $C = 2\pi r_g$ and the area of the circle is $A = \pi r_g^2$; therefore the dipole moment is:

$$\mu = \frac{qv_{\perp}}{2\pi r_g} \ \pi r_g^2 = \frac{1}{2} q v_{\perp} r_g = \frac{m v_{\perp}^2}{2|\mathbf{B}|} \tag{2.18}$$

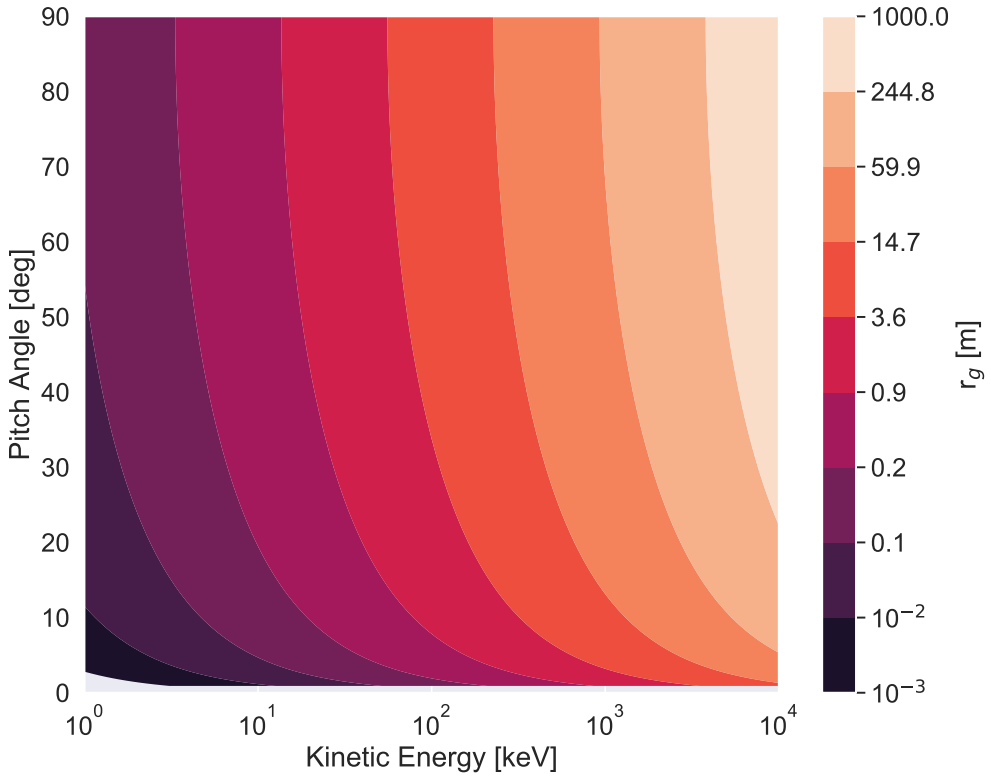

Figure 2.2: Plot of electron gyroradius r_g versus kinetic energy and pitch angle for a typical near-Earth magnetic field intensity of 50 μT. The relativistic formulation using the B-field-perpendicular momentum component is used to maintain the validity of this formulation at high electron kinetic energies.

This equation defines μ, which is known as the **first adiabatic invariant**. We'll add in the multiplicative factor γ to the kinetic energy in the numerator to allow this quantity to be valid for relativistic velocities, where $\gamma = (1 - (v/c)^2)^{-1/2}$ is the Lorentz factor and is as function of the electron's velocity v and the speed of light c. The conservation of the first adiabatic invariant is an approximation that is more accurate when processes that affect the electron's energy and momentum direction occur on time scales much slower than the electron gyroperiod, which is on the order of microseconds to milliseconds.

By writing $v_\perp$ as a function of the pitch angle, we can form a ratio that remains constant through the particle's motion that relates pitch angle and the amplitude of the magnetic field

between two points, marked with subscripts 1 and 2:

$$\mu_1/\mu_2 = \frac{\gamma m v^2 \sin^2(\alpha_1)}{2|\mathbf{B}_1|} \Big/ \frac{\gamma m v^2 \sin^2(\alpha_2)}{2|\mathbf{B}_2|} \tag{2.19}$$

where this ratio is equal to unity since μ is a constant. This substitution replaces $v_\perp$ with the total energy of the particle, which, since no other forces are acting on the particle and we assume adiabatic transport between the two points, is conserved and therefore constant between any two points within the magnetic field. We can then write the relationship

$$\frac{|\mathbf{B}_1|}{|\mathbf{B}_2|} = \frac{\sin^2(\alpha_1)}{\sin^2(\alpha_2)} \tag{2.20}$$

In a uniform magnetic field, the initial pitch angle would not evolve and the motion would be a consistent function of the particle's initial conditions, or initial position and velocity in the field. The pitch angle evolution is therefore driven by the spatial gradient in magnetic field intensity that occurs with the changing altitude and latitude of a particle as it travels along a magnetic field line. We can use the dipole field model described above to find $|\mathbf{B}|$ at various points in the near-Earth region.

Ultimately, in the absence of collisional interactions, wave-particle interactions, and other non-adiabatic effects such as spatial "kinks" in the magnetic field, a particle's pitch angle will follow the behavior described by Equation 2.20 exactly. We can rewrite Equation 2.20 as:

$$\sin(\alpha_1) = \sin(\alpha_2)\sqrt{\frac{B_1}{B_2}} \tag{2.21}$$

Given a magnetic field strength B_2 and a known pitch angle α_2 at location 2, and known magnetic field strength B_1 at location 1, we can determine the pitch angle of the particle when it reaches location 1. Furthermore, in some magnetic field configurations B_1/B_2, a particle's pitch angle α_1 can reach 90° and **mirror** along the magnetic field line, but only if the magnetic field B_1 is stronger than B_2. This bounce motion between mirror points, known as the magnetic bottle effect, is shown earlier in Figure 1.2 (e.g. Beskin, Gurevich, Istomin, Istomin, & Istomin, 1993).

Above the Earth's atmosphere, wave-particle interactions are one of the main drivers of radiation belt precipitation and are reviewed later in this chapter. A region where non-adiabatic

effects do occur consistently is within Earth's atmosphere. When a particle reaches altitudes lower than approximately 100 km, scattering interactions become dominant over the magnetized motion and precipitation becomes likely. A survey of these scattering interactions is presented in the next section, and if we simply assume precipitation will almost surely occur at or below 100 km, we can distinguish particles based on whether or not they will reach this altitude.

For any particle at point $\mathbf{r}_1$ in the dipole that mirrors at or below an altitude of 100 km can be described as being within the **loss cone**, whose boundary, the *loss cone angle*, is given by:

$$\alpha_{LC} = \sin^{-1} \sqrt{\frac{B(\mathbf{r}_1)}{B(h = 100 \text{ km})}} \tag{2.22}$$

By forming a ratio of the magnetic field strength at two points using Equation 2.2, we find that, in the near-Earth region (<1000 km) where the particle latitude is approximately the same, the ratio is a primarily a function of altitude:

$$\alpha_{LC}(h) \simeq \sin^{-1} \sqrt{\left(\frac{R_{Earth} + 100 \text{ km}}{R_{Earth} + h)}\right)^3} \tag{2.23}$$

Figure 2.3 shows the **bounce loss cone** (BLC) that forms when the loss cone edge α_{LC} is rotated around the magnetic field line in gyrophase.

In addition to the bounce motion explained above, various drift motions are possible that happen on timescales much slower than the gyro and bounce frequencies; of note are $E \times B$ drift that occurs in the presence of an electric field and affects auroral electron motion, magnetic gradient (grad-B) drifts that affects particles moving from a region of high to low (or low to high) magnetic field strength, and gravitationally-induced drift that becomes important when particles are closer to the Earth (e.g. Ejiri, 1978). The grad-B drift has a charged dependence that affects drift direction, and is responsible for the equatorial drift motion that particles experience (Daglis, Thorne, Baumjohann, & Orsini, 1999).

Of note, Earth's magnetic field is not a true dipole, and one of the ways it deviates from this model is in a dramatic weakening of the field over the Southern Atlantic Ocean. This phenomenon is referred to as the South Atlantic Anomaly (SAA) and is responsible for the formation of the

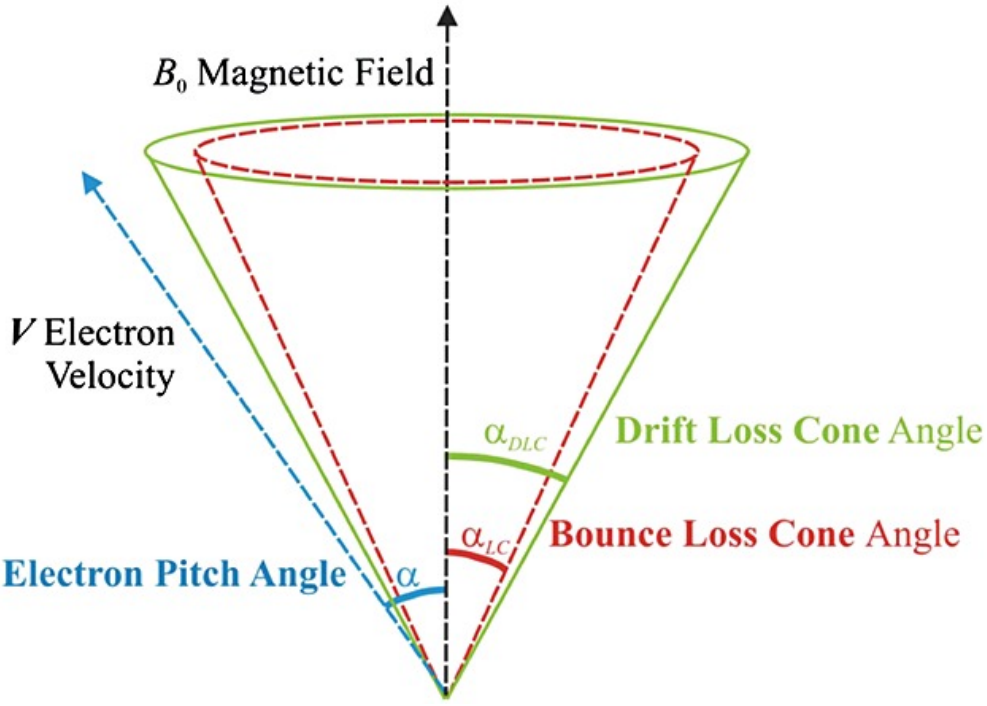

Figure 2.3: Diagram of the bounce loss cone (BLC) and drift loss cone (DLC) formed from the combination of electron adiabatic motion in a spatially varying magnetic field and energetic particle precipitation into the atmosphere below 100 km altitude. Figure from Rodger et al. (2013).

drift loss cone (DLC) that forms when particles circulate the Earth longitudinally and are lost through precipitation at the SAA. When particles drift in the equatorial direction around Earth, they can leave a region where they were locally trapped just outside of the BLC, and enter a region where the BLC expands (and maximizes to the angular size of the DLC) to contain the particles. Particles will subsequently precipitate in the region of the weaker magnetic field; these electrons are referred to as the "quasi-trapped" population. The relationship $\alpha_{DLC} \geq \alpha_{BLC}$ leads to interesting dynamics in the radiation belt and are outside the scope of this work (e.g. Bhatia & Lakhina, 1980; Tiwari & Varma, 1993; Bučík et al., 2005).

2.2 High Energy Electron and Photon Scattering Interactions

This section describes a selection of relevant scattering interactions that affect charged particles and photons and is relevant to the physics involved in EPP, X-ray detection, and charged

particle background on charge-sensitive instrumentation in space. Bremsstrahlung radiation, a charged particle mechanism that produces photons, is described in detail, followed by impact ionization, the primary ionization method from EPP, and various other photon and electron scattering mechanisms. The background generated by charged particles in photon instruments is expanded upon in Chapter 3, and X-ray interactions in terms of detection characteristics are expanded upon in Chapter 4.

2.2.1 Bremsstrahlung Radiation

The bremsstrahlung (from German, "breaking radiation") interaction is a charged particle phenomenon that results in a high-energy photon emission, typically at X-ray (∼keV) to gamma ray (∼MeV) energies. This process occurs when a free charged particle (e.g. an unbound electron) scatters sufficiently close through the Coulomb field of another particle such that one or both of the particles' trajectories are deflected. In doing so, one or both of the particles experience a force that decelerates the incident charged particle in a laboratory frame of reference, and accelerates the target, or previously stationary, particle. Since the total energy of a system must be conserved, the virtual photon that modulates the Coulomb interaction between the particles is converted into a real photon and is emitted, where it can freely propagate away from the interaction site (Koch & Motz, 1959; Bunkin & Fedorov, 1966). The initial and final particle momentum vectors, together with the photon energy and propagation direction, constitute a conserved system. Since this phenomenon is driven by a unbound particle and results in a photon, it's sometimes referred to as free-free radiation. A simplified diagram of this process is shown in Figure 2.4.

This process becomes relevant at ∼keV kinetic energies for electrons and has a strong dependence on the atomic number Z of the target scattering species for the reason mentioned above. In the context of radiation belt electron precipitation, this process occurs between electrons with 10s of keV to MeV kinetic energies and neutral atmospheric species, typically nitrogen (Z = 7) or oxygen (Z = 8). The atmosphere below 100 km is primarily comprised of nitrogen and oxygen gas, i.e. N_2 and O_2, but the bremsstrahlung interaction occurs between a single nucleus of these

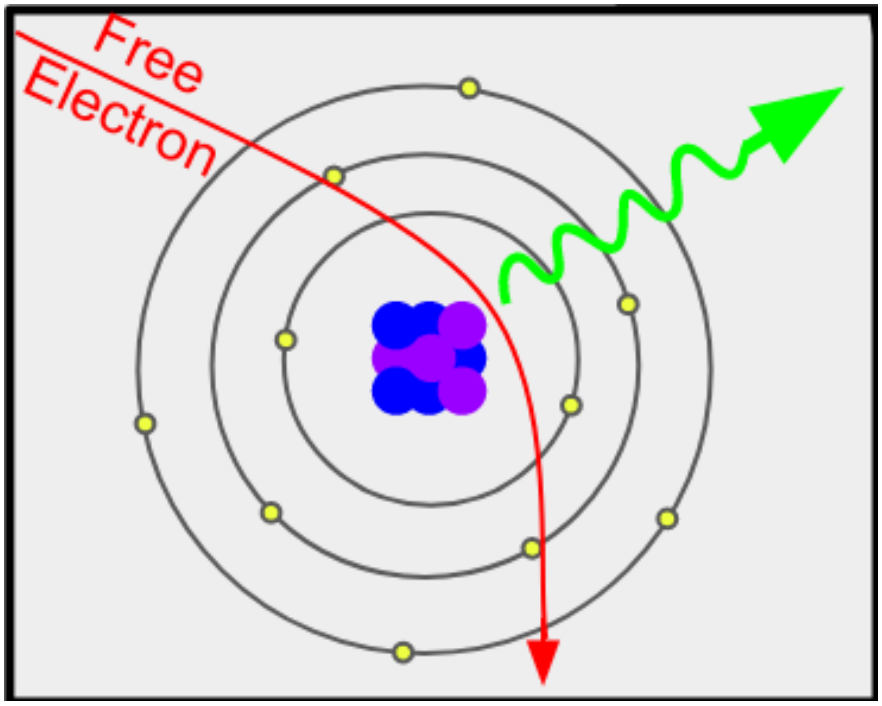

Figure 2.4: A qualitative illustration of the bremsstrahlung process, showing a free electron (red) which has its trajectory diverted by the Coulomb force from an atomic nucleus (blue and purple). Since the nucleus is typically much heavier than the electron, the electron experiences a deceleration and a photon (green) must be emitted to conserve the energy of the system. More accurate cross sections include the screening effect from the atom's bound electrons (yellow).

species so using the atomic number of the constituent atom of the gas is appropriate. This process can be used to remotely assess precipitation, and X-ray observations of Earth have been conducted previously by spacecraft for this purpose (see Section 2.5) (Imhof, Nakano, Johnson, & Reagan, 1974; Imhof, Kilner, & Reagan, 1985).

The bremsstrahlung cross section is parameterized by the target scattering species atomic number Z, the incident electron energy E, emitted photon energy $\hbar\omega$, and three angles: the electron incidence angle, the final electron propagation direction, and the photon emission angle. The initial electron direction and photon emission direction can be reduced to one solid angle element Ω by rotating the photon emission angle into the frame of the incident electron. Under this rotation, and by integrating over all possible final electron emission directions, the cross section can then be described with a differential cross section with only one angle $d\sigma(E)/d(\hbar\omega)d\Omega$. Without some

manner of approximation, many bremsstrahlung formulations are not solvable in closed form, so various trade offs are necessary in finding or approximating descriptions of this process.

If we instead integrate over final electron momentum directions, and choose not to rotate into the frame of the incident electron, we can write the triply-differential cross section with respect to two angles: electrons within the solid angle $[\Omega_p, \Omega_p + d\Omega_p]$ and photons within the solid angle $[\Omega_k, \Omega_k + d\Omega_k]$, where the solid angle differential element is defined as $d\Omega = \sin\theta \; d\theta \; d\phi$, from Koch and Motz (1959):

$$\frac{d\sigma}{d(\hbar\omega) \; d\Omega_k \; d\Omega_p} = Z^2 \; \alpha \; \left(\frac{r_0}{2\pi}\right)^2 \; (1 - F(q,Z))^2 \; \frac{1}{\hbar\omega}\frac{1}{q^4}\frac{p}{p_0}\left\{\frac{p^2 \; \sin^2\theta}{(E - p\cos\theta)^2}(4E_0^2 - q^2) + \right.$$

$$\frac{p_0^2 \; \sin^2\theta_0}{(E_0 - p_0\cos\theta_0)^2}(4E^2 - q^2) - \frac{2pp_0 \; \sin\theta\sin\theta_0\cos\phi(4EE_0 - q^2)}{(E - p\cos\theta)(E_0 - p_0\cos\theta_0)} +$$

$$\left.\frac{2(\hbar\omega)^2(p^2\sin^2\theta + p_0^2\sin^2\theta_0 - 2pp_0\sin\theta\sin\theta_0\cos\phi)}{(E - p\cos\theta)(E_0 - p_0\cos\theta_0)}\right\} \quad (2.24)$$

where $F(q,Z)$ is an atomic form factor, and the total momentum transferred to the nucleus q is defined as

$$q^2 = p^2 + p_0^2 + (\hbar\omega)^2 - 2p_0\hbar\omega\cos\theta_0 + 2p\hbar\omega\cos\theta - 2p_0p(\cos\theta\cos\theta_0 + \sin\theta\sin\theta_0\cos\phi) \quad (2.25)$$

where $\alpha \approx 1/137$ is the fine structure constant, r_0 is the classical electron radius, p_0 and p are initial and final momentum of the electron, E_0 and E are the initial and final electron energies respectively, θ_0 and θ are incident and final in-plane electron angles with respect to the photon emission direction, and ϕ determines the rotation of the plane of emission. This equation is in canonical units (e.g. momentum in units of m_0c) such that photon energy and electron momentum are directly comparable.

The full differential cross section that is reached by different starting assumptions and including various effects such as electronic screening of the nucleus is lengthy and is described in Appendix A. The general behavior of the process, fixing other quantities, is a spectrum proportional to $Z^2/\hbar\omega$ for photon energy, and total likelihood proportional to the electron energy, for

incident electron kinetic energies from keV to MeV. Figure 2.5 shows the photon angular emission distribution with initial electron energy from a non-relativistic dipole radiation pattern approximation to the bremsstrahlung interaction from J. D. Jackson (2007). Note the forward beaming with respect to the incident electron direction that occurs with higher electron energies, and conversely the higher degree of isotropy at lower electron energies.

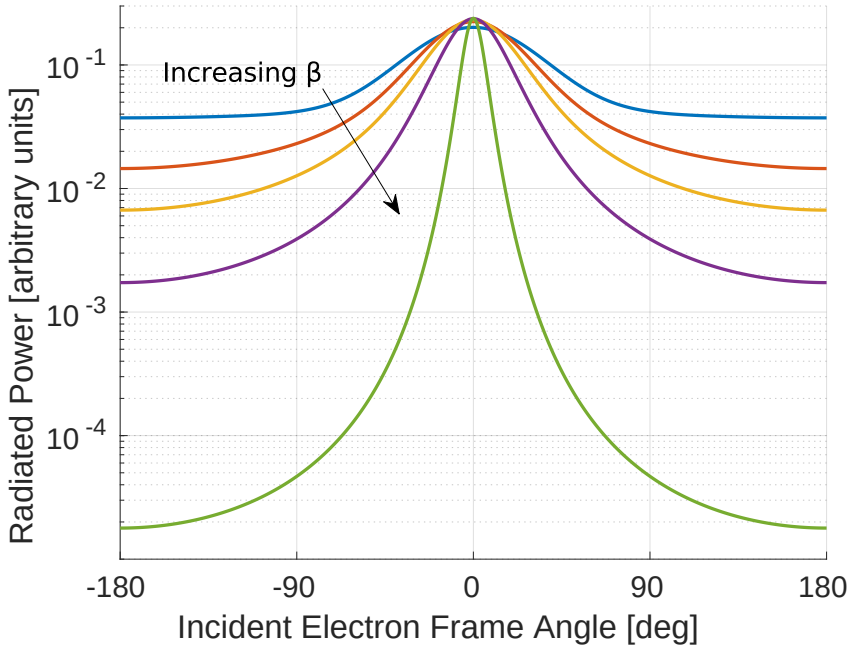

Figure 2.5: Thick target (electron-neutral) bremsstrahlung radiated power (proportional to likelihood of photon emission) vs. photon emission angle (relative to incident electron plane), for relativistic velocity ratio $v/c = \beta = 0.5, 0.7, 0.8, 0.9$, and 0.99 (electron kinetic energies of 80 keV - 3 MeV). This cross section comes from the J. D. Jackson (2007) dipole radiation pattern approximation, and is less accurate when the electron β approaches unity, i.e. highly relativistic electrons.

Various other approximations and derivations exist to quantify bremsstrahlung that are valid in various regimes. One of these is the electronic screening term, which incorporates the effect of the collective negative charge the electron shells have on the nucleus that reduce the magnitude of the Coulomb force on the incident electron (Tseng & Pratt, 1971). Another mathematical factor is the Gaunt correction factor, which, if starting from hard sphere scattering, can account for relativistic effects that alter the mass of the incident electron at high kinetic energies (Brussaard & Van de Hulst, 1962; Feng, Lamoureux, Pratt, & Tseng, 1983).

An important role bremsstrahlung plays in precipitation is in the transport of energy deeper into the atmosphere. When an electron produces an X-ray photon through bremsstrahlung, that photon will tend to continue forward, which, depending on the scattering interaction plane and photon emission direction, may allow deeper penetration into the atmosphere. From there, a Compton electron or photoelectron can be generated by the photon that may have significant kinetic energy, such that it can in itself generate another bremsstrahlung photon. When repeated until the energy is depleted, this process is referred to as an electromagnetic shower and is responsible for energy transport down well into the mesosphere and stratosphere from EPP. For sufficiently high energy precipitation events, a secondary ionization peak will form below the primary ionization peak from bremsstrahlung transport. For the formulas for bremsstrahlung see Seltzer and Berger (1986), and for analytical estimates of bremsstrahlung in planetary atmospheres, see M. Berger and Seltzer (1972).

Bremsstrahlung is more likely in dense, high Z-number materials and is similarly described by the formulas described in this section. This effect is expanded upon in Chapter 3 where shielding is designed to mitigate the bremsstrahlung background from charged particles incident on instrument materials such as tungsten.

2.2.2 Impact Ionization

One of the ionization methods in Earth's atmosphere from radiation belt precipitation is impact ionization of neutral species by the energetic electrons. This interaction is complicated in that it encapsulates many possible scattering interactions, but for energies above than the atomic binding energies, the cross section can be described by a smooth function, for example in Figure 2.6. When the electron energy is closer to the atomic electron transition energies, the interaction become more complicated and less continuous.

The cross section at keV electron kinetic energies behaves as $\sigma \propto \ln(E)/E$ in gases, which is illustrated in Figure 2.6 for energetic electrons passing through an atomic hydrogen gas (Lotz, 1967). There exists a peak in the cross section at medium energies: this can be thought of as

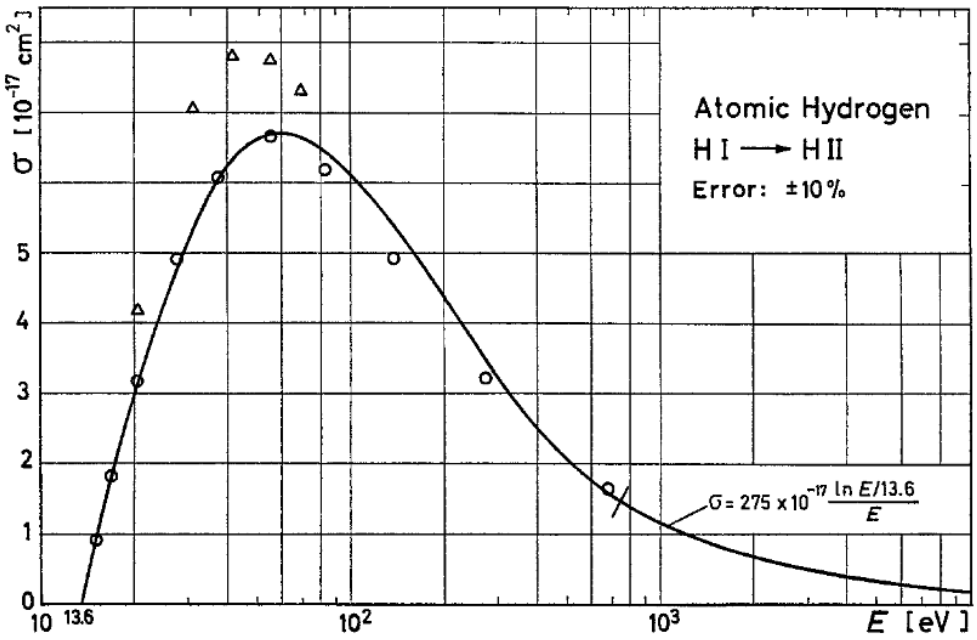

Figure 2.6: Empirical formula for impact ionization of hydrogen by electrons from Lotz (1967), showing the curve beginning above first ionization energy of hydrogen of 13.6 eV and behaving proportionally to $\ln(E)/E$ at high energies.

the maximum of "interactivity time": at higher energies, electrons are travelling more quickly and interact with the neutral molecule for less time, and at lower energies, electrons interact longer but do not have as much momentum to transfer to the bound electrons to free them. This is an illustrative description and the true nature of this interaction is quantum in nature and must be calculated with full wave methods.

In precipitation, the effect of the energy-dependent cross section that peaks at medium energies, combined with the exponentially increasing density combine to create sharp peaks in ionization profiles that may only be 1–2 km wide and are one to many orders of magnitude higher in ionization rate than the profile outside of this peak. The characteristics of these ionization profiles versus altitude are expanded upon in Chapter 5 where a full 3D Monte Carlo model of impact ionization and other scattering interactions are simulated. For more details on the intricacies of characterizing impact ionization, see Mark (1982) for derivation from first principals and Märk and Dunn (2013) for a review of electron impact ionization.

2.2.3 Compton Scattering and the Photoelectric Effect

Various interaction processes describe how photons interact with and generate electrons. These interactions occur within the atmosphere after bremsstrahlung radiation is produced, and are described here. Compton scattering and the photoelectric effect are alike in that they both occur between an energetic photon and a "cold" or stationary (relative to the speed of light) electron. The difference lies in the end products of the scattering interaction: the photoelectric effect requires that the photon is absorbed completely, while Compton scattering occurs at higher energies where the photon continues propagating in addition to the newly freed electron (Eisenberger & Platzman, 1970; Pratt, Ron, & Tseng, 1973).

Compton scattering is typically a medium energy phenomenon (relative to the photoelectric effect at lower energies and pair production or nuclear interactions at higher energies) and the exact cross section for the interaction depends upon the material. Figure 2.7 shows the relative influence of each scattering process through an intermediate, material-specific quantity, the photon attenuation coefficient μ, versus photon energy to illustrate how the dominant cross section varies.

Although photons are massless, they carry energy and momentum, and the loss of energy from the photon is conserved via the acceleration of the electron, i.e. the collision is inelastic in nature. The loss of energy of the photon manifests as a shift in wavelength of the photon as well as a redirection of the photon trajectory, both of which are coupled and can be described by

$$\lambda' - \lambda = \frac{hc}{m_e c^2}(1 - \cos\theta) \tag{2.26}$$

where λ and λ' are the photon wavelength before and after scattering, respectively, $h/m_e c$ is the Compton wavelength of the electron, and θ is the re-emission angle of the photon after scattering with respect to the initial photon angle. From the shift in wavelength in Equation 2.26, the energy of the re-emitted photon E'_{ph} can be found through

$$E'_{ph} = \frac{E_{ph}}{1 + (E_{ph}/m_e c^2)(1 - \cos\theta)} \tag{2.27}$$

Note that the loss of energy of the photon is maximized at the backscatter case of $\theta = \pi$ and

minimized at the forward scatter case of $\theta = 0$. These formulas are valid for the "cold electron" assumption, i.e. the photon energy is much greater than the electron energy, $\hbar\omega \gg E_e$, such that the electron is considered stationary relative to the photon. When the electron $\beta = v/c$ factor gets closer to unity, this assumption breaks down, and in the extreme case where β approaches one, the electron can energize the photon: this is referred to as inverse Compton scattering, which needs a different treatment and is described in the next section. The phenomenon of inverse Compton scattering occurs in galactic centers, near pulsars, and in the radiation belts of Jupiter. The Klein-Nishina cross section formula with electronic screening encapsulates these effects and is the current best estimate for a full description of Compton scattering (Klein & Nishina, 1928; Moderski, Sikora, Coppi, & Aharonian, 2005; Krajewska, Vélez, & Kamiński, 2015).

In the more dense part of the atmosphere, photons undergo a random walk caused by Compton scattering collisions where the collision frequency is dependent upon the photon energy and the atmospheric number density (Madej, 1989). These two effects combine into an effective random walk intensity that can be described by the mean free path l of photon collisions, which ultimately statistically determines the depth at which a photon can no longer escape upwards beyond the atmosphere, or the atmospheric depth at which the photon loses its energy and is absorbed into the atmosphere. This stochastic random process is well-modeled by a closed form mean free path formulation when the collision cross section behaves smoothly; however, at higher energies the occurrence of certain scattering interactions becomes rarefied and a Monte Carlo approach is necessary. A kinetic formulation of the mean free path when one species is travelling much faster than another can be modeled as

$$l = \frac{1}{n\sigma} = \mu^{-1} \tag{2.28}$$

where n is the number density of the material and σ is the total interaction cross section. μ is the photon mass attenuation coefficient and can be related to the mean free path by taking the reciprocal of μ. High energy photons in particular typically interact "catastrophically," (e.g. Lorence Jr, Morel, and Valdez (1989)) in that when the photon interacts with another particle the photon is

either transmitted or absorbed completely, instead of having its wavelength or trajectory altered, such that the Beer-Lambert absorption law effectively describes high energy photon transport:

$$I(x) = I_0 \; e^{-x/l} = I_0 \; e^{-\mu \; x} \tag{2.29}$$

where I_0 is the incident flux or intensity and $I(x)$ is the flux or intensity after transiting distance x through a medium with mean free path l or mass attenuation property μ. The mean free path for photons with energies 1 keV – 20 MeV in air at sea level and in various materials is shown in Figure 2.8, showing the characteristic energies of each material at electronic shell energies. The values range from micrometer mean free paths at low photon energies in dense, high Z materials, to 100s of meters in air at MeV energies (Judge et al., 2015). The energetic attenuation coefficient, sometimes written as μ_{en}, accounts for radiation produced in the material that is transmitted through the material, but is distinctly not the incident radiation. Note that in Figure 2.8 the mean free path calculated from the energetic attenuation coefficient is longer than the mass attenuation coefficient and is more pronounced as higher incident photon energies.

2.2.4 Other Interactions

There are a variety of other charged particle and photon interactions that are relevant to precipitation of radiation belt electrons. They occur either only at very high photon energies, such as pair production which requires a photon that has energy that is twice the electron's rest mass energy (1022 keV); or lower energies, when electrons lose the majority of their energy and are closer to the thermal plasma energies of the ionosphere, where bound electron line transitions, Joule heating, and electron capture cross sections become important (e.g. Bauer, 1994) (Motz, Olsen, & Koch, 1969). Inverse Compton scattering is another interaction that occurs between ultra-relativistic electron energies and low energy photons, such as in Jupiter's radiation belt from solar optical photons, and is expanded up in Chapter 6 (Jones, 1968).

Electron-positron pair production in the atmosphere occurs when a photon with energy greater than or equal to 1022 keV (i.e. 2×511 keV, the sum of the electron and positron masses)

interacts with an atomic nucleus. The nucleus experiences recoil since a massive particle is needed to mediate the interaction and conserve momentum, and at least 1022 keV of the photon's energy is spontaneously converted into an electron-positron pair. Excess photon energy and the recoil of the atomic nucleus also contribute to the pair's kinetic energy, which does not necessarily have to be equally distributed to each particle. Both particles are free to propagate away from the interaction site; however, the positron has a high capture cross section in a collisional gas medium, which subsequently causes electron-positron annihilation. Annihilation results when a free or valence electron combines with the positron, causing the pair to spontaneously be converted into two 511 keV photons that necessarily propagate in direct opposite directions from each other. This 511 keV *annihilation line* commonly shows up in atmospheric X-ray spectra, as it is a common by-product of GCR interactions with the upper atmosphere as well as high energy precipitation (e.g. Knödlseder et al., 2005; L. Blum et al., 2015). Pair production can be thought of as the inverse process of bremsstrahlung, and the cross sections for these processes are strikingly similar except for small differences. The Feynman diagram of these processes are the same, with the bremsstrahlung interaction converting the interaction between two charged particles to a photon in the forward direction, and pair production converting a photon into two charged particles in the reverse direction.

In contrast, at lower energies when the electron has propagated through the atmosphere and has lost energy to radiative and collisional interactions, the electron kinetic energy is now on par with atomic binding energies. At 100s eV kinetic energies, the electron can now excite a bound electron instead of freeing it from its orbital shell. In the process of deexcitation, a characteristic photon is emitted in the visible to ultraviolet wavelengths, which is responsible for the formation of the visible aurora, or aurora borealis in the northern hemisphere and the aurora australis in the southern hemisphere. These characteristic emissions come from the atmospheric constituents between 80–120 km, which are primarily atomic oxygen O and the diatomics O_2 and N_2.

The combination of the interactions mentioned above are often combined into one "friction force" formulation that is proportional to particle velocity, or energy, alone. This method is similar

to the continuous slowing down approximation (CSDA) made in charged particle stopping power calculations, such as those included in the NIST ESTAR stopping power tables (M. J. Berger, Coursey, Zucker, et al., 1999). This method does not account for what has historically been referred to as "delta ray" production, or the combination of secondary electron emission and photon production, which must be calculated and implemented separately in simulation if CSDA physics are used.

2.3 Radiation Belt Drivers of Precipitation

The radiation belts are a dynamic and interconnected population of highly energetic charged particles. The outer radiation belt in particular is highly variable in location, flux intensity, and energy content. Ultimately, the primary driver of the outer radiation belt is the Sun; the solar wind is the source of a portion of the electron flux, and solar conditions dictate the energy content and fluxes present in the radiation belts. Coronal mass ejections (CME) and co-rotating interaction regions (CIR) are two solar events that indirectly impact the outer radiation belt and subsequently drive geomagnetic storms, space weather, and eventually precipitation (Longden, Denton, & Honary, 2008).

One way to quantify the intensity of a geomagnetic storm induced by solar activity is through the disturbance storm time (Dst) index. The Dst index is a magnetic intensity perturbation measurement made at the equator that serves as a measure of geomagnetic storm intensity: the Dst dips negative proportionally to the intensity of a geomagnetic storm, then gradually recovers to near 0 nT, i.e. the nominal unperturbed state (Rostoker, 1972; Mayaud, 1978). The Dst is directly an observation of the ring current, which, when enhanced during a geomagnetic storm, generates a magnetic field that opposes the Earth's at the equator, which is why the negative directional is associated with stormtimes. Enhanced precipitation rates are temporally correlated with the recovery phase of a geomagnetic storm as the Dst slowly returns to its nominal state, when wave activity is higher (Gonzalez, Tsurutani, & Clúa de Gonzalez, 1999; Balan, Otsuka, Nishioka, Liu, & Bailey, 2013).

The state of the outer radiation belt is mediated by electromagnetic and plasma wave activity (Thorne, 2010). The whistler mode wave is a plasma wave that is right-hand circularly polarized with frequencies less than the local ion gyrofrequency and greater than the electron gyrofrequency. Whistler mode waves interact with radiation belt electrons in the keV – MeV energy range and can drive precipitation (Kersten et al., 2011; Tao & Bortnik, 2010). Whistler mode waves include chorus, hiss, and lightning-generated whistler (LGW) varieties (Stenzel, 1976). These wave modes can be generated from atmospheric lightning, anthropogenic very low frequency (VLF) transmitters, and magnetospheric plasma instabilities (Sonwalkar & Inan, 1989; Koons, Edgar, & Vampola, 1981; Burtis & Helliwell, 1976). See Ripoll et al. (2020) for a review of wave modes and open research questions on magnetospheric plasma waves.

Wave-particle interactions can accelerate particles through Landau or cyclotron resonance and cause loss by pitch angle scattering of electrons into either the bounce or drift loss cones (Narita, 2017; Artemyev, Vasiliev, Mourenas, Agapitov, & Krasnoselskikh, 2013; Omura et al., 2019). Figure 2.9 shows electron velocity component $(v_\perp, v_\parallel)$ diagrams and how electron populations are heated and scattered through wave-particle interactions.

One of the open topics in the study of EPP is in linking the driving mechanisms to precipitation characteristics. Forming a relationship between plasma wave activity to precipitating electron spectra and precipitation region size would increase the understanding of the magnetosphere-atmosphere coupling.

Some of the smallest spatial scales in precipitation arise from a specific type of EPP called **microburst** precipitation. Microbursts are primarily correlated with two wave modes: whistler-mode chorus and another wave mode, the electromagnetic ion cyclotron (EMIC) wave. Whistler-mode chorus is associated with lower energy precipitation signatures, while the microbursts associated with EMIC waves feature fast temporal scales and enhancements at MeV energies (L. W. Blum et al., 2015; Capannolo, Li, Ma, Shen, et al., 2019). Fluctuations in microburst precipitation is on the order of 10 – 100 milliseconds and is associated with slowly varying X-ray signals on the scale of 5 – 15 second measured above the atmosphere by rocket missions, and fast varying signals on the

scale of 50 ms within the atmosphere by balloon missions (Tsurutani, Lakhina, & Verkhoglyadova, 2013; Anderson et al., 2017). This discrepancy in X-ray time signatures is likely due to instrument limitations. The spatial scales of microburst precipitation is bounded by data analysis from the Van Allen Probes, and the FIREBIRD-II and AeroCube-6 CubeSat missions (L. Blum, Bonnell, Agapitov, Paulson, & Kletzing, 2017; Shumko et al., 2018, 2020).

Pulsating aurora is a primarily lower energy, high latitude phenomenon that may have high energy signatures from relativistic electrons with energies up to multiple MeV and may also be related to the microburst precipitation phenomenon described above (Johnstone, 1978; Johnson et al., 2021; Kawamura et al., 2021). Pulsating aurora can have temporal signatures on the scales of 1 to a few Hz and is driven by many of the same processes as radiation belt precipitation (Nishimura et al., 2010). The spatial scales or auroral precipitation are more readily studied using optical-wavelength all-sky imagers (Royrvik & Davis, 1977).

2.4 Atmospheric Effects from Precipitation

On the other side of EPP is the Earth's atmosphere. Energetic electrons that enter the atmosphere from EPP can cause a variety of direct and indirect effects in the atmosphere (C. Randall et al., 2005, 2006). Precipitating electrons collide with the neutral constituents of the atmosphere and cause excess ionization from the top of the atmosphere down to ∼50 km or even lower, which enhances ionospheric conductance, in turn feeding back into magnetospheric behavior (Voss & Smith, 1980; Galand & Richmond, 2001; Khazanov et al., 2018). Figure 2.10 shows a schematic of the depth into the atmosphere different particle populations penetrate and some of their consequences.

The solar forcing on the atmosphere through the radiation belts can be quantified by remote measurements of molecular compounds, such as NO_x and HO_x (Andersson, Verronen, Rodger, Clilverd, & Seppälä, 2014). NO_x and HO_x are generated by EPP indirectly through excess ionization, which causes a perturbation in the atmospheric chemistry balance. Figure 2.11 shows the descent of NO_x into the stratosphere over the course of months from a variety of datasets, including measurements and modeling. Importantly, the "truth" value (top left) is taken from the MIPAS data

set which is a remote measurement of NO_x, and the lines drawn on the figure reflect the contours of this data set. The subsequent modeling efforts are not able to reproduce the NO_x descent measured by MIPAS under the current parameterizations of EPP forcing (Flaud et al., 2003; J. Pettit et al., 2019).

Modeling NO_x is important since it can catalytically destroy ozone in the mesosphere and stratosphere. Enhanced EPP is also correlated with modification of the polar vortex behavior and with sudden stratospheric warming events (Holt et al., 2013a; C. Randall et al., 2009). The behavior of atmospheric waves, and therefore atmospheric energy and mass transport, are affected by EPP.

2.5 Previous Missions studying Energetic Particle Precipitation

There have been a number of previous missions dedicated to studying EPP from different perspectives using various direct and indirect measurement techniques. In-situ charged particle and wave measurements of the radiation belts from spacecraft have a history dating back to the discovery of the radiation belts in 1959 (Van Allen, 1959), while remote or indirect atmospheric measurements first became viable with the advent of radio wavelength transmitters and receivers in the early 20th century (Bailey & Martyn, 1934). EPP causes excess ionization in the atmosphere which modifies the conductivity and wave reflectance properties of the ionosphere, which is detectable by a battery of methods (Obayashi & Hakura, 1960b). This section provides a brief and illustrative review of previous missions studying radiation belt precipitation from early charged particle detectors to modern X-ray telescopes conducting observations of Earth.

Spacecraft-based missions to study radiation belt precipitation using charged particle detectors are an in-situ view of the acceleration mechanisms and energetic charged particle populations that go on to precipitate and enter the atmosphere. Of note are the SAMPEX, DEMETER, and FIREBIRD missions, each of which focused on in-situ charged particle measurements from low-Earth orbit (LEO) to quantify secular and periodic loss of electron flux in order to associate radiation belt losses with the dynamic driving phenomena (D. N. Baker et al., 1993; Lagoutte et

al., 2006; Johnson et al., 2020). These missions flew charged particle detectors, often in the form of the relativistic particle telescope design, which stacks solid state detectors to increase energy range and resolution of the measurements. The measurement of pitch angle-resolved spectra is desirable to study and track the evolution of electron populations with wave activity, however not all charged particle instruments have angular resolution, or do not cover an energy range that is sufficient to study radiation belt electrons.

Other missions often used to study the radiation belts are the Polar Orbiting Environment Satellite (POES) and Meteorological Operational (MetOp) satellite series, which are number of satellites that have achieved continuous coverage in LEO with charged particle instruments on board (e.g. Edwards & Pawlak, 2000; Davis, 2007). POES energetic particle data have been used on its own and in conjunction with other missions in myriad studies, e.g. in the construction of a decades-long LEO electron data set in J. M. Pettit, Randall, Peck, and Harvey (2021), in studying radiation belt dynamics that reach LEO in Rodger, Clilverd, Green, and Lam (2010), and in conjunction with RBSP in W. Li et al. (2013), among many others. The POES and MetOp satellites are operational missions with other instrumentation onboard and have long periods of coverage, versus science missions, e.g. FIREBIRD, and RBSP, which have specific instrumentation for sampling waves and particle measurements, but have limited lifetimes.

In general, analysis of transport and time-evolution of charged particle phenomena can be achieved with multi-point measurements between spacecraft with similar or complementary instruments (Whittaker, Gamble, Rodger, Clilverd, & Sauvaud, 2013; Crew et al., 2016). A common analysis technique used between multiple spacecraft is through magnetic conjunction analysis. A conjunction is a small window in time and space when two (or more) spacecraft are co-located on the same magnetic field line at different altitudes.

However, these opportunities are limited in their occurrence frequency and carry the uncertainty of the magnetic field model used to determine magnetic conjugation. Nonetheless, these analysis types have been successfully carried out between multi-point spacecraft-based measurements and ground-based EPP measurements (e.g. L. W. Blum et al., 2015). Figure 2.12 shows

the relative altitudes at which various measurements can be made by various instruments and techniques.

The Van Allen Probes (previously known as the Radiation Belt Storm Probes, or RBSP) mission was equipped with a suite of instruments to study radiation belt sourcing and acceleration and serves as one of the leading missions in the field of heliophysics (Fox & Burch, 2014). Through coincident measurements with other spacecraft, ground-based, and balloon-based instrumentation, the scope of the science questions that can be addressed through these missions can be expanded. Balloon Array for Radiation-belt Relativistic Electron Losses (BARREL) is one such balloon mission that coordinated with RBSP to focus on radiation belt losses. X-ray measurement are recorded from stratospheric balloons as a proxy for radiation belt precipitation (Millan et al., 2013). Specifically, a focus of this mission was in linking wave activity in the radiation belts to the intensity of microburst precipitation (e.g. Woodger et al., 2015; Anderson et al., 2017). Due to the 10s km path length that an X-ray must transit through the middle atmosphere to reach balloon altitudes, a fraction of the spectrum is absorbed by the time it reaches BARREL's detectors, and thus only a subset of the X-ray spectrum can be observed. An inversion technique was implemented in order to estimate the precipitating flux and spectrum from the reduced X-ray spectrum measurement, which has high uncertainty without supporting in-situ measurement information from LEO to constrain the inversion procedure (Clilverd et al., 2017).

In addition to mid-atmosphere measurements of X-rays, ground-based measurements of excess ionization are possible in the D- and E- regions of the ionosphere with radar. VLF remote sensing of the ionosphere to detect regions affected by EPP is also possible, (e.g. Cummer, Bell, Inan, & Chenette, 1997; Gasdia & Marshall, 2023; Sanchez et al., 2022; Ma et al., 2022).

Ephemeral measurements of X-rays from above the atmosphere can be obtained by rocket missions. Østgaard et al. (1998) details correlation between pulsating aurora and X-ray production by coincident observation. A review that includes a history of such measurements is Tsurutani et al. (2013), which reports slowly varying X-ray signals (5–15 seconds) associated with EMIC waves and microburst precipitation.

The observation of X-ray photons may be performed more simply from "above" the atmosphere with an instrument pointed towards nadir in order to provide a measurement of EPP bremsstrahlung photons. Figure 2.12 shows the geometry of this configuration, relative to ground- or balloon- based observations. X-rays that leave the optically-thin atmosphere upwards are less susceptible to the spectral absorption issues experienced by BARREL, namely Compton scattering and photoabsorption that limit the energy spectra and obscure the photon generation source location. Observations of Earth in the X-ray band from outside the atmosphere have been performed and missions that are especially relevant to precipitation imaging are summarized next. Figure 2.13 shows a collection of terrestrial observations of hard X-rays made by spacecraft, which are summarized below.

In the hard X-ray band (∼10s to 100s of keV) energy band are the similarly-named Atmospheric X-ray Imaging Spectrometer (AXIS) instrument on the Upper Atmospheric Research Satellite (UARS) mission with an energy range of 6–150 keV, and the Polar Ionospheric X-ray Imaging Experiment (PIXIE) onboard the Polar satellite that imaged the Earth in the 2–60 keV X-ray band (Winningham et al., 1993; Imhof et al., 1995). PIXIE was able to image the entire auroral oval at the apogee of its orbit with ∼700 km spatial resolution (Bhardwaj, Elsner, et al., 2007). However, due to the lower energy range and limited dynamic range on AXIS and PIXIE, the instruments primarily observed auroral precipitation instead of the higher energy radiation belt precipitation. Additionally, contamination occurred at the instruments' low to middle energy ranges from solar X-ray albedo reflected off of Earth's atmosphere and celestial X-ray sources. The spatial resolution of these instruments was also insufficient to identify the spatial scales of precipitation that would allow for L-shell discrimination.

The Chandra X-ray Observatory has also obtained intermittent measurements of X-rays in the 0.1–10 keV band from Earth's atmosphere, but without extended campaigns cannot provide a basis for a sufficient statistical study The observation campaign of Bhardwaj, Gladstone, et al. (2007) found that Earth's soft X-ray component is highly variable, but clearly shows nitrogen and oxygen K_α line emissions at 0.39 keV and 0.52 keV, respectively, in addition to the bremsstrahlung

X-ray continuum. Measurements of opportunity have occurred when Earth passes through International Gamma-Ray Astrophysics Laboratory (INTEGRAL) spacecraft's line-of-sight during a fixed-pointing campaign. INTEGRAL is primarily an astronomical X-ray telescope for observing stellar X-ray sources. Observations of Earth in the hard X-ray and gamma-ray bands (10s keV to 10s MeV) are described in Churazov et al. (2007) using data from the INTEGRAL spacecraft.

These previous missions have observed Earth in various X-ray energy bands that cover auroral to radiation belt precipitation for limited periods of time. However, gap exist corresponding to radiation belt precipitation photon energies as well as the spatial coverage necessary(in MLT and latitude) to sufficiently observe radiation belt precipitation. The stronger auroral optical signal can obscure radiation belt precipitation signals; therefore X-ray spatial, spectral, and flux information is desired to answer questions related to the drivers of radiation belt EPP. This spatial information is needed to close the gap in hard X-ray observation, will enable the construction of much more complete EPP models, and will lead to an enhanced understanding of the drivers behind EPP.

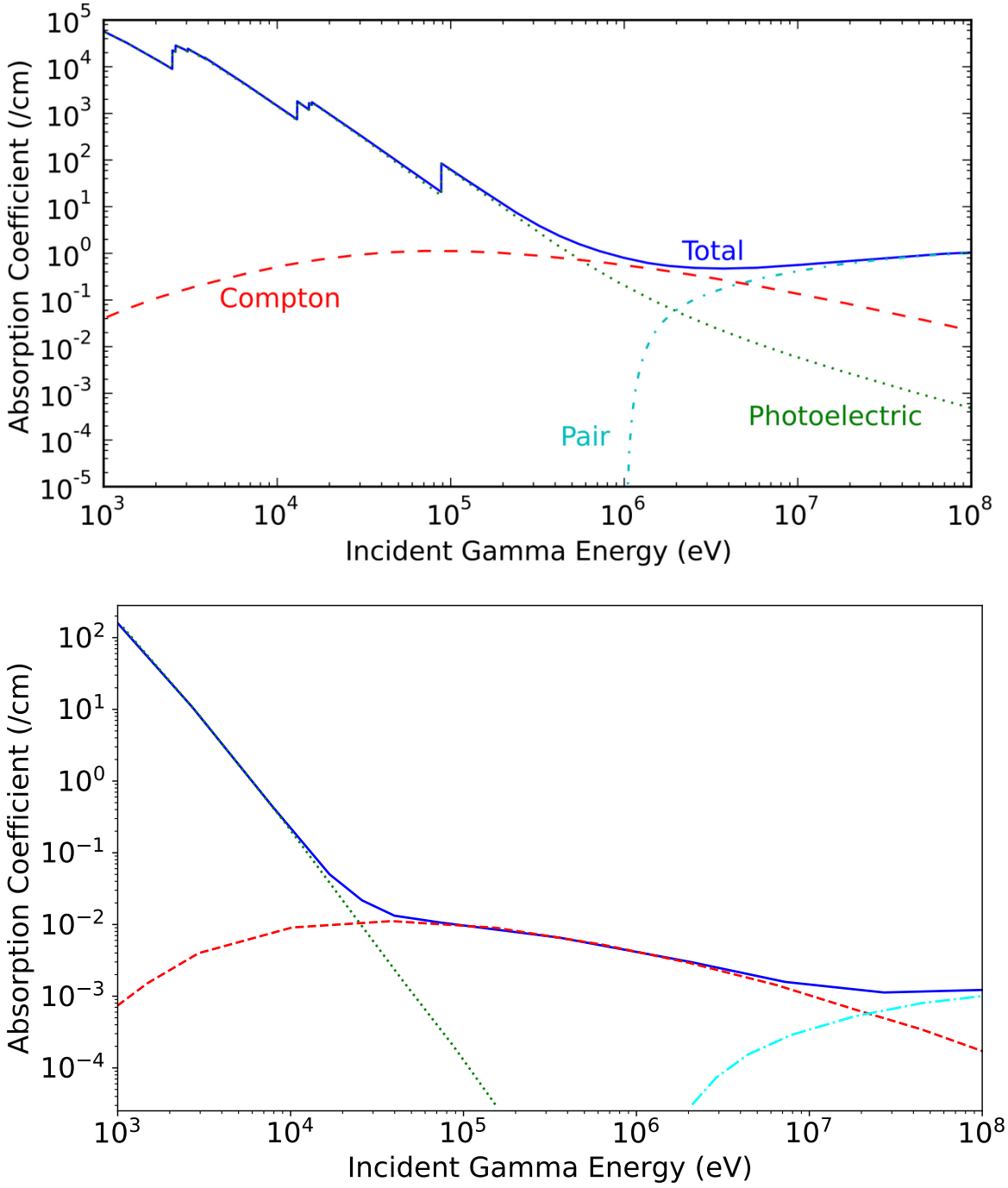

Figure 2.7: The photon absorption coefficients in (top figure) lead and (bottom figure) nitrogen gas with incident photon energy are shown, highlighting the relative contribution of the photoelectric effect, Compton scattering, and pair production at increasing energies. Note the electronic shell line transitions in lead in the X-ray photon regime but not in nitrogen, where those transition fall into optical and UV photon energies. Top figure by Joshua Hykes - Own work, CC BY-SA 3.0, `https://commons.wikimedia.org/w/index.php?curid=16310574`, bottom figure adapted from Carlson (2010).

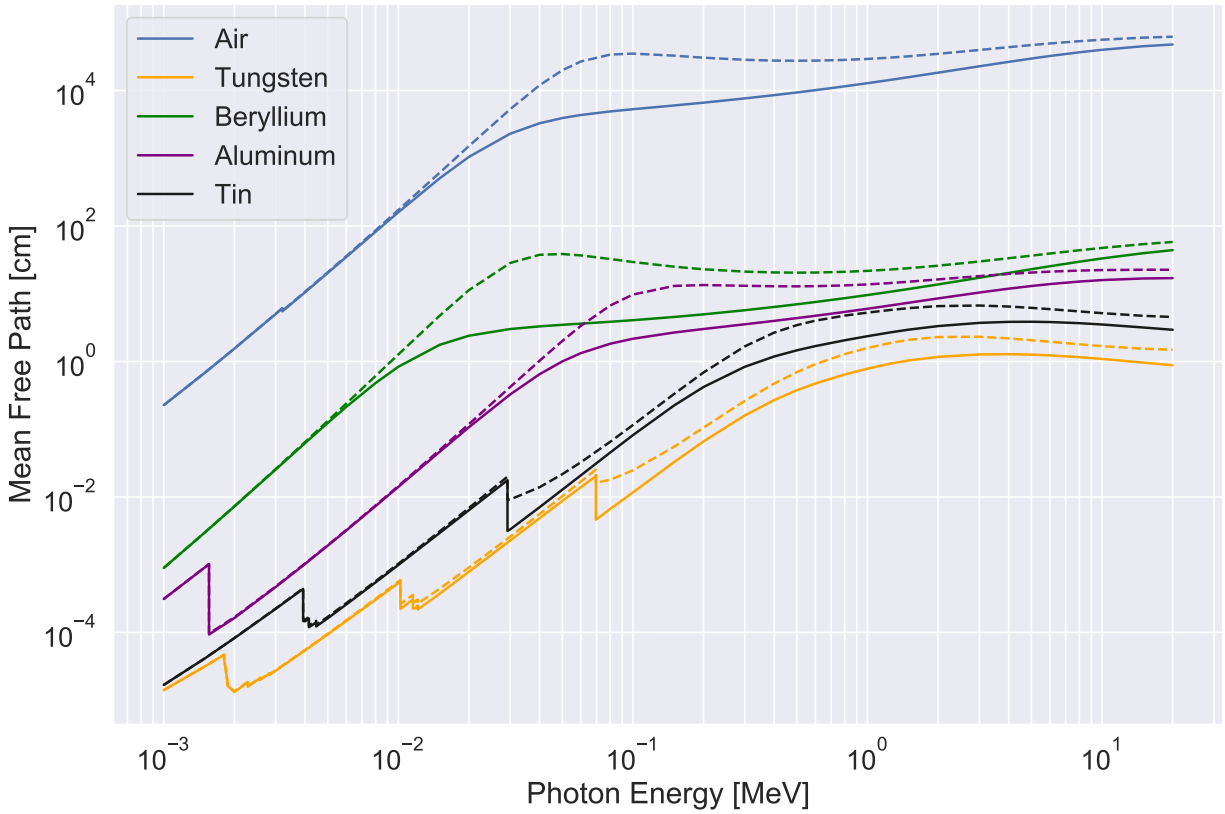

Figure 2.8: Photon mean free path in various materials, with the solid line showing (solid line) the mean free path calculated from mass attenuation coefficient and (dashed line) using the energetic attenuation coefficient (see text for an explanation of these quantities). Note the mean free path increases dramatically at the electronic shell transition energies in the higher Z metals. Mean free path values are derived by inverting mass attenuation coefficients from the NIST attenuation coefficient database (Hubbell & Seltzer, 1995).

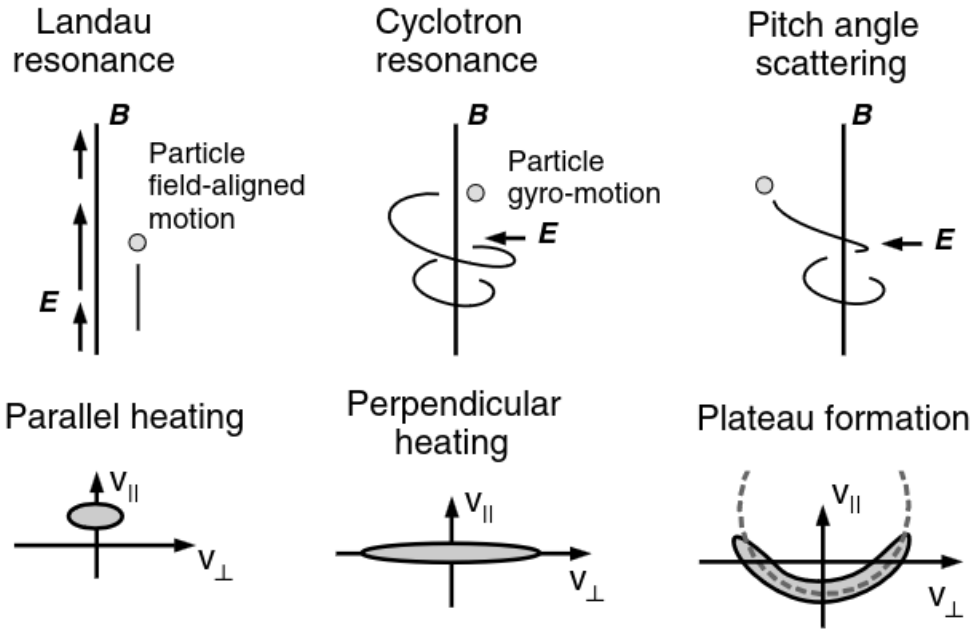

Figure 2.9: A schematic of how wave-particle interactions affect electron populations. The $(v_\perp, v_\parallel)$ diagrams show the component of the electron population that is altered by the plasma waves. Landau resonance directly accelerates particles, while pitch angle scattering interactions can cause a loss of the portion of the population in the loss cone. Figure from Narita (2017).

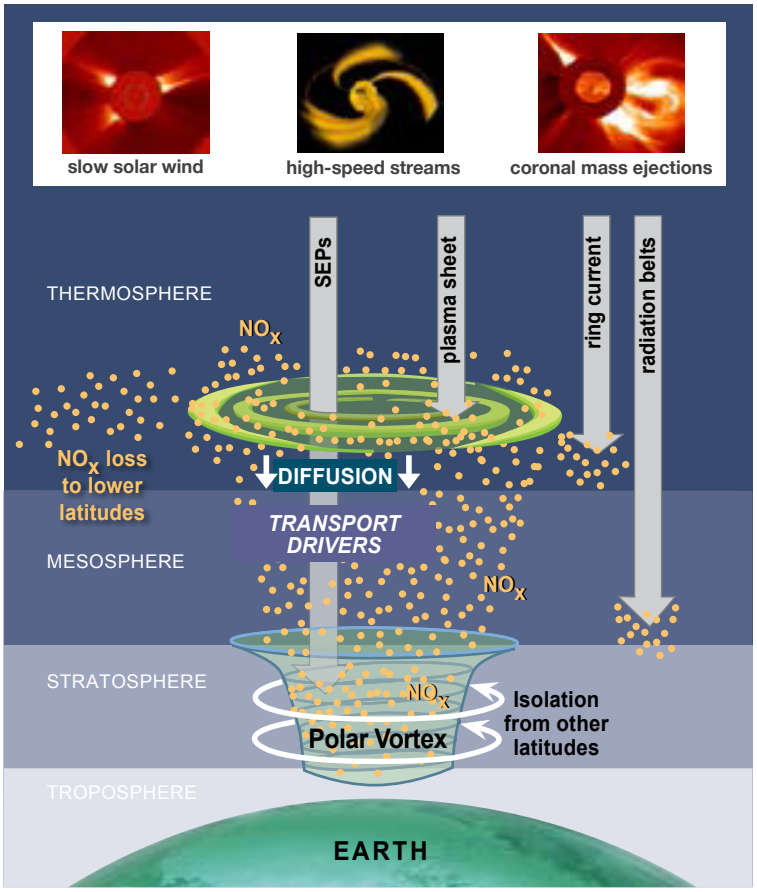

Figure 2.10: Schematic showing how precipitation from various charged particle populations affect different altitudes and layers of Earth's atmosphere. NO_x is generated as an indirect consequence of EPP and is transported into the stratosphere by the polar vortex. Figure courtesy of C.E. Randall.

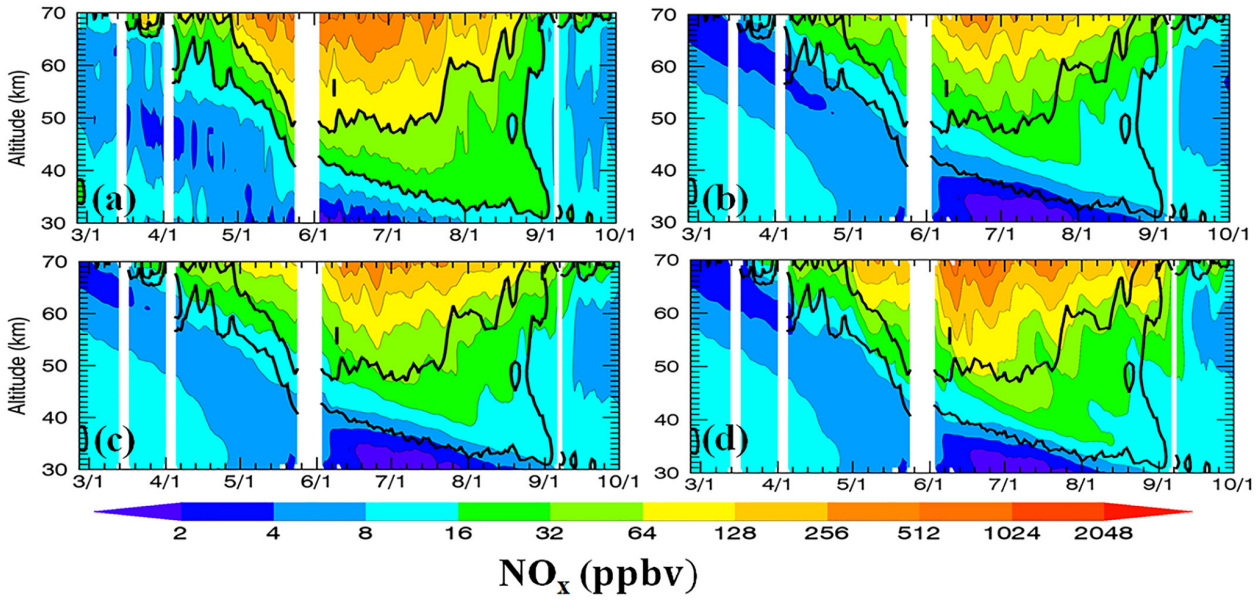

Figure 2.11: (a) Michelson Interferometer for Passive Atmospheric Sounding (MIPAS) data set measurements of NO_x descending from the mesosphere into the stratosphere, where black lines highlight the constant-density contours that show the "truth" data for this study. Plot (b) shows MIPAS baseline data during geomagnetically quiet times, and plots (c) and (d) show CMIP6 and WACCM simulation results, respectivley. The modeling efforts are performed with current state-of-the-art models that do not sufficiently reproduce NO_x descent with the current parameterizations of EPP forcing. Figure from J. Pettit et al. (2019).

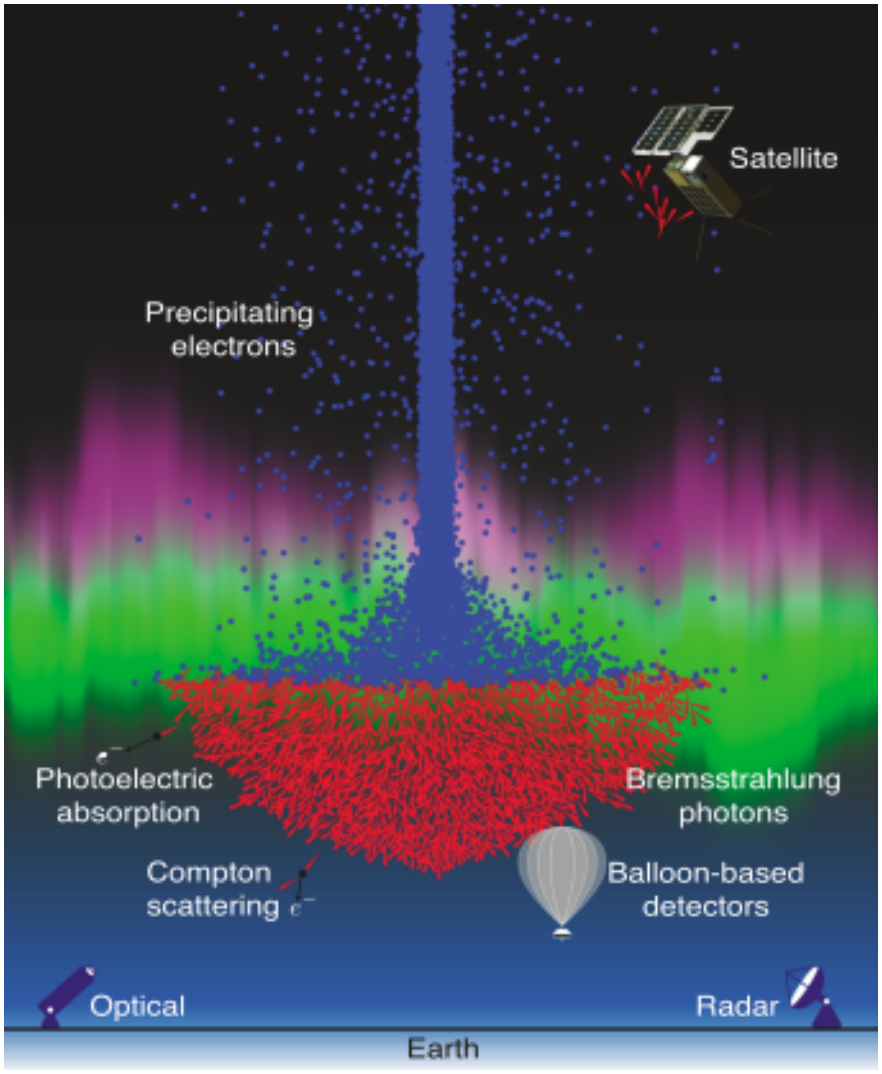

Figure 2.12: Diagram showing a column of precipitating electrons and resulting bremsstrahlung photons that are produced from interactions that occur in the atmosphere. A variety of in-situ and remote sensing measurement techniques are shown, including spacecraft charged particle measurements and balloon photon measurements. Figure from Xu et al. (2018).

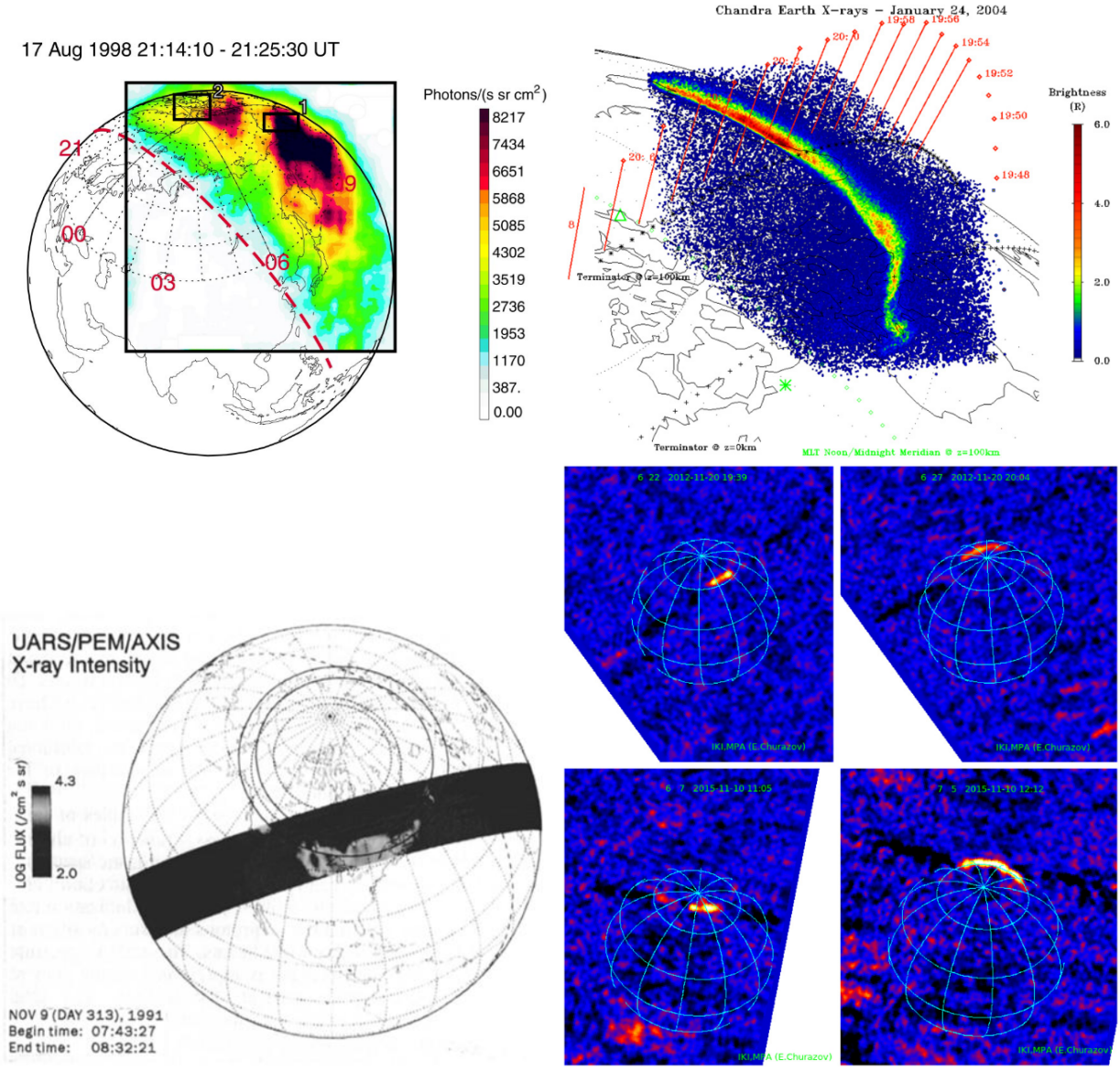

Figure 2.13: A collection of previous X-ray observations of Earth from (top left) the PIXIE instrument on the Polar spacecraft in the 2 – 12 keV band from Petrinec et al. (2000), (top right) the Chandra High Resolution Camera (HRC) in the 0.1 – 10 keV band from Bhardwaj, Gladstone, et al. (2007), (bottom left) the AXIS instrument onboard the UARS spacecraft in the 3 – 100 keV band from Sharber et al. (1993), and (Bottom right) an observation of opportunity during Earth occulation by the INTEGRAL spacecraft in the 17 – 60 keV band from Churazov et al. (2007).

Chapter 3

Atmospheric Effects of Precipitation through Energetic X-rays (AEPEX) CubeSat Mission

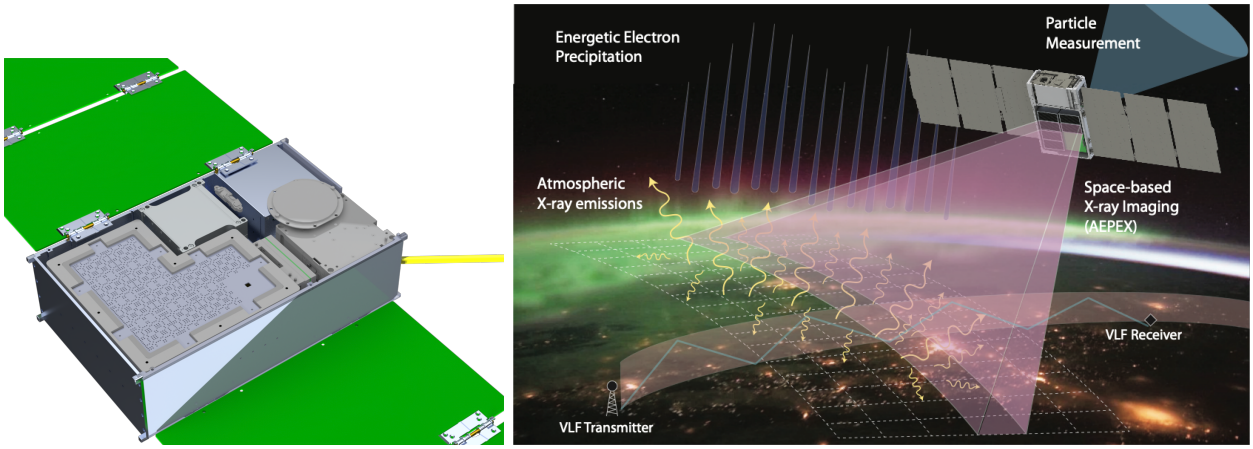

Figure 3.1: (Left) View of the nadir-facing side of the AEPEX spacecraft, with beryllium window and spacecraft panel removed to show the AXIS instrument and X-ray apertures. (Right) AEPEX mission concept, showing backscattered photons from bremsstrahlung interactions, as well as the enhanced atmospheric ionization that is detectable by very-low frequency (VLF) remote sensing of the atmosphere. The AFIRE instrument faces zenith to detect precipitating and trapped electrons and the AXIS instrument nadir (more precisely, downwards along the magnetic field vector) to detect anti-Earthward propagating X-rays.

The Atmospheric Effects of Precipitation through Energetic X-rays (AEPEX) mission is a NASA-funded 6U CubeSat mission (R. A. Marshall et al., 2020) slated to launch in late 2023 or early 2024. The mission will support two instruments: the Atmospheric X-ray Imaging Spectrometer (AXIS), developed at CU Boulder, and the AEPEX FIREBIRD[1] Instrument for Relativistic

[1] FIREBIRD in itself is an acronym standing for the Focused Investigation of Relativistic Electron Burst Intensity, Range, and Dynamics

Electrons (AFIRE) instrument, a heritage electron solid-state detector from the FIREBIRD CubeSat missions (Berland, Marshall, Martin, et al., 2023; Crew et al., 2016). Figure 3.1 shows a CAD model of the Earth-facing side of AEPEX and a graphic showing the geometry of the nominal science operation and photon observations.

The AEPEX mission is a collaboration led by the University of Colorado Boulder, with co-investigators at the Laboratory of Atmospheric and Space Physics (LASP), the University of Washington, the University of Calgary, the University of New Hampshire, and the University of Iowa. The goal of this mission is to constrain the estimates of energy loss from the radiation belts and subsequent energy input into the atmosphere that occurs through the magnetospheric loss process of radiation belt precipitation, as discussed in the previous chapter. The radiation belt and atmospheric science questions the AEPEX mission aims to address, from R. A. Marshall et al. (2020), are the following:

(1) How much energy is deposited into the upper atmosphere through EPP?

- How is it related to geomagnetic storm and substorm activity? How does it vary over seasons, latitudes, and magnetic local time?

(2) What are the spatial scales of precipitating regions during EPP events?

- What does this tell us about the total particle and energy flux removed from the radiation belts and deposited in the atmosphere?

The two instruments will work in tandem when AEPEX is in radiation belt latitudes or above (geomagnetic latitude >40°), where outer radiation belt precipitation maps to Earth's atmosphere. AXIS will take 10 second exposures of the bremsstrahlung X-ray signal to increase counting statistics, with 16 logarithmically-spaced differential energy channels spanning 50–250 keV, providing 20% energy resolution. The X-ray optics will provide ∼100 km spatial resolution at the sub-spacecraft point from 500 km altitude. Figure 3.2 shows semi-transparent CAD models of the AXIS and AFIRE instruments, and Figure 3.3 shows hardware images of the two science instru-

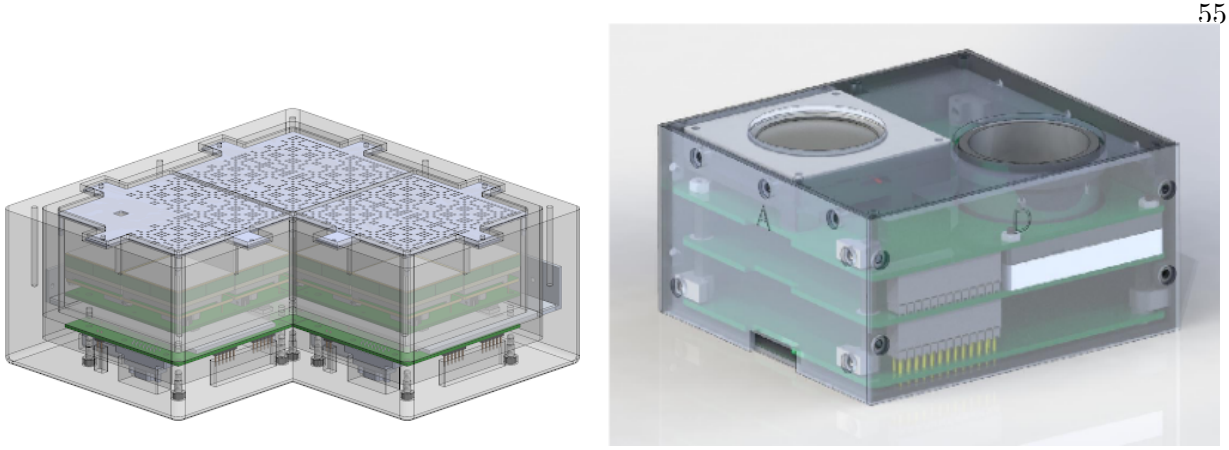

Figure 3.2: (Left) A semi-transparent CAD model of the AXIS instrument, showing the X-ray optics, shielding layers, and detectors. (Right) CAD model of the AFIRE instrument, showing the electron detection windows and electronics board stack.

ments in the AEPEX bus during the payload integration phase of development.

The AFIRE instrument will measure the in-situ electron population at a 1 Hz cadence with two detectors that are sensitive to electron energies from 200 keV to 1 MeV with 6 logarithmically-spaced integral energy channels per detector, offset to provide higher energy resolution. The counts recorded between the two detectors with multiple energy channels can be converted into an estimate of the differential electron flux.

In order to combine the remote photon measurements and in-situ electron measurements to answer the AEPEX science questions, an inversion method to estimate the precipitating electron spectrum from was developed in Xu and Marshall (2019) and updated in Berland, Marshall, and Capannolo (2023). Using this method, the photon flux and spectra, constrained by the electron measurements from AFIRE, can be used to find the maximum-likelihood precipitating electron flux and spectra in order to answer the questions of energetic input into the upper atmosphere (see Chapter 5 for more details on the inversion method). Combined with direct photon imaging, the spatial scales of precipitation can be determined on an instantaneous, per-orbit basis, as well as over time with various magnetospheric conditions during the nominal 1 year mission.

Figure 3.4 shows the nominal concept of operations for the AEPEX mission, including launch and commissioning, the primary science operation phase of the mission, and the atmospheric dis-

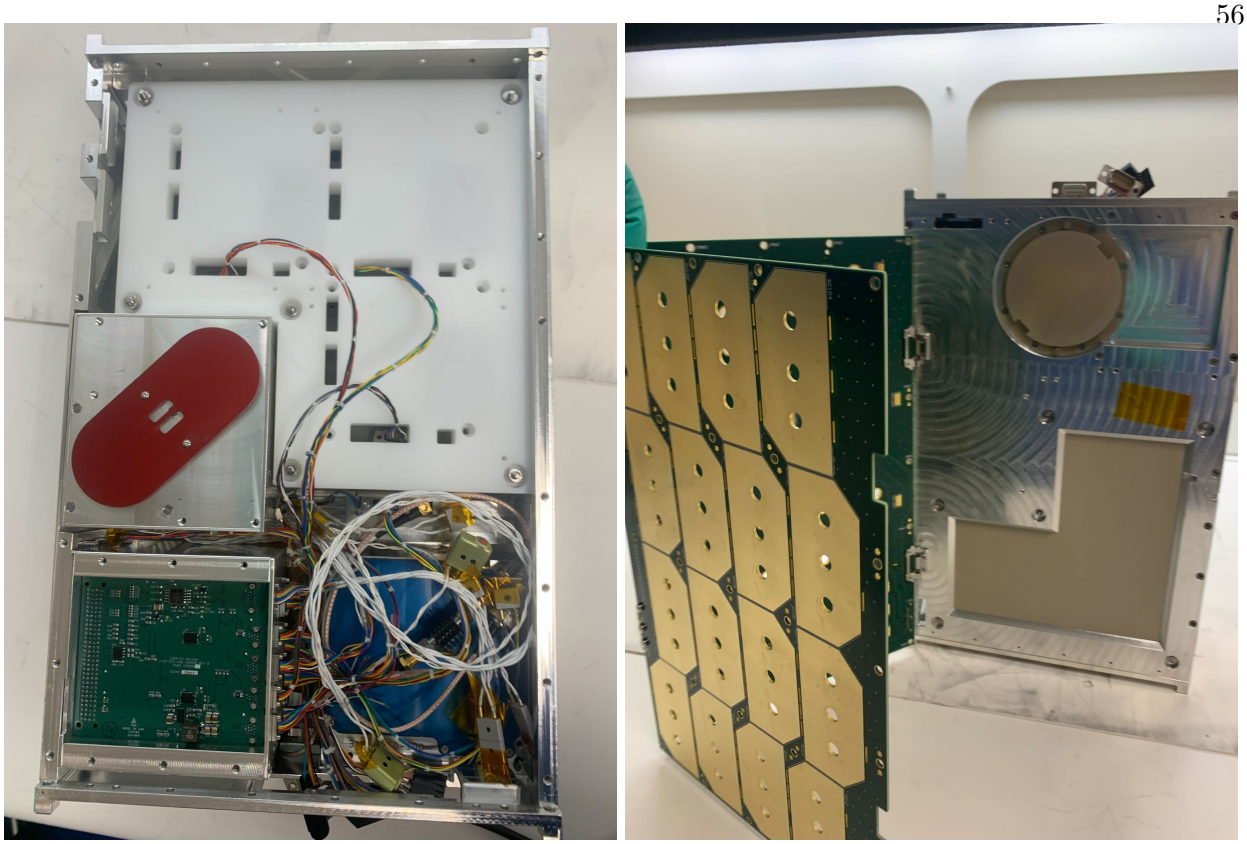

Figure 3.3: Images of the AEPEX CubeSat bus and instruments during payload integration. The left image shows the zenith-facing side of the spacecraft, which shows the AFIRE instrument with red covers over the electron detector windows, and flight board stack, as well as the back of the AXIS instrument. The right image shows the nadir-facing side of AEPEX with the AXIS window (L-shape) and S-band radio (circular shape), as well as the fold-out solar arrays.

posal phase, the last of which is required of all LEO CubeSat missions. In order to achieve these mission steps, the AEPEX CubeSat is designed for the parameters noted in Table 3.1.

The mission is design using the STK analysis software to compute power generation, data and link budgets, and orbit perturbations. The concept of operations is valdiated using models of orbits at different inclinations with various right ascension of the ascending nodes. Ultimately, the mission is data-constrained; data is downlinked one ground station located at the Laboratory of Atmospheric and Space Physics (LASP) in Boulder, Colorado through an S-band radio and uplinked from the same ground station via UHF radio.

This chapter discusses the AEPEX mission, with a focus on the design and development

Parameter	Requirement	Reference Design
Altitude	400 – 600 km	500 km
Inclination	>70°	90°
Eccentricity	<0.02	0
Mass	<14 kg	13 kg CBE
Average Power	<37 W	26.5 W
Data	<210 MB/day	151 MB/day
Ground System	UHF/S-band	LASP UHF & S-band

Table 3.1: AEPEX Mission Parameter Current Best Estimates

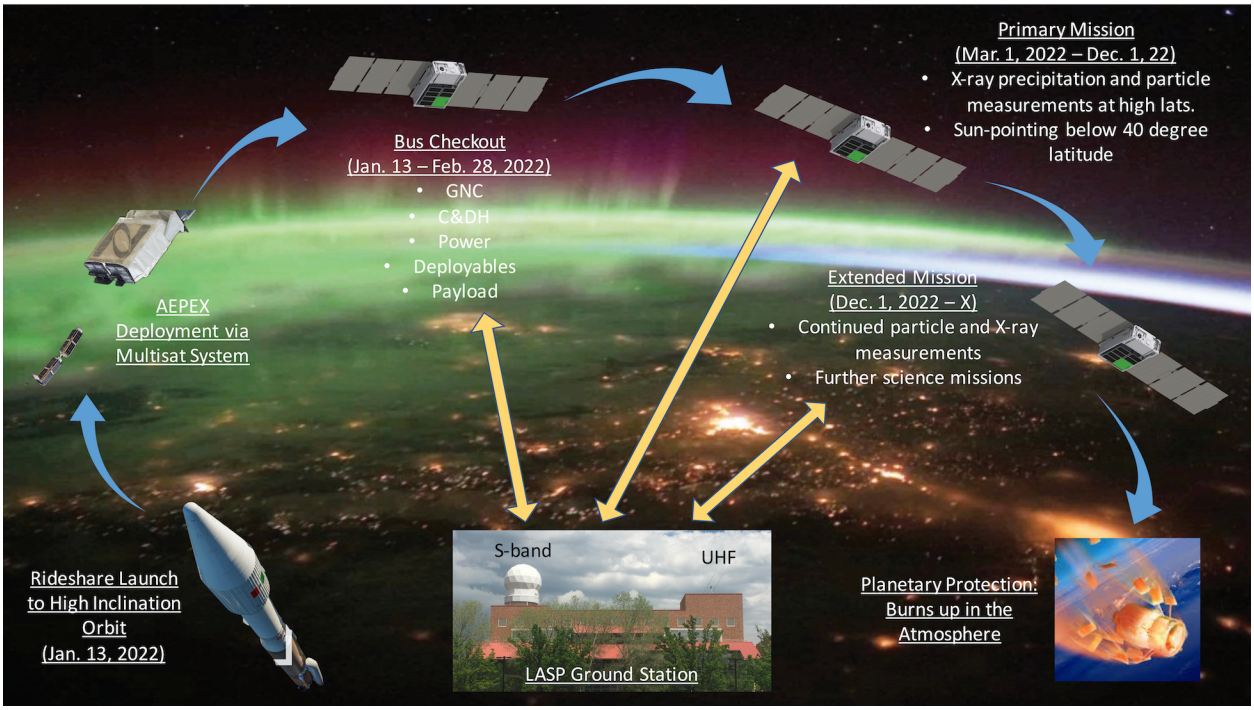

Figure 3.4: AEPEX mission concept of operations diagram, showing launch, deployment, commissioning, the primary mission, and finally disposal to the atmosphere. The mission is planned for 1 year duration of science operation, but extended mission options are available where different science targets can be assessed. The dates shown here are an example mission duration given a Q1 2022 launch.

of the AXIS hard X-ray imaging spectrometer instrument. The selection and testing performed on the detectors, graded-Z shielding, as well as the calibration of the instrument are detailed. The estimates for the signal and background that the AXIS instrument expects to measure is documented and explained here. Additionally, the AFIRE instrument is described and aspects of

the instrument that are specific to the AEPEX mission are included here.

3.1 Atmospheric X-ray Imaging Spectrometer (AXIS) Instrument

The Atmospheric X-ray Imaging Spectrometer instrument is a novel, wide field-of-view, hard X-ray imaging spectrometer designed and built at the University of Colorado Boulder. The instrument aims to measure X-ray photons that are generated via the bremsstrahlung interaction in the upper to middle atmosphere from precipitating electrons. The photons that escape the atmosphere and reach the AEPEX spacecraft's nominal altitude of 500 km will have their energy and directional information measured in order to estimate EPP intensity and spatial scales. Table 3.2 shows the requirements that flow down from AEPEX mission science goals discussed in the previous section that drive the design specifications and testing plan discussed in this section. The AXIS instrument description and testing described herein have been published in Berland, Marshall, Martin, et al. (2023).

The AXIS instrument is comprised of 12 solid state X-ray detectors. The 12 detectors share the same field-of-view, in order to co-image and sum the images they generate, increasing counting statistics. The system includes X-ray optics to focus/collimate photons, graded-Z shielding and a beryllium window to reject in-situ sources of charged particle background, and electronics and software that record and process data. Figure 3.5 shows a cross-section view of the AXIS instrument, which shows the 11 coded aperture optics and one pinhole aperture; the pinhole imager is held out of the image co-addition, and is instead used for coded aperture imaging validation and inversion constraint purposes. The following subsections describe each component of the instrument, its design process, and test results that predict in-flight performance. The X-ray optics and coded aperture are covered separately in Chapter 4.

AXIS was largely designed around the off-the-shelf X-ray detectors, but a single detector does not have a large enough aperture to provide sufficient signal. In order to increase the SNR of the system, multiple detectors that share the same field-of-view are implemented, where their images will be co-added to increase signal statistics. This image addition method gains its advantage

Component	Instrument Requirement
X-ray sensitivity	AXIS shall measure the X-ray flux with a sensitivity equal to or better than 10^1 photons cm^{-2} sr^{-1} s^{-1}.
X-ray dynamic range	AXIS shall measure the X-ray flux up to at least 10^4 photons cm^{-2} sr^{-1} s^{-1}.
X-ray energy range	AXIS shall measure the X-ray spectrum in the photon energy range from 50 to 250 keV.
X-ray energy resolution	AXIS shall measure the X-ray energy spectrum with a maximum energy resolution of 20%.
Imaging resolution	AXIS shall image X-ray emissions from the atmosphere with less than or equal to 200 km spatial resolution at 50 km altitude.
Imaging FOV	AXIS shall image X-ray emissions from the atmosphere with a minimum $90^\circ \times 90^\circ$ field-of-view.
Time resolution	AXIS shall measure the X-ray flux with a time resolution equal to or better than 10 seconds.
Time accuracy	AXIS shall provide X-ray measurements tagged with an absolute timing accuracy of better than or equal to 1 second.
Pointing knowledge, relative to spacecraft	The AXIS instrument's pointing direction shall be characterized with respect to the spacecraft with at worst 1° uncertainty.
Calibration Mode	AXIS will provide a calibration mode that enables imaging calibration using stellar X-ray sources
Mass	The AXIS instrument shall be designed with a mass less than or equal to 7 kg.
Size	The AXIS instrument shall consume no more than 3U of the internal volume of the 6U CubeSat.
Power	The AXIS instrument shall consume no more than 15 W of orbit-averaged power during science operations.

Table 3.2: AXIS Instrument Requirements

because the background noise acts as an independent 2D Poisson random process that affects each detector in a similar manner, and in contrast the signal of interest is a fixed object that may be weak relative to the background but projects a consistent image distribution to each detector. The co-addition of independent images then increases the signal-to-noise ratio (SNR) by the square root of the number of detectors co-adding images, since the background noise is also being co-added. This description is formalized in Chapter 4. Co-addition has a similar effect on imaging SNR as

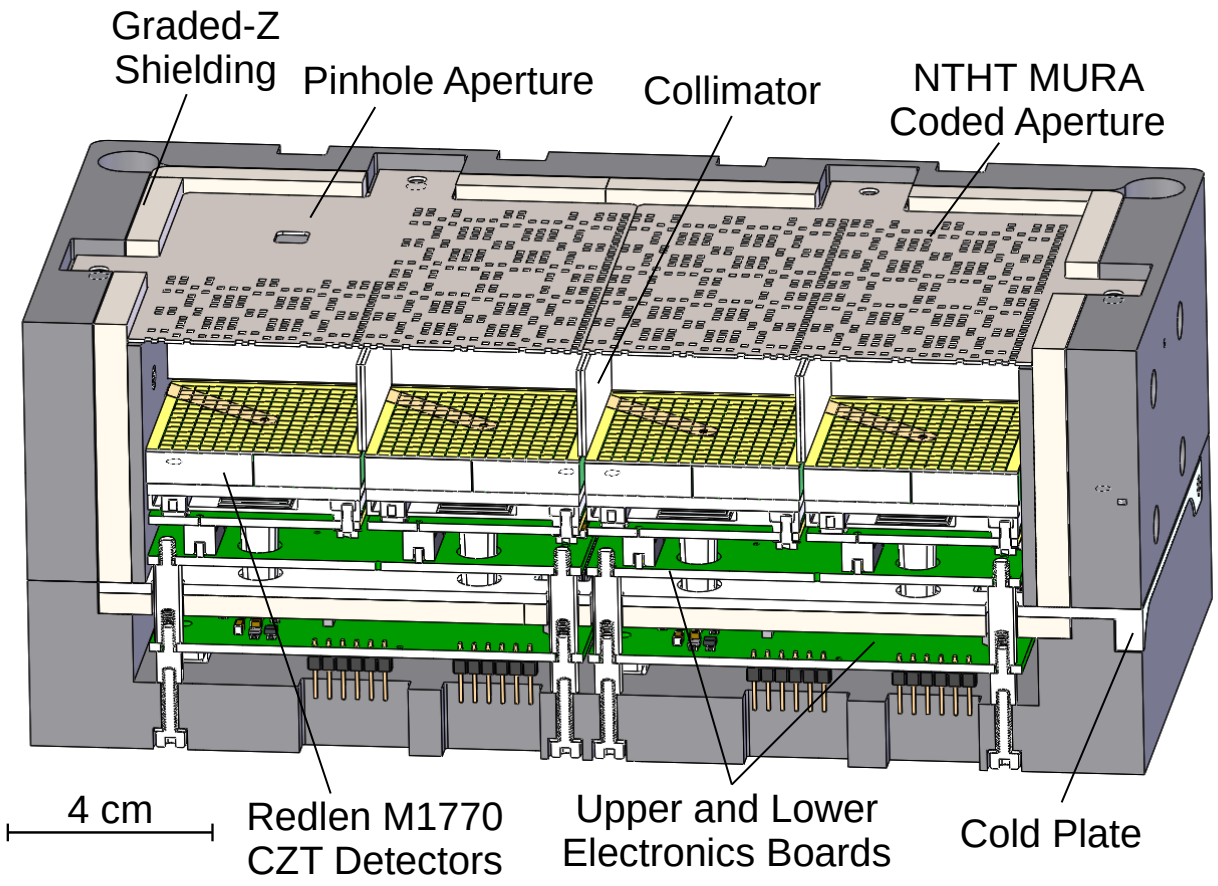

Figure 3.5: Cross section of the Atmospheric Imaging X-ray Spectrometer (AXIS) instrument, showing the graded-Z shielding, coded apertures, detectors, and electronics boards. Not shown is the beryllium electron-rejecting window located above the coded apertures.

increasing the exposure time, and in fact the SNR is proportional to the square root of the product of the exposure time and the number of detectors, i.e. SNR $\propto \sqrt{N * t}$.

The AXIS instrument must operate in such a fashion that minimizes exposure time in order to reduce motion blur (from the orbiting spacecraft) while obtaining acceptable SNRs for scientific interpretation. The exact imaging cadence and influence of motion blur versus exposure time is bounded by the spatial resolution requirement, which sets a maximum exposure time. However, below that max exposure time, the exposure is not strictly constrained by the science requirements, so some explanation of design parameters and the final operation modes are described here.

We are interested in quantifying the amount of spatial blur that occurs due to this integration

period. In a circular low Earth orbit at 500 km, a satellite will travel at approximately 7.6 km/s, which would imply, for a fixed observation angle between AEPEX and the Earth, the integration blurs the signal of interest over $7.6 \times \Delta t$ km. However, the spacecraft is magnetic field tracking, so there is a slow counter-rotation that ultimately reduces the blur distance. Assuming a dipole magnetic field model, the rate of change of the magnetic inclination I with respect to time can be written from the relationship between inclination and magnetic latitude λ

$$\tan(I) = 2\tan(\lambda) \tag{3.1}$$

and then differentiating with respect to time yields

$$\frac{\partial I}{\partial t} = \tan^{-1}(2\tan(\omega)) \tag{3.2}$$

where $\omega = d\lambda/dt$ is the angular orbit rate of the spacecraft. We can convert the spacecraft velocity to an angular rate, knowing that the spacecraft distance from the center of the Earth is R_{Earth}+500 km to find an orbit angular rate of 1.1×10^{-3} rad/s. This slew rate can be converted into a ground track speed by multiplying the magnetic field-tracking slew rate of the spacecraft of approximately 2.2×10^{-3} rad/s $\approx$1.3 deg/s with the altitude of 500 km to find a counter rotation ground speed of 1.1 km/s. This rotation acts in the anti-ram direction bringing the total blur distance per integration period to $6.5 \times \Delta t$ km. The nominal science mode operation of AXIS selects a 10 second exposures, which produces a 65 km ground-track blur distance, which is approximately half the spatial resolution of the AXIS imager at the sub-spacecraft point.

Figure 3.6 shows the two primary science operation modes for AXIS. On the top left is the nominal science mode that integrates the frame for 10 seconds, collecting photon counts that are grouped according to pixel address and energy bin. In addition, shown at bottom left is the " light curve" (photometric time series), that is integrated across all energies and pixel addresses in order to capture time dynamics with periods faster than 10 seconds in the X-ray signal. On the right side of the figure is the timing science mode, which exchanges spectral information for temporal information by taking 16 exposures in 10 seconds and collapsing the spectral information.

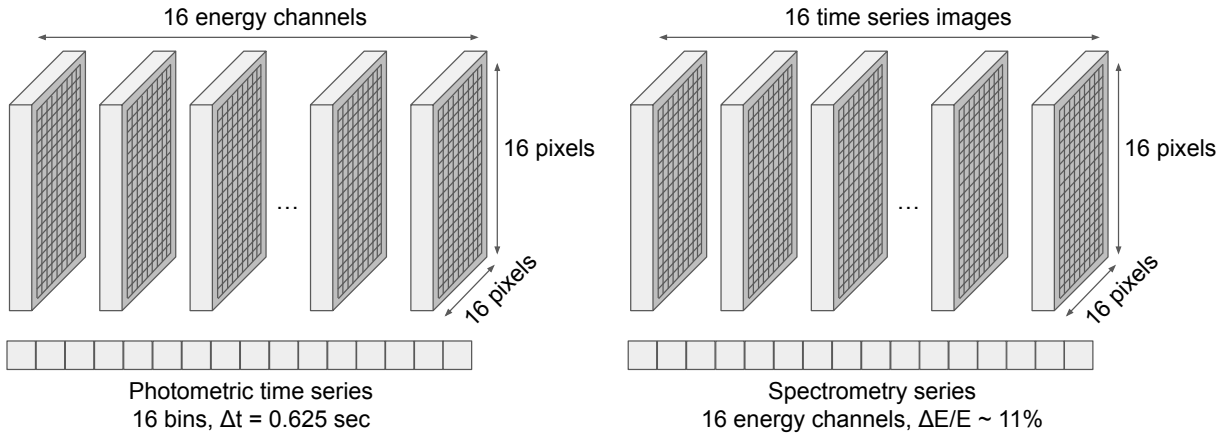

Figure 3.6: AXIS operation modes, showing (left) the nominal science mode that records 16 energy channels, spatial information in each energy channel, and a photometric time series of integrated X-ray counts at a faster time resolution. (Right) The timing science exchanges energy resolution for temporal resolution by taking 16 snapshots in 10 seconds, spatial information per integration, and this mode preserves spectral resolution by taking an average spectrum measurement over 10 seconds.

Below, the light curve in the nominal science mode is replaced with the temporally- and spatially-integrated energy spectrum (spectometry series) that includes a single integrated spectrum with 16 energy bins. The size of the data produced by both modes is exactly the same, simplifying integration of the AXIS instrument with the spacecraft bus during ground testing, as well as AXIS operation during flight operation. Figure 3.7 shows the AXIS instrument microcontroller state diagram. The nominal mode is the science mode, in which the instrument will operate while above 40° magnetic latitude. A calibration mode offers individual register-tagged photon events instead of energy-binned and histogrammed events in order to adjust calibration coefficients on the ground to be uplinked to the instrument. Idle and safe modes are for non-operation times and in the case of erroneous instrument readings, respectively. The data product from these two modes are the same in returning the heartbeat packet and any error codes that arise during the operation of these modes.

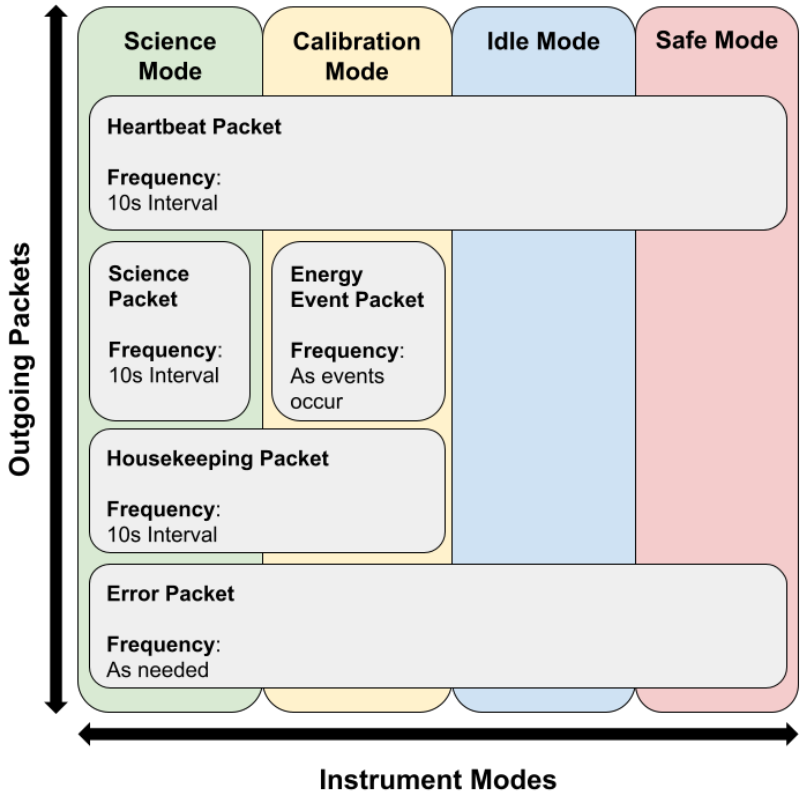

Figure 3.7: Diagram of the operation modes of AXIS, showing the nominal science operation mode, calibration mode, and other modes for use during non-science times. The heartbeat science, housekeeping, and error packets are shown when used in their respective modes.

3.1.1 X-ray Detector Selection

The X-ray detectors chosen for the AXIS instrument are the Redlen cadmium-zinc-telluride (CZT) solid state detectors. These detectors are commercial-off-the-shelf with vertically-integrated front-end electronics that process both the analog and digital portions of the signal chain and were originally developed for medical imaging and nuclear security. The Redlen detectors are not appropriate for vacuum operation without sufficient alterations, which are detailed later in this section. The detectors are shown from above in Figure 3.8.

The Redlen X-ray detectors have high-altitude heritage on the EPEx balloon mission that also aimed to image bremsstrahlung X-rays but from within the atmosphere (C. Cully, personal communication, 2021). The detectors do not have spaceflight heritage; they were implemented

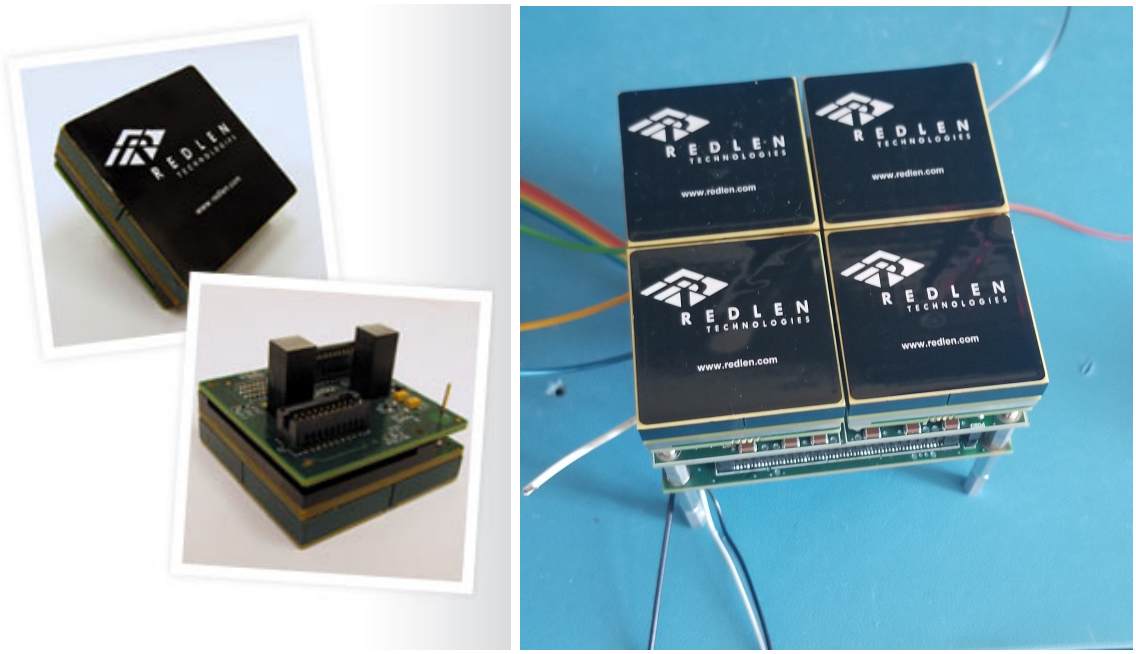

Figure 3.8: The Redlen M1770 cadmium-zinc-telluride (CZT) X-ray detectors, showing (left) the top view of the sensitive CZT crystal and from below the aluminum mounting brackets, high-voltage pin, and front-end electronics. (Right) The Redlen detectors mounted into the AXIS engineering model, which is a 1/3 version of the full flight instrument.

on the CXBN-1 CubeSat mission, but that mission did not return data, so the detectors are not considered qualified (Simms et al., 2012). Figure 3.9 shows a Redlen X-ray detector mounted into an instrument processing board as well as in a state of disassembly. In the bottom image, the detector crystal and front-end electrons are separated from the aluminum heat sink and mounting apparatus. The FPGA, stack connectors, and high voltage pins which connect the two sides of the detector are shown.

The Redlen detectors are pixelated with 16 pixels $\times$ 16 pixels with approximately 2.2 mm pixel size and a $\sim$0.3 mm between pixels to make up the 4 cm $\times$ 4 cm detection area. The CZT material is 6 mm thick which, in combination with front-end electronics, makes the detectors sensitive to photons within approximately 50–240 keV with energy resolution $\Delta E/E = 6.5\%$. The detectors have a maximum count rate of 60,000 counts/second per detector module and consume approximately 1.1 W of power. The efficiency of the detectors are quoted as 60% at the 122 keV peak of a ^{57}Co source, but the efficiency away from this peak is not well characterized. This

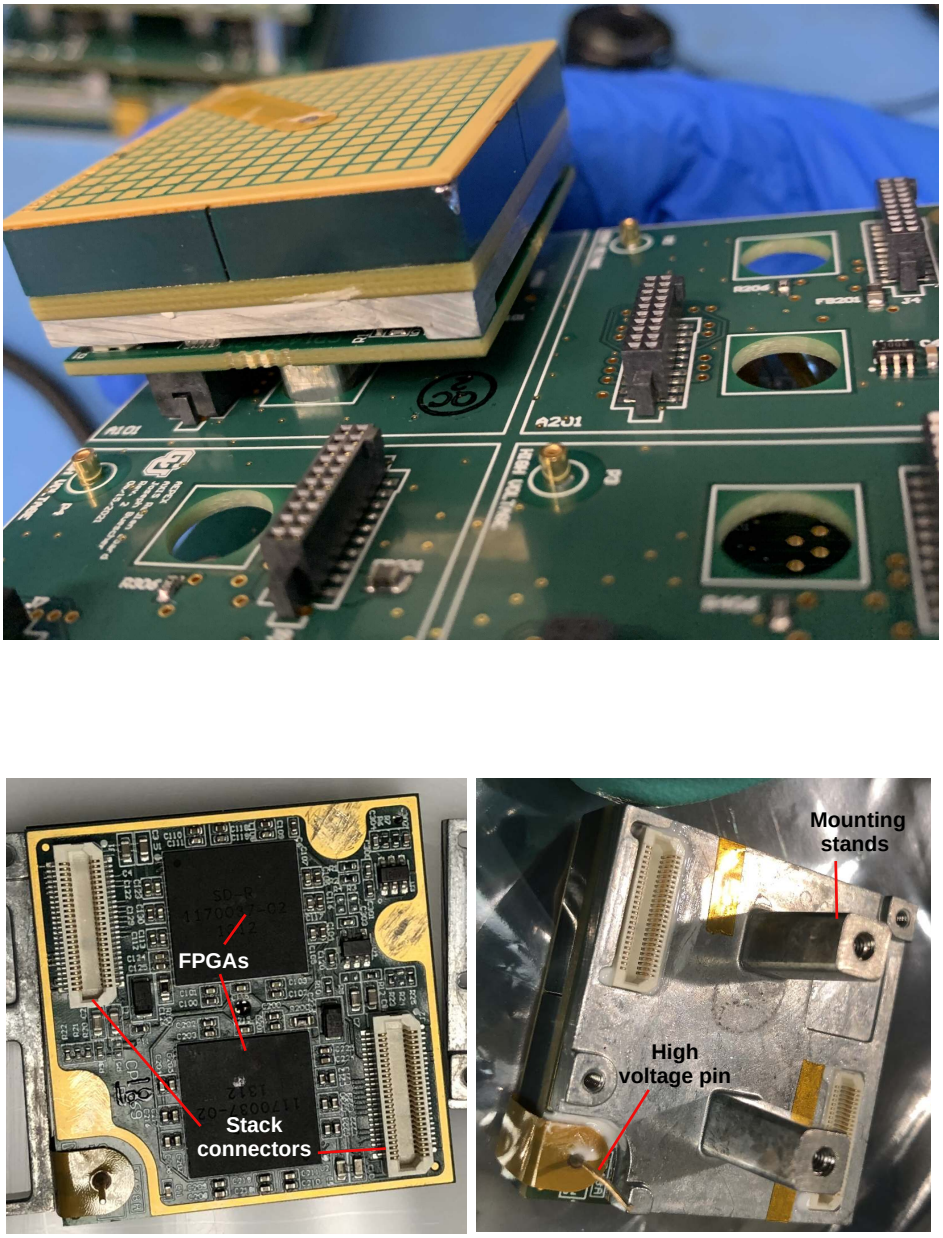

Figure 3.9: (Top) Redlen CZT X-ray detector mounted in the AXIS electronics boards. (Bottom) Redlen board front-end analog and digital signal processing electronics, aluminum mounting stands, and aluminum heatsink.

efficiency is a function of energy, and the photon absorption versus energy is shown in Figure 3.10.

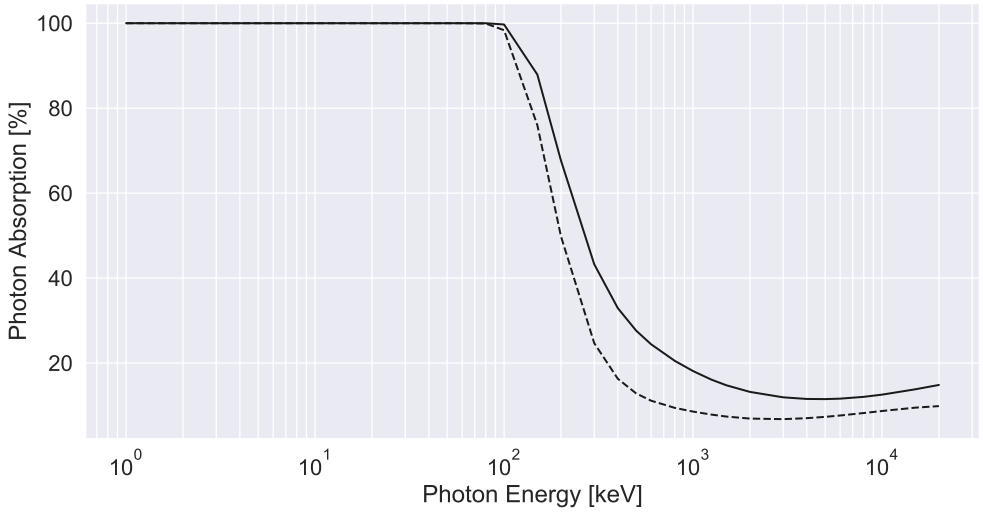

Figure 3.10: The photon beam flux absorption fraction from 6 mm of cadmium-zinc-telluride is calculated from the attenuation coefficient versus energy (Hubbell & Seltzer, 1995). The solid line is calculated using the mass attenuation coefficient, and the dashed line using the energetic attenuation coefficient. Note that this curve does not necessarily indicate detection efficiency, but the detection efficiency is a function of photon absorption.

In order to operate the Redlen detectors in vacuum both for laboratory testing and in space operations, changes to the internal components of the detectors were made. The lower panel in Figure 3.9 shows the connection between the aluminum heat sink and the application specific integrated circuits (ASICs), where a silicone heat transfer pad was used to make thermal contact between these two components. During thermal vacuum (TVac) testing, these silicone pads were the likely sources of a significant amount of organic material outgassing that showed up on a mass spectrometer monitoring the exhaust from the TVac chamber. This significant amount of outgassing is undesirable during vacuum testing in a chamber, although there is no strict requirement for the X-ray optics to minimize organic outgassing. This heat transfer pad was removed and the surfaces cleaned; a new thermal contact was made using silver nitride epoxy, and finally the boards were conformally coated with Arathane 5753 to protect against environmental contaminants. The detectors operate nominally in vacuum after these changes and with desirable thermal characteristics.

Each detector consumes an average of 1.1 W during operation; this heat must ultimately be

dissipated through thermal radiation from the spacecraft outer surface. The microcontrollers that operate the detectors and the electronics that step up and down the voltages on the electronics board consume additional power, such that the total power draw of the AXIS instrument is approximately 15 W. How this power is generated through solar panels at latitudes below 40°, when the spacecraft is not in science mode, is documented in R. A. Marshall et al. (2020).

Figure 3.11 shows TVac thermal testing of the 1/3-scale prototype of the AEPEX flight instrument that is used to verify thermal modeling for the Redlen detectors and housing which conducts heat away from the detectors and into the chassis of the spacecraft. The main channel in which heat is conducted away from the instrument is through an aluminum bracket[2] (labeled "Thermal bracket" in Figure 3.11) to which the detector thermal posts are directly attached. Additionally, a layer of thermal paste is applied between the posts and aluminum heat plate.

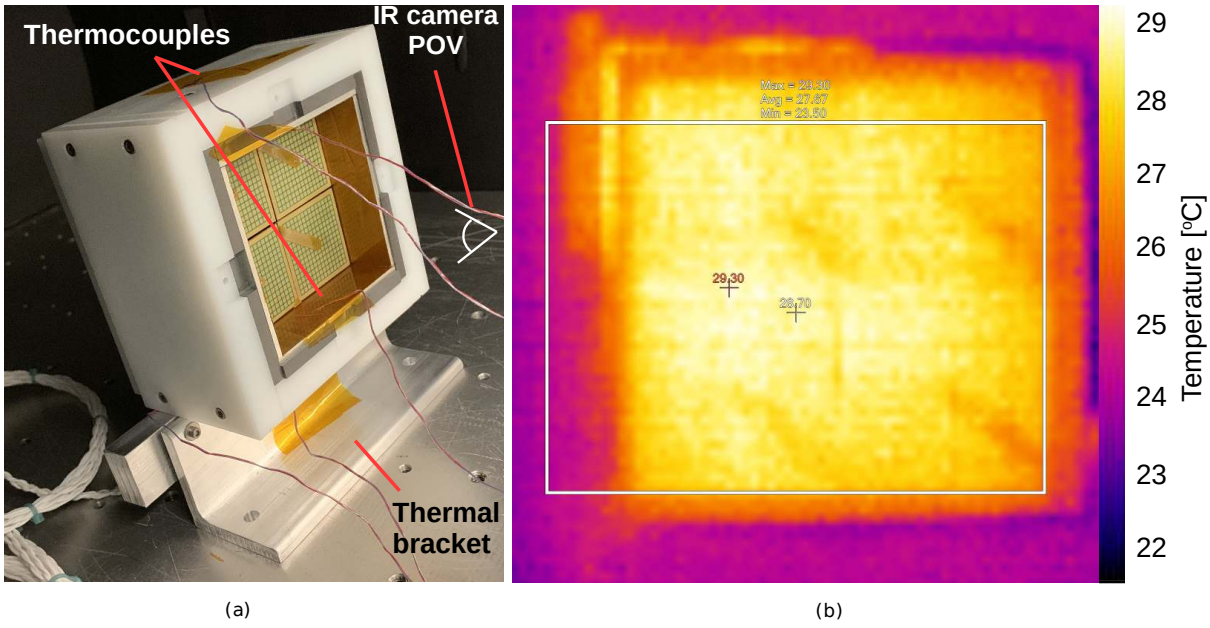

Figure 3.11: Thermal vacuum (TVac) testing of the AXIS instrument prototype, showing (left) the thermal bracket mounted to the chamber floor and the instrument outfitted with thermocouples for recording temperature. (Right) shows an infrared camera image of the detectors during operation to measure the heat output from operating the detectors.

[2] Of note, copper is considered in place of aluminum as copper has approximately twice the thermal conductivity of aluminum, but is ultimately ruled out as a viable shielding or hot plate material due to copper activation from proton bombardment. GCRs incident on copper can create radioactive isotopes, some of which emit X-rays within the 50 – 250 keV detection range.

An additional concern during flight operation is the appearance of "hot pixels," which exhibit nonphysical high count rates. While hot pixels do not have a formal definition in this work, they tend to behave consistently and predictably between power cycles of the detectors, and typical have count rates greater than 3σ higher than the count rates of the rest of the nominally-operating pixels on the detector. Figure 3.12 shows a more subtle example of a hot pixel during an time-integrated exposure of a ^{57}Co source, where a geometric fit to a near-field source emphasizes the hot pixel. The danger of hot pixels is in the co-addition of the images, where a hot pixel will be the dominate term in the addition of the same pixel address in the other detectors and effectively "wash out" the average value that we aim to capture with the imaging array. A similar issue exists with "dead pixels," which are pixels that are either not sensitive to photons or vastly under-count the incident photon flux incident. However, the issue of dead pixels less severely affects the co-addition than hot pixels since the typical dead pixel value of zero is much closer to the mean count rate of expected signals than the typical hot pixel value, which is bounded by the maximum value of an unsigned 16-bit integer of 65,535 counts in a 10-second integration.

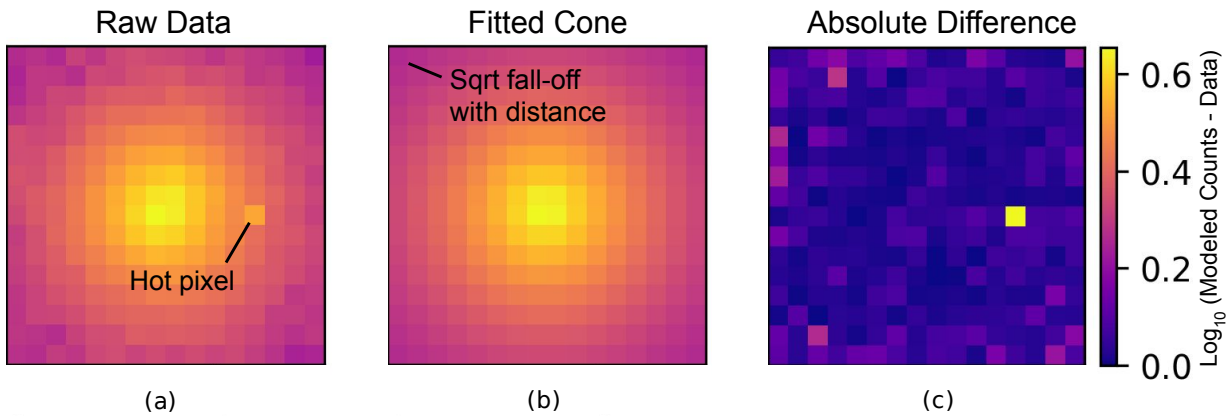

Figure 3.12: Example of a hot pixel in the readout of the Redlen detectors, showing (a) the raw data from a disk source placed in the middle of the detector, (b) the fitted cone function that models the expected count rate, and (c) the logarithm of the absolute different between panels (a) and (b). Of note, where the data and model match exactly, the value of the right figure is denoted as true zero.

In order to mitigate the effect of hot pixels on the co-addition of detector data, a moving-window median filter is implemented to detect the presence and location of a hot pixel. The difficulty

of detecting a hot pixel is akin to the prominence problem: that is to say, how much does a peak have to stand out of data before it's captured by a consistent statistical threshold? The image data itself is stratified due to the coded aperture mask pattern, so many peak-finding algorithms have difficulty detecting an artificial hot pixel without also partially selecting the desired data in an automated fashion. Instead, implementation and testing of the hot pixel detection method is based on a variable threshold set by the photon statistics generated per exposure and the validation of this algorithm is the subject of future work.

3.1.2 Graded-Z Shielding Design

In order to protect against the background counts that are induced by both charged particles and radiation (photons) in the LEO environment, shielding is designed to attenuate the flux that penetrates to the detectors. The predominant sources of background for charged particles are the radiation belt electrons themselves, which are also the source of the signal of interest. Therefore, when the signal becomes stronger, the magnitude of the background will also increase. Instrument design elements to increase signal-gathering ability are discussed in the previous section; here we discuss the main way to reduce background, through the development of shielding. The shielding design is largely based off a charged particle and radiation transport simulation built in GEANT4. The GEANT4 background simulations are detailed fully in Section 3.4.

Graded-Z shielding can be shown to provide better shielding against a charged particle flux than any single monolithic material for a fixed mass (Fan, Drumm, Roeske, & Scrivner, 1996). Graded-Z shielding works on the principal of layering materials with different Z numbers, typically in order of high-Z to low-Z. The outermost high-Z material stops charged particles and high energy photons, but produces subsequent bremsstrahlung and fluorescence photons, which are then absorbed and re-emitted at lower energies and fluxes from the lower-Z materials. The design for AXIS is slightly different: it begins with a thick, low-Z material, followed by a high-Z material, then a slightly lower-Z material. This configuration is shown to optimally reduce detector background given the fixed mass and volume requirement of the CubeSat form factor.

The materials selected to shield against the LEO background are, in order from outside to instrument internals, high density polyethylene (HDPE) plastic, tungsten-nylon composite, and tin. Additionally, the aluminum of the spacecraft bus chassis both provides a measure of shielding and generates bremsstrahlung radiation, which is overall a negative effect in terms of the background rate but is ultimately unavoidable. Figure 3.13 shows the ordering and thickness of the graded-Z shielding.

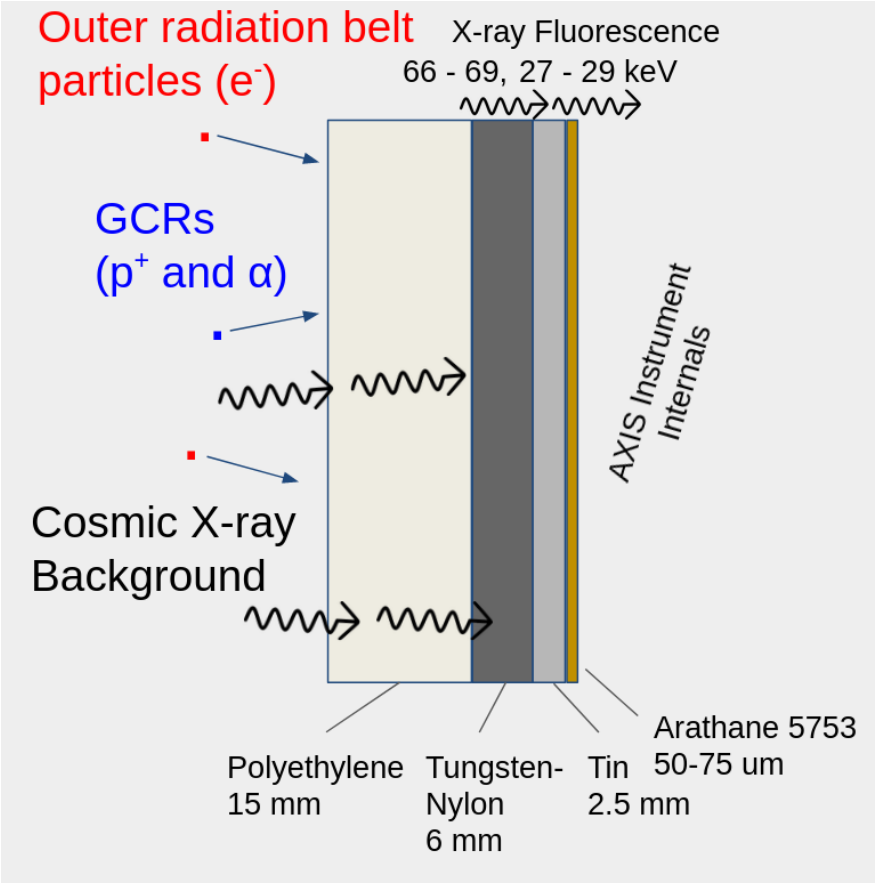

Figure 3.13: AXIS graded-Z shielding, from the left (external to the instrument) polyethylene plastic to stop low- to medium- energy electron, tungsten-nylon composite material for high energy electrons and photons, and (closest to the detectors) tin to absorb characteristic line emissions from tungsten. Not shown here is the thin aluminum shell of the spacecraft bus that offers additional shielding but produces more bremsstrahlung radiation.

The HDPE layer (Z∼4) is essentially a tub of material that the instrument sits in. The goal of this material selection is to "slowly" stop charged particles incident on the instrument;

that is to say, the ratio of collisional to radiative stopping power is high since the material is comprised of low-Z elements carbon, hydrogen, nitrogen, and oxygen. Additionally, there is a high density of hydrogen atoms per material mass, so we can say that the specific (mass normalized) collisional stopping power for plastic materials is high.[3] Similar boronated plastics have been used in GCR mitigation (e.g. Thibeault et al. (2012); Yang and Bayazitoglu (2020); Sihver, Barghouty, and Falconer (2021)). This layer is 15 mm thick on the sides and 12 mm thick on the zenith-facing side of the spacecraft, which yields an average stopping power of 1.8 MeV/cm for 100 keV – 10 MeV electron kinetic energies and has a radiation yield (the fraction of energy converted to bremsstrahlung radiation) on the order of 0.1%. Critically, the low-Z elements in polyethylene do not produce K-shell fluorescence in the X-ray band. Due to mass and volume requirements, the back side (zenith-facing) of the shielding is thinned relative to the sides of the shielding. The design choice to thin on the backside of the instrument shielding comes from the angular distribution of trapped electrons: only during times of high loss cone filling will there be a significant flux on the back of the instrument.

The middle layer of the shielding is comprised of a nylon-tungsten (Z = 74)[4] composite material produced by Ecomass Technologies, Ltd. (Durkee III, 2006). This material is selected in place of a pure tungsten layer due to CubeSat atmospheric re-entry requirements, which state that all materials in the spacecraft must completely burn up before reaching sea level, or must reach sea level with lower than 15 J of kinetic energy. Tungsten has a high melting point of 3,422°C, which ensures that it will not ablate before reaching ground level (Langmuir, 1915). Based on the required size of the tungsten shielding components, their kinetic energy upon reaching the ground would significantly exceed the 15 J required maximum.

Instead, a composite material comprised of tungsten powder embedded in a PA-12 (polyamide-12, i.e. nylon) matrix allows AEPEX to meet the atmospheric re-entry requirement. Due to the

[3] The total stopping power of tungsten is approximately 10x that of plastic, but plastic is approximately 20x less dense than tungsten, which causes the *specific* stopping power to be comparable between the two materials, at least in the collisional stopping power regime (electron energy $\lesssim$10 MeV).

[4] The calculation of the Z-number is mass-weighted, so for a composite like this the Z number is very close to that of pure tungsten although the mass density is affected.

packing ratio of tungsten powder, this material has approximately the density of lead (11 g/cm^3) versus pure tungsten (19 g/cm^3); the thickness of the tungsten-nylon composite can be scaled by the ratio of mass densities to provide an equivalent amount of shielding as pure tungsten, with approximately the same total mass. The tungsten-nylon layer is 6 mm thick around the entire instrument. The reduced-density tungsten material provides an average stopping power of 15 MeV/cm for electrons within 100 keV – 10 MeV, but has a radiation yield on the order of 1%, approximately 10 times that of the HDPE plastic layer. Additionally, tungsten has a K-shell fluorescence line at 69 keV, within the AXIS detection range. In addition to stopping charged particles, tungsten also has a high mass attenuation coefficient to reduce X-ray background, both from stellar sources that comprise the cosmic X-ray background and from bremsstrahlung radiation generated in the aluminum of the spacecraft bus.

The innermost layer of shielding is a layer of tin (Z = 50), which is the middle of the atomic number order. The purpose of the tin material is to further attenuate charged particles and photons, and also to absorb and re-radiate the tungsten K-shell fluorescence line. Tin has a K-shell fluorescence of ∼30 keV, which is sufficiently below the AXIS detection range. Tin will tend to grow "whiskers" that can contact and short electronics (Arnold, 1966; Lee & Lee, 1998), so a layer of Kapton tape separates the instrument internals from the innermost tin layer.

By layering the materials in this manner, the shielding against the charged particle background is more efficient than the equivalent mass in say, pure tungsten. The evaluation of the shielding is performed with analytical, Monte Carlo (GEANT4), and finally laboratory testing in the next sections. Other candidate materials were investigated but ruled out for various reasons. For example, copper would be a similarly useful medium-Z material, but it becomes activated by proton bombardment and becomes a radioactive isotope; tantalum would similarly not burn up upon re-entry into the atmosphere and an appropriate composite of tantalum is not easy to manufacture.

An additional component to the shielding is a beryllium (Z = 4) window placed over the tungsten apertures that rejects charged particles that are within the instrument's field-of-view

while mitigating radiation production in the material. The window thickness chosen is 2 mm, which completely blocks up to 650 keV electrons and 12 MeV protons and partially attenuates electrons and protons at higher energies than this while minimizing bremsstrahlung radiation production. These electron and proton energies are on the upper end of the expected background that is directed away from the Earth in the anti-loss cone, or at the very edges of the shielding in the trapped population. Charged particles at very high energies are not easily blocked or attenuated by the beryllium window, but high energy particles are not expected within the field-of-view. The beryllium is on average 96% transparent to X-rays within 50 – 250 keV, which makes it ideal for mitigating the electron background while allowing for hard X-ray detection. An additional benefit is that the beryllium metal is opaque to visible and UV radiation, which seals the housing that holds the X-ray detectors to low energy photons, which, in large fluxes, can cause background on the detectors. Interestingly, for the purpose of rejecting charged particles and hard X-ray transparency, borosilicate glass materials (e.g. Pyrex) work nearly as well as pure beryllium for a significant price reduction, but obviously do not block visible photons.

3.2 X-ray Signal Estimate

In order to design the AXIS instrument with the appropriate detector and aperture parameters in order to measure the precipitation X-ray signal with confidence, a model of the expected signal strength is needed. This work is detailed in R. A. Marshall et al. (2020), which uses the Energetic Particle Monte Carlo (EPMC) code developed originally in Lehtinen, Bell, and Inan (1999) and updated in Xu et al. (2018) and Xu and Marshall (2019). The EPMC model is the atmospheric forward model shown in Figure 3.14 that maps the relationship between precipitating electrons and X-ray photons that reach the AEPEX spacecraft altitude. The next step after determining the photon flux at 500 km is simulating these photons through an instrument response model. The GEANT4 AXIS simulation described below takes the EPMC outputs as inputs in order to estimate the instrument response. This section details the model inputs, outputs, and assumptions that go into each step of the signal estimation portion of the AXIS design.

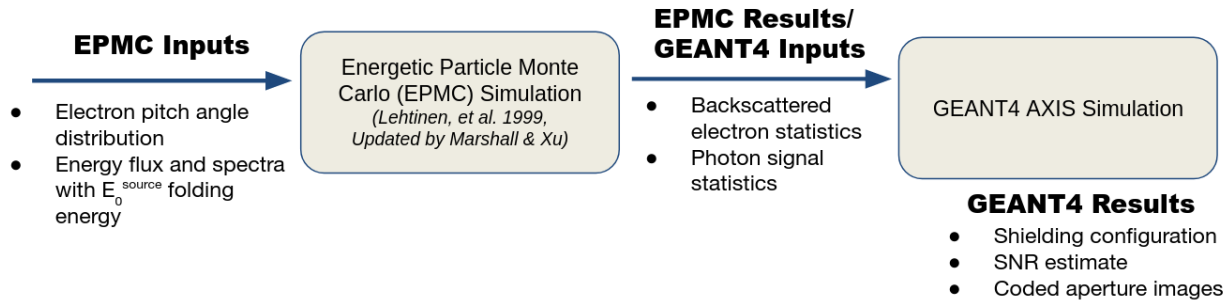

Figure 3.14: Simulation flow diagram showing, from left to right, the precipitation characteristics that are input into the EPMC model to find X-ray flux at 500 km altitude, which are subsequently input into the GEANT4 instrument response model to determine the shielding configuration, imaging characteristics, and signal-to-noise ratio.

Starting from radiation belt precipitation fluxes and forward modeling electrons through the EPMC model, the precipitating electron spectrum begins with an ansatz of an exponential energy distribution:

$$f(E) = f_0 \frac{1}{E_{e,0}} e^{-E/E_{e,0}} \tag{3.3}$$

characterized by an electron folding energy $E_{e,0}$ and energy-integrated flux f_0. A survey of realistic folding energies that describe the spectral behavior of the electrons is performed using data from the DEMETER mission where the folding energies of 100, 200, and 300 keV are selected (Whittaker et al., 2013). These folding energies have been observed in-situ and bound the radiation belt precipitation energy flux. In order to estimate the precipitating flux for the electron energies of interest, the AE-8 model is used to find a nominal integral flux of 10^5 cm^{-2} s^{-1} sr^{-1} (Vette, 1991; Whittaker et al., 2013). This value represents the input signal strength to which the AXIS instrument is designed, and is later linearly scaled both up and down an order of magnitude in integral flux to determine the detection limits of the AXIS instrument. To support these precipitation parameters and further design the AEPEX mission, POES data is analyzed to estimate the frequency of EPP events with flux greater than this 10^5 cm^{-2} s^{-1} sr^{-1} threshold in order to determine a mission lifetime that will observe a sufficient number of precipitation events. The POES data threshold analysis is presented in R. A. Marshall et al. (2020).

These precipitation cases are simulated through the EPMC model and the photon flux at

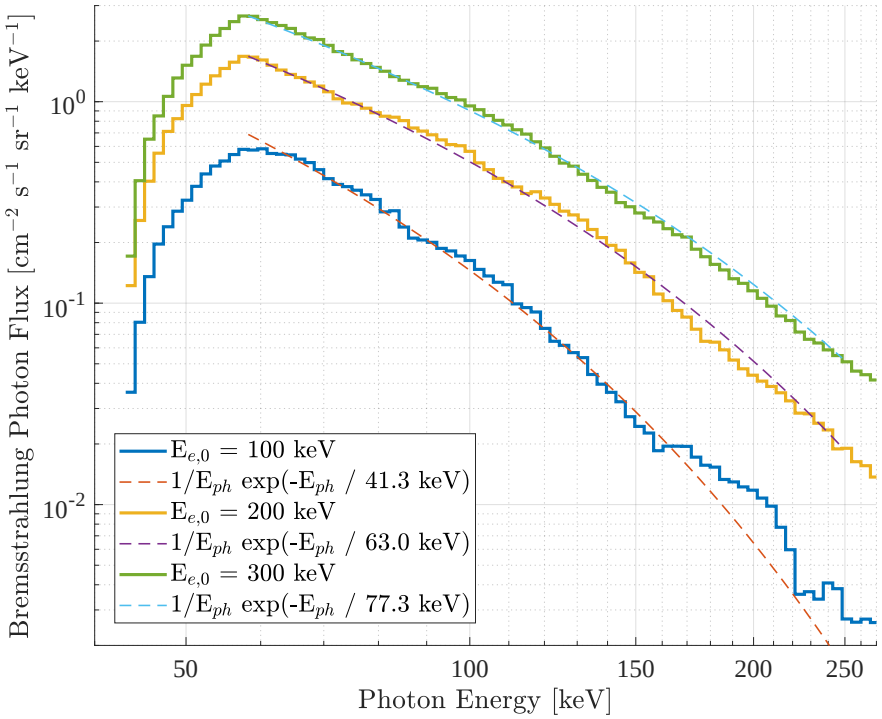

Figure 3.15: The atmospheric X-ray response to EPP is shown for an input electron flux of 10^5 cm^{-2} s^{-1} sr^{-1} and three electron folding energies $E_{e,0}$ of 100, 200, and 300 keV. The resulting differential photon spectrum is shown with optically thin thermal bremsstrahlung (OTTB) model fits to the EPMC model output, showing photon folding energies of 41, 63, and 77 keV.

500 km altitude is recorded. More details on the EPMC model and this process are discussed in Chapter 5. The X-ray spectra outputs of the EPMC model from the three nominal input cases are shown in Figure 3.15. The spectra show a characteristic peak at 60 keV, which is a result of Earth's oxygen-nitrogen atmosphere and the bremsstrahlung cross section to relativistic electrons. At energies higher than 60 keV, the high energy tail of the distribution drops off at different rates that are dependent upon the input precipitating spectrum. An optically thin thermal bremsstrahlung (OTTB) model is fit to the distributions above 60 keV of the form

$$f_{OTTB}(E_{ph}) \propto \frac{1}{E_{ph}} e^{-E_{ph}/E_{ph,0}} \tag{3.4}$$

which is a distribution used in astronomy observations of active galactic nuclei (Brown & Emslie, 1988). This model is similar in form to the input electron spectrum with a characteristic energy $E_{ph,0}$ that is shifted lower in energy from the input electron spectral folding energy $E_{e,0}$. The values

of $E_{ph,0}$ corresponding to the $E_{e,0}$ inputs are 41, 63, and 77 keV, respectively. There is also a factor of ∼5 difference in the X-ray flux generated from the same input electron flux between folding energies of 100 keV and 300 keV, which is approximately linear in terms of photon production efficiency, consistent with our understanding of bremsstrahlung production dependence on electron energy.

By integrating the portion of the signal within the AXIS detection limits of 50–250 keV, we can determine the total signal count rate that would be expected through a detection model that converts X-ray flux to instrument counts. Determining and verifying this detection model is a subject of Section 3.3.

We find that photons that reach AEPEX's altitude are sufficiently collimated that they should fall within the AXIS imager's wide field-of-view.[5] Other aspects of the EPMC model outputs include the X-ray flux fall off with distance for a one-dimensional input beam (i.e. a column of ionization), which is plotted in Figure 3.16. A Gaussian distribution is fit to each profile to show the variation of the photon integral flux with radial distance from a precipitation source. The fall-off is characterized by a standard deviation σ of 165 km, or a full-width half-max value of approximately 390 km, consistently between varying E_0 values. Another useful quantity generated by the EPMC model is the spectrum and intensity of atmospherically backscattered electrons, which are within AXIS's more sensitive field-of-view; this population is addressed as a background source and is discussed in Section 3.4. The AXIS instrument and aspects of the AEPEX mission are ultimately designed using the signal estimates from the EPMC model.

3.3 AXIS Calibration

The calibration campaign of the AXIS instrument includes testing to quantify and adjust the spectral and flux estimates generated by photon measurements. In order to perform these tests,

[5] This collimation is due in part to the atmosphere itself: the majority of bremsstrahlung photons are generated between 60 – 80 km altitude, which means upward-propagating photons must transit some distance through the atmosphere to escape towards the spacecraft. Photons propagating at oblique angles must transit a longer path length through the atmosphere which are more likely to be absorbed, leading to a bias towards photons that escape with vertical, or zenith, propagation directions.

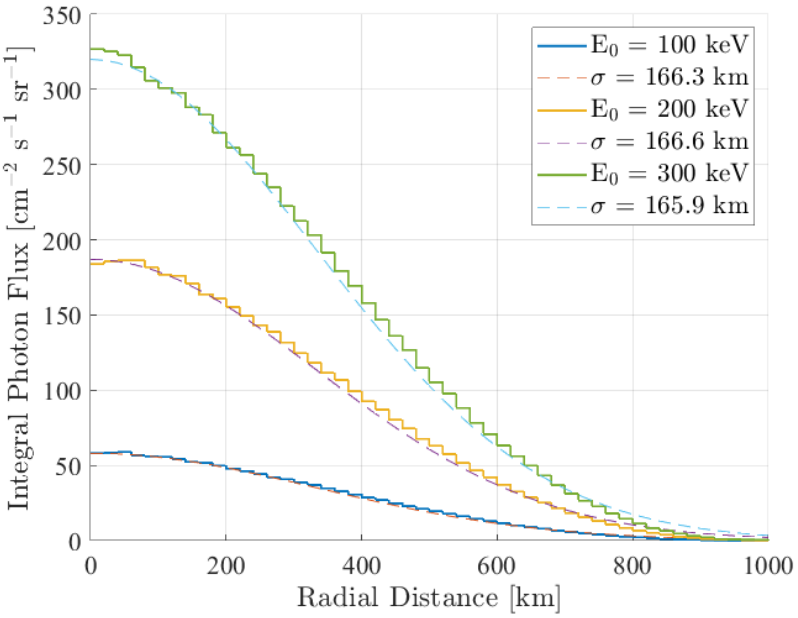

Figure 3.16: The radial fall-off the photon signal at 500 km altitude in response to a 1D input electron beam. A Gaussian distribution is fit to the three profiles resulting from folding energies E_0 of 100, 200, and 300 keV where the relative magnitudes are different but the slope of the tail is the same. The spreading of the X-ray signal above the precipitation source location is estimated to have a standard deviation σ of 165 km.

sealed radioactive disk sources are used to probe the detection behavior of the Redlen detectors in terms of spectral performance, and the photon flux that penetrates the aperture and window. This formulation uses an effective geometric factor, i.e. $G_{eff} = \eta_T G$, where η_T is the product of the various efficiencies in the detection system and can be a function of energy and angle within the field-of-view, and G is the product of the field-of-view and detector area, which is in units of cm^2 sr. The radiation sources utilized are ^{57}Co, ^{241}Am, and ^{133}Ba, which have a well-measured activity level that decays in a predictable manner.

In order to convert between intrinsic quantities (e.g. source activity) and our quantities of interest for calibration (e.g. count rate), we need a detection model. The model used here is the same used in Berland, Marshall, Martin, et al. (2023):

$$\frac{N}{\Delta t\ \Delta E} = A_s\ \eta_B(E)\ G(h) \cdot QDE \cdot \rho \tag{3.5}$$

where $N/\Delta t/\Delta E$ is the differential count rate in counts/second/keV, ρ is the coded aperture mask

open fraction, QDE is the average quantum detection efficiency over the detection range, $\eta_B(E)$ is the branching ratio for emissions within $[E, E + \Delta E]$, $G(h)$ is a 1D model of attenuation due to the source-to-detector distance h for isotropic source emissions that accounts for detector size, and A_s is the source activity in Becquerels (i.e. disintegrations per second into 4π steradians). The factors of Δt and ΔE are the integration duration and detection bin width, respectively. The attenuation model $G(h)$ can be expressed as the geometric relationship between a point source and a finite-sized detector:

$$G(h) = \frac{1}{2} - \frac{2}{\pi} \tan^{-1} \left(\frac{1}{\sqrt{1 + 1/2 \ (s/h)^2}} \right) \tag{3.6}$$

where s is the detector side length of 4 cm. This model asymptotes to $1/2$ in the limit of large s/h where the source is very close to the detector, such that it acts as an infinite plane that accumulates half of all emissions, and varies as h^{-2} in the limit of small s/h, where the disk source acts as a true point source far from the detector.

Count rate testing is performed using a ^{57}Co disk source, which has an activity level of approximately 10 μCi, placed at various distances from the detector in order to obtain measurements where the source signal dominates over the laboratory background. Figure 3.17 shows the result of the model described in Equation 3.5 and the laboratory testing. This test is performed primarily to verify or adjust the multiplicative detector efficiency terms $QDE \cdot \rho$ which are vital in converting flux to counts. The results show that, except for when the source is very near the detector and near-field effects related to the finite thickness of the coded aperture mask are in effect, the modeled and measured count rates agree to within the Poisson counting variance of $\pm\sqrt{N}$. The figure shows both the predicted count rate from the theoretical model and the $\pm 2\sigma$ of the data, which follows a Poisson detection distribution.

In order to calibrate the energy response of the Redlen detectors, the detectors are placed in full energy resolution mode and the three disk sources are employed. The right plot of Figure 3.18 shows the full energy resolution ^{57}Co spectrum with $\Delta E/E = 6.5\%$ where various interesting aspects can be seen. At energies lower than the main peak at 122 keV a Compton shoulder forms;

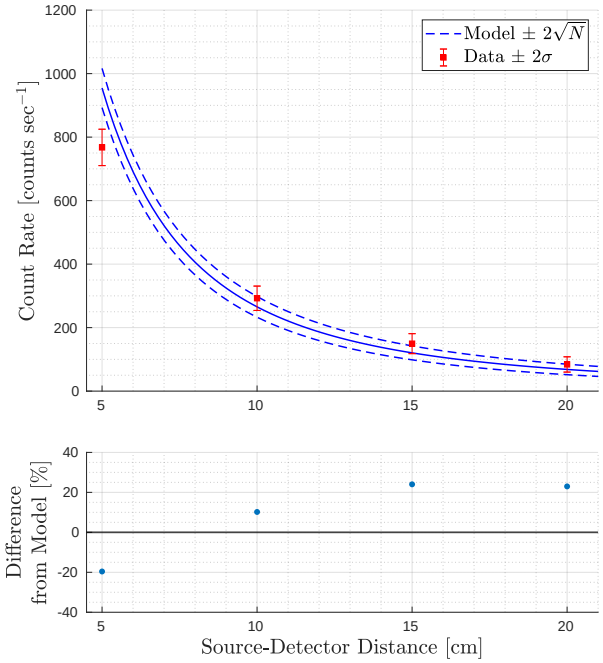

Figure 3.17: (Top) Plot of energy-integrated count rate versus distance, showing the modeled count rate (blue) that is dependent on detection efficiency and data from a ^{57}Co disk source (red). (Bottom) Residuals between data and model, showing the highest discrepancy at a low source-detector distance, which is likely due to mask self-collimation effects due to the high angle photons must traverse to enter the mask when the source is close to the aperture.

the shoulder is generated from Compton scattering within the detector material, which spreads the energy response from the main peak due to the partial energy deposition in the material. The Compton shoulder is approximately 25% of the intensity of the main peak and is made up of contributions from both intrinsic ^{57}Co source peaks at 122 keV and 136 keV. A Gaussian mixture model with two components is fit to this data in order to quantify the peak location in the Redlen energy register space, which is then scaled such that it corresponds to the known peak values in energy space. The Gaussian mixture model also quantifies the spread in the peak that corresponds to the detector energy resolution. A linear scaling of the form $E = a_{ij}\ R$ is used to relate the Redlen energy registers R to the energy E through a per-pixel calibration coefficient a. Affine and nonlinear forms of the calibration relationship are tested for higher accuracy performance, but the results show that the linear scaling most accurately maps the disk source line emissions to their appropriate energies.

The right plot of Figure 3.18 shows a composite spectrum comprised of the following sources, in order of emission energy: ^{241}Am, ^{133}Ba, and ^{57}Co. The calibration coefficient matrix is found using the ^{133}Ba source which has an emission at 81 keV, then verified with other sources. This plot uses 25 energy bins to ensure proper calibration in the lab versus the 16 energy bins that make up the flight instrument energy resolution.

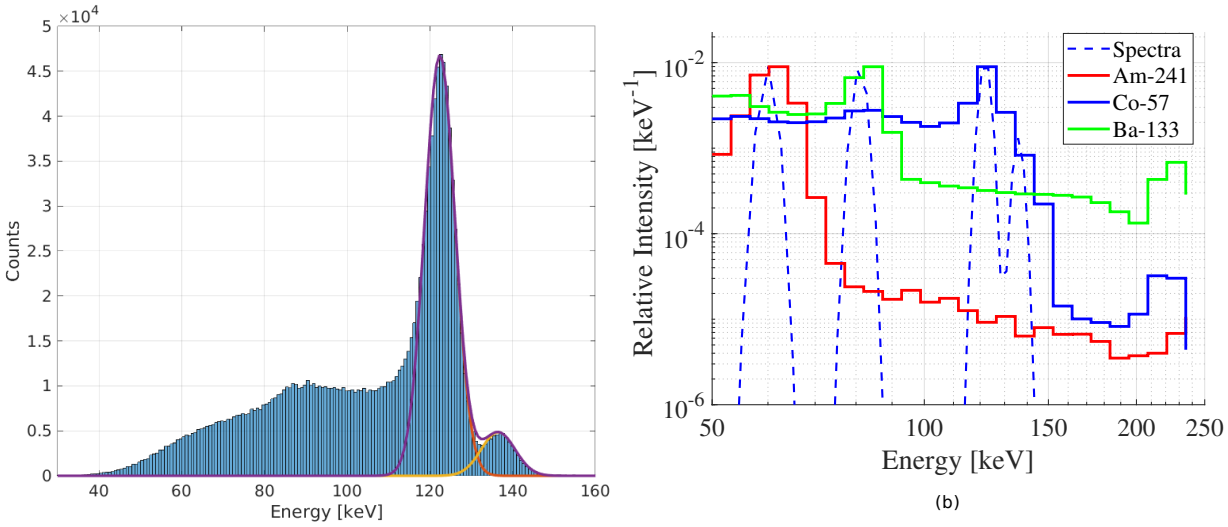

Figure 3.18: (Left) the recorded ^{57}Co spectrum, showing the main peak at 122 keV (86%) and a secondary peak at 136 keV (11%). Note the Compton shoulder that forms at lower energies than the 122 keV emission from Compton interactions and incomplete energy deposition in the detector material. (Right) the energy calibration spectra of three sources; ^{241}Am with a 60 keV emission, ^{133}Ba with a 81 keV emission, and the ^{57}Co source.

These calibration techniques are performed for each of the 12 detectors during the integration and testing phase of the the AEPEX development cycle. Additionally, metrics are formed to rank each detector's performance in order to track inefficiencies in each detector (e.g. flux insensitivity, hot pixel proclivity, etc.) to be accounted for during data analysis.

In-flight verification and re-calibration of the spectral response and imaging performance can be performed by leveraging stellar X-ray sources. Figure 3.19 shows a notional stellar X-ray pointing campaign for in-flight verification of the calibration of the AXIS instrument. These X-ray photons come from a variety of stellar objects with various spectra and intensities, and are all point sources relative to the AXIS angular resolution. The sources are included in the all-sky hard

X-ray observation campaign from the INTEGRAL X-ray telescope (Krivonos et al., 2010, 2012). A relatively short exposure (100s seconds) will provide a sufficient signal to verify the calibration of the instrument.

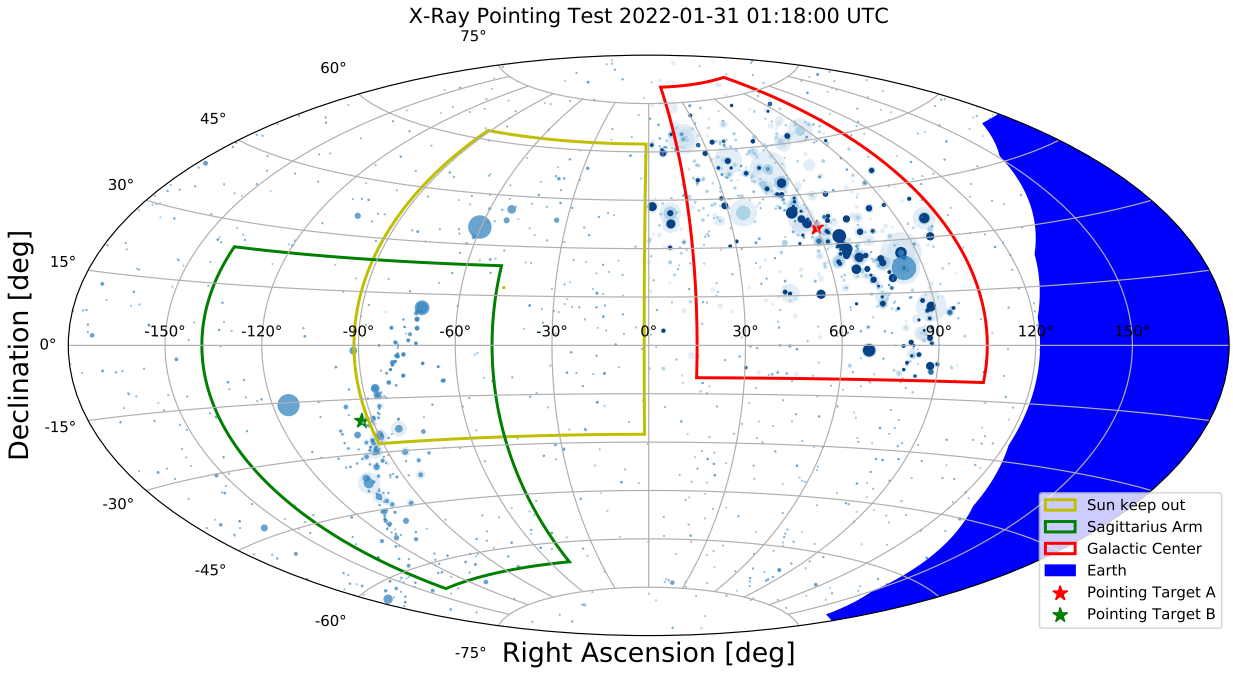

Figure 3.19: Stellar X-ray targets for AXIS in-flight calibration including the galactic center and the Sagittarius Arm of the Milky Way. The shade of blue corresponds to the spectral hardness of the X-ray source (darker blue being higher energy) and the size corresponding to the relative intensity of the source. These sources are all point sources given the AXIS angular resolution. Boxes correspond to the square field-of-view of AXIS.

3.4 Background Estimate

In order to determine the amount of noise induced on the detectors from the energetic charged particle and photon background in the LEO environment, a combination of analytical estimation, simulation, and lab experiments were performed. The simulation framework used here is GEANT4, a popular physics solver for charged particle instruments and space instrumentation (Agostinelli et al., 2003; J. Allison et al., 2006). Using this framework, an instrument mass model was built and simulated using a representation of the LEO space environment. In order to validate these

Background Source	**Data/Model**	**Background Contribution** [counts/s/detector]
Trapped and precipitating electrons	AE-8 electron flux Demeter energy spectra	10 – 100
Atmospherically backscattered electrons	*Marshall, et al. 2018* *Berland, et al. 2023* Xu EPMC Studies	1 – 10
Galactic Cosmic Rays	*Nymmik, et al. 1996* CREME86	100
Cosmic X-ray Background	*Hasinger, et al., 1996* *Gruber, et al., 1999*	10
Detector Background	Lab testing	10 - 30

Table 3.3: Low Earth Orbit Detector Background Contributions

simulations and characterize detector response to electrons, an electron accelerator experiment was performed at NASA Goddard. This section describes the simulation, experiment, and ultimately the expected background spectrum on the AXIS instrument during operation.

3.4.1 1D Modeling

High energy photon sources and very high energy charged particles are not easily mitigated with shielding and typically have well-defined behavior. For the purpose of obtaining an estimate of the background, we employ a 1D shielding model with appropriate solid angle distributions to the cosmic X-ray background (CXB), which has a non-negligible component in hard X-ray energies, as well as galactic cosmic rays (GCR).

In order to determine the instrument response to the GCR spectrum, we apply a CSDA stopping power formulation in a 1D simulation:

$$E_{i+1} = E_i - \left(\frac{dE}{dx}(E_i)\right)\ \Delta x \tag{3.7}$$

where the initial condition E_0 is swept over the range of GCR energies, and the step size Δx is chosen to be sufficiently small such that the energy lost per step is comparable to the resolution of dE/dx. The simulation reaches its end when the number of iterations N propagates the particle to a non-zero final energy E_f by satisfying $T\sec(\theta) = N\Delta x$, where θ is the angle of incidence of

the particle with respect to the shielding normal vector, and T is the thickness of the shielding material. This formulation assumes a high energy charged particle does not deviate significantly from its original trajectory.

The linear energy transfer (LET) coefficients $S(E)$ are obtained from the NISt pStar and aStar tables, which are tabulations of proton and alpha stopping power, respectively, and are used in the formulation $S\rho = dE/dx$ to obtain the stopping power, where ρ is the material mass density.

From this simulation, we obtain a shielding response function $\mathcal{H}(E_0, E_f)$ for charged particles which accounts for both the magnitude of attenuation at an initial energy E_0 as well as the energy loss that occurs from passing through the shielding. Figure 3.20 shows a plot of $\mathcal{H}$. The shielding

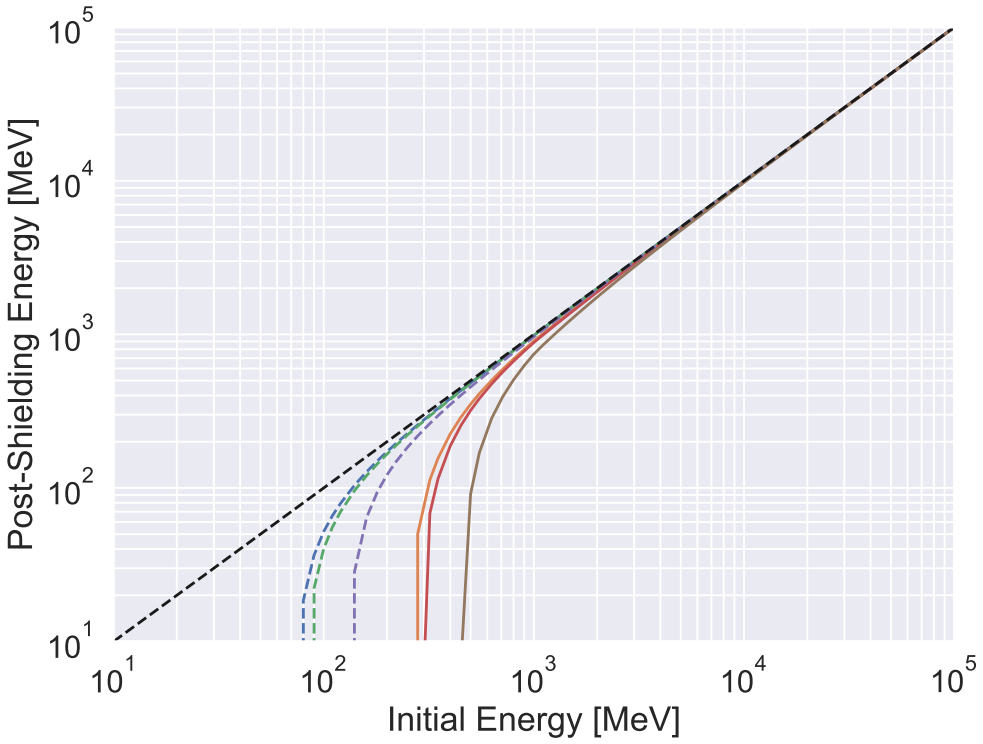

Figure 3.20: Plot of the polyethylene-tungsten-tin shielding response function $\mathcal{H}$ to protons (solid lines) and alpha particles (dashed lines) at 3 incidence angles: 0°, 35°, and 70°. Where the lines drop below 10^4 keV indicates complete blocking of the primary particle and where the curves asymptote to the dashed black line indicate no blocking.

response function can be convolved with the differential flux GCR spectrum to obtain a post-

shielding integral energy flux spectrum $f'_E(E)$ that would be incident on the detectors

$$f'_E(E_f) = f(E) \star \mathcal{H}(E_0, E_f) = \int f(E_0)\ \mathcal{H}(E_0, E_f)\ E_0\ dE_0 \tag{3.8}$$

If we instead multiply the two quantities point-wise, we can obtain a scaled differential input flux spectrum that penetrates the shielding, but we lose information on the shift in final energies. Regardless, our goal is simply a background rate estimate; the GCR background spectrum can be easily verified on-orbit during geomagnetic quiet times.

The GCR spectrum is taken from the Badhwar-O'Neill model halfway between solar minimum and maximum at a 500 km polar orbit (O'Neill, 2010). This model gives the differential and integral spectra for protons and alpha particles and accounts for magnetic shielding of the magnetosphere. Figure 3.21 shows the two differential spectra plotted as functions of particle energy.

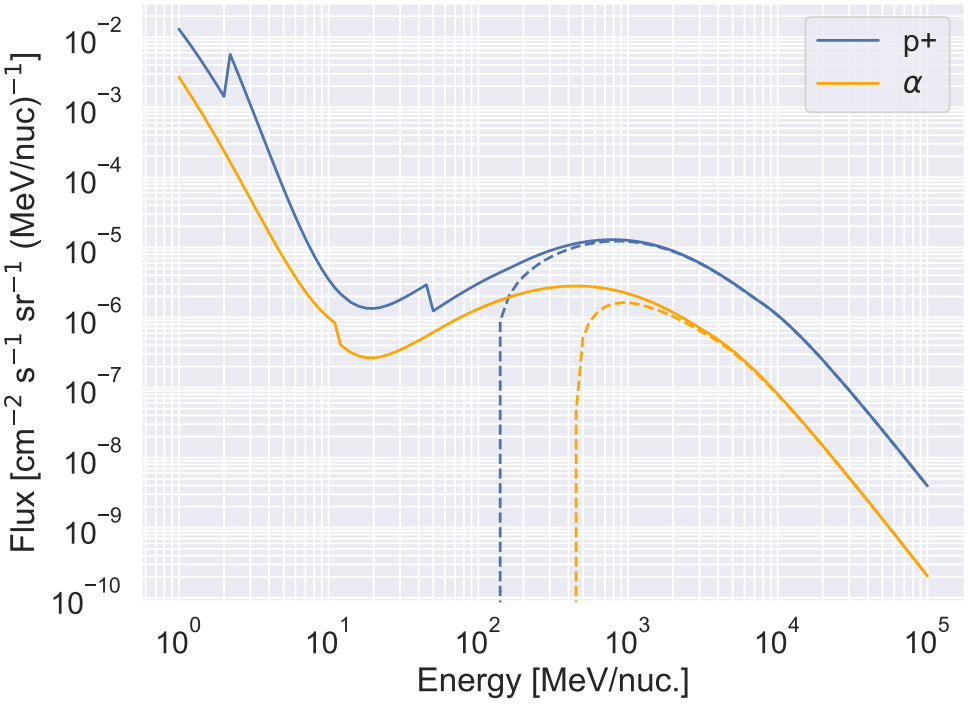

Figure 3.21: (Solid lines) The galactic cosmic ray (GCR) differential flux spectra for protons and alpha particles from the Badhwar-O'Neill model. (Dashed lines) The shielding-attenuated differential GCR spectra after convolution with the shielding response function $\mathcal{H}$. These spectra have penetrated the shielding and are incident on the detectors, and these curves do not account for secondary production.

Once we have a post-shielding flux f' we can assume that the Earth acts as an efficient shield to half of the spacecraft, so the solid angle used here is $\Omega = 2\pi$ sr, and the total area is taken as the back (zenith-facing) and sides (limb-facing) of the AXIS instrument, totalling 1200 cm^2, as particles incident on the spacecraft will likely scatter and create secondaries that will hit the detectors. Using these values, we can use a simple linear detection model to find the count rate C on the detectors

$$C = f' \ \Omega \ A \tag{3.9}$$

From these calculations, the background rate on the detectors from proton primaries is ~30 counts/second/detector and for alpha particles is 3 counts/second/detector. We assume the count rates corresponding to higher Z GCR species are on the order of the alpha particle count rate and are not impactful relative to the proton rate.

With the addition of thicker or higher Z shielding, the effective energy penetration of the shielding can (perhaps unintuitively) become higher due to inelastic collisions that generate secondary particles and radiation that are more easily transported through shielding material. When analyzing GCR penetration of shielding, electromagnetic interactions are joined by proton-nucleus and nucleus-nucleus interactions, which are two additional scattering mechanisms that can generate secondary radiation and target fragments. The fundamental description of inelastic particle interactions at high energies are incomplete (unlike electromagnetic interactions) and empirical models must be used to model inelastic interactions. In this work, we take the results of Zeitlin (2021) which show that, for aluminum shielding, the effective shielded dose rate from the GCR spectrum is 1.5 times the un-shielded dose rate. As dose rate is an incomplete analogy for particle flux due to the convolution of biological quality factors with the penetrating spectrum, an additional factor of 2 is taken here to more conservatively estimate the combined effects of the higher Z material and the non-biological application. Ultimately, the background count rate from GCRs is multiplied by 3 to capture the effects of secondary radiation production and target fragmentation.

Similarly, we can calculate the photon attenuation capability of the shielding using an ana-

lytical approximation of photon attenuation. Starting from the photon attenuation of a monolithic material with attenuation coefficient μ:

$$\frac{I(x)}{I_0} = e^{-\mu\ \Delta x} \tag{3.10}$$

we can amend this formula to let I_0 be the photon flux intensity on the boundary between shielding materials and iterate over k shielding layers:

$$\frac{I(x)}{I_0} = e^{-(\mu\ \Delta x)_k}\ e^{-(\mu\Delta x)_{k+1}} ... = \prod_k\ e^{-(\mu\Delta x)_k} = e^{-\sum_k (\mu\Delta x)_k} \tag{3.11}$$

We next define the total attenuation as $M(E) = \sum_i\ \mu_i(E)\Delta x_i$ where the sum of Δx is the total shielding thickness. We can then apply this attenuation law to the expected X-ray background from the CXB spectrum. This work uses the fit to X-ray and gamma-ray measurements of the CXB spectrum from the work of Gruber, Matteson, Peterson, and Jung (1999). Figure 3.22 shows the total attenuation M and the attenuation applied to the CXB spectrum.

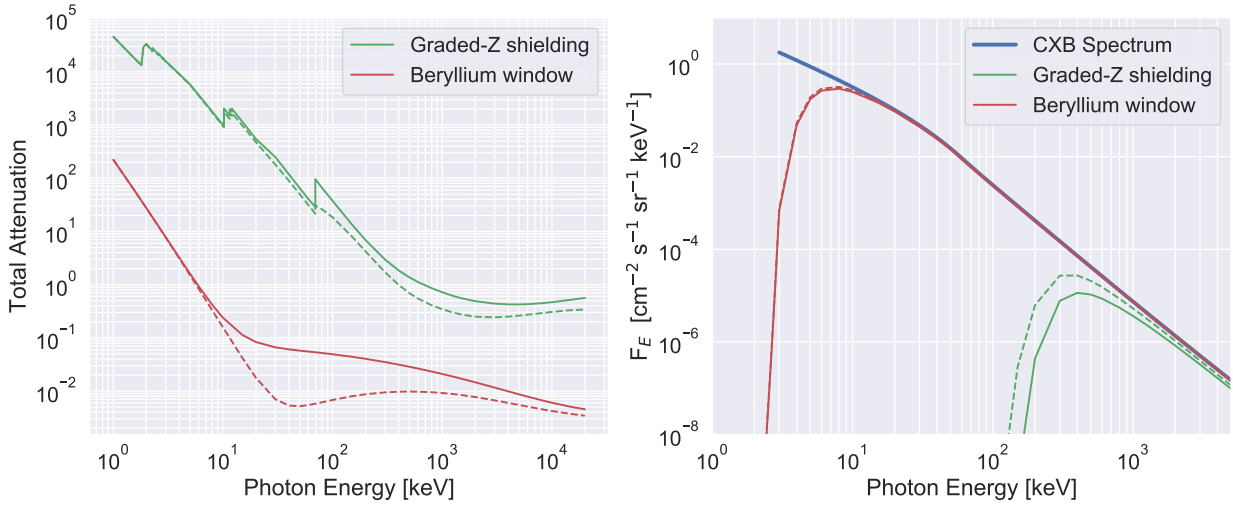

Figure 3.22: (Left) The total attenuation $M(E)$ for the graded-Z shielding and the beryllium window using the mass attenuation coefficient (solid lines) and energetic attenuation coefficient (dashed lines) is plotted as a function of photon energy. (Right) The CXB spectrum from Gruber et al. (1999) is plotted along with the attenuated spectra from passing through the graded-Z shielding and the beryllium window. The solid and dashed lines here also correspond to the mass and energetic attenuation, respectively.

By integrating the shielded CXB spectrum and multiplying by the geometric factor of the

back and sides of the AXIS instrument in a similar manner as for charged particles, we find that the background count rate contribution from the CXB is on the order of 10^1 counts/second/detector.

Of note, another potential source of noise in the AXIS imaging scenario is Earth's albedo, or reflectivity, in the X-ray band. This reflectivity would be relevant during a solar flare event, for example. Earth's X-ray albedo is modeled in Churazov, Sazonov, Sunyaev, and Revnivtsev (2008), where it is found that the combination of low X-ray flux incident on the Earth and the low albedo in hard X-ray ensures that atmospheric reflection of non-terrestrial X-rays is a negligible contribution to the AEPEX signal of interest.

3.4.2 3D Monte Carlo Modeling

A GEANT4 instrument response model has been built in order to quantify the photon scattering and detection behavior of the AXIS instrument. Another purpose of this simulation is to provide a realistic picture of the background that is induced on the detector from radiation belt electrons in the LEO space environment. In order to perform these simulations, the following steps were taken:

- AXIS geometry definition and material assignment:

  A low-fidelity model of AXIS was built in GEANT4 using the native CLHEP C++ geometry library and build system (Lönnblad, 1994). This library includes simple shapes (e.g. rectangles, spheres, cones) and Boolean operations between those objects (e.g. subtract, add, intersect) in order to build a representation of the "mass model" version of the instrument. The polyethylene, tungsten, tin, cadmium-zinc-telluride, and other supporting materials were assigned to their respective geometries. Care was taken to ensure no gaps or interference exist between materials and that a particle must pass through a thickness of material that is representative of the physical graded-Z shielding. The detector CZT material is pixelated in order to discretely measure the energy deposited in each pixel volume from photons and charged particles.

- Numerical implementation of background energy and angular distributions:

  The background angular distributions chosen to represent a realistic LEO environment are trapped electrons with either sine, sine-squared, or isotropic pitch angle distributions, and isotropic gyrophase distributions. These distributions are of the form

$$f_{sine}(\alpha, \theta) \propto \sin(\alpha) \ \frac{1}{\Delta\theta} \tag{3.12}$$

$$f_{sine-squared}(\alpha, \theta) \propto \sin^2(\alpha) \ \frac{1}{\Delta\theta} \tag{3.13}$$

$$f_{isotropic}(\alpha, \theta) \propto \frac{1}{\Delta\alpha_{LC} \ \Delta\theta} \quad , \tag{3.14}$$

  where $\alpha \in [0, \alpha_{LC}]$ and $\theta \in [0, 2\pi]$. The energy distribution chosen for these simulations were exponential energy distributions of the form e^{-E/E_0} with folding energies E_0 of 100, 200, and 300 keV to match the signal generation simulations for comparison and for SNR calculation purposes. The electron flux fraction and energy distribution in the loss cone and anti-loss cone are taken from R. Marshall and Bortnik (2018). The energy distribution of the backscattered electron flux is an exponential with a folding energy E_0' shifted down in energy and in flux. Importantly, most often the majority of the trapped flux is incident on the sides of the spacecraft, versus the nadir or zenith-facing sides, due to the angular distribution of the trapped electron population, where most particles are near 90-degree pitch angles at LEO.

- Adjustment and iteration through simulation settings:

  The simulation is now ready to run. Through monitoring the variance in the final background spectra and count rate estimates, the number of simulation particles that produces smooth results that are convergent to the accepted solution is determined. This number of simulation particles is 10^8 per background distribution and electron folding energy. For simulation settings, a proxy for spatial step size in the materials, the energy cuts (see Chapter 5 for more details on energy cuts) are set such that the highest energy electrons

must take multiple steps through the thinnest material. Care is paid to remove geometric "pinch points" where particles get stuck and artificially lose their energy.

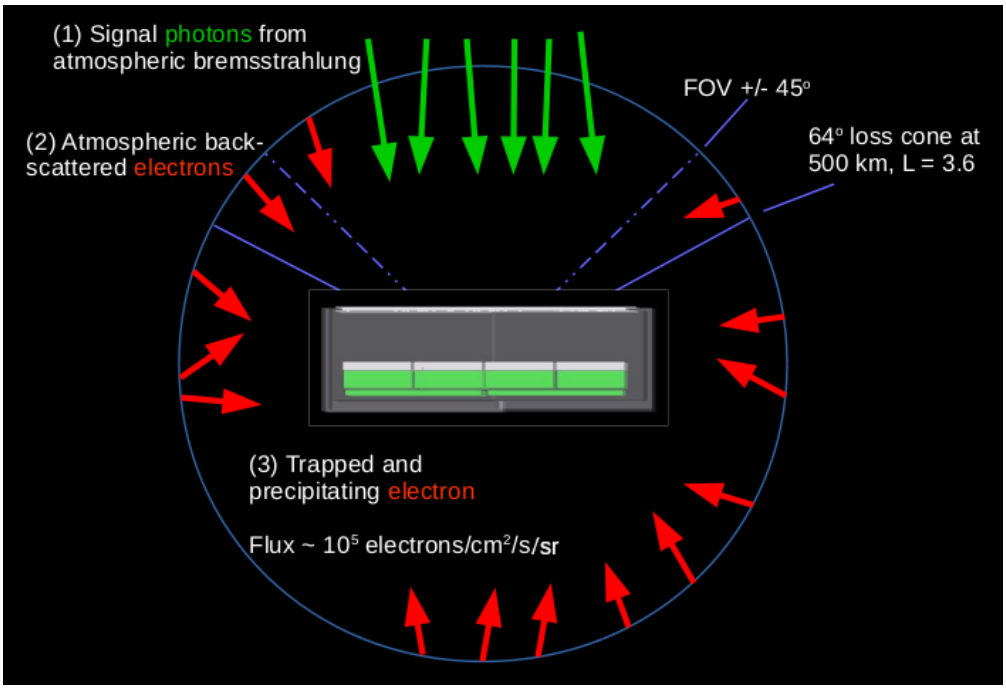

Figure 3.23: Schematic of the GEANT4 background and signal simulation, showing (red arrows) electrons and bremsstrahlung photons (green arrows) incident on the AXIS instrument. The field-of-view and edge of the loss cone are labeled, showing the loss cone, trapped, and anti-loss cone electron populations.

Figure 3.23 is a cartoon schematic of the AEPEX background and signal simulation in GEANT4, showing the grouping of the trapped and precipitating electrons which follow a sine, sine squared, or isotropic angular-spatial distributions, atmospherically backscattered electrons within the field-of-view, and signal photons generated from the atmosphere. Figure 3.24 shows a side view of the AXIS instrument geometry modeled in GEANT4 with incident trapped and precipitating electrons in the left image and atmospherically backscattered electrons in the right image.

Figure 3.25 shows histograms of the background spectra induced on the detectors for the three folding energies E_0 = 100, 200, and 300 keV. The background counts are re-binned at the AXIS energy resolution using the detection model for electron energy deposition. This plot represents the background that is induced by an isotropic pitch angle distribution, which is the worst-case

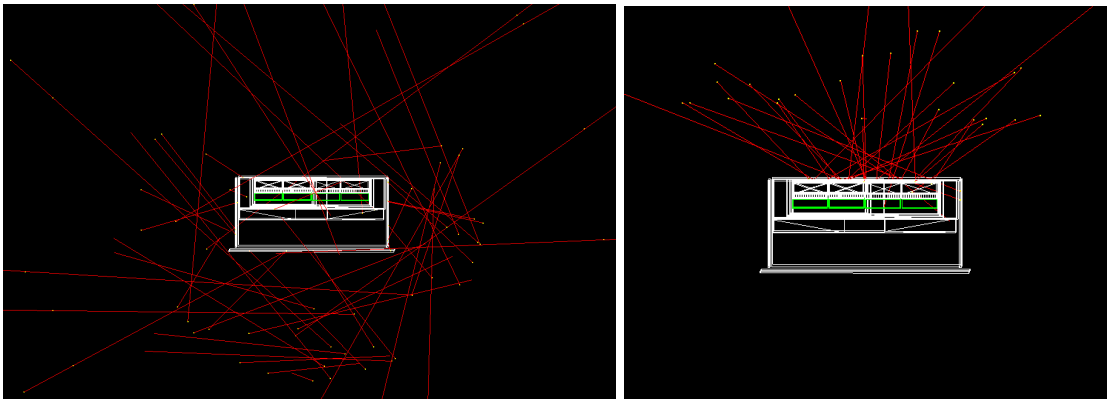

Figure 3.24: The AXIS instrument built using the GEANT4 CLHEP geometry library, showing (left) the trapped and loss cone electron populations, (right) anti-loss cone and atmospherically backscattered electrons that are within the AXIS field-of-view. Yellow dots indicate electron simulation steps and red lines indicate trajectories.

for background on the instrument but best-case for signal generation in the atmosphere. This case ultimately provides the highest SNR estimate for the AXIS instrument detailed in Section 3.5, and is therefore not used; the more conservative sine pitch angle distribution is used instead to design for the worst-case SNR that AXIS would reasonably encounter.

3.4.3 Goddard Electron Accelerator Testing

In order to validate the graded-Z shielding design and GEANT4 background simulations, a verification test is desired. To perform this test, the NASA Goddard Space Flight Center (GSFC) Radiation Effects Facility (REF) is utilized. The test is designed for two instrument configurations: configuration 1 where the electron beam is aimed directed through the beryllium window and tungsten coded aperture, and is incident on the detectors; and configuration 2 where the beam is directed through the graded-Z shielding onto the sides of the detectors. Figure 3.26 shows these instrument configurations with the chamber door open, where a red arrow indicates the beam direction.

The facility has a 2 MV accelerator that can generate electrons with energies ranging from 35 keV to 1.7 MeV with beam intensities of 10^{-9} to 1 μA/cm^2 (beam fluxes of 10^4 – 10^{13} cm^{-2} s^{-1}) over a 250 cm^2 beam spot size, which drives electron rates on the instrument of 10^6 – 10^{15} elec-

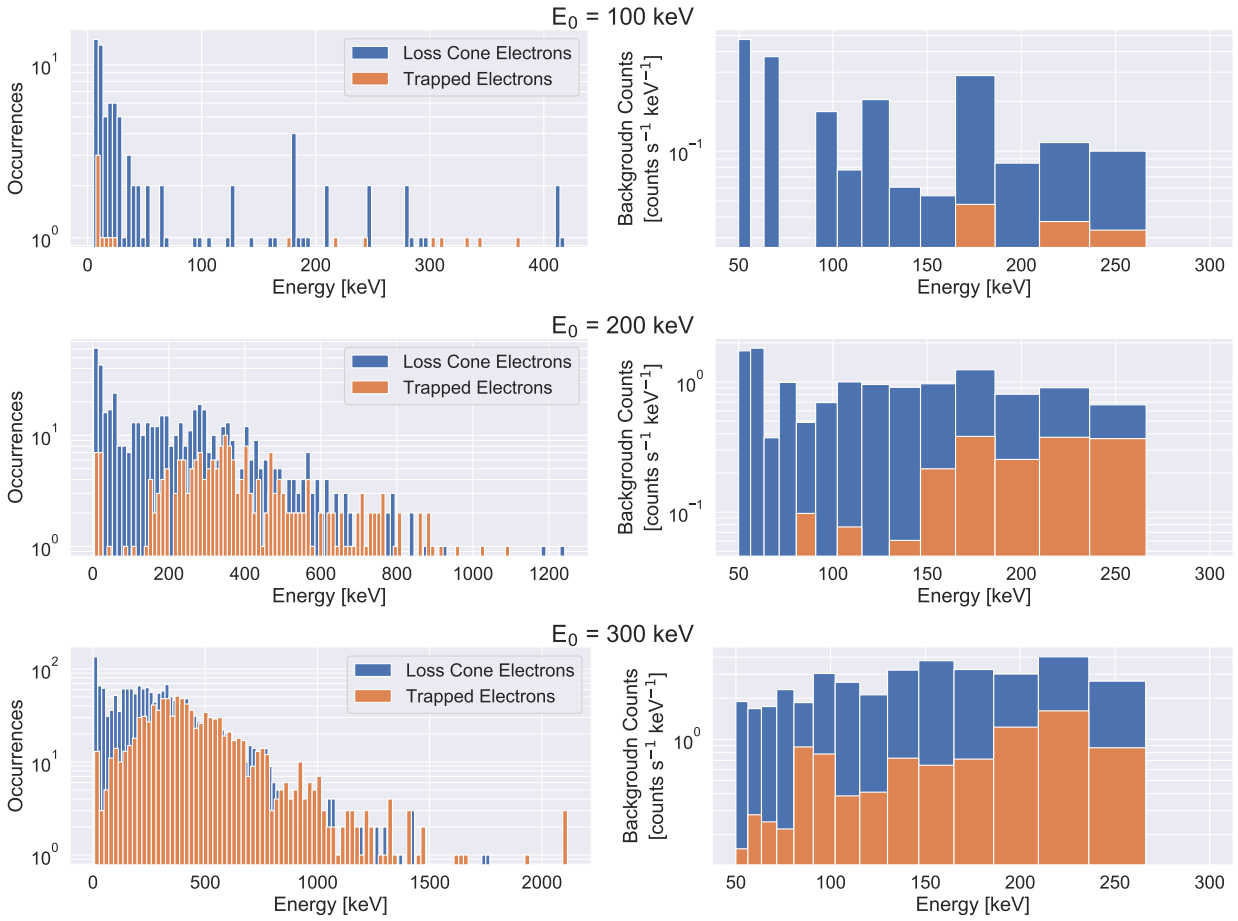

Figure 3.25: (Left) A histogram of the background noise induced on the detector from electron background sources. (Right) The background induced from electron sources re-binned at AXIS energy resolution. The rows correspond to the background folding energy cases of E_0 of 100, 200, and 300 keV for an isotropic pitch angle distribution, which represents the worst-case for background induced on the detectors and best-case for photon signal generation in the atmosphere.

trons/s. The test procedure is then to illuminate the instrument with 10 energies per configuration for approximately 12 minutes per beam energy in order to obtain sufficient detection statistics.

In order to maintain the instrument temperature, a hose with liquid nitrogen is placed so it circulates past the mount holding the thermal bracket, which is then modulated during testing to maintain operation temperature. Feed-thrus are designed to power the instrument, send commands, and received data during testing, which are connected to a 5 V laptop USB connection. The power line is boost-converted to 12 V onboard the instrument, and the RS-422 low voltage differential signal (LVDS) is translated to standard USB with an inline translator.

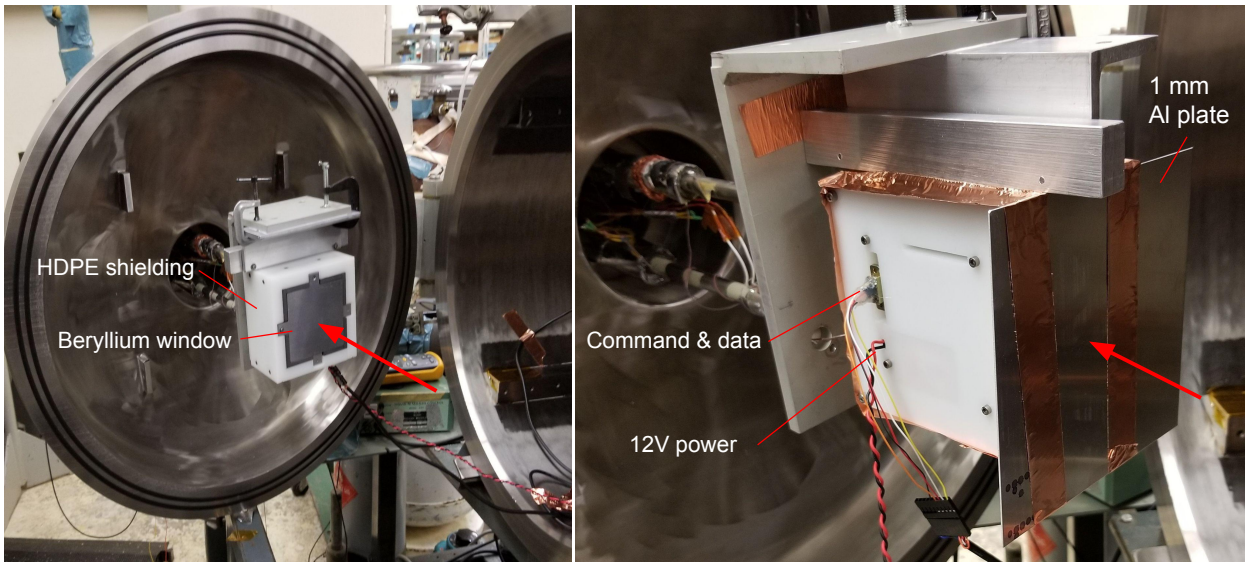

Figure 3.26: NASA Goddard Radiation Effects Facility (REF) electron beam test setup, showing (left) configuration 1 where the beryllium window and tungsten aperture are facing the electron beam and (right) configuration 2 where electron beam is incident on the graded-Z shielding. The aluminum L-bracket is mounted to a temperature-controlled surface in order to cool the instrument during vacuum operation, and feed-thrus transfer power, commanding, and data to the instrument from a laptop.

During testing, a measurement of opportunity was made when the facility placed a 3.8 cm aluminum Faraday cup in front of the beam to measure beam current for beam adjustment purposes. This configuration was modeled in GEANT4, and it was found that bremsstrahlung photons are produced and are the vast majority of the particles that reach the instrument. In this way, the experiment measures both electrons and photons incident on the prototype instrument.

Before the beam illumination, during the changing of the instrument configuration, and again after the experiment, the energy calibration is verified on-site with an ^{241}Am source, which has a strong line emission at 60 keV. A 82 $\pm$ 5.3 keV emission was discovered in the spectral data that has an intensity proportional to the background rate on the instrument. This is likely either a gold K-shell emission or lead M-shell emission from materials in the detector front-end electronics.

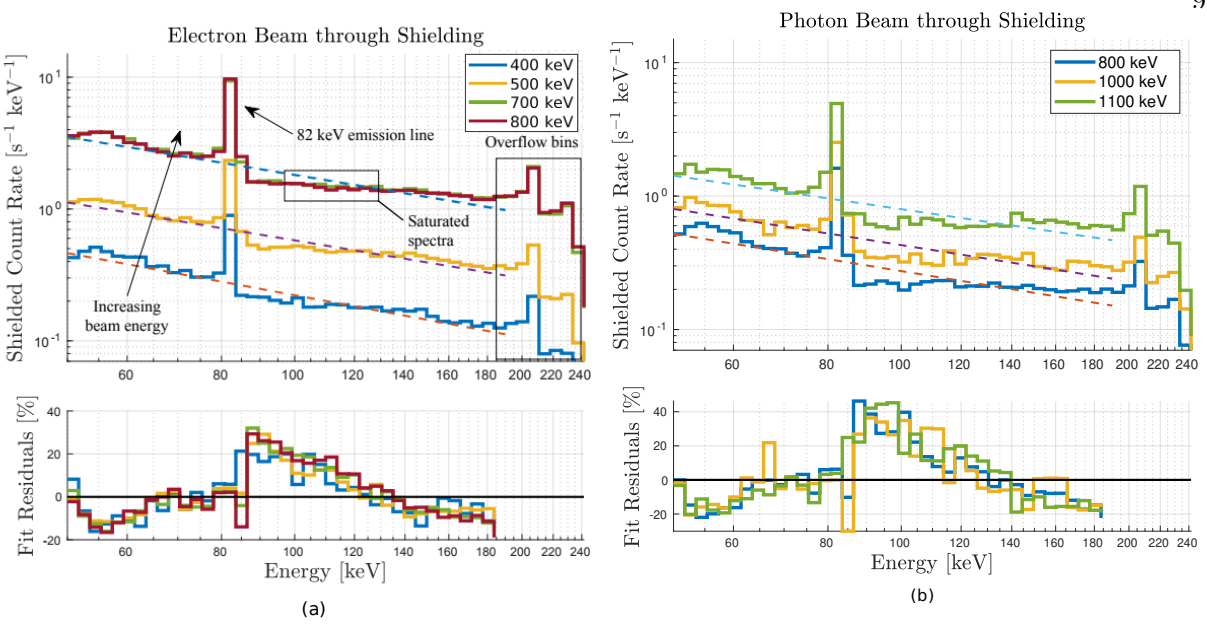

Figure 3.27: (a) Normalized shielded spectra generated during the electron beam bombardment. The 82 keV feature is removed for the background model fit, although some residuals remain between 90 – 100 keV from the 8-point boxcar smoothing method. Beam energies for the left plot are 400, 500, 700, and 800 keV. (b) Spectra generated during electron beam on, Faraday cup down conditions that produce a photon beam incident on the graded-Z shielding. Beam energies for the right plot are 800, 1000, and 1100 keV.

The measured spectra for the two configurations and the status of the Faraday cup ("up" corresponding to electrons, "down" corresponding to photons) are shown in Figures 3.27 and 3.28. These figures show the differential count rate per beam configuration, as well as power law fits to the data after removing the feature at 82 keV. The power law fits are of the form

$$f(E) = A\,\frac{\Gamma - 1}{E_{min}}\left(\frac{E}{E_{min}}\right)^{-\Gamma} \tag{3.15}$$

where the total or integrated beam flux A, the spectral index Γ, and incident beam flux and energy are tabulated below. E_{min} in this case is the lower end of the detection range, 50 keV. Figures 3.27 and 3.28 also plot the residuals of this power law fit, where high residuals likely indicates higher secondary electron penetration that does not act according to the spectral power law, which likely measure photons generated in the shielding. The power law fit is worse in the immediate vicinity before and after the 82 keV line emission, which is indicative of absorption and then re-emission of

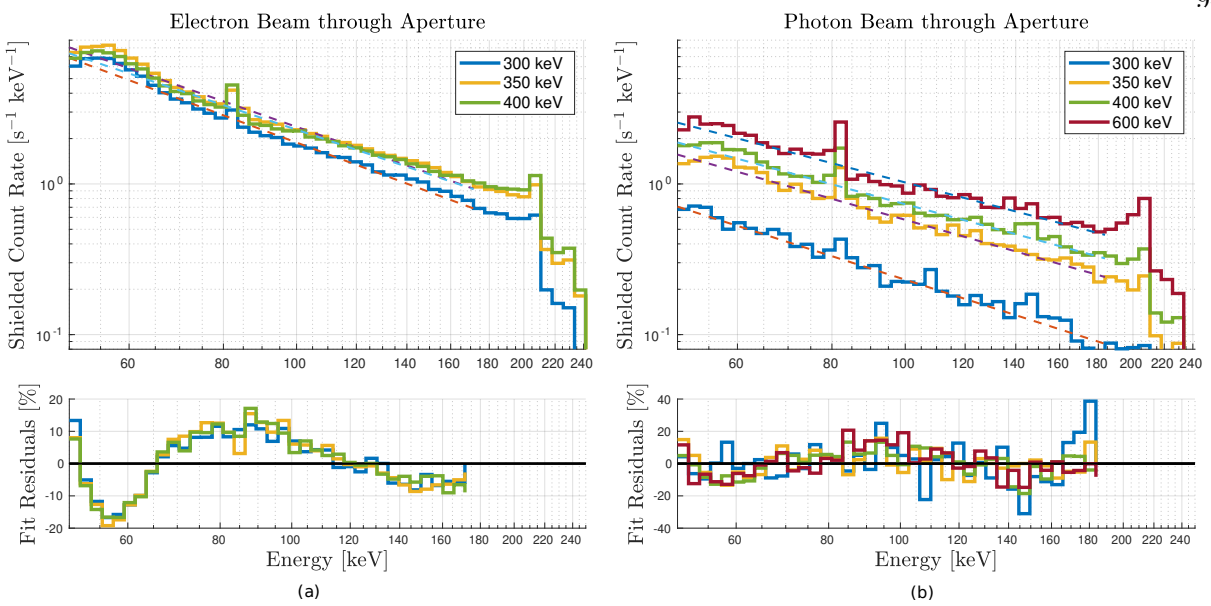

Figure 3.28: (a) Shielded spectra from the electron beam incident on the beryllium window and tungsten aperture. There is higher penetration of low energy electrons relative to the graded-Z shielding portion of the background model, likely due to the lack of low-Z materials to attenuate low energy electrons. (b) Electron beam on, Faraday cup down conditions through the aperture, showing both higher penetration and higher spectral indices than the graded-Z shielding. Beam energies for both plots are 300, 350, and 400 keV.

both charged particles and photons by the material that causes this characteristic emission. Since it is not possible the remove the material responsible for the line emission, the proportionality of the line emission is characterized as a function of the background count rate and spectra in order to remove the effect of the line emission on the X-ray data during the AEPEX mission.

The instrument electronics are configured in full energy resolution mode in order to capture a high resolution measurement of the spectrum that penetrates the aperture and shielding. However, due to instrument development limitations, the data transfer rate between the instrument's RS422 connection and the laptop is sub-optimal and cannot handle the full event rate at combined high beam energies and fluxes, and due to facility limitations, the beam current could not be adjusted lower. This caused spectral "saturation" at high beam energies when the penetrating fraction of radiation increases. The saturated spectra are shown for example in the left panel of Figure 3.27 where increasing beam energy does not shift the curve upwards. The spectral shape is still

responsive to changes in beam energy and therefore spectral information is still recorded. To further support this claim, testing in the CU Boulder lab was performed with four radiation sources placed at close range that similarly saturate the detector, and all spectral lines are resolved, since the photon arrivals at the detectors are random in time and space. Expected count rates with the effects of saturation are reported in Tables 3.4 and 3.5, and the count rates are extrapolated at higher beam energies in this analysis to estimate the count rate during high energy, high flux conditions.

Faraday Cup	**Beam Energy** [keV]	**Beam Flux** $[\text{cm}^{-2}\ \text{s}^{-1}]$	Γ	**Total Count Rate** $[\text{s}^{-1}]$
Up	400	9.36×10^5	1.06 ± 0.04	35.0 ± 5.92
Up	500	9.36×10^5	0.95 ± 0.09	90.9 ± 9.53
Up	700	9.36×10^5	0.95 ± 0.26	301 ± 17.4
Down	800	–	0.93 ± 0.04	45.6 ± 6.75
Up	800	7.49×10^5	0.96 ± 0.26	299 ± 17.3
Up	900	6.87×10^5	0.98 ± 0.25	295 ± 17.2
Down	1000	–	0.90 ± 0.06	71.5 ± 8.46
Up	1000	1.25×10^6	0.99 ± 0.24	293 ± 17.1
Down	1100	–	0.83 ± 0.09	136 ± 11.7
Up	1100	1.04×10^6	0.99 ± 0.24	288 ± 17.0
Up	1300	9.36×10^5	1.01 ± 0.24	284 ± 16.9
Up	1400	1.37×10^6	1.01 ± 0.24	284 ± 16.8
Up	1500	9.36×10^5	1.01 ± 0.25	288 ± 17.0

Table 3.4: Electron Beam Experiment Results, Graded-Z Shielding.

Faraday Cup	**Beam Energy** [keV]	**Beam Flux** $[\text{cm}^{-2}\ \text{s}^{-1}]$	Γ	**Total Count Rate** $[\text{s}^{-1}]$
Down	300	–	1.44 ± 0.17	85.9 ± 9.27
Up	300	4.62×10^5	1.87 ± 0.81	289 ± 17.0
Down	350	–	1.36 ± 0.19	109 ± 10.4
Up	350	9.36×10^5	1.75 ± 0.92	368 ± 19.2
Down	400	–	1.32 ± 0.25	157 ± 12.5
Up	400	5.43×10^5	1.68 ± 0.82	354 ± 18.8
Up	500	8.11×10^5	1.49 ± 0.63	360 ± 19.0
Up	600	9.36×10^5	1.39 ± 0.55	354 ± 18.8
Up	700	8.11×10^5	1.39 ± 0.58	354 ± 18.8

Table 3.5: Electron Beam Experiment Results, Beryllium Window & Tungsten Aperture.

These results are compared to a GEANT4 simulation of the electron beam incident on the

instrument in the two experiment configurations. The resulting total count rates match to within the Poisson detection noise on the detector for the non-saturated cases, and the spectral shapes are similar. The experimental results for the spectral shapes are used to adjust the simulation results in order to generate an electron detection background model for the Redlen detectors. In matching the electron beam results to simulations over the energy range expected on orbit, the GEANT4 LEO background simulations are verified. The results of this analysis show that the expected variation due to modeling errors is within the Poisson noise expected on the detectors given the background rates, so this experiment verifies the simulations and background modeling work.

3.5 Signal-to-Noise Ratio Estimate

The combination of the modeled signal and background yield the expected signal to noise ratio:

$$SNR_{\text{Total}} = \frac{S\sqrt{n_{det}\ \Delta t}}{\sqrt{S+B}} \tag{3.16}$$

where S is the signal count rate, B is the background count rate, n_{det} is the number of detectors co-adding their image (in this case 11), and Δt is the exposure time per frame (10 seconds). The combination of the multiple detectors and exposure time yield a 10.5x SNR advantage for any given imaging scenario (S, B). We combine the results of the signal modeling in Section 3.2 and the background modeling and experiments in Section 3.4 using Equation 3.16 to calculate the total expected SNR of the AXIS instrument. Total SNR is related to the detectability of a signal out of background noise, and the SNR per pixel is related to imaging capability. Figure 3.29 shows the SNR estimate under the nominal precipitating electron flux of 10^5 cm^{-2} s^{-1} sr^{-1} and is scaled linearly to 10^4 and 10^6 cm^{-2} s^{-1} sr^{-1} to show the effects of weaker and stronger precipitation events, respectively, on the AXIS SNR.

Also plotted in Figure 3.29 is also the Poisson pixel, or imaging SNR, which is a metric that describes the capability of the instrument to image the source. The pixel SNR is calculated by

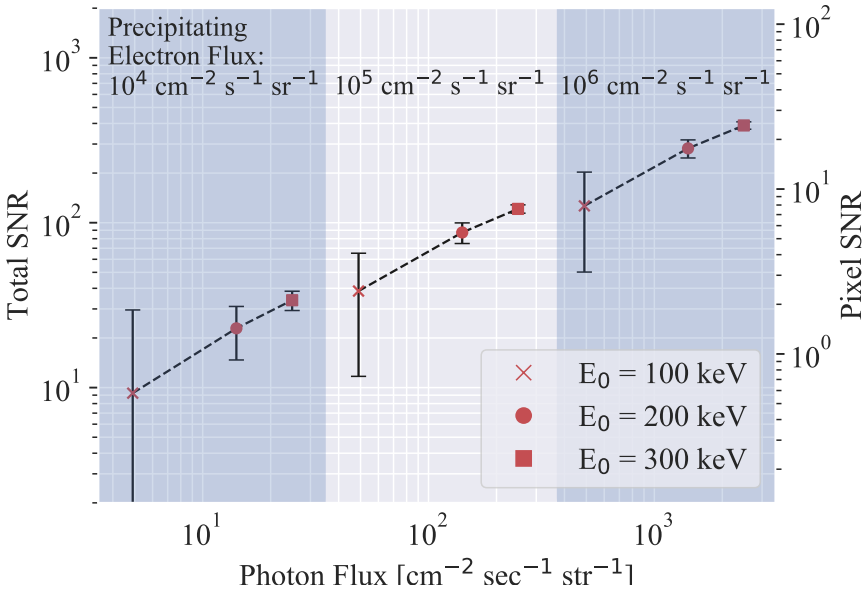

Figure 3.29: Total and pixel (imaging) signal-to-noise ratio (SNR) estimates for the three nominal precipitation energy cases detailed in Figure 3.15, scaled up and down by one order of magnitude in electron flux from the nominal flux of 10^5 cm^{-2} s^{-1} sr^{-1}. The SNR is plotted for each precipitating electron spectrum folding energy E_0 of 100, 200, and 300 keV.

considering each pixel as an independent detector, which can be formulated in the following way: let us replace the signal per detector S with the signal per pixel S'_{ij}, which we can relate to the total signal through summation. We'll treat the background in the same fashion, and also make the assumption that the signal is distributed in a uniformly random sense across the pixels such that we can write

$$S = \sum_{i=1}^{16} \sum_{j=1}^{16} S'_{ij} = 256 \times S'_{ij} \tag{3.17}$$

for the 16×16 pixel Redlen detectors. We can now rewrite Equation 3.16 as

$$SNR_{\text{Pixel}} = 256 \; \frac{S'_{ij}\sqrt{n_{det}\;\Delta t}}{\sqrt{256\;S'_{ij} + 256\;B'_{ij}}} = \frac{16\;S'_{ij}\sqrt{n_{det}\;\Delta t}}{\sqrt{S'_{ij} + B'_{ij}}} \tag{3.18}$$

We can now write the relationship between total and pixel SNR simply as $SNR_{\text{Total}} = (1/16)\; SNR_{\text{Pixel}}$. It's found experimentally that a pixel SNR of ~1.2 is needed to form an image with sufficient confidence to make scientific interpretations. That is to say, the uncertainty in image interpretation is commonly taken as inversely proportional to the SNR (e.g. Wagner & Brown, 1985; Kellman & McVeigh, 2005), so we find that imaging SNRs above 1.2 attribute sufficient confidence for

interpreting the spatial scales of precipitation X-ray patches in simulation.

3.6 AFIRE Electron Detector

The AFIRE instrument is a built-to-print copy of the electron detector instruments used on the FIREBIRD-II CubeSats (Crew et al., 2016; Johnson et al., 2020). The instrument is comprised of two electron detectors sensitive to electron energies between ∼200 keV – 1 MeV that share look-directions but have different fields-of-view, such that a portion of the field-of-view (approximately 0.5 sr) is overlapping. The "surface detector" (so-called because the detector sits at the instrument surface) has an approximately 2π sr field-of view and the "collimated detector" has a 45° field-of-view. Figure 3.30 shows the electronics stack and detector housing, with the detectors covered for

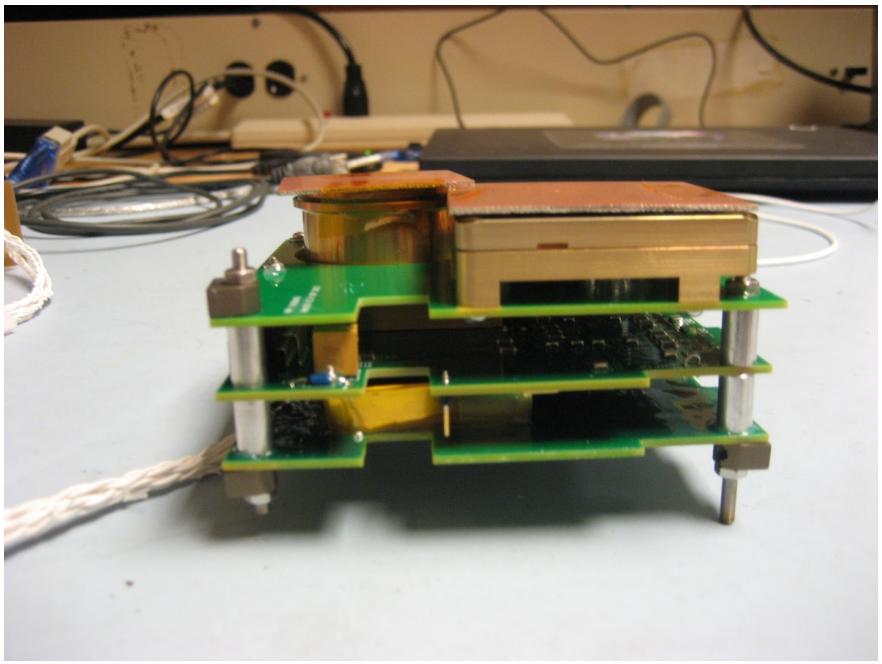

Figure 3.30: An image of the AFIRE engineering model, showing the electronics board stack and detector housing, covered by pieces of aluminum to keep dust off the silicon surfaces. The collimated detector with a 45° field-of-view is on the left and the surface detector with a 2π field-of-view on the right.

cleanliness. The silicon detectors are 1500 μm thick, which can fully stop 1050 keV electrons, and have a diameter of 32 mm (Johnson et al., 2020). The detector material and front-end electronics

are manufactured by Micron Technology, Inc.

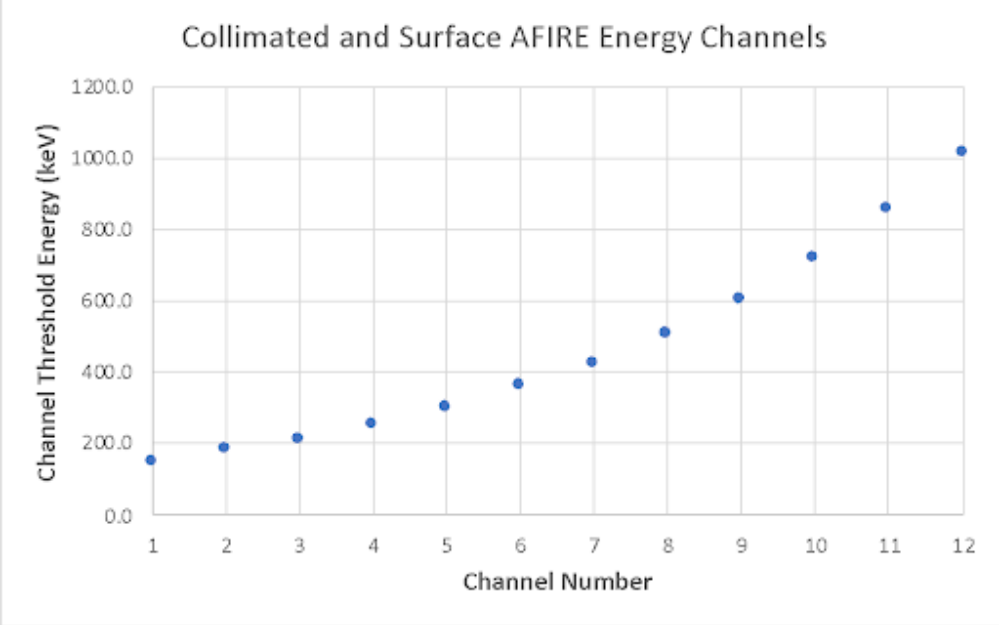

Figure 3.31: The energy channel threshold edges of the AFIRE instrument's two detectors. The odd number channels correspond to the surface detector and the even number channels correspond to the collimated detector in order to "feather" the 6 channels per detector to provide higher energy resolution.

The detector energy channel edges are shown in Figure 3.31, where the odd numbered channels belong to the surface detector and the even numbered channels correspond to the collimated detector. By interleaving the energy bin edges in this manner, the energy resolution of the final electron spectrum estimate is increased.

In addition to differential electron spectra in energy, a coarse estimate of the pitch angle distribution can be made using the semi-overlapping fields-of-view. We'll assume a physics-based functional form for the pitch angle distribution $f(\alpha)$ and form an integral that describes the differential count rate on each detector when the detectors point up the magnetic field line:

$$\text{Count rate}(E) = \int\int f(E,\alpha)\ G(\alpha)\ \sin(\alpha)\ I_{\alpha\in\text{FOV}}(\alpha)\ d\alpha\ d\theta \tag{3.19}$$

where $I_{\alpha\in\alpha_i}$ is the indicator function that constrains the integration to pitch angles that fall within the specific instrument's field-of-view α_i, $G(\alpha)$ is the geometric factor that combines the detection

area and field-of-view, and $f(E, \alpha)$ is the combined flux spectrum and pitch angle distribution. A plot showing this calculation in polar space is shown in Figure 3.32. By combining the instruments

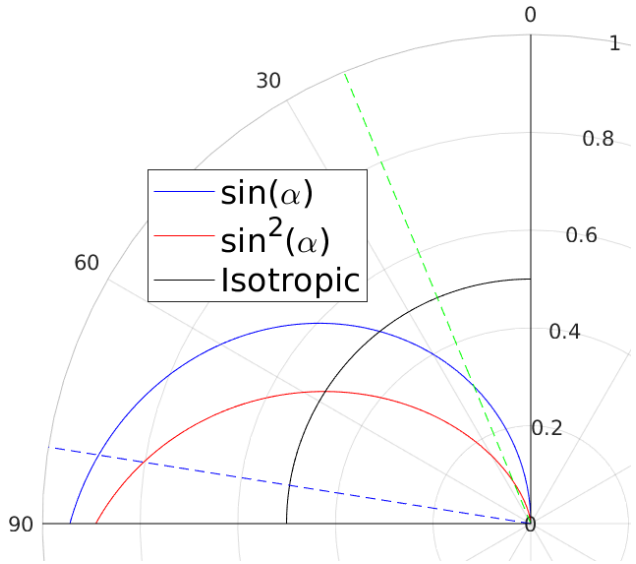

Figure 3.32: The AFIRE fields-of-view of the two detectors are plotted with dashed lines on the unit polar circle, and three proposal pitch angle distributions are shown in polar space. Note how much of each distribution falls within the collimated field-of-view versus the larger field of view.

angular response through the geometric factor for the collimated detector (col) and the surface detector (surf), we can form the ratio

$$\frac{\text{Count rate}_{\text{col}}}{\text{Count rate}_{\text{surf}}} = \frac{\int f(\alpha)\ G_{col}(\alpha)\ \sin(\alpha)\ I_{\alpha\in\text{FOV col}}(\alpha)\ d\alpha}{\int f(\alpha)\ G_{surf}(\alpha)\ \sin(\alpha)\ I_{\alpha\in\text{FOV surf}}(\alpha)\ d\alpha} \tag{3.20}$$

The angle α_{col} and α_{surf} here are the half-angles of the fields-of-view since the 2π integration covers a full rotation in gyrophase space and cancels out in the ratio in Equation 3.20. This method is verified by Monte Carlo simulation in GEANT4 using the FIREBIRD mass model of AFIRE. An example of the spectral ratio calculated with Equation 3.20 resulting from these simulations is shown in Figure 3.33. The simulated data using a sine pitch angle distribution generally agrees below the highest energy channels, where electron scattering and bremsstrahlung in the spacecraft bus and AFIRE instrument itself may force the electron distribution to appear more isotropic in pitch angle space.

The goal of this calculation is to be able to distinguish the "family" of pitch angle distribution

that AFIRE is measuring; for example, being able to fit the coefficient n from a $\sin^n(\theta)$ distribution, or state whether the pitch angle distribution is more isotropic will be a valuable data product even though it is short of an angular-resolved electron pitch angle measurement. Further simulation and investigation of the efficacy of this method is the topic of future work.

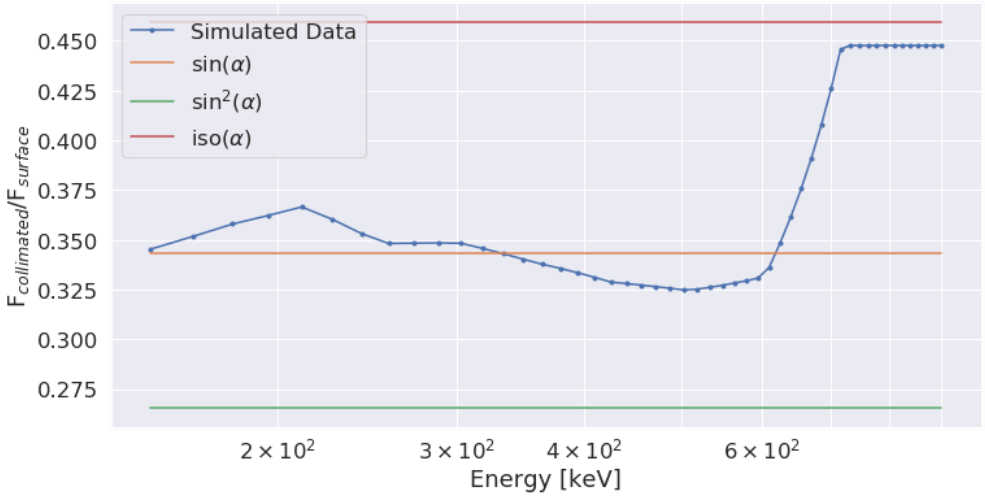

Figure 3.33: Results of Equation 3.20 from a GEANT4 simulation of a sine pitch angle distribution, over-sampled relative to the AFIRE energy resolution by a factor of 10. The trend of the simulated matches the expected value of the ratio at all energy channels except the highest, which is likely due to scattering within the spacecraft bus and AFIRE instrument.

Chapter 4

Wide Field-of-View Coded Aperture Imaging

The AXIS imaging spectrometer is a novel, wide field-of-view coded aperture imager that will be mounted nadir-facing on the AEPEX CubeSat spacecraft, where it will make measurements of X-rays produced by radiation belt electron bremsstrahlung interactions with the neutral atmosphere. AXIS aims to answer the question of the spatial scales inherent to this process; in order to address that science question, spatial resolution must be captured in the hard X-ray wavelength range. AXIS implements the coded aperture mask system to obtain true 2D imaging of X-ray photons. This chapter describes the theory behind X-ray detection, spectroscopy, and the theory and practice of coded aperture imaging with respect to the AXIS X-ray optics design.

4.1 Introduction to X-ray Detection and Imaging

Remote observation of X-ray photons have been used for a wide range of scientific inquiries since their discovery in the late 19^{th} century. By some definitions, X-rays are photons generated from energetic processes that affect or are a product of the electronic shell of an atom. However in this work we group photons energies by detection behavior: we assume all photons above approximately 100 eV are X-rays, and that the behavior of high energy X-rays (e.g. 100s keV) and gamma-rays (MeV energies and above) is sufficiently similar to be treated with the same detection techniques (Bearden, 1967; Als-Nielsen & McMorrow, 2011).

X-rays have myriad uses in material science, geology, and micro-manufacturing due to their short (nanometer or picometer) wavelengths. X-rays also have uses in medical imaging, radiology,

and material identification (F. Smith, 1999; Bunaciu, UdriŞTioiu, & Aboul-Enein, 2015). However, there are a number of difficulties in the measurement of energetic photons: the same advantage X-rays have in their high energy and penetration ability in these fields make them difficult to wield in other contexts. For many energetic physical processes, remote observations of X-rays can shed light on specific parameters of the processes. For instance, in astronomy a primary energetic loss mechanism of galaxies is electron-electron thermal bremsstrahlung radiation (Fabian, 1994; White, Jones, & Forman, 1997). By observing the X-ray spectrum generated by this process, the average temperature and other details about the galaxy can be estimated.

At Earth, X-rays are completely absorbed by the atmosphere before they can reach sea level (Watanabe, 1958). This prevents extra-terrestrial X-ray detection by ground-level instrumentation. Remote observations of X-rays were thus delayed until the implementation of balloon and rocket payload-hosted X-ray detectors, which enabled the first direct astronomy observations in the X-ray wavelength (Bradt, Ohashi, & Pounds, 1992). After the discovery of X-rays through radio-sensitive films, a new difficulty was revealed: focusing and imaging. In order to obtain angular information, which in turn is used to determine spatial information of an X-ray source, predictable deviations in incoming X-ray trajectory angle must measureable in order to form an image (Mould, 1995). X-rays can only be reflected at very shallow angles of incidence due to their approximately unity index of refraction in most materials (Bragg & Bragg, 1913). Snell's law can be used to describe this phenomenon which is known as **total internal reflection** (TIR):

$$\frac{n_2}{n_1} = \frac{\sin(\theta_1)}{\sin(\theta_2)} \tag{4.1}$$

where n_i are the indices of refraction in two materials and θ_i are the incidence and transmission (or reflection) angles relative to the normal of the boundary the photon is incident upon. By transferring from vacuum propagation with $n_1 = 1$ to an index of refraction of n_2 which is very close to but slightly lower than unity and is wavelength-dependent ($1 - n_2/n_1$ is within the range of 10^{-4} – 10^{-6} for many materials in X-ray wavelengths), the right hand side of Equation 4.1 becomes approximately unity at most angles, resulting in $\theta_1 \approx \theta_2$. When the two angles are approximately

equal, we can conclude that X-ray photons will tend to continue onwards with only a slight deviation in incidence angle versus the incidence angle with which it arrived at the material, which is the case of pure transmission.

In order to reflect an X-ray, a shallow incidence angle, known as the **critical angle** θ_c is required. This critical angle is found from

$$\theta_c = \arcsin(n_2/n_1) \tag{4.2}$$

which is defined when $n_2 \leq n_1$. This critical angle for X-ray is highly limiting in X-ray mirror design; for example, a value of $n_2 \sim 1 - 10^{-4}$ yields a critical angle of 89.2°, which leaves a range of 0.8° incidence angle from the parallel plane of a mirror surface that can be used to focus the photon. Another case (not modeled by Snell's law) is absorption by the material which is described by the Beer-Lambert absorption law and by capture cross sections of the electric shell transitions which cause photon absorption and re-emission in the form of characteristic line emissions. These line emission are unique to the electronic structure and orbital state of a material and can be leveraged in parameter estimation and inversion problems using remote X-ray observations.

The principle behind Wolter-type X-ray telescope designs is based on leveraging the grazing incidence angles calculated in Equation 4.2 of photons to make many small deviation in their angles over a long path length (Chase & VanSpeybroeck, 1973; Werner, 1977). Wolter telescopes are able to achieve high degrees of focusing but are limited in the wavelengths that they can focus. Wolter telescopes are also more effective at lower X-ray energies (100s eV – 10s keV) and become intractable or unmanufacturable for gamma-ray energies due to the high degree of surface polishing and path lengths needed to focus high energy photons (Aschenbach, 2009). Additionally, Wolter telescopes require exotic materials and coatings, as well as a high degree of surface uniformity on the atomic level in order to perform as designed. Large spacecraft are needed to house Wolter telescope designs, particularly due to the length of the telescope. For example, the Chandra X-ray observatory is 13.8 m×19.5 m in its deployed state (Weisskopf, Tananbaum, Van Speybroeck, & O'Dell, 2000). The associated fields-of-view of these instruments are also relatively small (often on

the scale of arcminutes).

An optical design that is more popular in higher energy, hard X-ray and gamma-ray imaging is the **coded aperture mask** (Caroli, Stephen, Di Cocco, Natalucci, & Spizzichino, 1987; Stephen, 1991; Ranieri, Badiali, Cardini, Emanuele, & Auriemma, 1981). This design uses a similar "focusing" technique as a pinhole imager; that is, a photon's trajectory is not focused through reflection or refraction, but is instead only allowed to pass through a transparent element with a well-known location relative to a position-sensitive detector such that the photon's angular information is recorded by the detector via its energy deposition location in the detector. The drawback of a single pinhole design is that the pinhole must be small relative to the detector size to have any angular resolution, and therefore the effective geometric factor of these imaging systems is necessarily small. In contrast, a major advantage of the coded aperture mask is in having many holes, which increases the geometric factor and enables detection of high energy, low strength signals (T. M. Cannon & Fenimore, 1980). Another major advantage of the coded aperture mask is that these imaging systems can have a high level of angular, and therefore, spatial, resolution over a wide energy range (Accorsi, Gasparini, & Lanza, 2001). A compromise in geometry can be made with a slit aperture where the transmission element is narrow in one dimension and wide in the other, instead of one small open element, but imaging capability in the long dimension is lost. Table 4.1 details a qualitative trade-space study of the various X-ray optical designs that were considered for the AXIS instrument. Not mentioned here, micropore optics (Mutz, Bonnet, Fairbend, Schyns, & Seguy, 2007; Catenza, 2022) are a series of microchannels on a shaped plate with specified pointing directions that collimate the field-of-view above a single pixel; these systems are appropriate only for low energy (soft) X-rays due to material penetration at higher photon energies and are not suitable for the AEPEX mission.

Instead of changing the geometry of the pinhole, coded apertures increase the open area and signal-gathering ability of an aperture by including many holes in a carefully-designed pattern. Coded aperture design and theory are expanded upon in Section 4.2. Further, the scale size of the optical system here are far from the photon diffractive regime (50–250 keV corresponds to

Aperture Type	**Advantages**	**Disadvanges**
Wolter Type I or II Telescope	Highest possible imaging quality for high-energy photons	Low dynamic energy range, bigger advantage for soft X-rays, volumetrically large and complicated
Micropore Optics	Simple, low mass	Soft X-rays only, poor focusing ability
Pinhole Aperture	Simple, low mass, large dynamic energy range	Small geometric factor
Coded Aperture	Simple, low mass, large dynamic energy range, large aperture	Complicated image reconstruction, only distinct patterns available

Table 4.1: Trade-space Study of X-ray Optical Designs

25 pm–5 pm wavelengths) so geometric optics are assumed for all cases in this chapter.

Another important component to X-ray detection is measuring the energy of the photon. By measuring the energy of many photons from an energetic source, a differential energy spectrum can be estimated that holds vital information on the X-ray generation process. In this sense, X-rays are valuable for their ability to be inverted towards quantities of interest, e.g. galactic temperatures, elemental properties, plasma wave acceleration processes, etc. (Lampton, Margon, & Bowyer, 1976; Arnaud, Smith, & Siemiginowska, 2011). The AEPEX mission utilizes solid state detection technology to infer electron distributions from X-ray photon measurements, more specifically a cadmium-zinc-telluride (CZT) pixelated detector where the supporting electronics implement complementary metal-oxide semiconductor (CMOS) circuits to process the analog portion of the signal chain.

In order to perform spectroscopy with the detector photons, some form of energy sensitivity must be present in the detection system. There are a number of ways in which energy sensitivity is achieved in X-ray spectroscopy, a field which has historically been led by astronomers. On older

rocket and balloon missions, proportional counters have been widely implemented, which were then upgraded to charge-coupled device (CCD) and solid state technology (Peterson, 1975; Bradt et al., 1992). Improvements from there have included silicon drift detectors (SDD), which were advanced by the use of cadmium telluride (CdTe) and various dopants (Sumner, Rochester, & Hall, 1988; Lutz, 2006). This section covers a brief history of relevant X-ray spectral detection techniques in order to provide the background for the detector selection and techniques for the AXIS instrument.

The detection of high energy photons typically occurs through the production of ion-electron pairs from both Compton scattering and the photoelectric effect, which are both scattering interactions in which an incident photon frees a bound electron from a nucleus (e.g. (Kruse, 2005)). For more details on these scattering mechanisms, see Section 2.2. Historically, proportional counters provided enough information to meet the open science questions of the time. Proportional counters work by pressurizing a gas that has a low binding energy to its outermost (valence) electron shell. Argon and xenon have been used in proportional counters in the past. A high energy photon passing through the pressurized gas creates a trail of ion-electron pairs, which, under the influence of an applied electric field, causes charge separation which can be accumulated with charge-sensitive amplifiers and other pulse-shaping electronics. For certain combinations of electronics, gas species, and photon energies, the charge collected is proportional to the energy of the incident photon. This proportional counting phenomenon only occurs in a specific regime of those three variables and limits the range and accuracy of energy detection, and at higher energies the photons fall into the Geiger-Müller regime where the detection is only capable of counting photons (i.e. flux detection) and cannot determine their energy.

With the progression of solid state physics and semiconductor technology, the photoelectric effect can be leveraged in solid materials in a more exact way in order to increase both detection sensitivity and the accuracy of spectral measurements. CCDs have remained the predominant detection device in high-energy astronomy due to their versatility in implementation and stability. CCDs are implementations of combinations of doped silicon materials which allow charges to move freely in a semiconductor's valence band under the influence of an electric field. Silicon materials

on average have a work function of 3.7 eV per ion-electron pair, meaning that a keV electron would free hundreds to thousands of electrons that are swept to one region of the material to be detected. This electron charge production is proportional to energy, and together with electronics that quickly sweep off the resulting electron charge cloud, enable accurate measurements of both energy and flux with high confidence. Further, pixelation of these materials enables imaging, making these devices highly attractive in astronomy.

CCDs work by coupling each row and column to a single readout where timing can be used to locate the pixel of origin that a charge has come from. In this way, the crystal material is pixelated and spatial resolution can be gathered from the row and column timing. Some drawbacks of silicon CCD detectors specifically are in their electronic noise: older detectors require cooling to low temperatures in order to drive down thermal noise. Various improvements have been made to CCD detectors, including orienting them in the "back lit" configuration which improves detection efficiency significantly. CCD readout schemes collect charge by row and column of the CCD array, which allows these types of detectors to achieve high readout speeds up to rates of 10 MBits per second (O'Donoghue, 1995).

An additional recent advancement in photon detection technology is the creation of CdTe dopants, including CZT. This material has a low work function of 4.6 eV which enables high sensitivity to photon energy and does not require cooling for high energy photon detection (Liang et al., 2012). This new detector material is used on numerous space missions and in terrestrial applications and the material is sensitive to photons within 10 keV – 6 MeV at room temperature (Bolotnikov, Camarda, Wright, & James, 2005). Of note, these detection methods are also sensitive to energetic charged particles.

The AXIS Redlen CZT detector is chosen for its crystal material and thickness, which enables the detection of hard X-rays within the range of 50–250 keV, and for the high development level of the front-end electronics, which include a CMOS ASIC and energy thresholding and binning. These detector features enable the short design, integration, and calibration cycle that is necessary for a CubeSat mission.

4.2 Coded Aperture Theory

Coded aperture imaging can be describe with an analogy to pinhole imaging: the coded mask can be modeled as a series of pinhole imagers projecting the same image but shifted on the detection plane (Martinello, 2012). The formulation of Accorsi (2001) is taken here, starting from the projection of the object distribution array $\mathcal{O}$ through an aperture array A to measure a detector signal R:

$$\mathcal{O} \times A = R \tag{4.3}$$

where the $\times$ operator is a 2D convolution of the two objects. In the case of a pinhole aperture, this convolution corresponds to the object distribution $\mathcal{O}$ but flipped, mirrored, and blurred according to the finite resolution of the pinhole. In the case of the coded aperture, the detected signal R is a linear combination of the object distribution, shifted, weighted, and summed together through the open elements of A; interpretation therefore requires an additional reconstruction step. The quantities described above are matrices that can be thought of as continuous two dimensional functions, which are discretized into spatial elements indexed by the ordered pair (i, j) according to the highest resolution element in the imaging system. This formulation is taken per energy bin for simplicity, and the behavior of the system in different energies, e.g. mask transmission, is accounted for later.

In order to represent the process of projecting an object distribution through a coded aperture, the aperture matrix A is made up of elements that can take the values in the range of -1 to 1, although the values are nominally taken as -1, 0, or 1. The topic of non-unity element selection is discussed in Accorsi et al. (2001) and Marcia, Harmany, and Willett (2009). The non-unity elements can be a function of the mask transmission at high photon energies and the aperture function used to describe the AXIS imager is described in Section 4.4.

In order to "undo" the encoding of the object distribution, we would like to describe the inverse of the aperture function. The decoder function D is an array that behaves according to

$$A \otimes D = \delta \tag{4.4}$$

where δ is the Kronecker delta in discrete space centered at the middle of the array and $\otimes$ is the correlation operation with circular boundary conditions defined by

$$f(x) \otimes g(x) = \int \int f(x)\ g(y \oplus x)\ dx\ dy \tag{4.5}$$

where $\oplus$ is modulo addition with period p. For the purpose of this work, the matrix D is prescribed by the choice of mask pattern. In this work, the calculation in Equation 4.5 is performed by Fourier-space multiplication via the convolution theorem

$$f(x) \otimes g(x) = \mathbb{R}\left[\mathcal{F}^{-1}\left(\mathcal{F}(f(\omega)) * \mathcal{F}(g(\omega))\right)\right] \tag{4.6}$$

where $\mathcal{F}$ and $\mathcal{F}^{-1}$ are the forward and inverse Fourier transforms, respectively, $\mathbb{R}$ is the real operator, $*$ indicates point-wise multiplication, and this calculation is treated with circular boundary conditions.

The delta function is the unity operator in this space, i.e. multiplication of any element with the unity element returns the original element, and therefore we aim to create an imager that behaves according to Equation 4.4. We can now perform that extra step, the **deconvolution** of the detected signal R according to the coded aperture mask pair (A, D):

$$\tilde{\mathcal{O}} = D \otimes R = D \otimes (\mathcal{O} \otimes A) \tag{4.7}$$

where $\tilde{\mathcal{O}}$ is the estimate of the reconstruction which, under perfect reconstruction and no background, is equal to the object distribution $\mathcal{O}$ recorded according to the resolution of the detection system. However, under the effects of the finite and discrete resolution of a detection system, background noise, and imperfect reconstruction $\tilde{\mathcal{O}}$ will differ from the original object distribution. This section describes how, for the AXIS imager, we quantify imperfections in the imaging system and how we interpret the results of images produced by the coded aperture system for scientific analysis. For a complete generalized treatment of coded aperture imaging, see Accorsi (2001).

Since this system operates largely by linearity, we'll analyze the combined effects of discretization by the finite resolution detectors and imperfect reconstruction together. The two effects can be quantified through the system point spread function (SPSF), which describes how well a point

source is reconstructed. A model of the SPSF is calculated by Fourier-space multiplication of the aperture and decoder functions,

$$D \otimes A = \delta + a \tag{4.8}$$

where a is an array describing the spatial artifacts, keeping in mind each of these quantities are arrays with indices (i, j), which in the case of the AXIS detectors are within the space $\mathbb{R}^{16\times16}$.

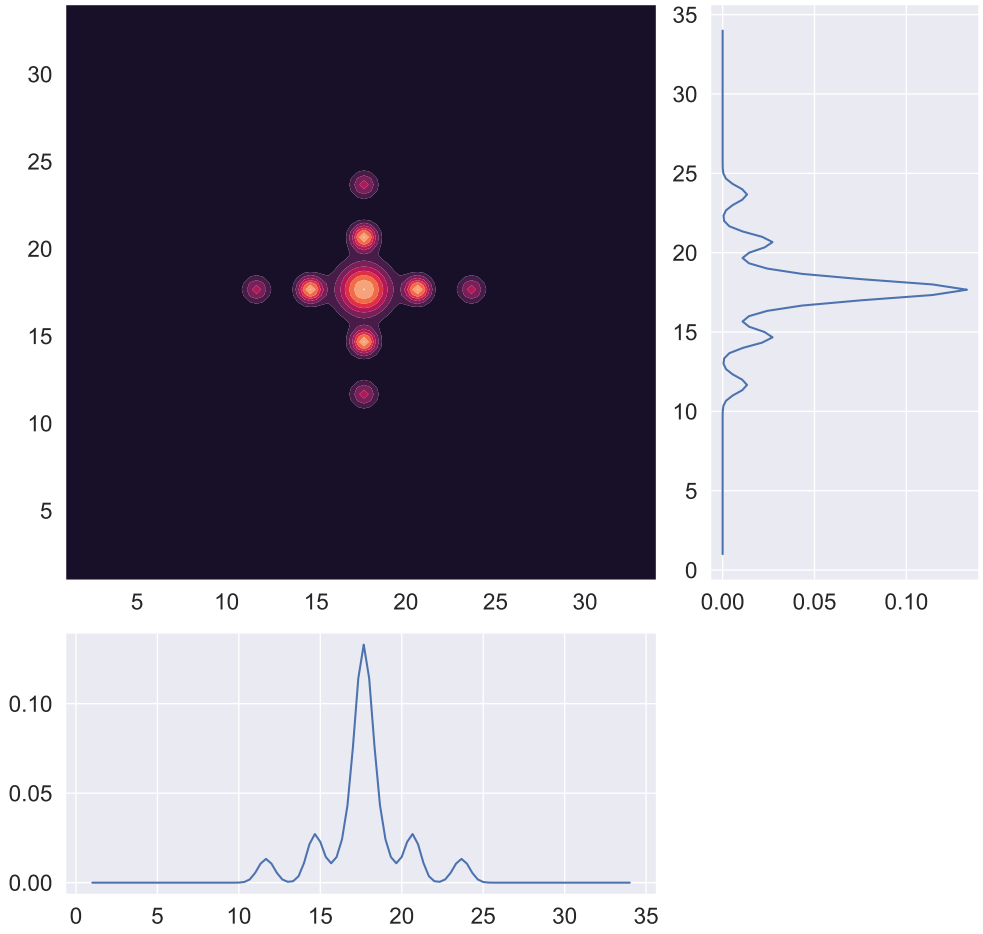

Figure 4.1: An example of the real part of the SPSF generated by the imperfect relationship $\delta + a$ that arises from Equation 4.8, where the central peak is the delta function and the ringing shown to the sides, above, and below the peak are the artifacts described by the matrix a. Note the side-lobes shown in the 1D integrations on either side of the 2D SPSF can become negative.

Ideally the multiplication of the decoder with the aperture function is a perfect delta function, but discretization, manufacturing errors, and other imperfections create spatial artifacts a. Figure 4.1 shows an example of the ringing that can arise from the Fourier-space multiplication method

of computing Equation 4.8 which leads to the development of side-lobes described by the matrix a which we aim to quantify and ultimately remove. We can now write the imaging reconstruction algorithm as

$$D \otimes R = D \otimes (A \otimes O) \tag{4.9}$$

which, through Equation 4.8, we can write as

$$(\delta + a) \otimes O = \delta \otimes O + a \otimes O \tag{4.10}$$

$$\tilde{\mathcal{O}} = O + a \otimes O \tag{4.11}$$

The term $a \otimes \mathcal{O}$ is the imperfection term that is a function of the object distribution that we aim to describe through testing and simulation. For work on minimizing the effect of this term, see Section 4.3. These imperfections in the imaging system can appear as banding or ringing artifacts from a convolution of the SPSF (e.g. like in Figure 4.1 which shows significant side lobes) with a source in the field-of-view. This topic is explored in Section 4.5.

We can also account for the effects of background on the detectors during the image integration with the 2D Poisson background process B. Through imaging with the effects of a background, we can write

$$(\mathcal{O} + B) \times A = R' \tag{4.12}$$

where R' is the "real" detector signal, and now the deconvolution process becomes

$$D \otimes R' = D \otimes (A \otimes (\mathcal{O} + B)) \tag{4.13}$$

$$= D \otimes A \otimes \mathcal{O} + D \otimes A \otimes B \tag{4.14}$$

$$= (\delta + a) \otimes \mathcal{O} + (\delta + a) \otimes B \tag{4.15}$$

where we can perform the expansion of the imperfect imaging process and regroup the terms to obtain

$$\tilde{\mathcal{O}} = \mathcal{O} + B + a \otimes (\mathcal{O} + B) \tag{4.16}$$

Since we assume that B is a Poisson random process, there is no consistent spatial structure to B such that both B and the term $a \otimes B$ are spatially incoherent. Therefore, we can write $\tilde{B} = B + a \otimes B$ as the total deconvolved background, and we can now write

$$\tilde{\mathcal{O}} = \mathcal{O} + a \otimes \mathcal{O} + \tilde{B} \tag{4.17}$$

where we can model $\tilde{B}$ as a uniform offset term plus Poisson shot noise characterized by an arrival rate (i.e. background rate) that describes the mean and standard deviation of the noise. The average noise can be subtracted to obtain a better reconstruction of the object distribution $\tilde{\mathcal{O}}$, and the Poisson shot noise must be tolerated. The subject of mitigating and estimating the background incident on the AXIS instrument is discussed in Chapter 3.

Coded apertures masks are often the optimal choice of optics for point sources with a high signal-to-background ratio (i.e. high signal strength sources), but they also provide a significant benefit for imaging extended sources in other signal-to-background regimes (Accorsi et al., 2001; Accorsi, 2001).

This formalism described in this section holds for any mask-decoder pair (A, D) that have the properties mentioned above. However, some coded aperture mask designs have more optimal properties for different imaging scenarios, which is discussed in the next section.

4.3 Pinhole Image-constrained Deconvolution Algorithm

An algorithm has been developed to perform the general image reconstruction via the deconvolution described in Equation 4.9 and to correct the image distribution-driven artifacts $a \otimes \mathcal{O}$ described in Equation 4.8.

The first part of the algorithm is the direct correlation method described in previous works on coded aperture imaging. In order to match the size of the arrays for point-wise multiplication in Equation 4.6, an empty row and column are added to the detector signal R to zero-pad the array, and the signal is linearly oversampled by a factor of 2 to obtain the 34×34 resolution of the decoder array, matching the size of coded aperture mask. This operation reduces the ringing when

performing the fast Fourier transform (FFT). Equation 4.6 is performed using two-dimensional FFTs and inverted back to the spatial domain with a 2D inverse FFT. The imaginary part of this multiplication was verified to be less than $\sim 10^{-3}$ in 2-norm magnitude versus the real part of this multiplication, and the real part is then taken as the reconstructed image. A large imaginary part to this multiplication would imply a poorly-conditioned detector signal R, where this algorithm is designed to avoid this scenario, e.g. by "rounding" the edges of the signal to prevent sharp spatial features which correspond to high spatial frequencies in Fourier space.

The result of the Fourier-space multiplication is a matrix with dimensions of 34×34, which is a factor of 2.125 times higher than the pixel resolution of the Redlen detectors. Some of these images in the next sections are kept at this "deconvolution resolution," although this is for illustrative testing purposes and care should be taken not to interpret small artifacts in these images. The science product is ultimately downsampled by the factor of 2.125 to return an image with resolution 16×16.

The selection of coefficients in the decoder array determines how the overall magnitude of the detector signal R is transformed relative to the reconstruction of the object distribution $\tilde{\mathcal{O}}$. For instance, decoder values of -1, 0, and 1 will produce an object distribution estimate that sums to zero and the relative heights of peaks and valleys in the image are to be interpreted relatively. The algorithm developed here integrates the detector signal spatially to calculate the total signal power and scales the reconstruction according to the signal power to conserve the total signal count detected. From there, using the detection model, a photon flux can be calculated from count rates on the detectors, yielding one of the ultimate science products and the subject of Chapter 3.

The second part of this algorithm is based on laboratory characterization of the artifact matrix a and an iterative estimate of $\mathcal{O}$. How well artifacts can be accounted for depends upon the extent of the dependence on $\mathcal{O}$; for more background on imperfect encoding by mask-decoder pairs, see Willingale, Sims, and Turner (1984). Starting from Equation 4.17, we assume the background can be estimated independently, e.g. by background exposures by AXIS and by the AFIRE count

rates, and aim to achieve

$$||\tilde{\mathcal{O}} - \mathcal{O}|| = ||a \otimes \mathcal{O}|| \searrow 0 \tag{4.18}$$

where the general goal is to minimize the difference between the image estimate $\tilde{\mathcal{O}}$ and the true object distribution $\mathcal{O}$. We can construct an anti-artifact matrix $\bar{a}$ that we can use to form a minimization problem:

$$\bar{a}^* = \arg\min_{\bar{a}} \sum ||\bar{a} \otimes a \otimes \mathcal{O}||_2 \tag{4.19}$$

where $\bar{a} \otimes a \rightarrow \delta$ in the limit of a perfect anti-artifact matrix $\bar{a}^*$, which yields the best image reconstruction of $\mathcal{O}$. This minimization is performed with the Wiener filtering technique (King, Doherty, Schwinger, & Penney, 1983), starting from an initial guess that $\bar{a}$ should behave similarly to the SPSF plotted in Figure 4.1, and iterating until the above equation is minimized. This constitutes a "blind" deconvolution technique where there is no knowledge of $\mathcal{O}$ besides the estimate taken by the imager. The CLEAN algorithm is perhaps the simplest implementation of a blind deconvolution technique applied to this form of imaging (Högbom, 1974).

Along the lines of the CLEAN algorithm, the matrix $\bar{a}$ can be applied after the cross-correlation deconvolution by iteratively selecting the strongest signals within the image and reducing the SPSF artifacts generated by that signal by an adjustable amount. Care must be taken to not overly apply the iterative artifact reduction to where it reduces the true signal. In order to provide a constraint on the extent of the artifact reduction and to provide an independent estimate of the object distribution, a pinhole aperture is implemented above one of the 12 detectors onboard AXIS. This imager provides an un-encoded, albeit low signal, estimate of $\mathcal{O}$, which can be used in a theoretical sense to estimate the object distribution in the $a \otimes \mathcal{O}$ term, and in practice as an input for iterative filtering.

For an implementation of the cross correlation algorithm, see Appendix C. The following sections document the simulation, laboratory testing, and performance characterization performed to verify the coded aperture design selected for the AXIS instrument. The topic of validating and tuning the novel pinhole-constrained deconvolution algorithm described here is the subject of future

work.

4.4 Coded Aperture Optical Design and Manufacturing

Comprehensive reviews of coded aperture mask designs are discussed in Skinner (1984), Accorsi (2001), and Gottesman (2007), among others. The design chosen for the AXIS imager is the Modified Uniformly Redundant Array (MURA) (Gottesman & Fenimore, 1989). The base design for the mask size is 17×17 elements, which abides by the MURA requirements of a prime number of elements and satisfies $n = 4p + 1$ for n elements and integer p. This mask resolution is chosen since it is the closest viable MURA mask size to the detector's native resolution of 16×16 pixels, such that the mask slightly oversamples the object distribution relative to the detector. In this way, the mask design is the maximum rank[1] it can be (related to angular resolution) without the elements becoming difficult or impossible to manufacture, since a higher rank for a fixed mask size causes the features in the mask to become small. Additionally, very high rank masks with many open elements must necessarily be made with small blocking elements in order to accommodate the detector's form factor: if the elements get too small, self-collimation of the open elements with respect to the mask thickness becomes an issue, especially with the AXIS large field-of-view design.

However, in theory a MURA pattern must have infinitesimally small connections between elements, i.e. the transition from 1 to 0 in Figure 4.2, which shows the 17×17 base pattern. With only a very small amount of material connecting each opaque element, this design is not resilient to the vibration environment that AEPEX will experience during launch. Instead, the optics implemented here are the base pattern modified by the no-two-holes-touching (NTHT) technique, which adds an opaque column and row between each open element. The mask pattern that results from the NTHT operation is shown in Figure 4.3. The decoding array is similarly modified with a column and row of zeros between each open element to account for the added material. The mask rank is now two times higher, and the NTHT MURA pattern implemented for AXIS has 34×34

[1] "Rank" here refers to the number of elements per dimension of the mask.

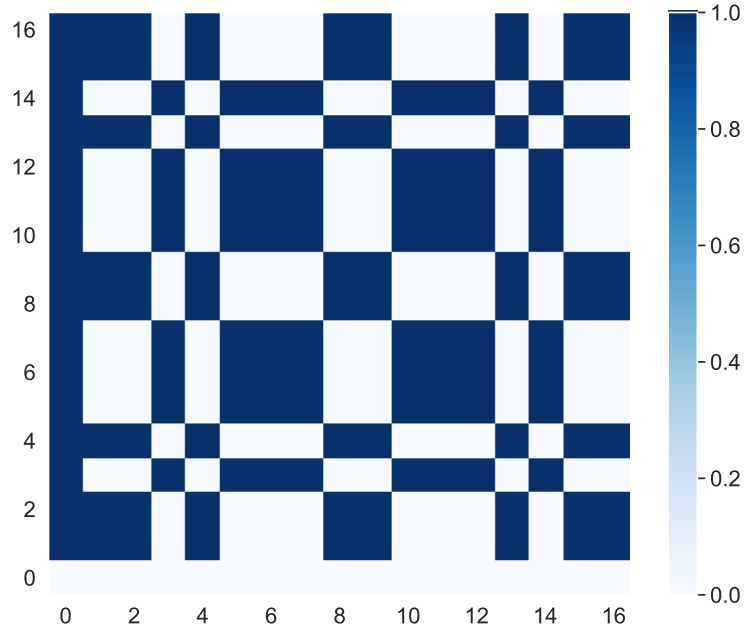

Figure 4.2: The 17×17 modified uniformly redundant array (MURA) base pattern from which the AXIS X-ray optics are based. One on the colorbar indicates a transparent element and zero indicates an opaque element.

elements.

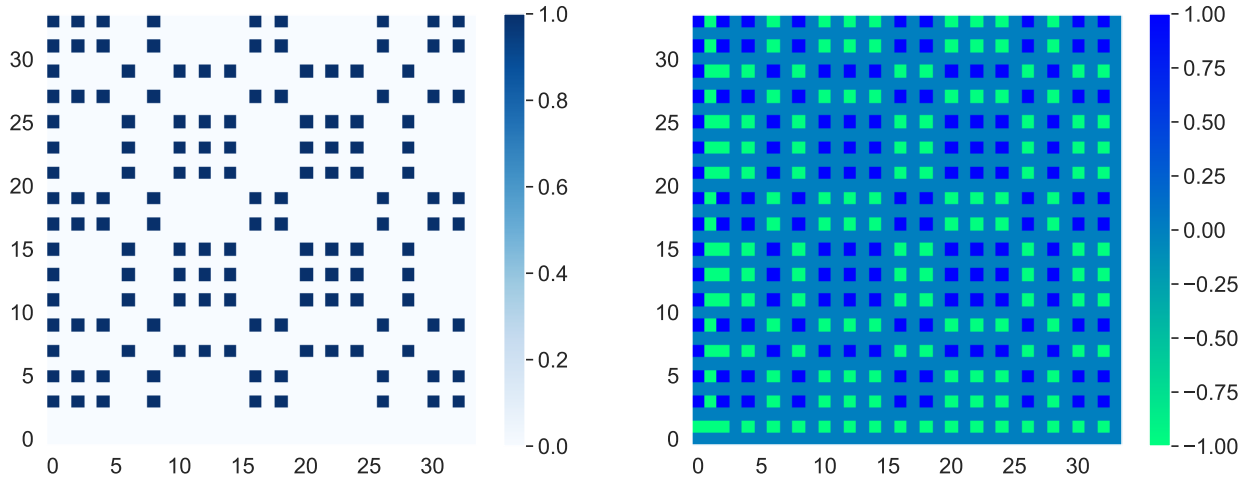

Figure 4.3: (Left) The 34×34 no two holes touching (NTHT) modified uniformly redundant array pattern that comprises the AXIS instrument aperture. (Right) The decoder array D for the NTHT MURA pattern, where the inserted column have a decoder coefficient value of zero, opaque elements have a value of -1 and transparent elements have a coefficient of unity.

Now, each collection of 2×2 holes projects to approximately one pixel, and the mask oversamples the object relative to the detector by a factor of 2.125. This modification brings the open fraction of the mask ρ to 12.5%, which is a significant advantage in geometric factor over a pinhole imager with the same spatial resolution, although well short of the theoretical maximum of 50% for the MURA coded aperture shown in Figure 4.2.

In order to quantify the advantage of the coded aperture mask over a pinhole, we can evaluate the SNR formulation from Accorsi (2001) for the NTHT MURA mask design:

$$SNR_{ij}^{NTHT\ MURA} = \frac{\sqrt{n_T\ S}\sqrt{\rho/2}(1-t)\psi_{ij}}{\sqrt{(1-t)\rho + t + \xi}} \tag{4.20}$$

where $n_T = 34 \times 34$ is the total number of open elements in the mask design, S is the signal rate that arrives at the instrument, ρ is the open fraction of the mask, ψ_{ij} is the image extent parameter at pixel (i, j), t is the transmission fraction of an opaque element, and ξ is the background-to-signal ratio B/S parameter. The parameter ψ_{ij} is in the range $(0, 1]$ which corresponds to an image where the entire field-of-view is filled, and $\langle\psi_{ij}\rangle = n_T^{-1}$, to a point source where $\psi_{ij} = 1$ at source location (i, j). It can be written as

$$\psi_{ij} = \frac{\mathcal{O}_{ij}}{\sum_{i,j}\mathcal{O}_{ij}} \tag{4.21}$$

where the denominator is the same as the total signal S. For simplicity, we'll let $t = 0$ for a perfectly blocking mask and fill in the NTHT MURA parameters of the AXIS design to obtain:

$$SNR_{ij}^{NTHT\ MURA} = \frac{8.5\sqrt{S}\ \psi_{ij}}{\sqrt{(1/8) + \xi}} \tag{4.22}$$

which is a function of the imaging scenario (ξ, ψ_{ij}) only. We take the SNR for a pinhole imager as a function of the same variables from Accorsi (2001), assuming a pinhole hole size that yields a comparable spatial resolution:

$$SNR_{pinhole} = \frac{\sqrt{S}(1-t)\psi_{ij}}{\sqrt{(1-t)\psi_{ij} + t + \xi}} \tag{4.23}$$

and form a ratio of the two SNRs to estimate the advantage the coded aperture mask will provide over the space (ξ, ψ_{ij}), assuming a perfectly blocking mask, i.e. $t = 0$:

$$\frac{SNR_{NTHT\ MURA}}{SNR_{pinhole}} = \sqrt{\frac{(n_T/2)(\psi + \xi)}{1 + \xi/\rho}} \tag{4.24}$$

A plot of this result is shown in Figure 4.4 over a range of $\xi \in [10^{-1}, 10^{1}]$ and $\psi \in [10^{-3}, 1]$. The SNR advantage over a pinhole imager for the AEPEX imaging scenario has an average of ∼8, which, according to a Poisson SNR formulation is a signal advantage of 64x. Additional, the worst case scenario for the coded aperture is a fully-filled field-of-view, i.e. $\langle \psi_{ij} \rangle = 1/n_T$, in which case the SNR advantage is approximately 6. Coded aperture masks are optimal for point source imaging with high signal, low background targets, but offer significant advantages over pinhole imagers away from this regime as well.

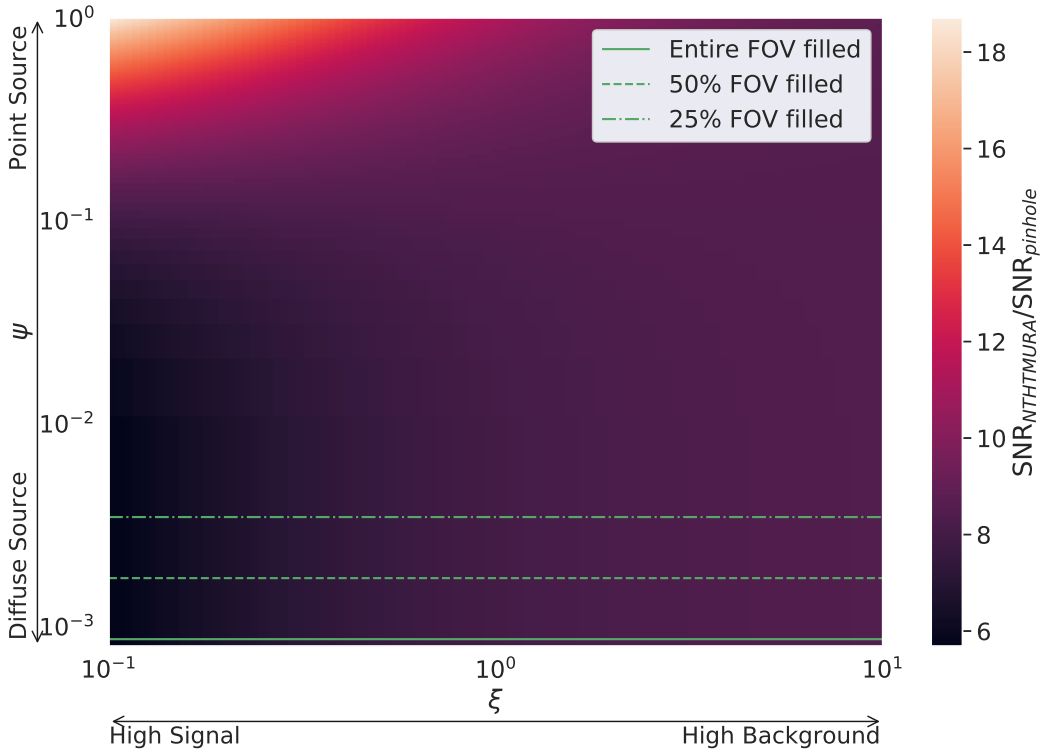

Figure 4.4: The SNR advantage of the NTHT MURA coded aperture mask over a similarly sized pinhole imager is plotted via the ratio of the two quantities. The ratio is plotted over the imaging scenario space (ξ, ψ), which constitutes the background-to-signal ratio and image extent parameter, for the fixed value of the AXIS mask design space (ρ, n_T), comprised of mask open fraction and number of open elements, and assuming the masks perfectly block photons $(t = 0)$.

The coded aperture SNR advantage is at its lowest for distributed objects (i.e. a uniform, diffuse source) with high signal which is also where a pinhole imager performs well. In order to

account for this scenario, one detector on the AXIS instrument is equipped with a 6 mm square pinhole aperture and is held out from the co-addition and downlinked separately. During times where the imaging scenario is out of this regime, the pinhole image can act as a constraint on the coded aperture inversion, which is described in Section 4.3.

The thickness of the mask is a component where theory differs from manufacturing. The Beer-Lambert extinction law describes a tungsten mask's X-ray attenuation where photon transmission t is given by:

$$t = \frac{I}{I_0} = e^{-\mu(E)\ \Delta x} \tag{4.25}$$

where $\mu(E)$ is the mass attenuation coefficient for tungsten in units of cm^{-1} and Δx is the total mask thickness in cm. The fraction I/I_0 illustrates that for a beam that initially has flux I_0, a flux of I should be expected after passing through Δx thickness of material with attenuation coefficient μ. The transmission as a function of energy is plotted in Figure 4.5, showing a K-shell electron transition at 69 keV. The mask thickness is chosen such that it offers the lowest level of photon transmission in its opaque elements without the effects of self-collimation, which occur when the open elements create channels that have an individual field-of-view smaller than the desired instrument's field-of-view. To form a $90^\circ \times 90^\circ$ field-of-view (i.e. 45° half angle), the mask thickness must be no greater than the smallest element size. The linear size of the smallest element is 1.25 mm, so the mask thickness is chosen to be the same. This produces a vignette effect that causes loss of sensitivity near the edges of the field of view that are accounted for with angular testing later in this chapter.

The design selected here is the box camera design where the mask pattern matches the detector size exactly (Hammersley, Ponman, & Skinner, 1992). The mask is manufactured by Elcon Precision out of 99.9% pure tungsten, and has dimensions 4 cm×4 cm×1.25 mm in length, width, and thickness, and is placed 2 cm from the detector plane to cover a $90^\circ \times 90^\circ$ field-of-view. This field-of-view will project over a swath approximately 900 km×900 km given a 500 km altitude orbit imaging the phenomenon of bremsstrahlung occurring at a mean altitude of 50 km. With this field-

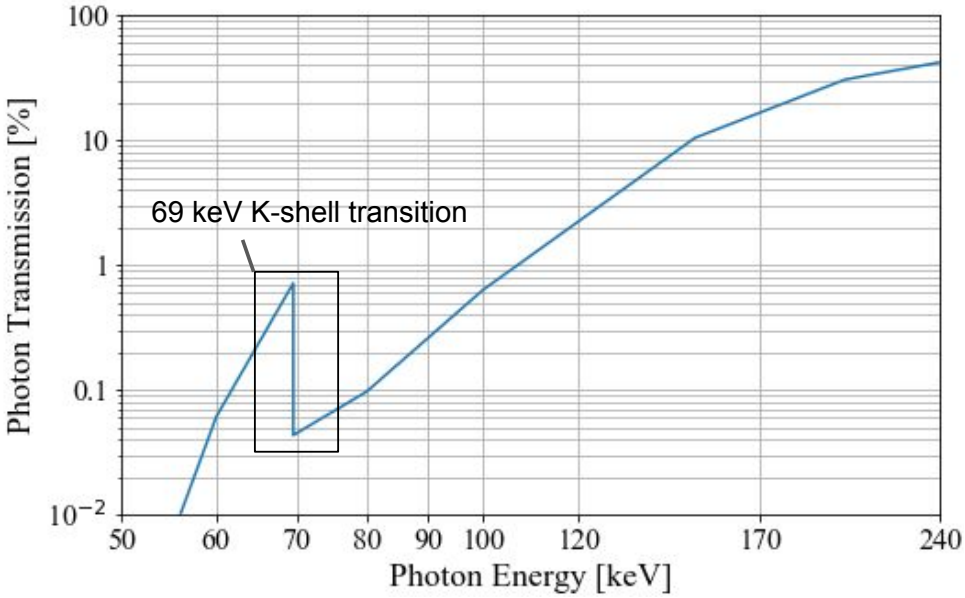

Figure 4.5: Photon transmission versus energy in 1.25 mm of tungsten over the Redlen energy detection range. Note the K-shell emission in which transmission jumps where photons of that energy exactly match the K-shell electron binding energy.

of-view and a detector linear resolution of 16 pixels, a pixel will project to a linear object distribution size of 56 km, which is the theoretical lower limit (i.e. best) spatial resolution of this system. In practice, the imperfect matching of the mask size, manufacturing defects, and background noise reduces this spatial resolution. Figure 4.6 shows the NTHT MURA coded apertures in their graded-Z housing for the 1/3-scale AXIS prototype. This setup is used for laboratory testing in Section 4.5.

Tungsten collimators are placed between each detector to ensure a photon from one detector's field-of-view does not enter the neighboring detector's field-of-view. This phenomenon would form an aliased image on the edges of the field-of-view for high incident-angle photons entering the coded apertures.

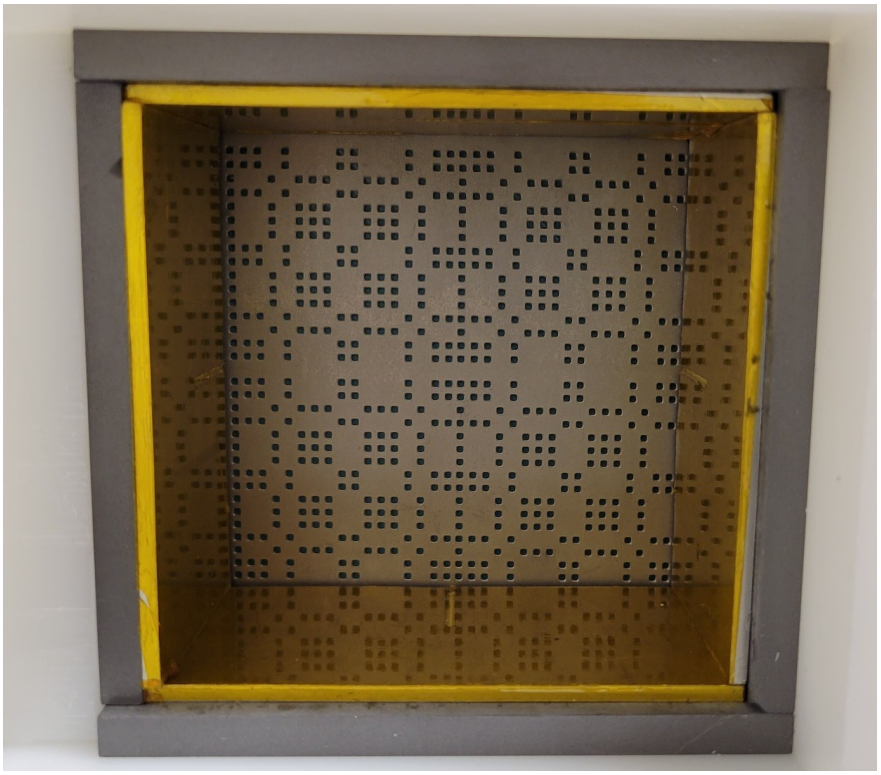

Figure 4.6: The 1/3-scale AXIS prototype version with 4 Redlen detectors, showing the tungsten coded apertures and graded-Z shielding. The shielding layers, from the exterior to interior of the instrument, are HDPE plastic, tungsten-nylon composite, and tin covered with Kapton tape.

4.5 Performance Simulation and Testing

In order to quantify the coded aperture design and imaging system as a whole, a mixture of simulation and laboratory testing is performed. This section covers simulation and laboratory testing of radioactive sources and notional EPP object distributions.

4.5.1 Simulation

Two imaging simulations are used to test and characterize coded aperture imaging performance. The first of which is a closed-form X-ray raytracing simulation included in the appendix of Accorsi (2001) that simulates coded aperture imaging by tracing an object distribution through each open element of the mask and the deposition location on the detector. The effects of photon penetration of the mask, as well as finite mask thickness collimation effects are simulated. This

simulation was developed for near-field imaging and is adapted for the simpler far-field case in order to be used for the AEPEX imaging scenario.

The second simulation is a 3D Monte Carlo photon transport code built using GEANT4. A finite thickness mask is implemented, along with pixelated CZT detectors and graded-Z shielding in order to simulate noise and blurring from photon scattering in the housing materials. This simulation is the same as the one used in Berland, Marshall, Martin, et al. (2023) and Chapter 3 to estimate the background induced by energetic electrons incident on the spacecraft, so the inclusion of the simulated background is a natural benefit of this model. Figure 4.7 shows the AXIS instrument with window and shielding removed to show the coded apertures built using the GEANT4 CLHEP geometry library, alongside the AFIRE instrument. Figure 4.8 shows a transparent side view of the AXIS instrument with photons simulated through the aperture from an infinitely far away point source (i.e. the particle trajectories are parallel, starting from the yellow dots at the top).

The simulation of a point source is paramount in determining the SPSF of the system. Figure 4.9 shows the results of simulating a single X-ray point source with unity strength at the center of the field-of-view. The leftmost plot shows the object distribution (i.e. the "truth" image), and the center plot shows the simulated detector signal R, which is a reconstruction of the 34×34 NTHT MURA mask pattern downsampled onto the 16×16 detector, closely resembling the 17×17 MURA base pattern. The rightmost plot shows the image reconstruction using the first half of the algorithm described in Section 4.3. Note the magnitude of the point source is amplified by being detected through the many holes of the coded aperture mask, and the subsequent reconstruction power is greater than unity. The flux calibration relationship discussed in Chapter 3 is necessary to relate the flux estimated by the reconstructed image to the true flux that arrives at the detector.

The results of Figure 4.9 show that, for a sufficiently small source in the far-field, the imager can reconstruct the source to one pixel resolution. Therefore, we can say that the system resolution is limited by the pixelation resolution of the detector, and the mask is designed appropriately as to not spread a point source to more than one pixel. Since this is a statistical method, the

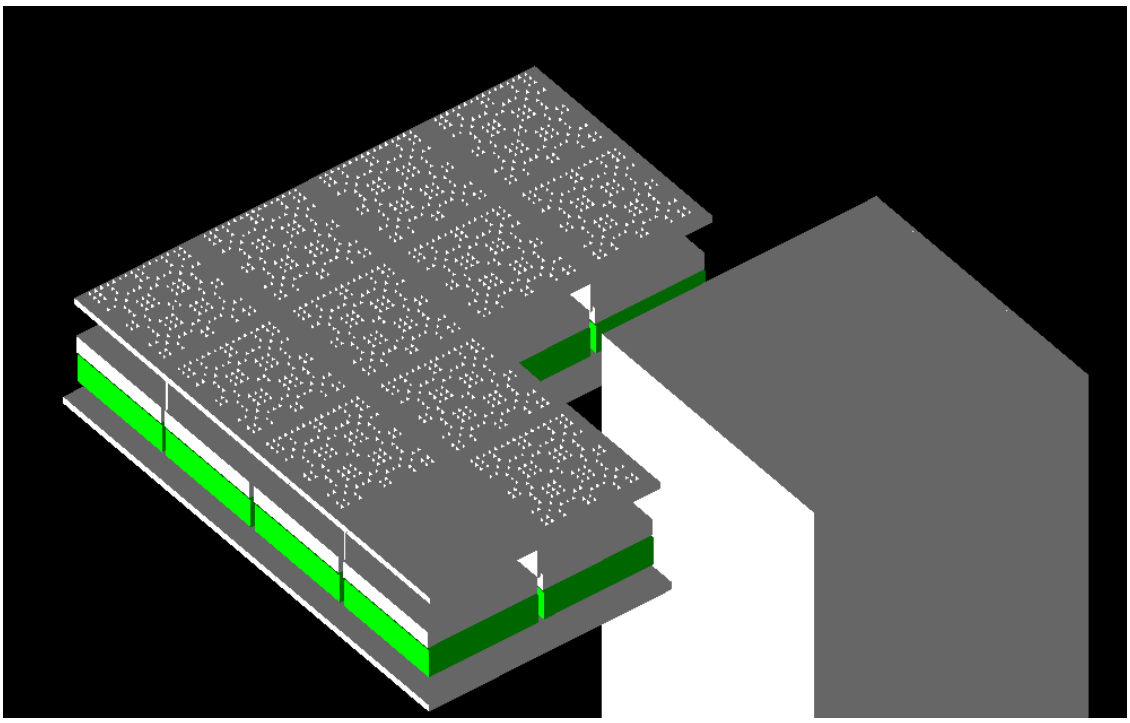

Figure 4.7: Image of GEANT4 simulation geometry with graded-Z shielding and beryllium window removed to show the NTHT MURA coded apertures and CZT detectors built using GEANT4's CLHEP geometry system. The rectangular shape on the right side of the image is the backside of the AFIRE electron detector pointing its aperatures to zenith.

resolution also depends on a sufficient number of photon detections, and a sufficiently high SNR: the investigation of the reconstruction performance with these parameters is a subject of future work. The source reconstruction does, however, have banding artifacts in the up-down direction that ring to either side of the point source. These artifacts are discussed in the previous section and are the topic of the second part of the imaging algorithm which aims to remove these artifacts in a routine manner.

Since we cannot determine the SPSF from a single point source due to being detector pixel-limited, the SPSF and spatial resolution of a point source can be found by simulating two point sources, moving them progressively closer to each other, and finding the distance at which they can no longer be distinguished from one another. There exist more strict criteria on this definition for higher resolution imagers, e.g. the point at which Gaussian fits to the sources are located one

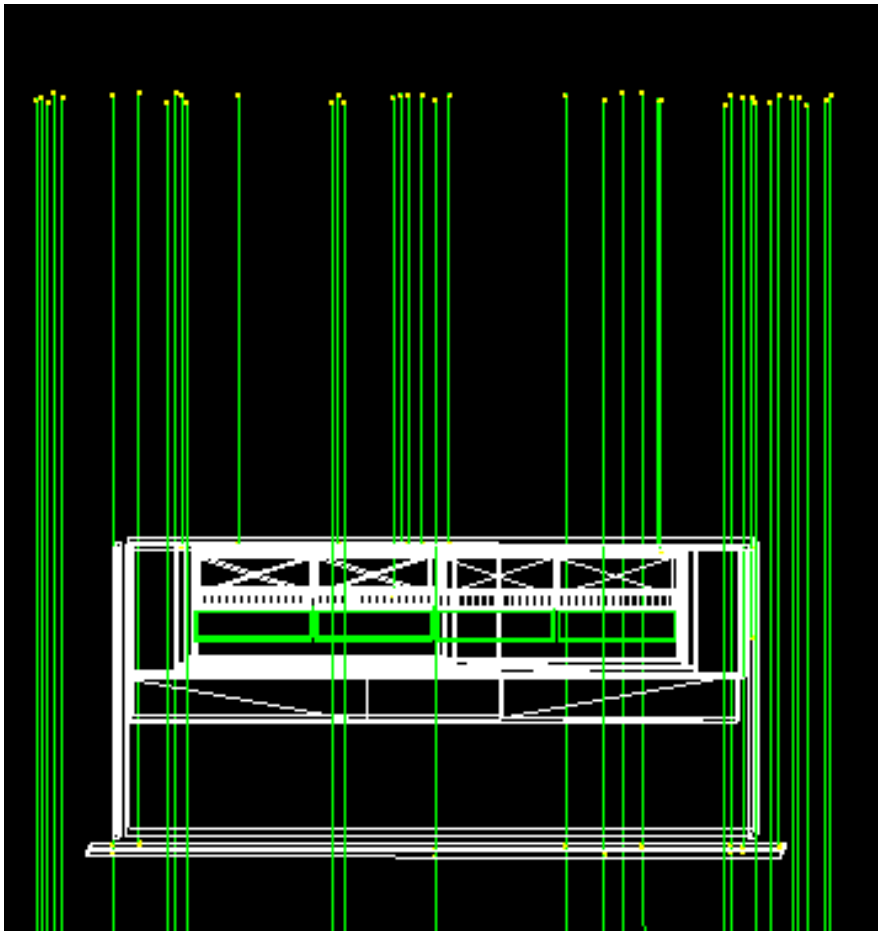

Figure 4.8: A side view of the AXIS instrument while simulating a point source infinitely far away through parallel photon trajectories, indicated by the green lines. Note that this simulation shows high energy photons (1 MeV) to illustrate the tendency towards "catastrophic" collisions at higher photon energies, that is to say, angular deviations through Compton scattering are unlikely and photons are either completely absorbed or completely transmitted through the materials.

full-width half-max (FWHM) distance apart. However, for this low resolution system, one pixel spacing between sources is taken as a sufficient criterion for resolved sources. Figure 4.10 shows the results of these simulations using the Accorsi raytracing simulation. The spacing between the points in the three plots are 420, 190, and 130 km respectively from an altitude of 500 km and a source generation altitude of 50 km. We conclude that the spatial resolution lies between the last two simulations at approximately 160 km spatial resolution at the sub-spacecraft point. This distance is the estimate of the FWHM separation given a series of higher resolution simulations that are downsampled to match the AXIS system resolution. This resolution is measured in the

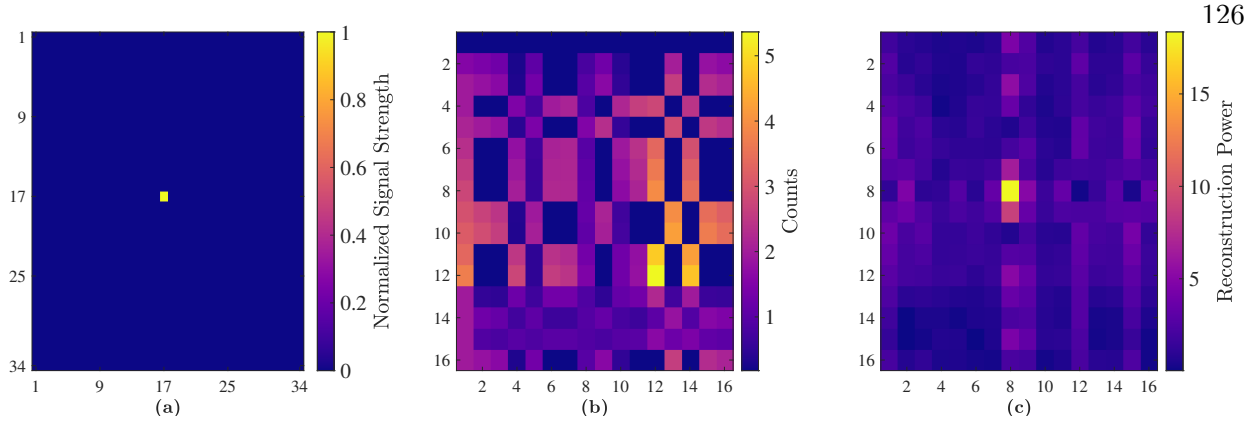

Figure 4.9: (a) The original object distribution $\mathcal{O}$ in the deconvolution space of 34×34, showing a point source of unity strength in the middle of the frame. Panel (b) shows the detector signal that is generated by a point source in the middle of the frame in the far field. (c) The reconstruction of the point source using the Fourier-space multiplication deconvolution method.

dimension with the banding artifacts, so it is the worse of the two dimensions.

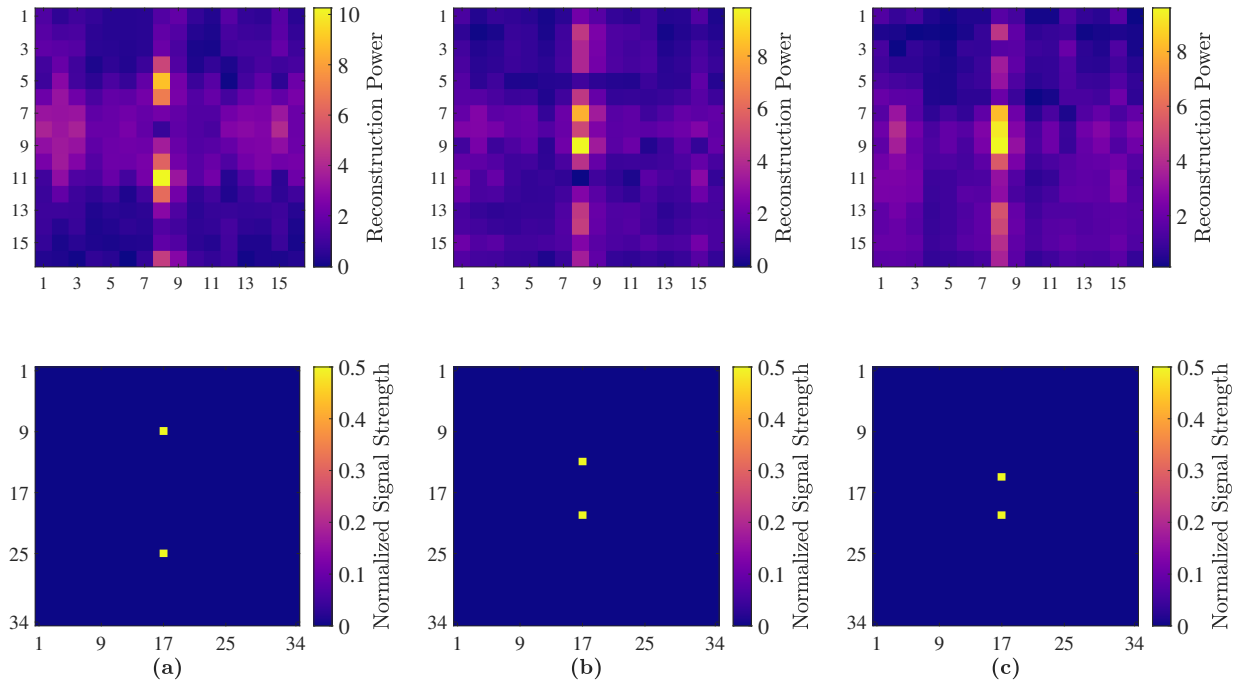

Figure 4.10: Ray tracing simulations of two point sources being moved closer together to determine point source resolution. The separations from a 500 km altitude orbit and an object distribution located at 50 km altitude are (a) 420 km, (b) 190 km, and (c) 130 km, where the bottom row are the object distributions and the top row is the image reconstructions after simulation through the coded aperture mask. The point source resolution is found from between panels (b) and (c) from a simulation of 160 km separation.

Now that the spatial resolution of the coded aperture imager is identified, the simulation of extended objects is desired, since that will likely more closely resemble the object distributions of patches of EPP. Figure 4.11 shows the simulation of a "line" source, with a band structure that stretches across the field-of-view. This could correspond to a precipitation patch that is narrow in latitude but extended in longitude, while the spacecraft orbits in the north-south direction. If this source is generated at 60 km altitude (corresponding to a lower-energy precipitation event than the previous simulation), then it has spatial structure of 135 km×880 km. The middle plot of Figure 4.11 is shown with the deconvolution resolution, while the right plot is shown with the native 16×16 detector resolution. From the native resolution reconstruction, we can surmise that the object distribution is between 110 and 175 km wide, due to some uncertainty with the edges of the bremsstrahlung region. The sharp drop off in the object distribution is likely the cause of the edge effects; EPP regions dropping off sharply in this manner are likely not physically realistic.

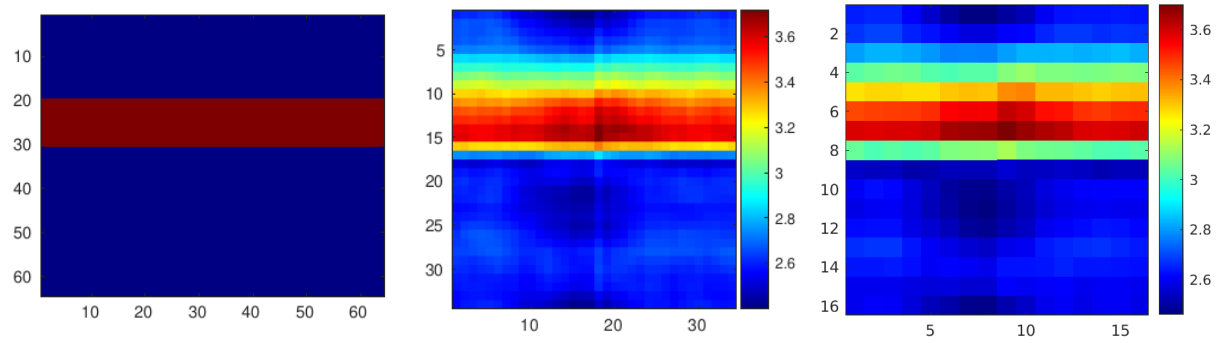

Figure 4.11: Raytracing simulation of an EPP banding structure generated at 60 km altitude with dimensions 135 km×880 km that stretches across the field-of-view. The left plot shows the object distribution and the center plot shows the deconvolution space reconstruction of the object distribution. On the right, the reconstruction is downsampled to the native detector resolution for interpretation.

The ratio of the MURA SNR over the pinhole SNR becomes less advantageous as the object distribution fills the field-of-view, so this distribution with low ψ is simulated to verify the imaging feasibility. Additionally, this simulation allows us to investigate imaging effects near the edges of the field-of-view, including spatial aliasing. Figure 4.12 shows an object distribution that fills half of the field-of-view, corresponding to an image extent parameter value of $\langle \psi_{ij} \rangle = 1.7 \times 10^{-3}$. Similar to the

simulation of the band of EPP, the sharp edge of the half-filled field-of-view induces some banding artifacts in the left-right direction. In addition to these artifacts, a mixture of lowered geometric factor near the edges of the field-of-view in the up-down direction cause the image reconstruction power to fall off at the edge of the field-of-view, and some aliasing is seen that "echos" back near the bottom of the image. The collimators implemented in the AXIS design should mitigate the aliasing effects seen by objects near the edges of the field-of-view.

These effects constitute an overall lower imaging performance in the up-down dimension of the imager. How these concerns are addressed operationally is to place this weaker imaging axis in the ram direction such that the images in this dimension benefit from the push-broom motion of the spacecraft, which will image one stationary point in the frame approximately 12 times as the spacecraft moves overhead.

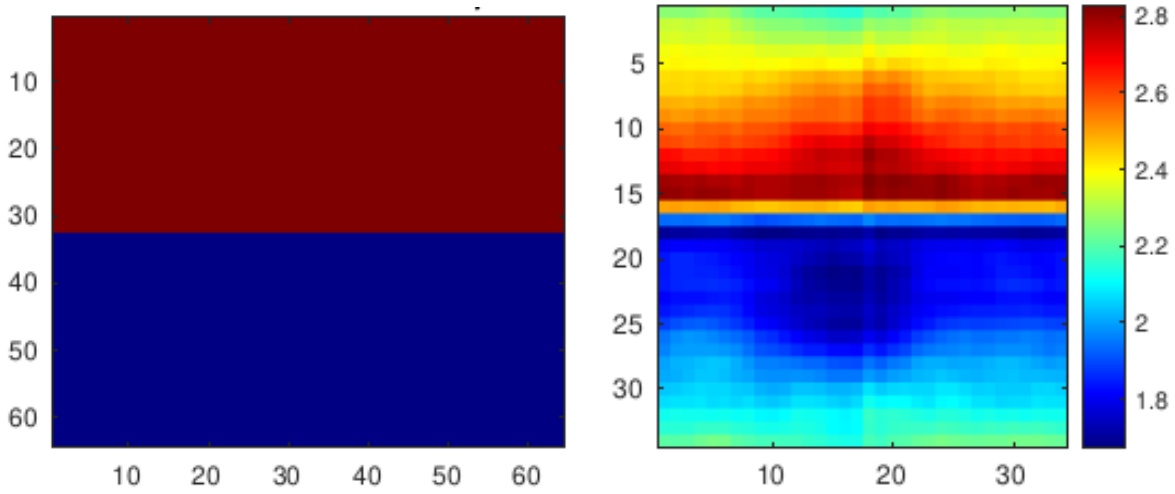

Figure 4.12: A raytracing simulation of the field-of-view half filled in the object distribution (left) and the image reconstruction (right). The strength of the signal is uniform across the field of view, and some banding artifacts and aliasing occur in the image reconstruction.

These simulations serve to estimate the SPSF of the coded aperture design and the span some realistic spatial distributions of patches of EPP. In order to validate these simulations and ultimately prove the optics of the AXIS imaging system, laboratory testing is required.

4.5.2 Laboratory Testing

This section details the imaging testing performed with the AXIS prototype. Details on the hardware and software implementations of the AXIS instrument are detailed in Chapter 3. In order to begin testing, an estimate of the background count rate from the laboratory is needed. Figure 4.13 shows a background exposure with no radioactive sources present, taken with the Redlen M1770 detector and with the TimePix2, a high resolution and calibrated solid state detector (Wong et al., 2020). Two spectral fits are made to the background data; a power law distribution with a spectral index of -4/5 and an exponential distribution with a folding energy of 200 keV. Both fits estimate a similar differential flux intensity of $6{\times}10^{-2}$ cm^{-2} s^{-1} sr^{-1} keV^{-1}. This background flux comes from a combination of GCRs and muons generated by GCR reactions in the atmosphere, radon in Colorado, and potentially trace levels of radioactivity in concrete, along with inherent detector noise. These measurements and fits constitute a characterization of the laboratory background that can now be subtracted from radioactive source exposures.

In order to verify the AEPEX imaging scenario, the tests in this section are conducted in the AXIS instrument's far-field. The coded aperture imaging technique requires a different treatment for near-field imaging scenarios, where angular deviations are the product of the spatial distribution of the object and are also a function of the object's distance to the imager. In order to determine the far-field distance of the instrument, the angular spacing between rays traced from the source to the detector are calculated using the geometric optics equation:

$$\delta x = h \tan(\delta\theta) \tag{4.26}$$

where h is the source-to-detector distance and δx is the linear spread on the detector from the effect of the finite distance h. The determination of the far-field distance h_{FF} for one detector is found when δx is smaller than the spatial resolution of the imaging system, in this case a 2.2 mm pixel. Another definition of the far-field used in Accorsi (2001) is when the angle $\delta\theta$ is small enough that $\cos^3(\delta\theta) \approx 1$. An added element to this determination is in the co-addition of images with multiple detectors. Not only must h satisfy the single-detector far-field condition, but the source must be

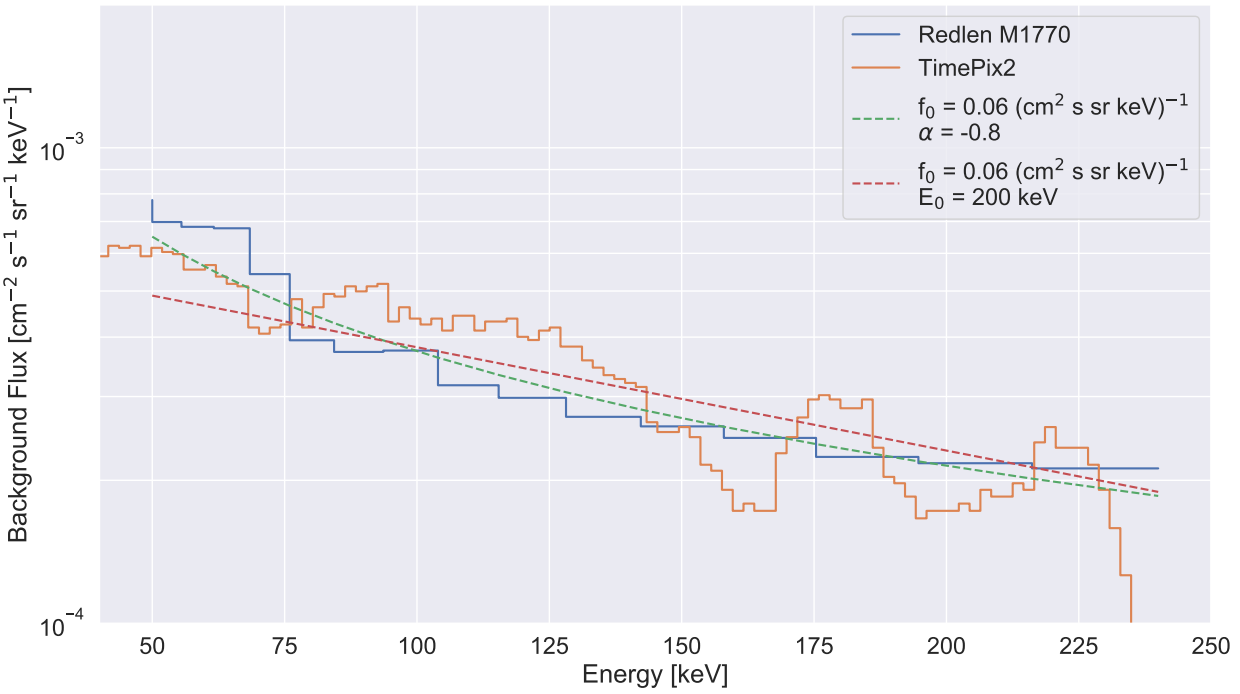

Figure 4.13: The background spectrum of the CU Boulder laboratory taken with two instruments independently, the Redlen CZT detectors and a TimePix2 silicon detector with higher spectral resolution. Two spectral fits are made to the background data; a power law with spectral index of -4/5 and an exponential with a folding energy of 200 keV.

sufficiently far enough from the instrument that the source appears at the same location in each image that is to be co-added. As the source distance to meet the far-field condition is not strictly defined, a simulation is performed to quantify an appropriate distance for laboratory testing that is not subject to near-field effects.

The simulation is performed using our GEANT4 model where the decay of a ^{57}Co source is simulated at a range of distances from the instrument. The closed-form calculation estimates that 70 cm is a sufficient distance for the far-field, while simulations show that 75 cm is appropriate. An example of the imaging scenario where both of the conditions of the far-field, the single detector and instrument criteria, are not met is shown in Figure 4.14. This figure shows the near-field effect in a single detector where the point source power is spread out over the image in the form of artifacts, and the co-added image cannot properly average to the same image.

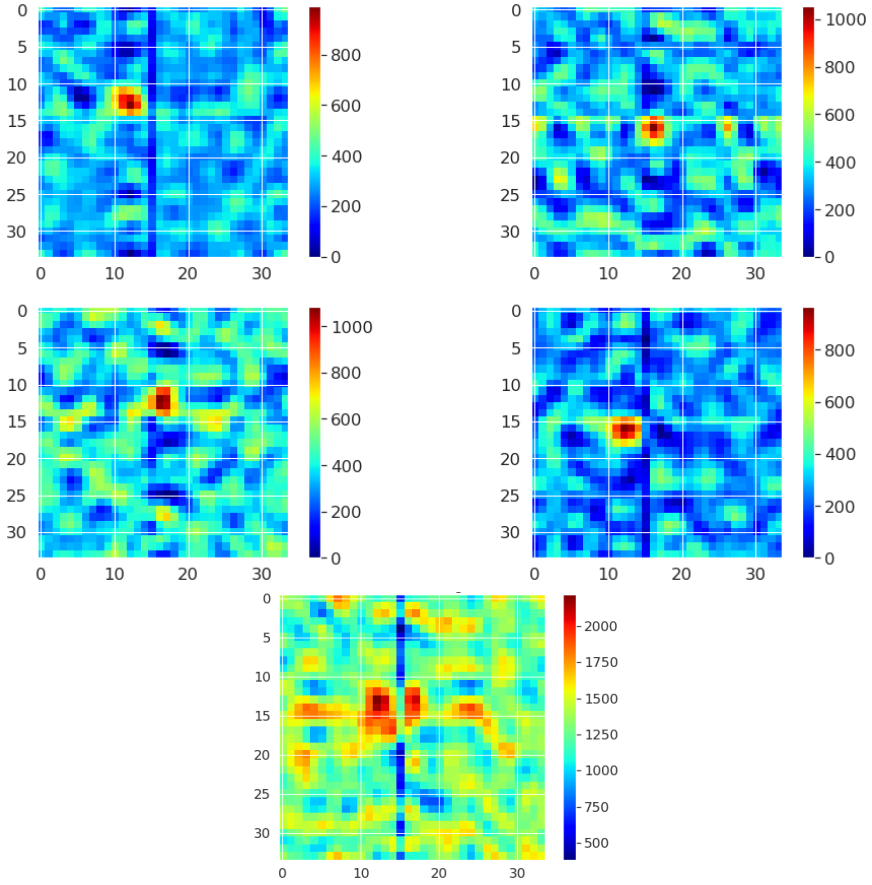

Figure 4.14: GEANT4 simulations of a ^{57}Co source at a distance of 20 cm from the AXIS instrument. The top four plots are the results of individual detectors after the direct correlation algorithm described in Section 4.3. The effect of the source in the near-field of the imager spreads the source power out over the image in the form of artifacts. The bottom plot shows the co-addition of the 4 detector images, where the image is again blurred due to the source being located at different spatial locations relative to each detector.

The simulation in Figure 4.14 is performed at a h distance of 20 cm. Figure 4.15 shows the simulation of a point source at a distance of 75 cm away, which exceeds the far-field calculated for the 4-detector configuration of 70 cm. Note that each individual detector image, as well as the co-addition of images, shows the proper image reconstruction of a point source near the center of the field-of-view. These image reconstructions were performed with the cross correlation algorithm described in Section 4.2 and are left in the deconvolution resolution, and the effects of imperfect reconstruction are addressed in coded aperture literature (e.g. Accorsi et al., 2001; Gottesman, 2007). The following laboratory tests are performed at a source-to-detector distance of 75 cm with

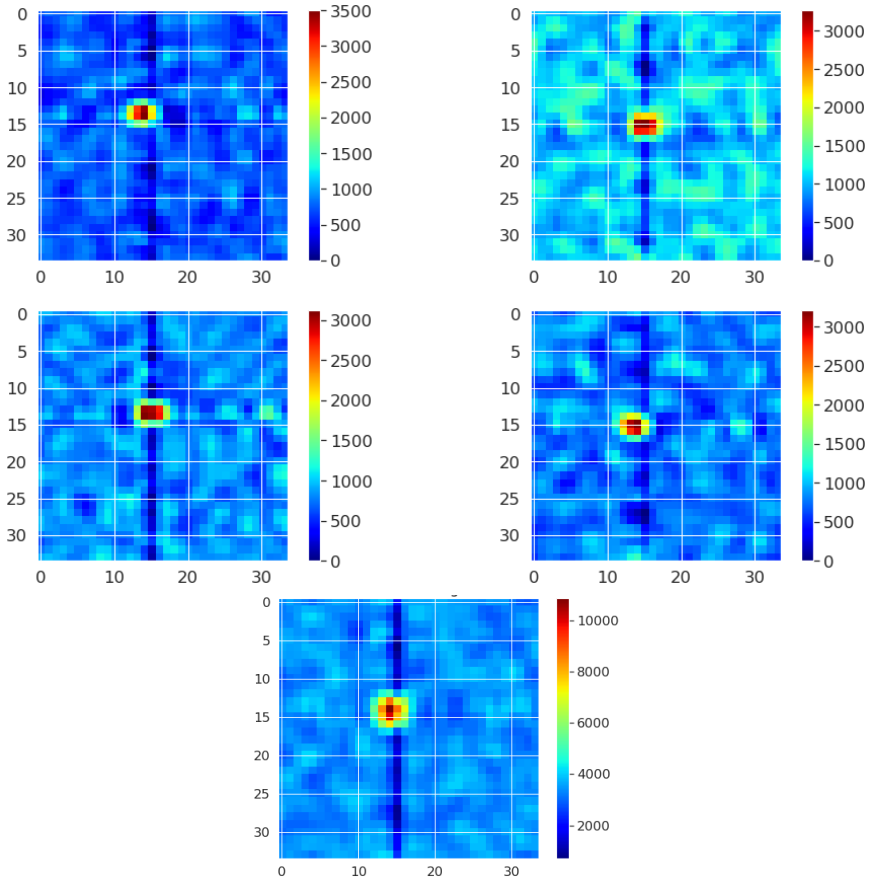

Figure 4.15: GEANT4 simulations of a radioactive disk source at a distance of 75 cm from the AXIS instrument. Note, in contrast to Figure 4.14, that each individual detector in the top 4 plots successfully reconstructs the point source, and the co-addition of the 4 detectors in the lower plot also reconstructs a point source near the middle of the field-of-view.

the 4 detectors, or a distance of 35 cm with one detector, which is found to satisfy the far-field condition for a singular detector.

The first light test of a 1 μCi activity ^{57}Co disk source is conducted with the source at the center of the field-of-view at 35 cm from the coded aperture plane (37 cm from the detection plane). Figure 4.16 shows the detector signal produced from the point source as well as the reconstruction of the disk source. The detection model is applied here to estimate the X-ray and background flux, which agrees with the known source strength and background flux in the 109–153 keV energy band around the 122 and 136 keV ^{57}Co line emissions.

The next tests involve moving the point source within the field-of-view to characterize the

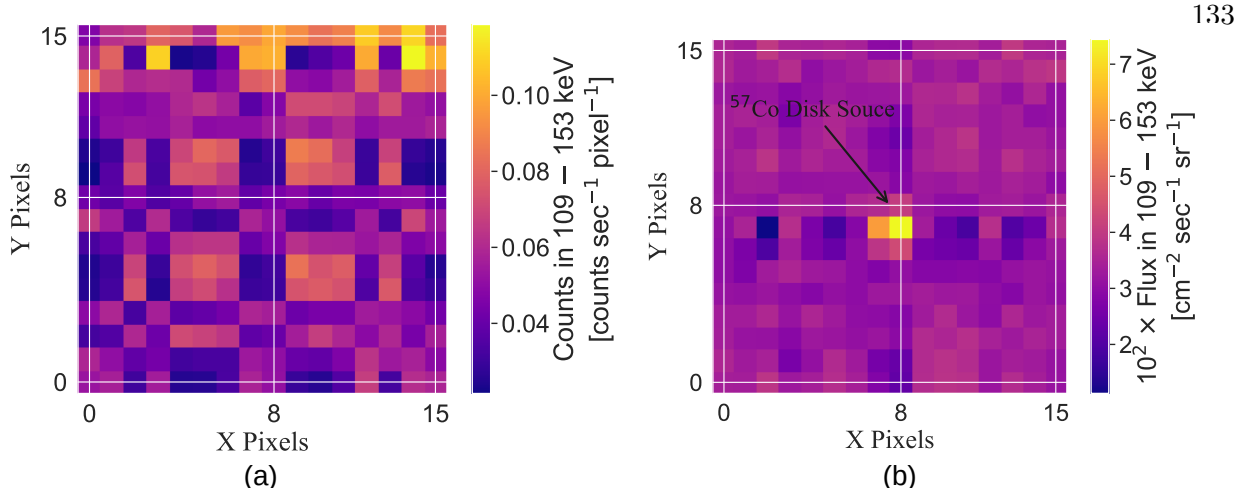

Figure 4.16: Plot (a) shows laboratory data of the detector signal from a ^{57}Co point source located in the center of the field-of-view. Plot (b) is the reconstruction of the disk source using the Fourier-space multiplication method in the 109 – 153 keV X-ray energy band.

detection behavior and artifacts produced as the point source is within different portions of the image. Figure 4.17 shows the results of moving the source along the center line in the left-right dimension in 5° increments. The left plots shows the detector signal as the mask pattern shift to the left with the motion of the point source, which is reflected in the central plots where the point sources are reconstructed. The pixel SNR of the peak of the source distribution is calculated and labelled above the plots. The rightmost plots show the uncalibrated 122 keV peak of the ^{57}Co source.

Using the results of the angular testing, the AXIS geometric factor as a function of angle $G(\theta)$ can be calculated to form the flat-field of the imager. Figure 4.18 shows the results of discrete exposures at 5° spacing between on-axis (0°)and the edge of the field-of-view (45°). The test is normalized by the on-axis geometric factor $G_0 = G(\theta = 0°)$ to indicate the fraction reduction with off-axis angle θ. A triangle function (i.e. two linear fits mirrored about $\theta = 0°$) is fit to the data with a slope of 1.12 rad^{-1} which is approximately 0.019 deg^{-1}. This function will be used to adjust the flux estimate away from the center of the field-of-view due to the reduction in signal strength that occurs from the reduced effective aperture area.

These tests are part of ongoing work to characterize the AXIS novel wide field-of-view coded

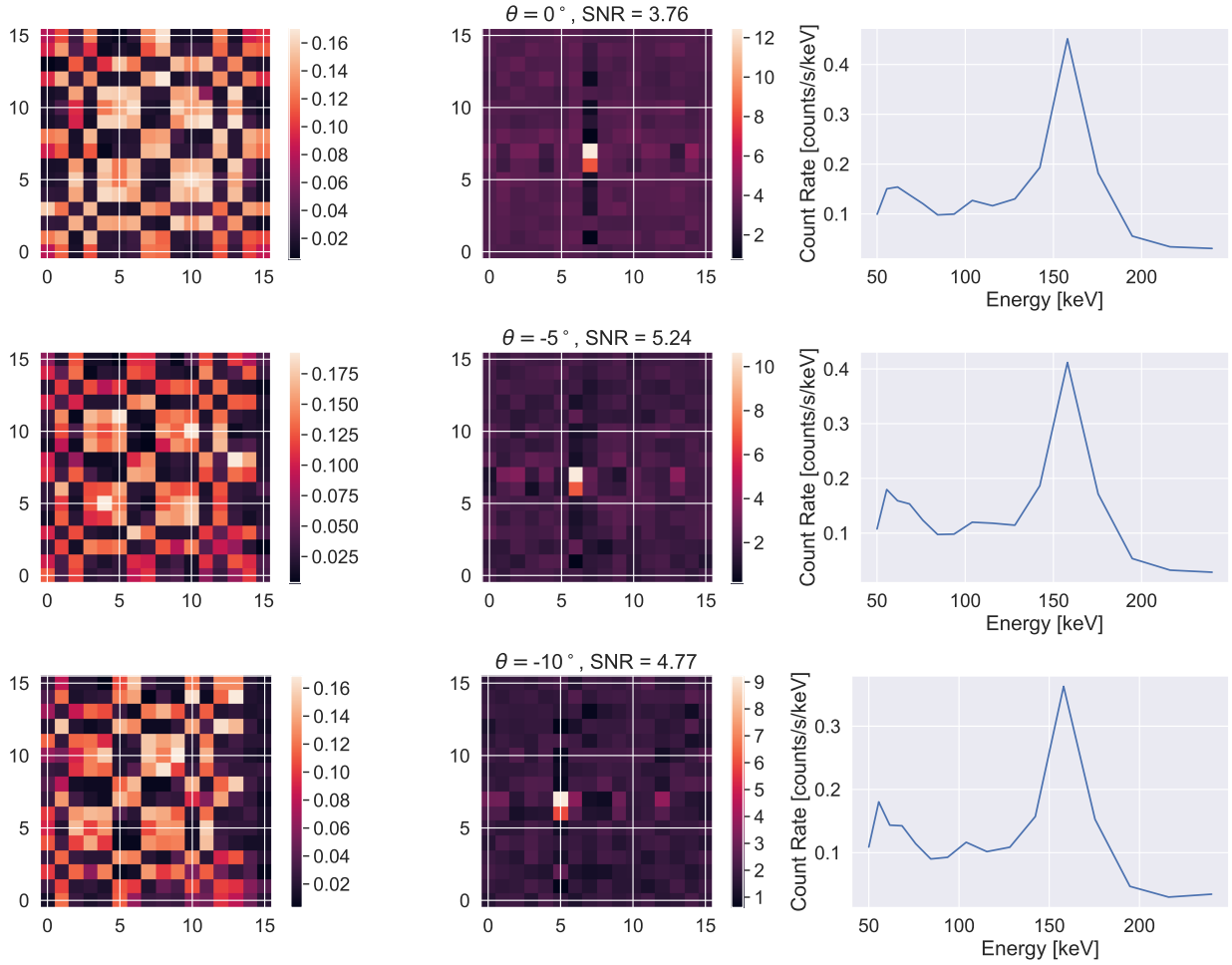

Figure 4.17: The left plots show the detector signal generated by the ^{57}Co source projected through the coded aperture mask that shift with source angle. The middle plots show the reconstruction of the disk source as well as the pixel SNR of the peak above the root mean square of the noise. The rightmost plots show the (uncalibrated) energy peak of the 122 keV line emission.

aperture imager. The simulation, laboratory testing, and algorithmic enhancement of X-ray images by the instrument constitutes a novel endeavor in wide field-of-view X-ray imaging from a LEO orbital platform.

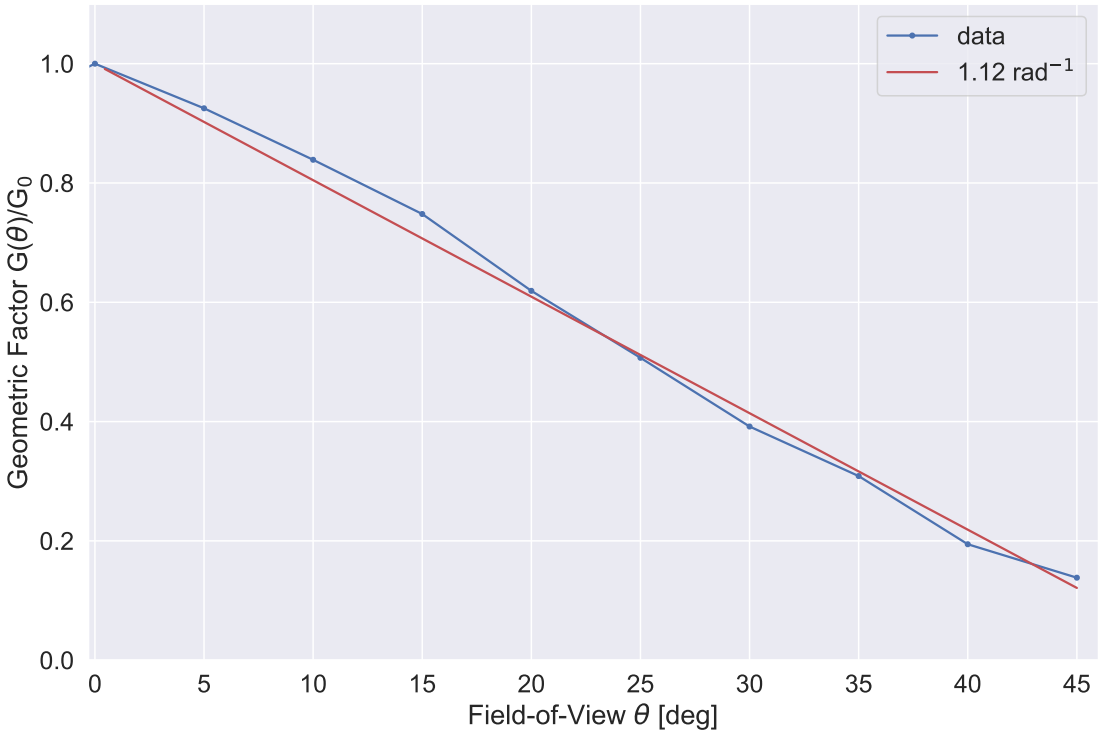

Figure 4.18: Plot of the AXIS geometric factor $G(\theta)$ with off-axis angle θ. The y-axis is normalized by the nominal geometric factor $G_0 = G(\theta = 0°)$ when measured a the center of the field-of-view. A triangle function is fit to the data with a slope of 1.12 rad^{-1} $\approx$ 0.019 deg^{-1} that describes the reduction in the geometric factor with angle.

Chapter 5

Energetic Particle Precipitation Modeling

Due to the large spatial scales and fast time scales of both the drivers of this process and the process itself, EPP is difficult to observe directly or in-situ. In order to quantify the effects EPP has on the atmosphere, a model is desired to describe the excess ionization of atmospheric neutrals that occurs from EPP, as well as other measurable quantities such as the production and transport of bremsstrahlung photons, electrons that backscatter from the atmosphere, and other measurable quantities caused by precipitating electrons. This section covers the modeling and data analysis work published in Berland, Marshall, and Capannolo (2023) in detail.

In whole-atmosphere models such as WACCM, EPP is parameterized as an input in order to account for the energy input and perturbative effect that EPP has on ionization and conductivity of the ionosphere and middle atmosphere (Liu et al., 2018a). An example set of parameters that describe EPP can be energy spectrum and flux, over some spatial scale and time duration; this set yields a total energy input into the atmosphere and energy spectrum can describe the depth of penetration into the atmosphere where the highest level of ionization occurs. An early analytical model that performed this calculation for input into TIME-GCM is the Roble and Ridley (1987) model, mostly aimed at quantifying the impact of auroral electrons (<30 keV). An update to this model came from Frahm et al. (1997) which included transport of bremsstrahlung photons and compared to X-ray data from the UARS mission (Sharber et al., 1993).

These models looked specifically at exponential and kappa electron energy distributions, but are limited to sub-relativistic energies (<MeV). In order to extend model predictions to higher

energies, Fang et al. (2008) used an analytical approach that considered higher energy electrons from fixed energy and pitch angle distributions for the WACCM-X model (Liu et al., 2018b). In Fang et al. (2010), monoenergetic, isotropic pitch angle beams are simulated in order to create arbitrary input distributions to atmospheric models.

The accuracy of the modeling results was improved by the work of Xu et al. (2018); Xu and Marshall (2019); Xu et al. (2020) which uses the Energetic Particle Monte Carlo (EPMC) code, which is well-suited to sampling rarefied high-energy interactions, such as bremsstrahlung, pair production, and so forth. Finally, Berland, Marshall, and Capannolo (2023) improves on these calculations by implementing a Geant4 Monte Carlo model with improved particle and photon tracking, and compares their results to ELFIN, BARREL, and FIREBIRD data. This chapter covers the model construction, output, results, and inversion methods implemented in Berland, Marshall, and Capannolo (2023) that validate and verify the model results.

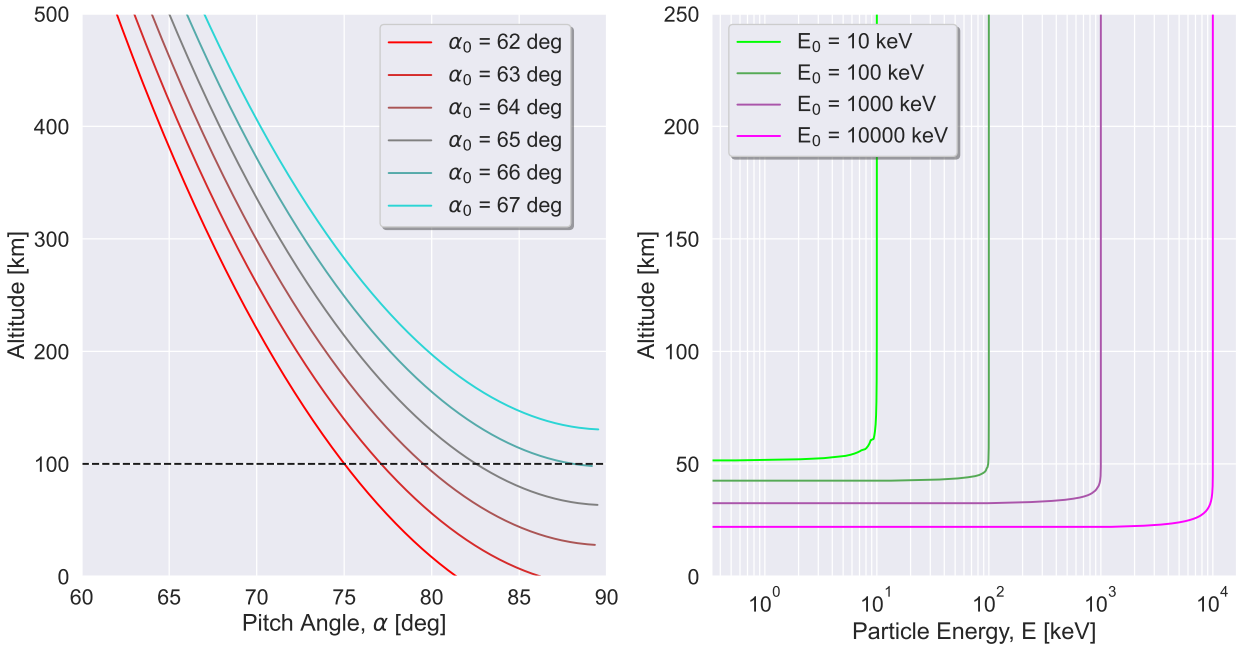

Figure 5.1: Example of the dynamics of charged particle motion showing (left) pitch angle evolution with altitude and (right) energy evolution with altitude. α_0 is the initial pitch angle at 500 km altitude, where the dashed line marks 100 km altitude, which is the reference altitude used to define the loss cone. The energy evolution shows initial particle energies from 10 keV to 10 MeV and the relative depth of penetration into the atmosphere from collisions with atmosphere neutrals.

The left plot in Figure 5.1 shows the pitch angle evolution with descending altitude, which is how a particle would behave near a magnetized and airless body which is devoid of collisional interactions. The figure shows the change in pitch angle as the particle descends into the stronger magnetic field, and demonstrates how velocity parallel to the magnetic field line is transferred to the perpendicular component. The right plot of Figure 5.1 shows the idealized energy loss of electrons through an exponentially increasing density atmosphere, which highlights the relative depth of penetration towards Earth of varying energy electrons.

5.1 EPP Model Description

The components that make up the EPP model are a physics solver and geometry handler framework combined with atmospheric and magnetic field models that defines the environment or material that a simulation particle (i.e. charged particle or photon) passes through within the simulation volume. The physics solver and geometry framework chosen for this model is Geant4 (GEometry ANd Tracking), which is a radiation and charged particle transport code that encapsulates radiation's interactions with matter (Agostinelli et al., 2003; J. Allison et al., 2006). Geant4 propagates particles by taking a semi-classical approach to particle position and momentum at pre- and post- step points via the incorporation of final state calculations that include quantum effects on a particle's state, where the state is comprised of the position $\mathbf{r}$ and momentum $\mathbf{p}$ at time t.

In order to solve for various quantities of interest that are a product of electron energy, where interactions occur, and the rate at which these interactions occur, we would like to employ a framework that allows us to describe the average behavior of many electrons and be able to describe the variation in that behavior in a formal way. To achieve this goal, we use the phase space density f, which is a smoothed distribution of electron behavior that is dependent upon the electron phase space coordinates $(\mathbf{r}, \mathbf{p}, t)$. This distribution behaves similarly to a probability distribution function in that operations can be performed on f which do not change its magnitude and, through tracking the evolution of f, we can draw conclusions about quantities of interest through statistical inference.

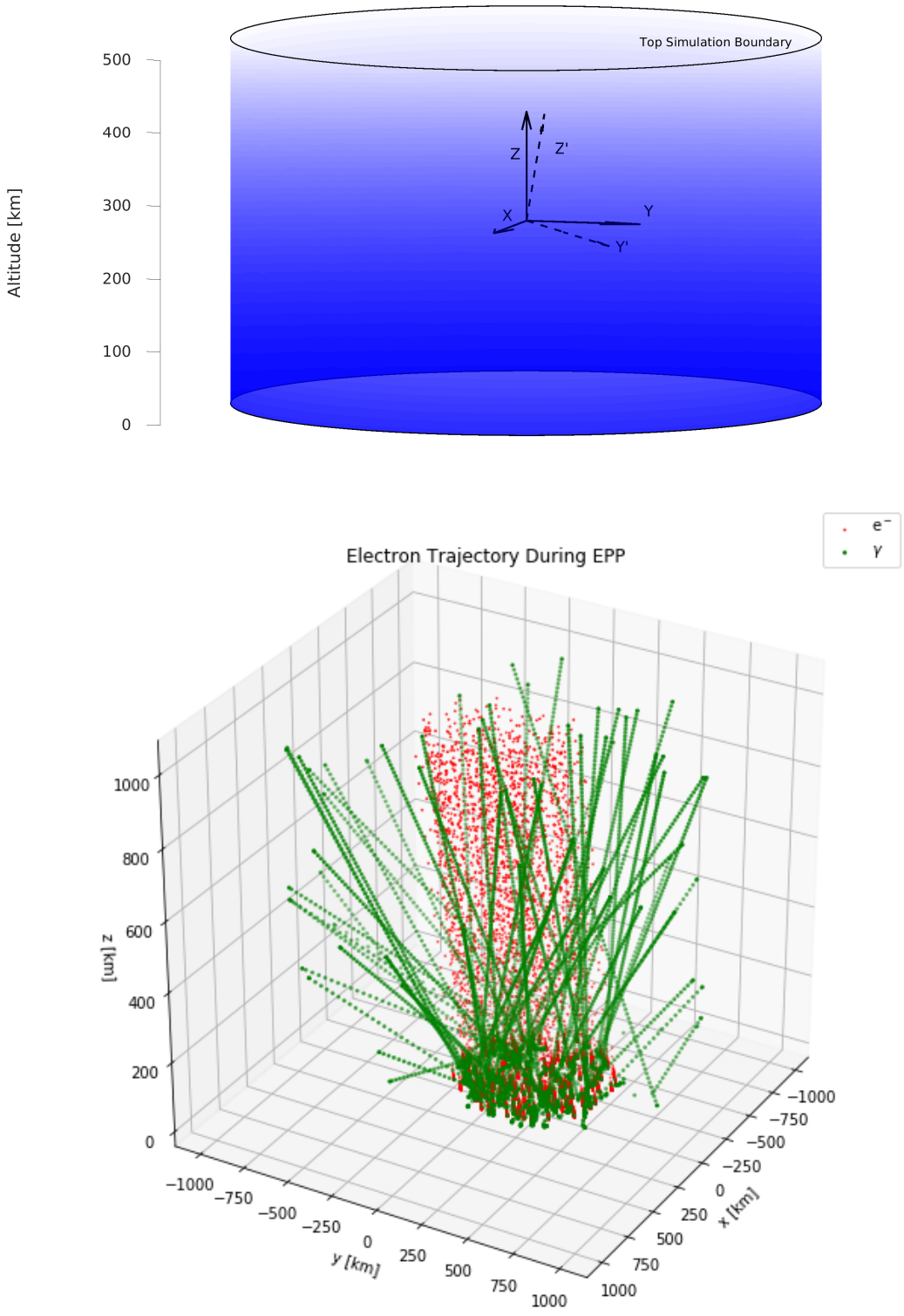

Figure 5.2: (Top) EPP model simulation volume, showing the Earth-centered Earth-fixed (ECEF) coordinate system and the magnetic inclined coordinate system, rotated 12° with respect to the ECEF coordinate system and notated with apostrophes. (Bottom) Electron and photon trajectories, showing bremsstrahlung photon backscatter that can be detected from space.

The evolution of the phase space density $f(\mathbf{r}, \mathbf{p}, t)$ over the duration of simulation time interval (i.e. the time from particle injection into the simulation to either escape out of a boundary or precipitation) is then calculated through an explicit stepping method that simulates the effects of electromagnetic forces, random collisions, and other rarefied interactions such as secondary production. Combining these effects and computing the total derivative in time yields the following transport equations, which are descriptions of the dynamical evolution of the electron distribution's phase space:

$$\begin{cases} \frac{Df(\mathbf{r},\mathbf{p},t)}{Dt} = \frac{\partial f}{\partial t} + \frac{\mathbf{p}}{m} \cdot \nabla f + \frac{\partial f}{\partial \mathbf{p}} \cdot \mathbf{F} & = 0 \qquad \text{Collisionless Boltzmann Equation} \\ & = \left(\frac{\delta f}{\delta t}\right)_{\text{coll}} \qquad \text{Collisional Boltzmann Equation} \end{cases} \tag{5.1}$$

where $\mathbf{F}$ encapsulates the conservative forces affecting the distribution function f, and the term on the right hand side in the collisional Boltzmann equation parameterizes collisions that alter the distribution. The collisionless Boltzmann equation is a statement of conservation of f, which is not an appropriate characterization when secondary production and loss terms change the magnitude of f.

At high altitudes sufficiently above the majority of the atmospheric density, where collisions are rare, the main force acting on a charged particle is the magnetic component of the Lorentz force, $\mathbf{F} = q\mathbf{v} \times \mathbf{B}$. We include a term that accounts for sources (secondary production) and sinks (precipitation), $S(t)$, to address the non-conservation behavior that describes precipitation to obtain the Vlasov equation:

$$\frac{\partial f}{\partial t} + \frac{\mathbf{p}}{m} \cdot \nabla f + \frac{\partial f}{\partial \mathbf{p}} \cdot q(\mathbf{v} \times \mathbf{B}) = \left(\frac{\delta f}{\delta t}\right)_{\text{coll}} + S(t) \tag{5.2}$$

for the transport and evolution of charged particles. If we exclude the magnetic force and replace the momentum to mass ratio with the velocity, we obtain

$$\frac{\partial f}{\partial t} + \mathbf{v} \cdot \nabla f = \left(\frac{\delta f}{\delta t}\right)_{\text{coll}} + S(t) \tag{5.3}$$

which describes the phase space evolution of photons. The relevant collision and source/sink terms for each particle species is included in Table 5.1. In general, at high altitudes (>100 km), particle

motion is dominated by magnetized cyclotron motion and at low altitudes (<70 km), the particle motion is dominated by random collisional motion ("unmagnetized" motion). For photons within the lower, more dense part of the atmosphere, a fraction of the photon number density will be absorbed during spatial transport, which is described by the Beer-Lambert law of absorption between two points:

$$\int_{\mathbf{p}} f(\mathbf{r},\mathbf{p},t)\ d^3\mathbf{p} = \exp\left(-\int_{\mathbf{r}_0}^{\mathbf{r}} \mu\ \rho(\mathbf{r}')\ d\mathbf{r}'\right)\ \int_{\mathbf{p}_0} f(\mathbf{r}_0,\mathbf{p}_0,t_0)\ d^3\mathbf{p}_0 \tag{5.4}$$

where by integrating over momentum space, the left hand side of the equation is the number density of photons in a differential volume $d^3\mathbf{r} = dx\ dy\ dz$, μ is the mass attenuation coefficient, $\rho(\mathbf{r})$ is the atmospheric mass density at point $\mathbf{r}$, and the bounds of integration define the path length travelled between the two points. The variation in mass density is solely a function of the z directional component and is determined by the mass density model.

The atmosphere model selected to parameterize $\rho(z)$ is the Mass Spectrometer Incoherent Scatter Radar-Empirical (MSISe) model (Picone, Hedin, Drob, & Aikin, 2002). This model takes as inputs the geographical latitude and longitude, altitude, date-time (including time of day), and solar parameter; the F10.7 cm solar radio flux index, and a geomagnetic parameter; the A_p index. MSIS outputs the atmospheric state at the position specified, which includes the average temperature and number density of molecular and atomic nitrogen, oxygen, argon, helium, as well as molecular compounds found in the atmosphere such as NO, NO_2; these outputs are specified from 0 to 1000 km altitude. Although MSISe00 (Picone et al. (2002) version) may be less accurate under more active geomagnetic conditions, MSIS (and especially the updated version MSIS2.0 (Emmert et al., 2021)) performs exceedingly well as a climatological, seasonally-averaged model of the neutral constituents of the atmosphere.

Using the MSIS constituent number density outputs versus altitude, and knowing the mass of each species, the total mass density ρ and species mixing ratios ψ_i can be calculated. These quantities, in addition to MSIS temperature and pressure from the equation of state, are used to fill a simulation volume that is 500 km diameter × 500 km tall column, with 1 km altitude

resolution. Particles are injected at 300 km with an initial pitch angle and energy, and are tracked until they either exit the simulation volume or their energy drops below a threshold, wherein the particles are considered precipitated.

An example of the pitch angle and energy evolution for various initial conditions through Equation 5.2 shown in Figure 5.1. The Vlasov equation formulation provides a framework to understand and describe the properties and behavior of many particles, and this model solves for the transport and collisional aspects.

Term/ Species	Contributions to $(\delta f/\delta t)_{collisions}$	Sources & Sinks $S(t)$
Electrons Eq. 5.2	Coulomb scattering Møller scattering Bremsstrahlung	(+) Photoelectron generation (+) Compton electrons (+) Pair production (+) Auger electrons (–) Electron capture (precipitation)
Photons Eq. 5.3	Compton scattering Photoelectric effect Pair production	(+) Bremsstrahlung photon emission (+) K-shell emission & fluorescence (+) Electron-positron annihilation (+) Particle induced X-ray emission (PIXE) (–) Photoelectron absorption (–) Pair production

Table 5.1: Terms included in the Vlasov Equation for Electrons and Photons

The average behavior of the distribution function f can be found through Equations 5.2 and 5.3 by assuming an initial conditions $f(\mathbf{r}, \mathbf{p}, t = 0) = f_0$ and by using a stochastic treatment of the scattering, source, and sink terms to find a maximum likelihood solution with the Monte Carlo method. This solution is found by simulating a large but finite number of electrons until both the average behavior is determined, and until a sufficient number of secondaries of interest are produced and their average behavior is similarly determined. This simulation does not solve for the quantity f directly, but instead tracks other precipitation quantities of interest that arise from the evolution of f and its effects on the atmosphere. Quantities of interest include the rate of excess ionization (pairs/cm^3/sec) from electron collisions in the atmosphere, which is proportional to the energy lost

from the simulation particles;backscattered electrons that exit the simulation volume at the top boundary; and photon generation statistics, among other quantities. See Section 5.2 for a full list of model outputs.

Since various physics processes can occur over vastly different spatial and temporal scales, the fastest or "shortest" interaction would always dominate the step size, which may be computationally expensive and a reductive implementation of the many types of physics that affect a particle.[1] Instead of limiting the path length transited per simulation step, Geant4 implements a more general formulation based on the energy lost per simulation step. The steps are ultimately conducted in proper time, i.e. the time that passes in the frame of the simulation particle, and combining these factors, the limiting step size is determined via this energy threshold, or "energy cut".

In order to solve for the helical gyromotion of the charged particles, a Runge-Kutta integrator is employed. Specifically, the Dormand–Prince 7-4-5 method is used, where a high order integrator is needed in order to accommodate the Brownian motion that occurs when random collisions dominate the motion of the particle (Dormand & Prince, 1980; Cartwright & Piro, 1992). Geant4 offers native selection of integration step size and energy cut limiting. In order to ensure numerical stability, the magnetic force integrator (akin to temporal step size) and energy cut limit (akin to spatial step size) must satisfy a Von Neumann stability criterion $\Delta t \leq 2(\Delta x)^2$. Once this condition is met by selecting the appropriate integrator step size and energy cut limit, the vast majority (>99%) of particles have convergent integrator solutions and propagate through the simulation volume. Geant4 struggles with charged particles propagation through a sparse gas in the presence of a magnetic field outside of the stable simulation regime, and will kill and log the remaining ∼1% of particles whose trajectory solutions do not converge.

The method of Xu et al. (2020) is implemented, wherein we simulate a series of mono-energy, mono-pitch angle electron beams that can be used to reconstruct arbitrary energy and pitch angle distributions. Electron beams range in input energy from 10 keV to 10 MeV at 19 pseudo-log-spaced

[1] For example, prioritizing the simulation of a single collision is relevant when there is a rarefied interaction such as bremsstrahlung production, but can effectively be summarized over many scattering interactions using continuous slowing down approximation (CSDA) physics otherwise.

energies. This energy range is above typical auroral precipitation energies and sufficiently captures the highest likely radiation belt electron energies (Østgaard et al., 2001; Laundal & Østgaard, 2009). The particles are injected at 300 km altitude, where for our nominal magnetic field model, the loss cone angle is 72.8°, so the range of pitch angles is between 0° and 75° in 5° increments. The input values of the mono-energy, mono-pitch angle beams (E_0, α_0) serve as the abscissa that can be combined in a linear weighted fashion to represent an input distribution in energy-pitch angle space. This is a part of the Green's function method and is expanded upon in Section 5.3.

An additional feature that is implemented in this model is the non-directional bremsstrahlung splitting method. This is a biasing method that is necessary at lower beam energies (<100 keV) where bremsstrahlung is less likely and therefore few photons are created in the Monte Carlo model. The splitting method samples the bremsstrahlung cross section N times for every true bremsstrahlung interaction that occurs, and then weights the scoring quantities (deposited energy, e.g.) of those photons and any secondary particles that are generated by those photons by $1/N$. Bremsstrahlung splitting methods will often offer a bias in the propagation direction of photons, for example to better understand shielding penetration from forward-propagating X-rays, but no directional bias is applied to the resulting photons in this case. This type of non-directional bremsstrahlung splitting bias has been used in other works (e.g. Kawrakow, Rogers, and Walters (2004); Ali and Rogers (2007)) and Geant4 offers a native implementation of this scheme. Figure 5.3 shows the influence of bremsstrahlung splitting on the smoothness of deposited energy versus altitude profiles, at altitude below the primary ionization peak, over 10 electron beam energies with a splitting factor $N = 100$.

5.2 Model Outputs and Results

The Geant4 EPP model outputs the energy lost, and therefore deposited into the atmosphere, from electrons and photons per simulation step which is histogrammed into 1 km altitude bins. The differential energy flux passing through an altitude-energy bin is also collected for electrons and photons in order to conserve differential information that can be used later for derived products like

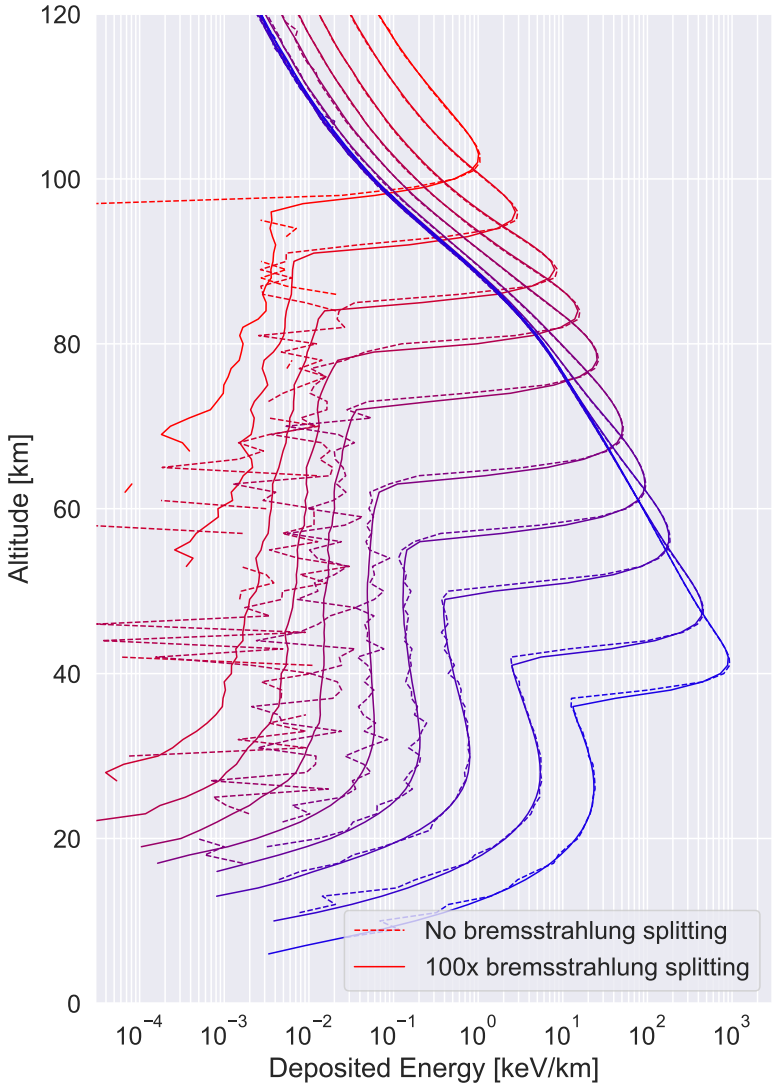

Figure 5.3: Energy deposition versus altitude for 10 mono-energetic electron beams, ranging from 10 keV to 10 MeV run with 10^5 electrons. The model is run with no biasing (dashed lines) and 100x bremsstrahlung splitting factor enabled (solid lines). The two model runs converge at higher energies where the bremsstrahlung interaction becomes increasingly likely.

radiation dose at a given altitude. Table 5.2 shows a collection of quantities of interest that can be derived from these model outputs. Additionally, by recording differential energy flux instead of, say

differential number flux, the weights from bremsstrahlung splitting can more easily be interpreted and applied for later analysis. An example of the energy-altitude histograms is shown in Figure 5.4 for 500 keV and 5 MeV beam energies with isotropic pitch angle inputs.

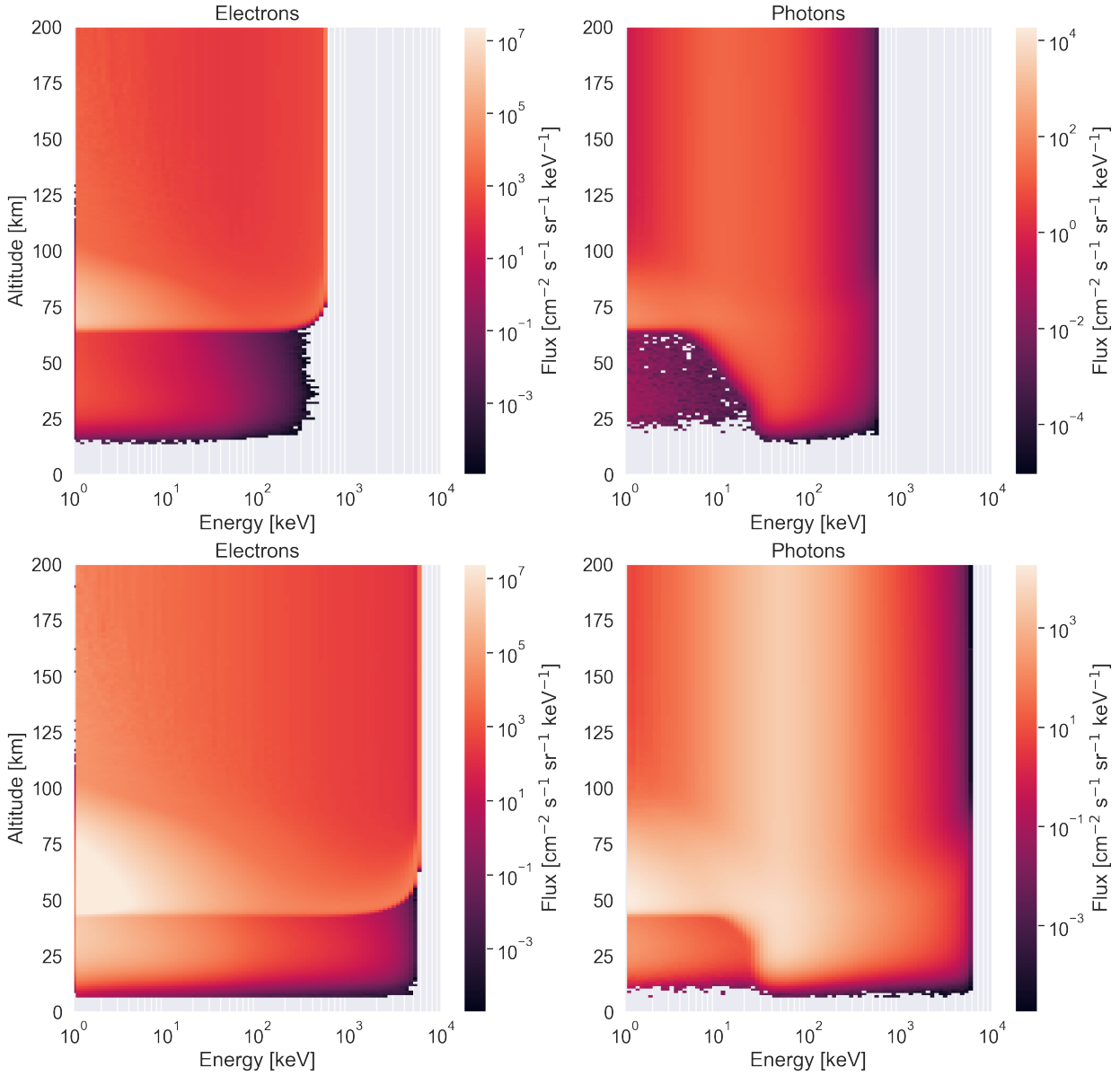

Figure 5.4: Energy-altitude spectra showing differential number flux of (left column) electrons and (right column) photons from mono-energy mono-pitch angle beam inputs for (top row) a 500 keV beam energy, isotropic pitch angle beam, and (bottom) row a 5 MeV beam energy, isotropic pitch angle distribution. Both of these beams represent an input electron number flux of 10^4 cm^{-2} s^{-1} sr^{-1} keV^{-1}.

In order to run a sufficiently large number of particles, the EPP model is run on 5 supercomputer nodes that each have 40 cores. Simulating 10^5 particles over 200 cores using one thread per core and sweeping over the input space yields run times on the order of 2 – 5 days, with higher pitch angle particles taking significantly more time than low pitch angle particles due to their increased path length.

Model Output	**Derived Quantity of Interest**
Energy deposition histograms	Atmospheric ionization rate Scattering efficiency
Energy-altitude histograms	Differential electron flux vs. altitude, energy Differential photon flux vs. altitude, energy Photons that escape the atmosphere Bremsstrahlung efficiency Radiation dose
Electron Statistics at 500 km	Electron backscatter

Table 5.2: EPP Model Raw and Derived Outputs

To convert from energy deposited in the atmosphere to electron-ion pairs produced via ionization, we need a relationship between energy rate and ionization rate. The typical value used in Earth's atmosphere is 35 eV/pair, which is the average first ionization potential for nitrogen and oxygen (Rees, 1989). However, Earth's atmosphere varies in composition with altitude, and additionally the scattering interaction that causes the ionization is not linear with energy. These two factors combined imply that a different relationship may be appropriate for relativistic electrons, and that the conversion factor may be altitude-dependent. Krause (1998) offers an ionization relationship that is a function of altitude:

$$I(h) = I_0 + \frac{\partial I}{\partial h} \cdot h \tag{5.5}$$

where h is altitude in kilometers, $I_0 = 39.78$ eV/pair and the slope parameter $\partial I/\partial h$ is -0.03 eV/-pair/km, where this relationship is valid between 45 and 240 km; beyond these altitude bounds, the left and right extreme values of Equation 5.5 should be used, respectively. These values vary from

the constant 35 eV/pair assumption by up to 10% and vary the shape of the ionization profile with altitude, due to the altitudinal dependence of I. Figure 5.5 shows the energy deposition histograms

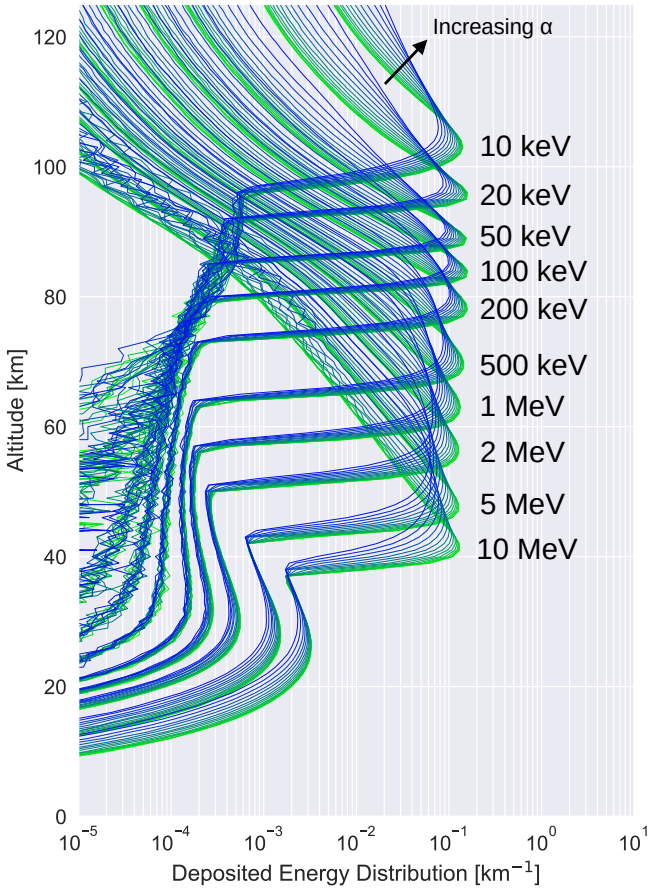

Figure 5.5: Deposited energy distribution versus altitude for a range of mono-energetic, mono-pitch angle electron beams from 10 keV to 10 MeV and from field-aligned pitch angle (green) to pitch angles near the edge of the loss cone (blue). Each profile is normalized so they integrate to unity in altitude.

for selected electron beam energies and pitch angles normalized to unity to illustrate the variation in deposited energy with the two input quantities. This figure illustrates the major difference between energy deposition profiles, which is in the altitude of maximum deposition. Figure 5.5 shows this peak descending in altitude with increasing input beam energy.

In order to convert between the number of simulation particles run in the numerical model and the physical flux of particles at the input, an additional conversion factor is needed. Since

there is no in-plane (x-y plane in Figure 5.2) variation in the input location of the electron beam, we say that all particles pass through a normalized simulation area $\Delta A = 1$ cm^2, and a simulation time of $\Delta t = 1$ second. Then, we can directly relate the number of electrons simulated N to an integral flux in units of particles-cm^{-2} s^{-1} at the top boundary. We would also like to be able to convert this quantity into units that are differential in solid angle, such that pitch angle distribution comparisons can be formed. In order to do that, we let our area and time elements be differential, dA_d and dt, and form a vector that represents the simulation surface unit normal, $\hat{k}_d$. We form a vector in momentum space $\hat{k}_s$ that represents the initial condition phase space distribution f. Finally, we take the differential solid angle that a particle passes through from distribution f into the simulation volume as $d\Omega_d$, whereupon the total number of simulation particles is given by:

$$N = -dt\ d\Omega_d\ \left(f(\hat{k}_s)\ \hat{k}_s\right) \cdot \left(dA_d\ \hat{k}_d\ \right) \left[\hat{k}_s \cdot \hat{k}_d < 0\right] \tag{5.6}$$

In this equation, the brackets denote the indicator function that follows the property $[\mathit{True}] = 1$ and $[\mathit{False}] = 0$, and the negative sign enforces inward particle directionality towards the simulation volume from the distribution f. We evaluate the dot product between the momentum space distribution and simulation surface normal into $f(\hat{k}_s) \cdot \hat{k}_d = f_0 \cos(\alpha_0)$, where α_0 is the discrete pitch angle selected for a given run, to obtain the relationship

$$\frac{N}{dt\ dA_d} = f_0 \int_0^{2\pi} \int_0^{\pi/2} \cos(\alpha_0)\ \sin(\alpha)\ d\alpha\ d\theta \tag{5.7}$$

where α is the pitch angle and θ is the azimuthal angle. From azimuthal symmetry, we can immediately integrate out the azimuthal angle. The indicator function restricts the limits of integration to $[0, \pi/2]$ instead of the full pitch angle range of $[-\pi/2, \pi/2]$. By integrating in azimuthal angle and rearranging, we can find a relationship between differential flux f_0 in units of cm^{-2} s^{-1} sr^{-1} to the number of electrons simulated N at discrete pitch angle α_0 :

$$f_0 = \frac{1}{2\pi \cos(\alpha_0)} \frac{N}{dt\ dA_d} \tag{5.8}$$

Note that this quantity remains finite since as the beam angle $\alpha_0 \to \pi/2$ (i.e. locally mirroring particles), the number of particles passing through the simulation surface N goes to zero. We

can also note that although the number flux passing through the surface is a function of α_0, the energy flux passing through the surface is identical at all initial beam angles for the same number of particles, so quantities that are derivative from energy flux do not need this conversion factor. Using Equation 5.8, we can relate the simulation outputs to the differential flux initial conditions.

A simpler approach can be taken to include a differential unit in energy: the quantity in Equation (5.8) can be multiplied by an energy distribution that integrates to unity in units of keV^{-1}, which yields a differential electron spectrum in units of cm^{-2} s^{-1} sr^{-1} keV^{-1} that fully describes an input electron flux and is comparable to flux estimates from in-situ electron instruments.

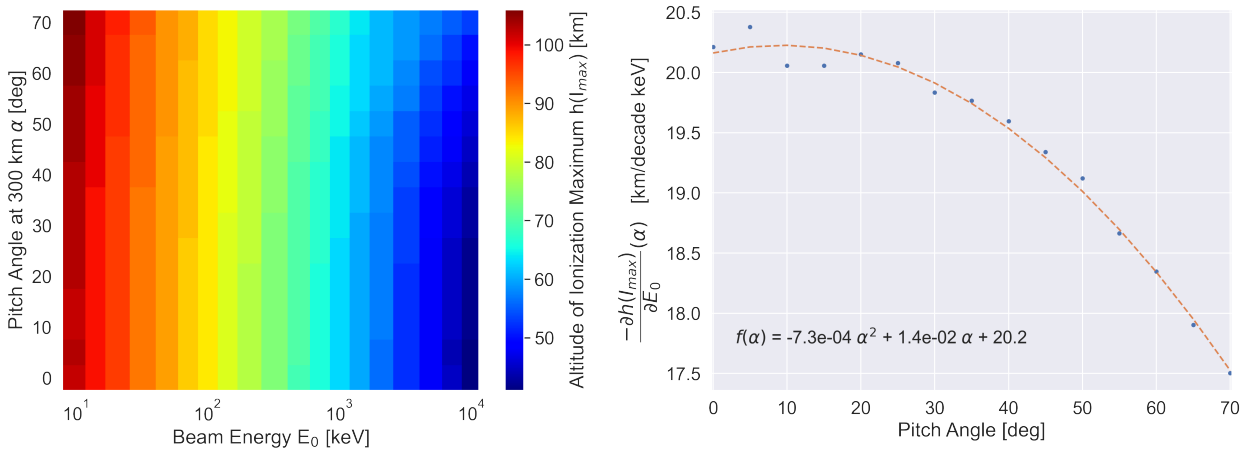

Figure 5.6: (Left) The altitude of maximum ionization $h(I_{max})$ surface versus electron beam energy and pitch angle, showing the lowest $h(I_{max})$ altitude is at high energies and low pitch angles. (Right) The partial derivative with logarithmic beam energy $\partial h(I_{max})/\partial E_0$, i.e. the descent in kilometers that occurs from increasing beam energy by a factor of 10, is shown versus pitch angle in the right panel. This quantity is more sensitive at field-aligned pitch angles, and a polynomial fit $f(\alpha)$ is shown.

Figure 5.6 shows the variation in the altitude of maximum ionization $h(I_{max})$ with input beam energy and pitch angle. The variation in this altitude with input energy $\partial h(I_{max})/\partial E_0$ versus input pitch angle is also plotted, showing that at lower pitch angles, the particles penetrate deeper into the atmosphere. The trend, averaged through pitch angle, shows an approximately 20 km descent in $h(I_{max})$ with a decade increase in input beam energy. There is also a weaker dependence on pitch angle, with higher pitch angles having high $h(I_{max})$ altitudes. This trend of

the descent of the altitude of maximum ionization with beam energy is plotted versus input pitch angle in the right plot of Figure 5.6. Another quantity of interest is the backscattered electron

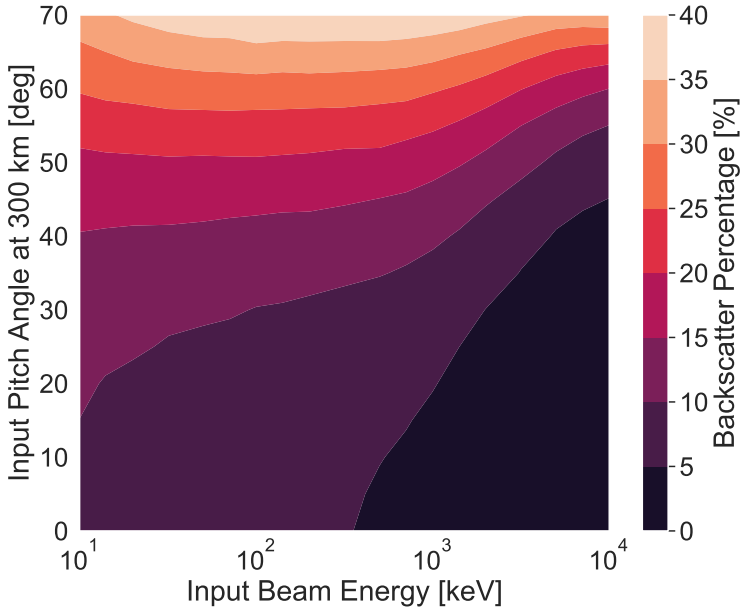

Figure 5.7: Surface showing backscatter percentage versus electron beam energy and pitch angle, showing backscatter percentages up to 40% for low energies and high initial pitch angles and low backscatter fractions for high energies and low initial pitch angles.

flux since this quantity is important for studying electron lifetimes, ionospheric conductance, and the total particle flux balance between the radiation belts and the atmosphere. This population includes both primary electrons that have their momentum direction turned around completely towards the zenith direction and effectively re-enter either the anti-loss cone or trapped populations, and also secondary electrons that are generated from the atmospheric interactions that rejoin the aforementioned populations. Figure 5.7 shows the efficiency of this backscatter mechanism as a function of input energy and pitch angle. Note that the backscattered electron number flux fraction can reach up to 40% at high initial pitch angles and low energies on a single bounce,[2] which is an important factor when calculating electron lifetimes and when considering the relative influence of loss processes.

[2] Note that this percentage can theoretically exceed 100% since it includes secondary electrons that are produced in the upper atmosphere.

The pitch angle and energy of backscattered electron flux is also coupled. This relationship is illustrated in Figure 5.8 which shows a correlation between electron energy and pitch angle recorded at 500 km. This spread of the 2D distribution in each dimesions changes with input pitch angle and beam energy; the dependencies of the 2D backscatter distributions are expanded upon and compared with spacecraft data in Section 5.4.3.

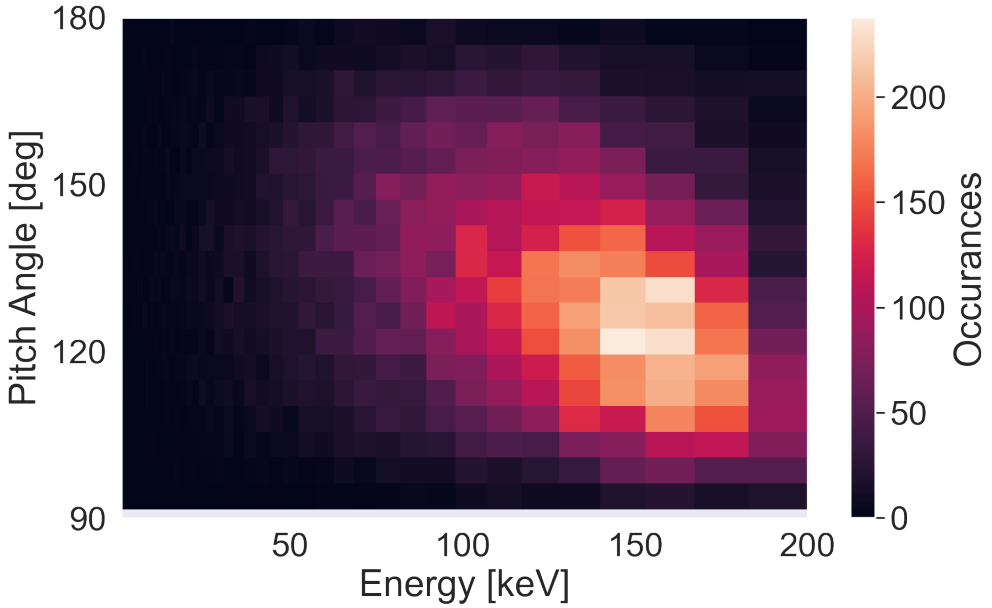

Figure 5.8: Energy-pitch angle spectrum of electron backscatter resulting from a 200 keV electron beam energy with an input pitch angle of 50° at 300 km. The colorbar indicates the number of simulation particles recorded in each energy-pitch angle bin and is not normalized for bin size, showing the raw output of the simulation.

Figure 5.9 shows 1D integrations, normalizing for bin size, of the 2D profiles for ten input beam energies which shows the variation in backscattered electron spectra and pitch angle distribution. The electron spectra show characteristic rising elements before a sharp fall off in flux above a peak for low to medium energies, and a flatter characteristic spectrum for higher energies. Additionally, the pitch angle dependence in the electron spectra, and conversely the energy dependence in the pitch angle distributions, affect both the efficiency of the backscatter process and the shape of the resulting distributions. Note that a significant amount of flux reenters the trapped population and does not precipitate on the next bounce, which must be accounted for to

fully describe the loss process of precipitation.

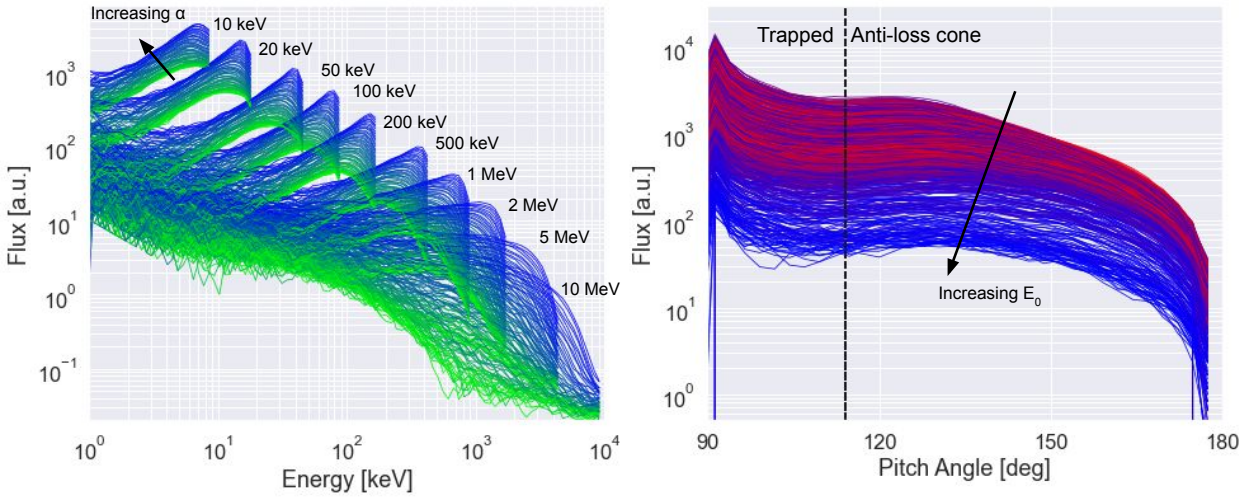

Figure 5.9: One dimensional integrations, in arbitrary flux units, of the 2D distribution shown in Figure 5.8 to produce (left) energy and (right) pitch angle distributions at 500 km altitude from backscattered electrons. The pitch angle dependencies in the electron spectra are shown from low input pitch angle (green) to high (blue), and the energy dependence in the pitch angle distributions is shown from low input energy (red) to high (blue).

Another important use of this model is in the generation of bremsstrahlung photon spectra from various input conditions. These distributions aim to support X-ray photon measurements from both above and within the atmosphere as proxy measurements for EPP. These results can be derived from the energy-altitude histograms of photon energy flux. Figure 5.10 shows the photon spectra generated from mono-energy, isotropic pitch angle beams from 25 – 35 km, which is a typical balloon altitude range, and from 250 – 300 km, which is sufficiently above the atmosphere to match observations from space. This figure also shows an important phenomenon related to the invertibility of photon spectra measured from within the atmosphere; the atmospheric "filter" effect that arises from the reabsorbtion of photons below ∼20 keV. This effect causes the spectrum to be essentially one-sided above the flux peak that forms at 60 keV. Conversely, above the atmosphere,

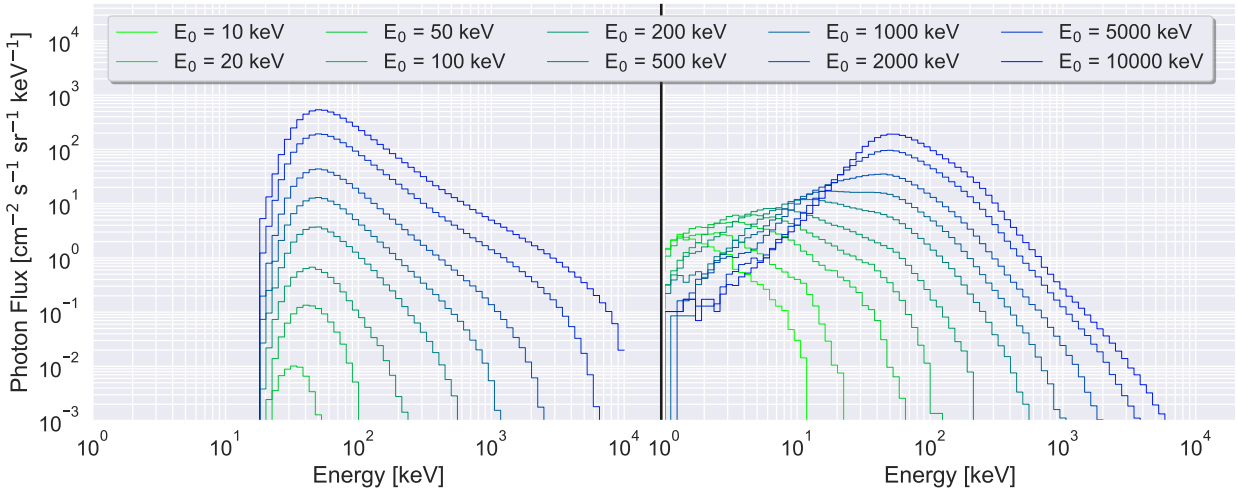

Figure 5.10: Photon spectra that are produced from different input mono-energy electron beams from 10 keV (green) to 10 MeV (blue), integrated from (left) 25 – 35 km and (right) 250 – 300 km. Note that electron beam energies of 10 and 20 keV do not produce X-rays that reach 25 – 35 km.

inversion information can be obtained from both the high and low energy tail of the distribution on either side of the flux peak. Electron flux inversion from X-ray spectra is expanded upon and compared to balloon X-ray data and in-situ electron in Section 5.4.2.

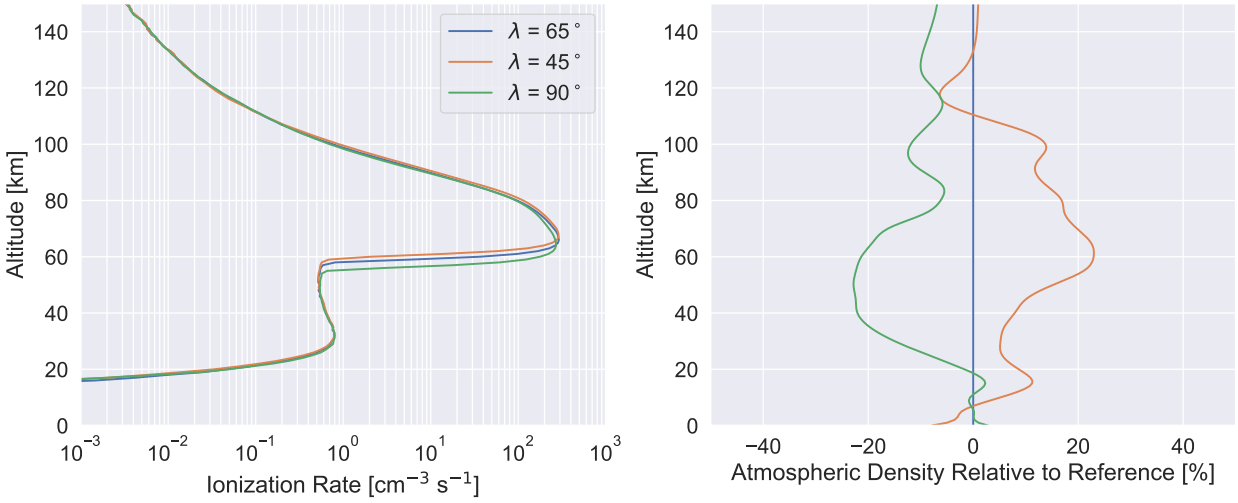

Figure 5.11: Variation of ionization profile versus altitude is shown given different atmospheric profiles. Additionally, the magnetic latitude varies, which produces a varying magnetic inclination which causes electrons to transit longer path lengths at lower magnetic latitudes. However, the effect of varying atmospheric profile is the dominant factor here. The magnetic latitude of Poker Flat Incoherent Scatter Radar (PFISR) station of 65° is taken as the reference atmospheric profile.

One of the important inputs for this model is the MSIS atmospheric profile which primarily describes the atmospheric mass density as a function of altitude, $\rho(h)$[3] . This quantity is variable depending on the season, time of day, geodetic location, and geomagnetic conditions, so having the ability to transform the results to be applicable under those conditions is desirable. In order to do this, we perform a pseudo-logarithmic transformation by letting the integral of the atmospheric density itself serve as the abscissa for the quantities of interest, e.g. ionization profile versus altitude, $I(h)$.

$$\mathcal{P} = \int_{\infty}^{h} \rho(h')\ dh' \tag{5.9}$$

We can then rewrite any quantity of interest that is a function of altitude as $I(\mathcal{P}(h))$ or $I \circ \mathcal{P}$. By performing operations on $\mathcal{P}$ to produce $\mathcal{P}'$, we can alter the quantity of interest to find the quantity of interest, e.g. I', in the new atmospheric profile through $I \circ \mathcal{P} \rightarrow I \circ \mathcal{P}'$.

This method works since $\mathcal{P}$ is generated with resolution such that the density value is unique at all altitudes and is monotonically increasing with decreasing altitude. A similar atmospheric rescaling method is performed and validated in Xu et al. (2020).

Another effect investigated in this work is the variation of quantities of interest with magnetic inclination, which is a product of magnetic latitude. The magnetic inclination as a function of magnetic latitude λ is described in Chapter 3, and can be used geometrically to find the excess linear distance travelled by an electron $\Delta d/d$ as a function of λ:

$$\frac{\Delta d}{d} = \sec\left(\frac{\pi}{2} - \tan^{-1}(2\tan(\lambda))\right) \tag{5.10}$$

where λ is the magnetic latitude in the tilted dipole model. The function is minimized at the poles where $\lambda = \pi/2$ and the magnetic field is oriented radially outwards, and maximized at the magnetic equator where $\lambda = 0$. Precipitation realistically only occurs at radiation belt latitudes and above, so L = 2 or $\lambda = 45^{\circ}$ is taken as the minimum value in this range to investigate. The nominal

[3] When using CSDA (continuous slowing down approximation) physics mass density is the key parameter. However, when considering rarefied interaction such as bremsstrahlung, the scattering target species is vital, and the atmosphere changes composition in the diffusive region above ∼80 km, so it is important to consider atmospheric mixing fraction.

atmosphere profile and magnetic inclination above PFISR at 65° magnetic latitude is taken as the reference as a mid-point between L = 2 and the poles.

This effect is studied using the same reference atmosphere as the nominal profile generated at $\lambda = 65°$ but by varying the magnetic inclination at $\lambda = 0°$ and $\lambda = 45°$. The results are then rescaled with MSIS atmospheric profiles generated from the those latitudes. Figure 5.11 shows the results of ionization profiles versus altitude from the two test cases. The vast majority of the variation in the quantities of interest from the three magnetic latitudes comes from the variation in atmospheric profile, so we conclude that the effect of the excess path length transited by the electrons is minimal and the effect of a specific atmospheric profile is dominant.

5.3 Green's Function Inversion Methods

In order to translate mono-energetic and mono-pitch angle electron beams, we need a framework to interpret modeled impulse responses from the atmosphere in terms of input, or forcing, distributions of our choice, with the end goal being to both estimates of quantities of interest from a input spectrum and to estimate the input spectrum from a measurement of a quantity of interest. We desire a form that lets us recreate an arbitrarily shaped energy or pitch angle spectrum in f in order to study the effects of realistic precipitating electron spectra on the atmosphere. Specifically, if we use our quantity of interest u to recreate a model output that is measurable, this formulation can be used to invert measurement in an estimate of the original forcing spectrum $f(E, \alpha)$. The observability, or how much information that can be uniquely inverted from u to estimate f, varies depending on the quantity of interest chosen as well as the measurement quality (e.g. SNR, spectral resolution, etc.). The formulation chosen here is the Green's function method (not to be confused with Green's *theorem*), which is a method used to solve a known partial differential equation given boundary conditions.

We describe precipitation as a linear differential process denoted by $\mathcal{L}$ that operates on an input forcing electron spectrum $f(E, \alpha)$ to produce a quantity of interest u. Below, we'll let the

quantity of interest be the photon spectrum $u(\hbar\omega)$ at a given altitude.

$$\mathcal{L}[u(\hbar\omega)] = f(E,\ \alpha) \tag{5.11}$$

We assume that the inverse of $\mathcal{L}$ exists and is also differentiable, and is a reasonably smooth function. By ansatz, we'll claim that $\mathcal{L}^{-1}$ acting on a Dirac delta function $\delta(E - E_0,\ \alpha - \alpha_0)$, for all bounded and finite E_0 and α_0, is equal to our Green's function G:

$$\mathcal{L}\ [G] = \delta \tag{5.12}$$

$$\mathcal{L}^{-1}[\delta(E - E_0,\ \alpha - \alpha_0)] = G(E, E_0, \alpha, \alpha_0) \tag{5.13}$$

where $G(E, E_0, \alpha, \alpha_0)$ constitutes one point of a multi-dimensional response surface to E and α for a chosen quantity of interest. Since we claim that $\mathcal{L}$ is linear, $\mathcal{L}^{-1}$ is therefore also linear, such that we can rearrange combinations of the arguments of Equation 5.13, introducing a function $S(E, \alpha) : \mathbb{R}^2 \to \mathbb{R}^1$ that will be used to weight the contributions from the input tuples (E, α):

$$\begin{aligned} &\mathcal{L}^{-1}\left[\textstyle\int_E \int_\alpha S(E', \alpha')\ \delta(E - E',\ \alpha - \alpha')\ dE'\ d\alpha'\right] \\ &= \textstyle\int_E \int_\alpha S(E', \alpha')\ \mathcal{L}^{-1}\left[\delta(E - E',\ \alpha - \alpha')\right]\ dE'\ d\alpha' \\ &= \textstyle\int_E \int_\alpha S(E', \alpha')\ G(E, E', \alpha, \alpha')\ dE'\ d\alpha' \end{aligned} \tag{5.14}$$

the function $S(E, \alpha)$ is continuous, finite, and abides by the rule of

$$\int_E \int_\alpha S(E', \alpha')\ dE'\ d\alpha' = 1 \tag{5.15}$$

so that multiplication with S will not change the amplitude of another function. This is the most general continuous-space combination of terms that we can show can be used to solve $\mathcal{L}$ for any bounded and finite boundary conditions $f(E, \alpha)$.

However, finding such a function $G(E, E_0, \alpha, \alpha_0)$ that is valid everywhere — over all energies and pitch angles — is intractable. Instead, we will approximate G at discrete input points (E_i, α_j) and rely on the smoothness of G to allow a finite set of delta function evaluations of G to describe the continuous surface in the local vicinity of the evaluation point. The integration over E and α becomes a discrete sum of N and M evaluation points, respectively. Our weighting function S

becomes a matrix of discrete evaluations of the function $S(E_i, \alpha_j)$ to form $S_{ij} \in \mathbb{R}^{N \times M}$ and we can write our integration instead as

$$\sum_{i}^{N} \sum_{j}^{M} S_{ij} \; G(E, E_i, \alpha, \alpha_j) \tag{5.16}$$

where the step size between evaluation points $\Delta E \; \Delta\alpha$ is incorporated into G for simplicity. We now have a framework to describe the Green's function response surface G that we claim is a valid inverse of $\mathcal{L}[f(E, \alpha)]$ near a discrete evaluation point (E_i, α_j). Ultimately, we want to use this surface to describe the relationship between the input or forcing spectrum f and our quantity of interest u. We can form an approximate representation of f by writing the sum:

$$f(E, \alpha) \approx \sum_{i=1}^{N} \sum_{j=1}^{M} S_{ij} \; \delta(E - E_i, \; \alpha - \alpha_j) \tag{5.17}$$

where S_{ij} are now the function evaluations of $f(E, \alpha)$ at the abscissa (E_i, α_j), which in the case of precipitation represents differential electron flux. The two sides become equal in the limit $N, M \; \rightarrow \; \infty$. Finally, from the framework we can now write a representation of our quantity of interest using the Green's functions and weighting matrix:

$$u(\hbar\omega) = \sum_{i=1}^{N} \sum_{j=1}^{M} S_{ij} \; G(E, E_i, \alpha, \alpha_j) \tag{5.18}$$

where u is written as a function of photon energy $\hbar\omega$. The question becomes, how do we approximate G? In this work, we use the Geant4 forward model described in the previous section to evaluate a variety of quantity of interests u at N energies and M pitch angles. Table 5.2 details the quantities of interest recorded or derived from the model outputs, many of which are directly of interest to the atmospheric modeling community or can be used to match to a remote or in-situ measurement for inversion problem estimates of the precipitation spectrum. Figure 5.12 shows a photon spectrum as the quantity of interest $u(\hbar\omega)$ at three different altitudes for a Green's function evaluation of the exponential energy input spectrum $f(E) \propto e^{-E/E_0}$ with folding energy $E_0 = 100$ keV and with an isotropic pitch angle distribution. The "resolution" of this estimation can be measured by the size of the coefficient matrix, i.e. $S_{ij} \in \mathbb{R}^{19 \times 15}$. For more details on how the resolution changes the quality of the Green's function estimates, see Patrick (2022) for X-ray and Xu et al. (2020) for ionization profile quantities of interest.

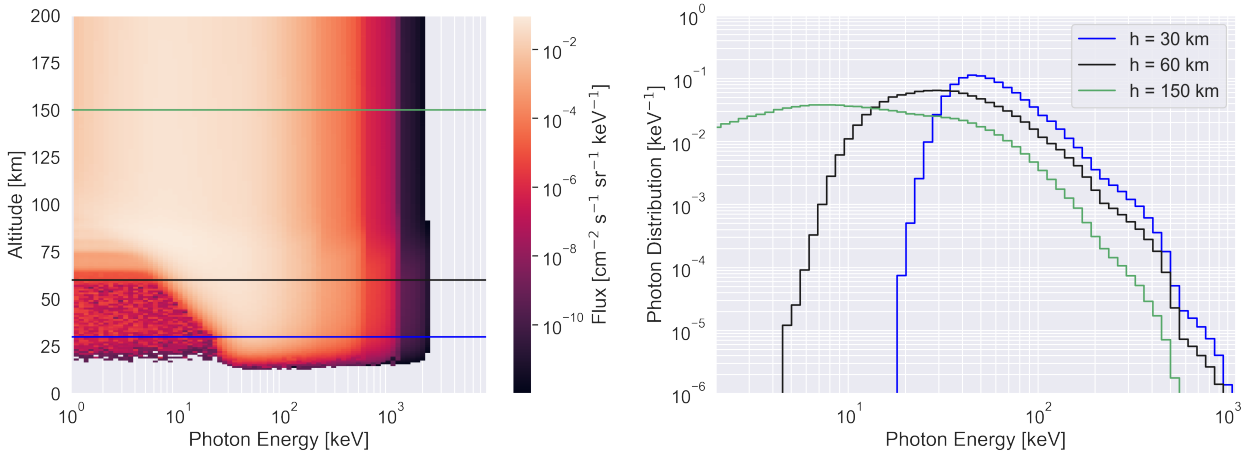

Figure 5.12: (Left) shows the energy-altitude photon number flux spectrum produced by a 10^5 cm^{-2} s^{-1} sr^{-1} keV^{-1} electron flux precipitation event with an exponential energy distribution with folding energy 100 keV. The lines and their colors relate to (right) the plot showing photon spectra at 30, 60, and 150 km altitudes, which are averaged over a 10 km bin size. Note the slope of the high energy tail is similar for each altitude, but the low energy tail differs in flux significantly.

In order to invert a measurement that can be related to model quantities, we must convert from a specific quantity such as instrument counts to a more general, physical quantity such as photon differential flux or column ionization rate. Once this quantity is obtained, it can be directly compared to linear combinations of the Geant4 model output, where the goal is ultimately to find the matrix of coefficients S_{ij} that most closely reproduces a measurement. The $N \times M$ coefficients can be found algorithmically by minimizing a cost function C that relates model output $u(x_k)$ for generalized abscissa x_k to measurement $g(x_k)$:

$$C = \sum_k \left(u(x_k) - g(x_k)\right)^2 = \sum_k \left(\left[\sum_i \sum_j S_{ij}\ G(E, E_i, \alpha, \alpha_j) \right]_k - g(x_k) \right)^2 \tag{5.19}$$

which forms the least squares error function. The problem formulation can then be written simply as

$$S_{ij}^{ML} = \underset{S_{ij}}{\arg\min}\ C \tag{5.20}$$

where S_{ij}^{ML} is the maximum likelihood matrix of coefficients that minimize the cost function C. Since many of these processes relate to rare events acting on non-thermal distributions, the spectral

outputs tend to be an exponential processes, i.e. the high energy component drops off quickly and is small relative to the low energy component. For this reason, we implement a logarithmic cost function that emphasizes the important but smaller magnitude numbers in the high energy tail of, say, a photon distribution:

$$S_{ij}^{ML} = \arg\min_{S_{ij}} \sum_k (\ \log u(\hbar\omega_k) - \log g(\hbar\omega_k)\ )^2 = \arg\min_{S_{ij}} \sum_k \log\left(\frac{u(\hbar\omega_k)}{g(\hbar\omega_k)}\right)^2 \tag{5.21}$$

This inverse method is general in form and is not limited to 1-dimensional quantities. The Limited-memory Broyden–Fletcher–Goldfarb–Shanno (L-BFGS) is a global minimization algorithm that is used to minimize the cost function (Dai, 2002). The algorithm allows for a large number of beams to be run from a personal laptop. A method implemented in the next sections to improve convergence of this algorithm are seeding the initial guesses with physics-based distributions in the local vicinity of the data. The initial proposal solutions are randomly perturbed and this minimization is performed in a Monte Carlo fashion in order to achieve the most likely true global minimum solution, since there is no guarantee of uniqueness in this generalized inversion procedure. The improvement of this inversion method and numerical investigation of uniqueness is left as future work once real data is obtained from the AEPEX mission.

The following section implements the methods described herein to present ionization profiles vs. altitude for realistic electron spectra and invert measurements of model observables towards estimates of electron forcing spectra.

5.4 Model Verification and Validation

We aim to verify that the ionization results are reasonably accurate and ionization profiles vs. altitude are the correct shape, so we compare with previous work, and validate the model results with data. The following section covers these steps: comparison with previous work, inversion with remote photon measurements and in-situ electron spectra, and inversion from in-situ pitch angle-resolved electron spectral measurements.

5.4.1 Comparison with Previous Models

The work of Xu et al. (2020) presents ionization profiles for a range of mono-energy mono-pitch angle beams to which we can compare the Geant4 EPP model results. Additionally, Xu et al. (2020) compares with the work of Fang et al. (2010), which in turn compares to the older work of Roble and Ridley (1987). Figure 5.13 shows the comparison between the Fang and Xu methods, where the difference is slight in ionization profile shape and altitude shift. However, these differences are vital in atmospheric forcing and therefore are an important quantity to refine through higher fidelity modeling (e.g. Thorne, 1980; Mironova et al., 2015; C. Randall et al., 2005, 2006, 2007, 2009).

Ionization profiles that account for electrons that are more energetic than the auroral population (>30 keV) are vital to predicting and interpreting quantities such as NO_x and HO_x production in the mesosphere and stratosphere. Figure 5.14 shows a comparison of the ionization profiles that result from mono-energetic electron beams with this work and Xu et al. (2020). Of note, the latter work does not include bremsstrahlung transport, although the EPMC model does consider the term in the stopping power formulation.

Another key difference between the works of Xu et al. (2020) and Xu, Marshall, and Tobiska (2021) and the work herein are in cross section implementations and particle transport. The entire list of Geant4 cross section implementations are included in Section 5.2, and a full comparison is outside the scope of this work. Instead, the differences are seen in the quantities of interest output by the models. A specific case study is in the EPMC and Geant4 bremsstrahlung implementations, which are detailed in the appendix of Köhn and Ebert (2014). The EPMC model relies on a non-relativistic formulation that is valid in the regime of $\hbar\omega \ll E_e$, i.e. the photon energy is a small fraction of the incident electron energy. Figure 5.15 shows how the difference in the bremsstrahlung and photon transport implementation play out in ionization profile: the altitude of maximum ionization is consistently predicted to be higher from Geant4 versus EPMC, and the magnitude of the secondary ionization peak is predicted to be slightly larger for energies under

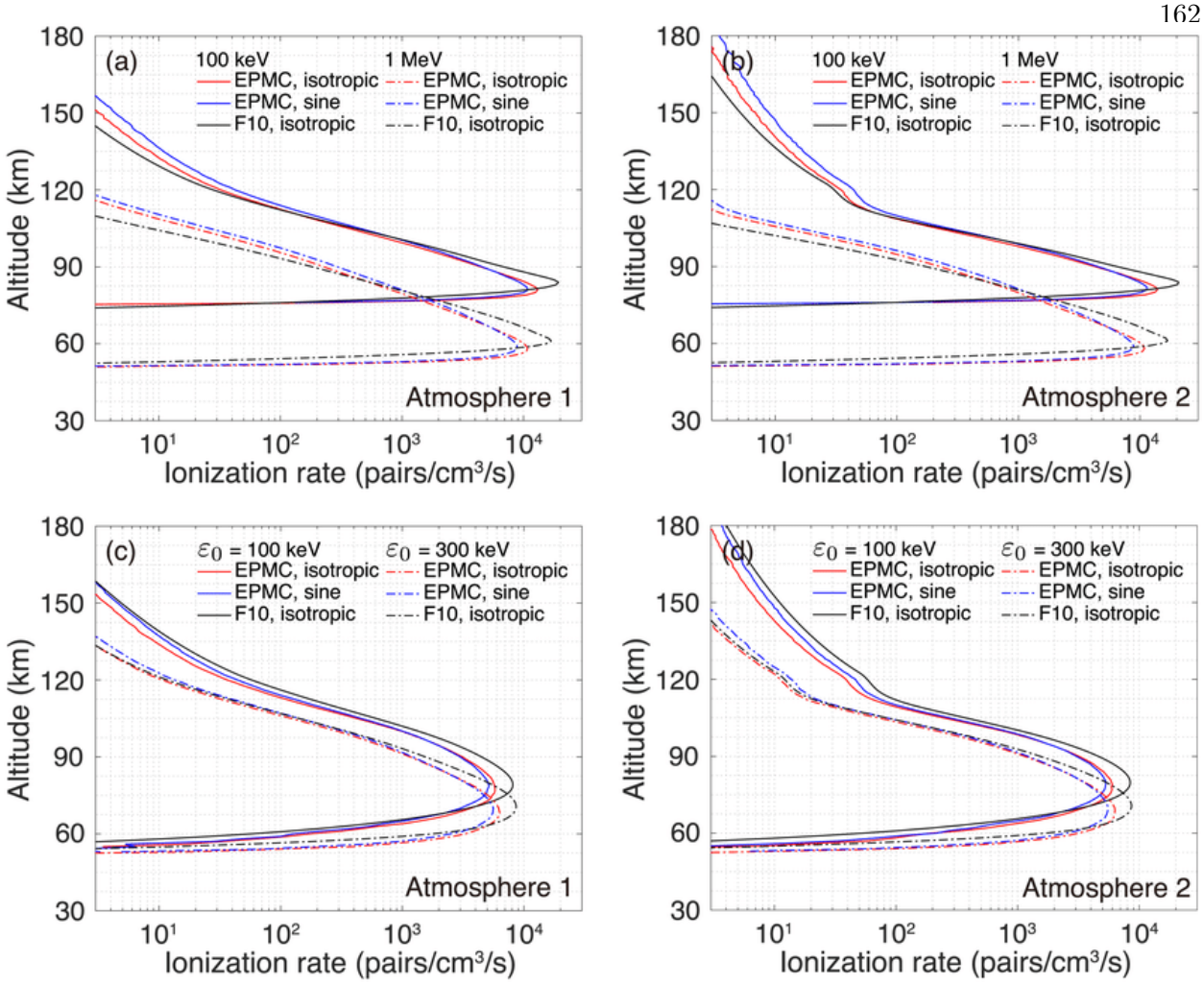

Figure 5.13: Comparison between Fang et al. (2010) and Xu et al. (2020), showing from Xu et al. (2020), showing the differences in the Energetic Particle Monte Carlo (EPMC) code versus the analytical Fang et al. (2010) method. Of note here are the differences that various pitch angle distributions impart on the ionization profile and how the altitude of peak ionization shifts between the two methods.

10 MeV[4] . From Köhn and Ebert (2014), the bremsstrahlung formulation used in EPMC splits the total cross section into two decoupled terms: a differential term in electron and photon energy, and a separate term from J. D. Jackson (2007) that parameterizes the photon angular emission direction, assuming a dipole radiation pattern. However, that angular formulation is classical in that it is intended for slowly moving charges and does not account for the beaming that occurs

[4] The highest electron energies are where the EPMC bremsstrahlung production formulation is most accurate, but where the directional sampling suffers due to the method of separation ansatz used in the EPMC implementation, discussed shortly after this footnote.

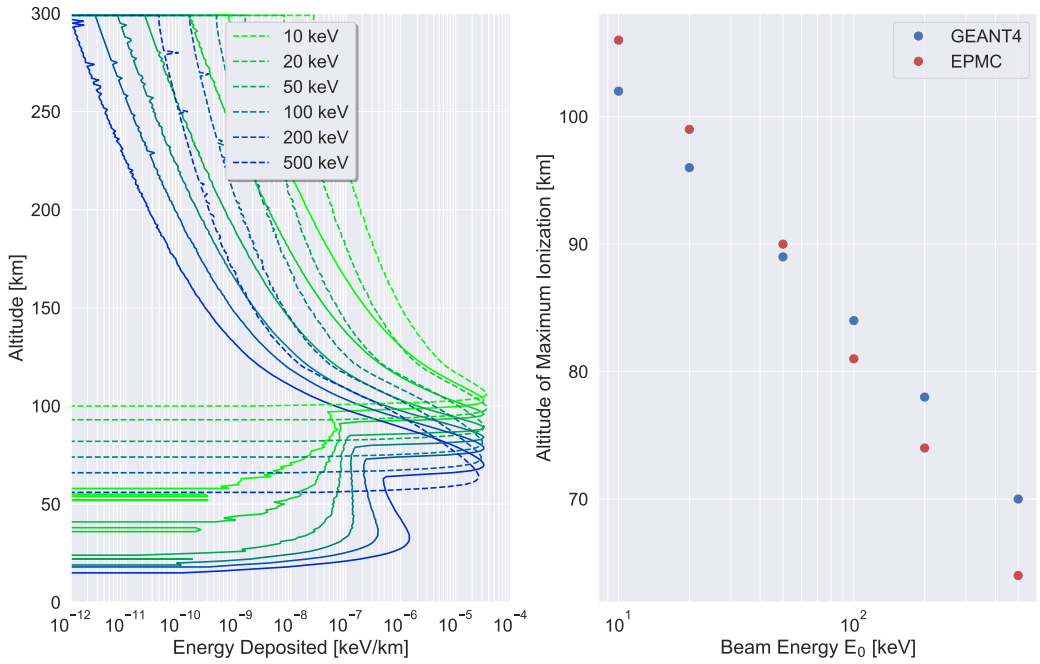

Figure 5.14: (Left) Comparison of ionization profile vs. altitude between the EPMC model (dashed lines) from Xu et al. (2020) and Geant4 (solid lines). Of note, photon transport is not included in the EPMC model, but the stopping power effects of bremsstrahlung are. (Right) Altitude of peak ionization vs. mono-energetic beam energy, showing agreement at energies of 50 keV – 100 keV, but disagreement at lower and higher beam energies.

for relativistic electron energies. This has important implications for backscattered photon signals estimated from EPMC that are resolved by Berland, Marshall, and Capannolo (2023).

5.4.2 X-ray Production in the Stratosphere with BARREL Data

X-ray production is a consequence of energetic electron interactions with neutral atmospheric particles, specifically, the bremsstrahlung interaction between a free, high energy electron and the atomic nucleus. Due to correlations between the photon and electron spectra, X-rays can be used as proxy measurements for EPP. The purpose of this study is to compare measurements of X-ray production in the stratosphere when in-situ "truth" data of the precipitating electron spectra is available. The Geant4 model results and inversion method can be used in order to validate both

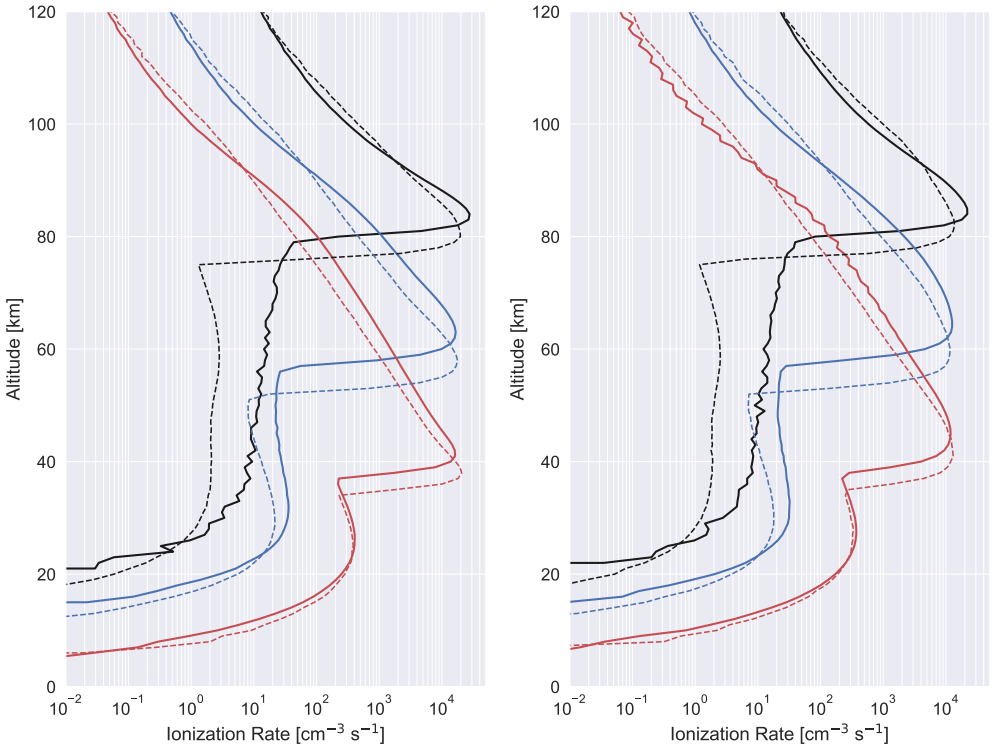

Figure 5.15: Comparison of ionization profiles produced by the Green's function method using the Geant4 forward model (solid lines) with those published in Xu et al. (2021) (dashed lines) that include the secondary ionization peak produced from bremsstrahlung photon transport to lower altitudes. The electron beam eneriges are 100 keV, 1 MeV, and 10 MeV for the black, blue, and red lines, respectively.

the X-ray production and transport processes, as well as the Green's function inversion method detailed in Section 5.3. This case study uses X-ray spectra measured from within the atmosphere by the BARREL mission and in-situ electron data from the FIREBIRD-II CubeSat mission during microburst precipitation.

The Balloon Array for RBSP Relatvistic Electron Losses (BARREL) mission was a series of balloon launches at high latitudes, from both Antarctica and Sweden, that aimed to quantify precipitation losses from the radiation belts by measuring X-rays generated in the atmosphere (Millan et al., 2013). The balloons flew in the stratosphere between 30 – 40 km altitude at latitudes that map to high L-shells, and many of these flights were chosen so that they flew in magnetic conjunction with the Van Allen Probes mission (a.k.a the Radiation Belt Storm Probes mission

or RBSP) (Fox & Burch, 2014). A series of these campaigns were flown from 2013 to 2014, with additional one-off campaigns flown after that.

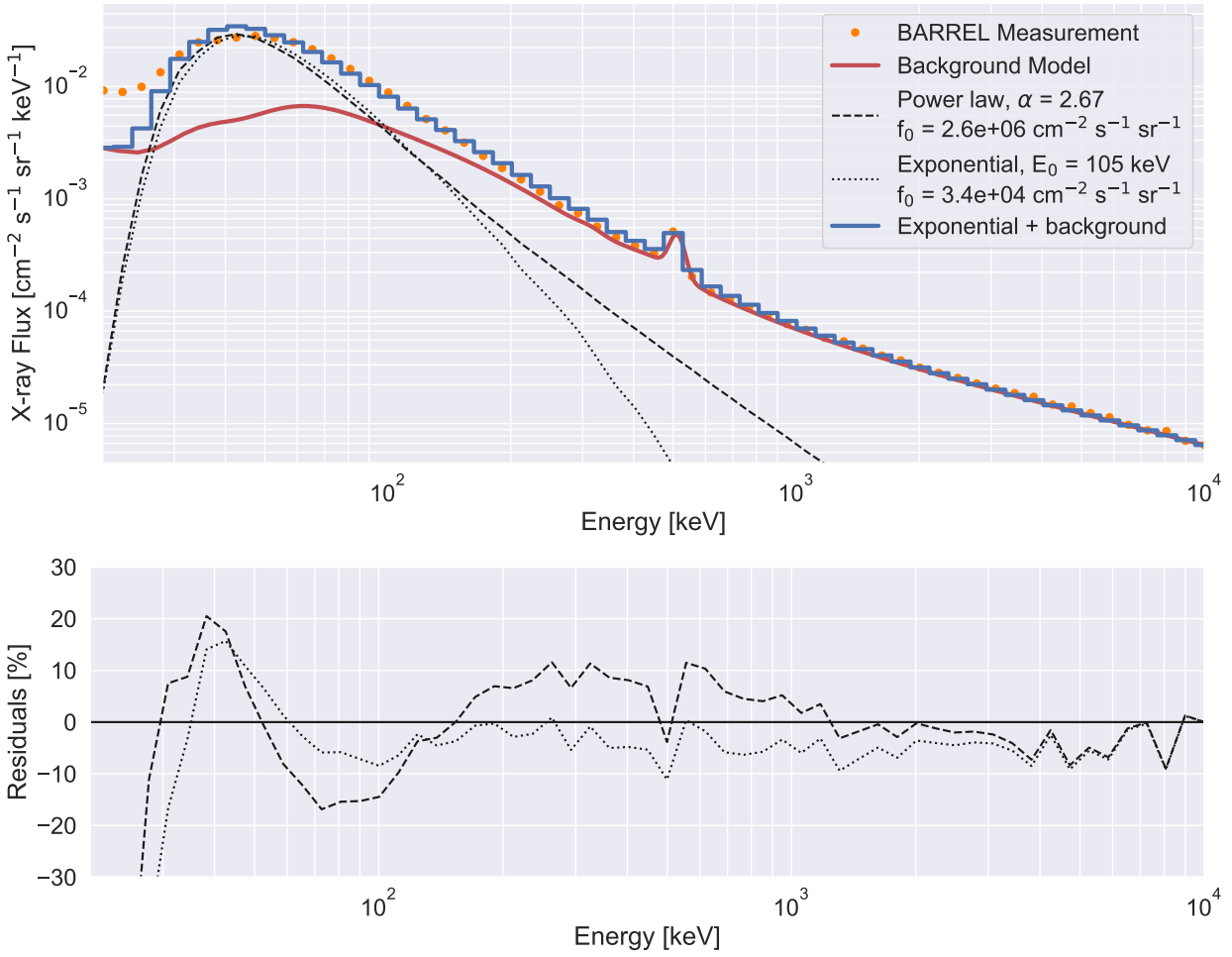

Figure 5.16: (Top) BARREL instrument counts per energy bin are shown as orange dots, above the background noise model which is shown as a solid red line. The black dashed and dotted lines correspond to the X-ray spectra generated by a power law and exponential precipitating electron spectra, respectively. The blue step plot indicates the X-ray spectra generated from an exponential energy electron spectrum added to the background model, which includes the 511 keV annihilation line peak. (Bottom) The residuals between the Geant4 X-ray spectrum and background model versus the BARREL measurements, showing that, within the fitting region of 30 keV – 10 MeV, the residuals are less than 20%.

The BARREL payload instruments include NaI (sodium iodide) scintillators, which operate on the principle of converting X-ray to optical photons, which are then recorded with photodiodes or photomultipliers. The BARREL instruments have 256 energy channels ranging from 20 keV –

10 MeV energies that sampled at a fast time cadence (50 ms exposures) to study the behavior of microburst precipitation, an impulsive form of precipitation that is characterized by hard electron spectra (X.-J. Zhang et al., 2022; Seppälä et al., 2018; Shumko et al., 2018).

In order to convert between instrument counts and a physical unit like photon flux, the geometric factor and instrument response must be well-characterized. The BARREL spectrum is estimated by dividing the differential count rate per energy channel by the geometric factor of 860 cm^2 sr (McCarthy, personal communication, 2023) and adjusting for the energy-dependent detection efficiency of NaI (Akkurt, Gunoglu, & Arda, 2014). The geometric factor is also energy-dependent since at high photon energies the sides of the detector housing becomes transparent, which is difficult to account for in the effective geometric factor. These regions are outside of the fitting energies, so this effect does not contribute substantially to the inversion process.

Figure 5.16 shows the raw count rate per channel (adjusted by the geometric factor to match the order of magnitude of the photon flux estimate), the estimated photon flux spectrum, and the Green's function reconstruction estimate from the Geant4 profiles. A background model (red line) shows the average X-ray and particle background at the altitude of BARREL during the measurements. The components of the background model are described in Berland, Marshall, and Capannolo (2023). A Savitzky-Golay filter is also applied to the X-ray data in order to smooth the jaggedness of the high energy tail of the spectrum since the noise is likely due to the nature of low photon detection data among atmospheric and instrument noise (Press & Teukolsky, 1990). The residuals of the X-ray to inversion fit are less than 20% for the power law and exponential input electron spectra.

The one-dimensional cost function detailed in Section 5.3 is implemented that takes as inputs the BARREL X-ray spectral measurement and the modeled proposed spectrum. A proposed distribution is entered as the initial guess to the global minimization algorithm and then perturbed point-wise with a randomly generated Gaussian variable with variance proportional to the value at the spectral point. In this way, the global optimization algorithm is used in a Monte Carlo sense and the minimum value of those cost function evaluations is taken as the maximum likelihood

X-ray spectrum. The pitch angle dimension of the input spectral beams is averaged to represent an isotropic pitch angle distribution, as the pitch angle distribution from an X-ray spectrum measured within the atmosphere is unobservable. The Green's function coefficients can then be used to generate the maximum likelihood precipitating electron spectrum, which can be compared with in-situ "truth" data.

Figure 5.17 shows the range of fits that are deemed optimal with respect to the log-least squares cost function. The optimal range of parameters are shown: energy-integrated fluxes f_0 and spectral parameters, and spectral index α for the power law and folding energy E_0 for the exponential distribution. This inversion is non-unique, likely because of the lack of measurement above the background in the high-energy tail of the X-ray distribution where these two electron energy distributions vary significantly.

The source of in-situ electron data is the Focused Investigations of Relativistic Electron Bursts: Intensity, Range and Dynamics II (FIREBIRD-II) CubeSat mission, which is a pair of two 1.5 U NSF-funded spacecraft that aimed to quantify various aspects of microburst precipitation. These spacecraft launched January, 2015 and operated for approximately 5 years. This mission orbited at 632 km by 433 km with an inclination of 99° (Crew et al., 2016). The payload onboard each of these spacecraft is a pair of electron detectors with coincident field-of-views.

This work describes a reanalysis of data used in the study of Anderson et al. (2017) and is published in Berland, Marshall, and Capannolo (2023). This study involves remote X-ray spectral measurements from BARREL while the FIREBIRD spacecraft, measuring in-situ electron spectra, were in magnetic conjunction with the footpoint of the field line in the vicinity of BARREL. The FIREBIRD spacecraft each carried two electron detectors: the first is the "surface detector" with a nearly 2π field-of-view, and the second is the "collimated detector" with a 45° field-of-view. The geometric factors as a function of energy from Johnson et al. (2020) are applied to the raw data in order to convert from instrument counts to differential electron flux. The electron spectra over the time duration when FIREBIRD was in the vicinity of the magnetic conjugate region are shown in Figure 5.17 averaged in time. Figure 5.17 also shows the Geant4 inversion estimate of the electron

spectrum that generated the BARREL-observed photon spectrum.

5.4.3 Atmospherically Backscattered Electron Analysis with ELFIN Data

An important data product that the EPP model outputs is backscattered electron energy-pitch angle spectra. For a given initial condition, the coupled energy-pitch angle distribution is recorded at 500 km and can be inverted using a similar error minimization method as performed in the previous section. The difference here is that the inversion quantity is two-dimensional, so the fitting method is now a surface instead of one-dimensional curve.

Backscattered electrons come from two populations: primary reflected electrons that were initially in the loss cone, and secondary electrons which are generated in the upper atmosphere and their stochastic momentum direction is in the zenith direction. Both of these electron populations primarily enter the anti-loss cone, although some can rejoin the trapped population at higher pitch angles, if they scatter above 100 km. To a LEO spacecraft, these two populations may be indistinguishable, as their spectra are similar. The exact energetic fraction that is backscattered has important implications for radiation belt modeling, magnetosphere-ionosphere coupling, and electron lifetime calculations (R. S. Selesnick, Looper, & Albert, 2004; R. Marshall & Bortnik, 2018; Khazanov et al., 2018).

For this study, in-situ electron data is desired in order to quantify both the precipitating and backscattered electron populations. We would like to validate the modeled electron backscatter, and provide a framework for generating atmospheric ionization profiles from LEO energetic electron data. The CubeSat selected is the Electron Loss and Fields Investigation with a Spatio-Temporal Ambiguity-Resolving (ELFIN-STAR, or ELFIN) mission, which are a pair of CubeSats that spin with solid state detectors to resolve electron pitch angle (Angelopoulos et al., 2020). ELFIN spins with a 3 second period to quickly resolve the entire pitch angle distribution between 50 keV and 5 MeV, which sufficiently covers the radiation belt electron energy range. The spectrum measured is denoted as $f(E, \alpha)$ which is in differential units of $\mathrm{cm}^{-2}\ \mathrm{s}^{-1}\ \mathrm{sr}^{-1}\ \mathrm{MeV}^{-1}$. ELFIN orbits at 450 km in a polar orbit that precesses sufficiently to achieve coverage in MLT. The events selected

for this study are specific electromagnetic ion cyclotron (EMIC) wave-driven events.

Precipitation from EMIC wave-driven events preferentially scatter ∼MeV energy electrons into the loss cone, and EMIC events are also associated with proton precipitation at lower latitudes (L. Blum, Remya, Denton, & Schiller, 2020; Carson, Rodger, & Clilverd, 2013; Capannolo, Li, Ma, Chen, et al., 2019; Capannolo, Li, Ma, Shen, et al., 2019). EMIC wave events cataloged in Capannolo et al. (under review 2023) are selected for this study. This catalog contains event data that are selected and calibrated to remove the effects of instrument error (e.g. low channel counts, high background rates).

Figure 5.18 shows the 2D spectra of the differential pitch angle-energy flux $f(E, \alpha)$ averaged over the EMIC event duration for two discrete events, and (bottom row) for 144 events averaged together. The loss cone at 450 km and ELFIN's angular resolution is between $0° - 66°$; the anti-loss cone is between $114° - 180°$; and the trapped population lies within the angles between the loss cone and anti-loss cone populations. These boundaries are denoted with dashed lines in the rightmost panels, with the trapped region in the middle. Also shown in Figure 5.18 are 1D integrations in both energy and pitch angle space to show the pitch angle distribution per energy bin and energy spectra per pitch angle bin, respectively. The characteristic MeV-enhancement on top of an exponential distribution is shown, as well as power law-like distributions.

In order to validate the model and inversion method, two analysis methods are performed: the first involves inverting the backscattered electron spectra to obtain an estimate of the precipitating population. From there, the precipitating spectrum estimate is compared with the "truth" spectrum that is directly measured by ELFIN. The second method involves direct forward modeling of the measured loss cone population through the atmosphere to obtain the model estimate of the backscattered spectrum. Now, this backscattered estimate can be compared with the measured spectrum in the anti-loss cone pitch angle range. The fit to the backscatter data and residuals are shown in Figure 5.20, and these methods are explained pictorially in Figure 5.19.

A cost function $C : \mathbb{R}^2 \to \mathbb{R}^1$ that maps the the 2D data $f(E, \alpha)$ to a one dimensional score is implemented in order to minimize the fit residuals of the proposal surface. In this case, the variation

in the energy dimension is much greater than the variation in pitch angle dimension, where the energy can vary by a factor of 10^3 whereas the pitch will vary by perhaps 10^1. A logarithmic transform is performed on the data in order to capture the variation in energy in the fitted surface, as the generated ionization profile is much more sensitive to the gradient in the energy dimension of Green's coefficient matrix than the gradient in the pitch angle dimension. The cost function then is

$$C = \sum_n \sum_m \Big(\log f(E_n, \alpha_m) - \log \tilde{f}(E_n, \alpha_m) \Big)^2 \tag{5.22}$$

$$= \sum_n \sum_m \left(\log f(E_n, \alpha_m) - \log \left[\sum_i \sum_j S_{ij} \; G(E, E_i, \alpha, \alpha_j) \right]_{n,m} \right)^2 \tag{5.23}$$

where $\tilde{f}(E, \alpha)$ is the reconstructed surface generated from the Green's function matrix S_{ij}. Figure 5.21 shows the ionization profiles generated from applying methods 1 and 2 to the data from Figure 5.18. The ionization profiles generated from the two methods overwhelmingly agree in shape and magnitude; only small adjustments are made in order to match the two methods. These adjustments are studied as a proxy for the backscattered model results and inversion method below.

It is found that the pitch angle distribution does not strongly affect the ionization profile or the backscatter population, so although the backscattered electron population is important, it is not strongly observable relative to the electron energy spectrum. We would like to formally quantify this effect, so we define the following statistic R that measures the Geant4 model and inversion method performance.

We start by integrating the differential flux spectrum to obtain the total input energy flux into the atmosphere, T, on the top boundary of the model:

$$T = \int_\Omega \int_E f(E, \alpha) \; E \; dE \; d\Omega \tag{5.24}$$

where Ω is the solid angle of the loss cone, i.e. $d\Omega = 2\pi \; \sin(\alpha) \; d\alpha$ for α between 0 and α_{LC} and rotated 2π in gyrophase:

$$T = 2\pi \int_0^{\alpha_{LC}} \int_E f(E, \alpha) \; E \; \sin(\alpha) \; dE \; d\alpha \tag{5.25}$$

The ELFIN processed data $f(E, \alpha)$ is numerically integrated with the respective pitch angle bin and energy channel sizes in order to obtain energy flux at the top boundary in units of eV cm^{-2} s^{-1}. This quantity should match the model output

$$\tilde{T} = 35 \text{ eV cm/pair} \cdot \int I_{model}(h)\ dh \tag{5.26}$$

which is the total column integrated ionization rate multiplied by the ionization efficiency to return the energy flux. We can form a ratio between these two quantities R that represents the deviation between the measured or inverted initial conditions and the model result:

$$R = \frac{\tilde{T}}{T_i} \tag{5.27}$$

where the denominator index i refers to the loss cone and anti-loss cone energy fluxes. Figure 5.22 shows the R statistic plotted for eight EMIC events alongside the loss cone and anti-loss cone to trapped ratios. When the R statistic has a value of unity, the inversion correctly estimates the total energy flux input into the atmosphere. The worst-case R statistic is 0.1, which is still within an order of magnitude of the correct flux estimated from data. A full statistical study of the model performance with the 144 EMIC events from the catalog published in Capannolo et al. (under review 2023), as well as precipitation during other wave-driven events, is the topic of future work.

The results of the inter-model comparison and the two data analysis studies both verify and validate the Geant4 model results and inversion methods. This modeling effort can now be applied more widely to other observations of EPP in order to study atmospheric effects from precipitation. Further, this work supports the future AEPEX mission data and inversion procedure that aims to answer the science question, “how much energy is input into the upper atmosphere through radiation belt EPP?”

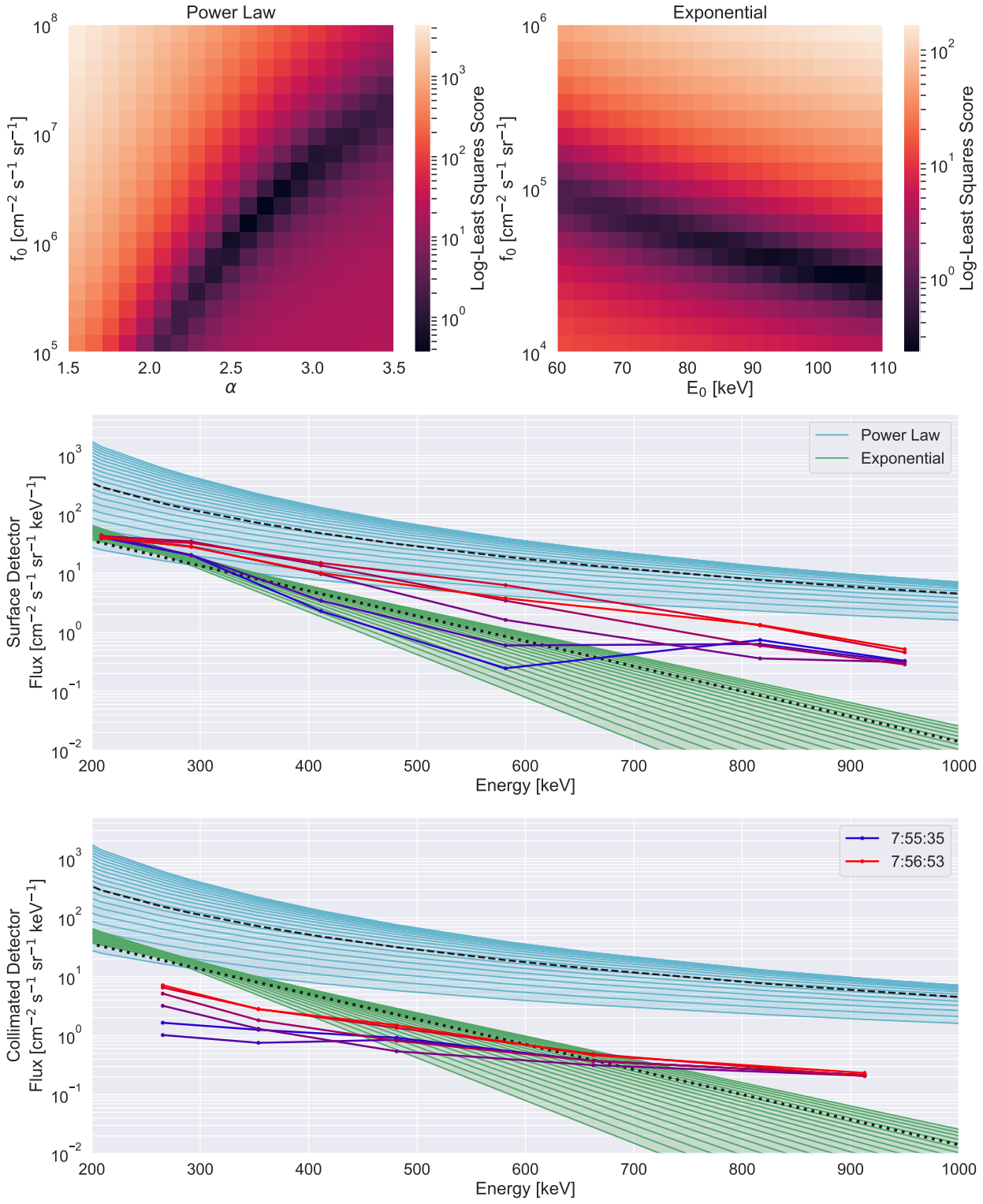

Figure 5.17: (Top) The log-least squares cost function evaluation score for the parameter space of (α, f_0) and (E_0, f_0) for power law and exponential energy distributions, respectively. The regime of minima indicate equally likely inversion spectra estimates. (Bottom) In-situ electron measurements from the FIREBIRD 180°-FOV surface detector electron spectra and 45°-FOV collimated detector electron spectra during the approximate conjunction between FIREBIRD and BARREL, where earlier spectra are in blue and progress to red, and the spectra are averaged over 13 seconds windows. The cyan region shows the regime of viable electron power law distributions and the green shows viable exponential energy distributions.

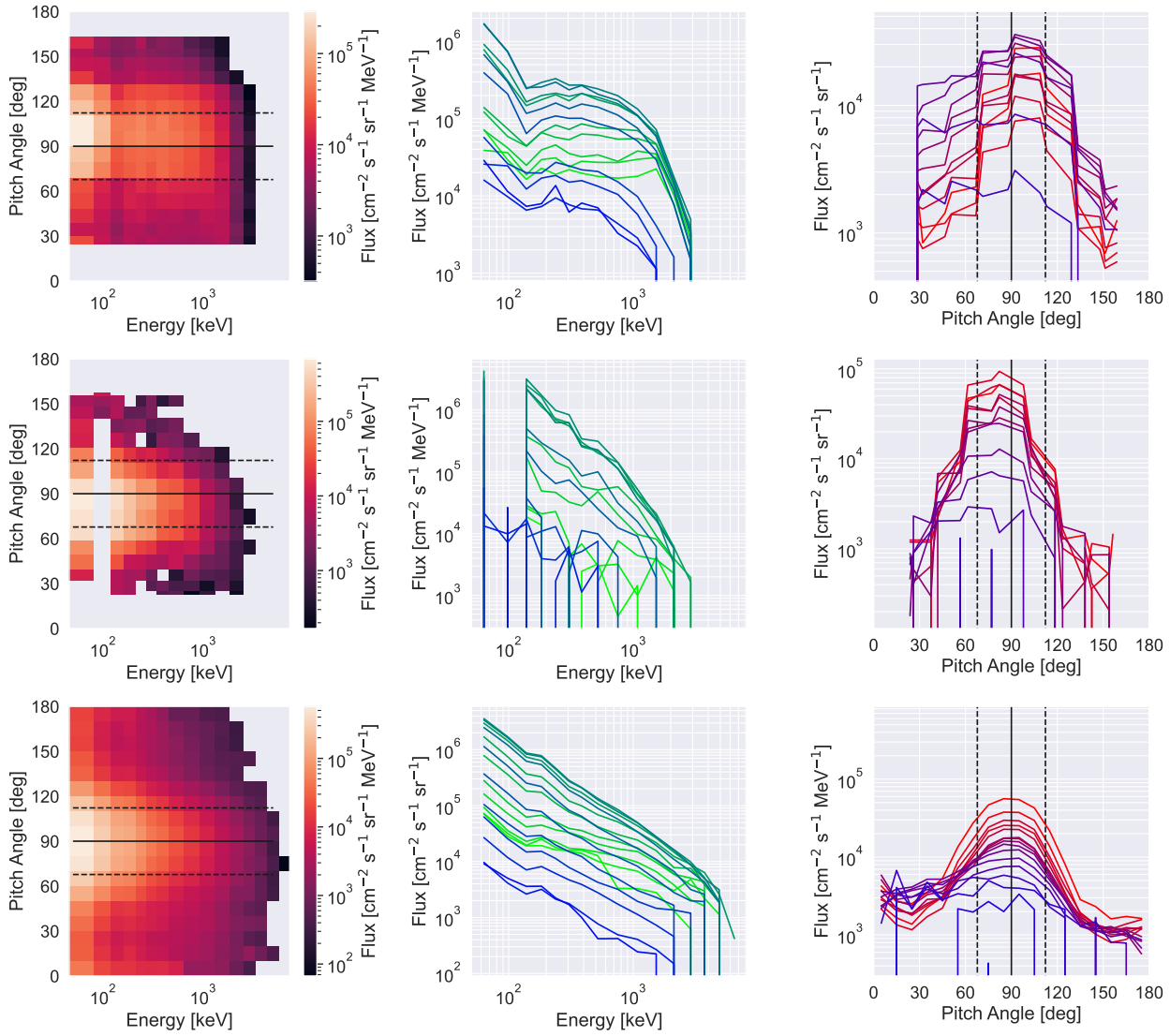

Figure 5.18: ELFIN data is shown from: (top row) ELFIN-a on 2020-10-06/23:51 UT, (middle row) ELFIN-a on 2020-12-13/14:16 UT, and (bottom row) ELFIN data averaged over 144 events during EMIC wave-driven precipitation. (N.B. the top and middle panels correspond to events 2 and 5, respectively, in Figure 5.22) The left column is the 2-D electron energy-pitch angle coupled spectrum, the middle column is integrated per pitch angle bin to show energy spectra, and the right column is integrated over energy bin to show pitch angle distribution.

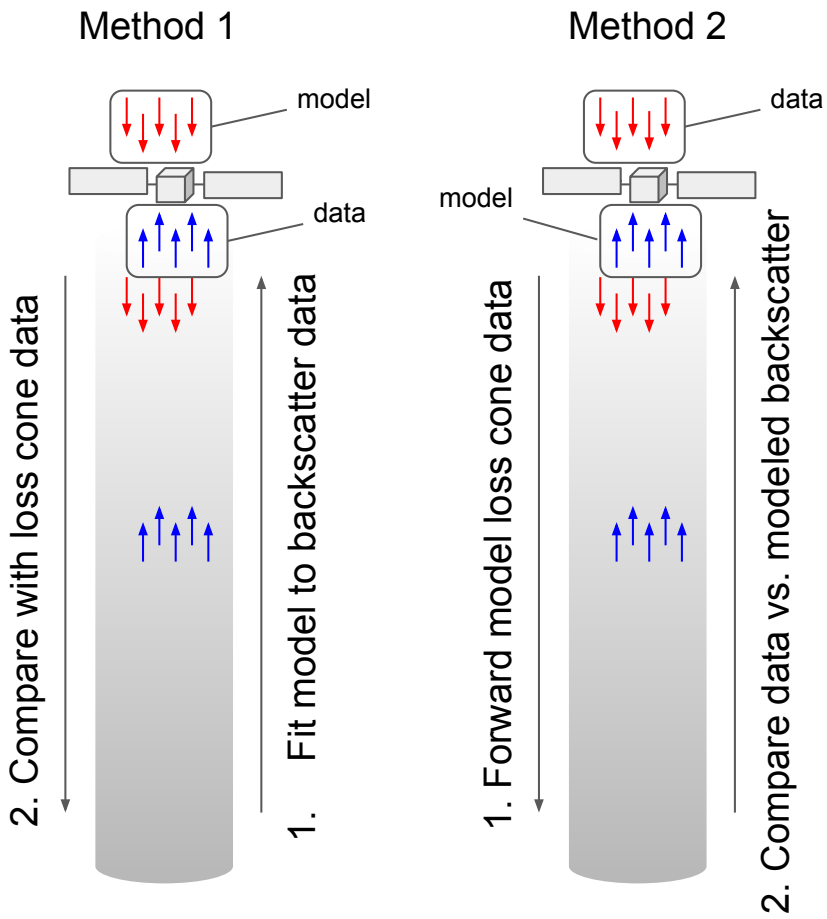

Figure 5.19: Diagram explaining the data inversion methods used to analyze ELFIN data. Method 1 uses as initial condition the backscattered electron flux and generates the precipitation spectrum for comparison with data, and method 2 uses the loss cone data as an initial condition for the model and produces backscattered electron flux for comparison.

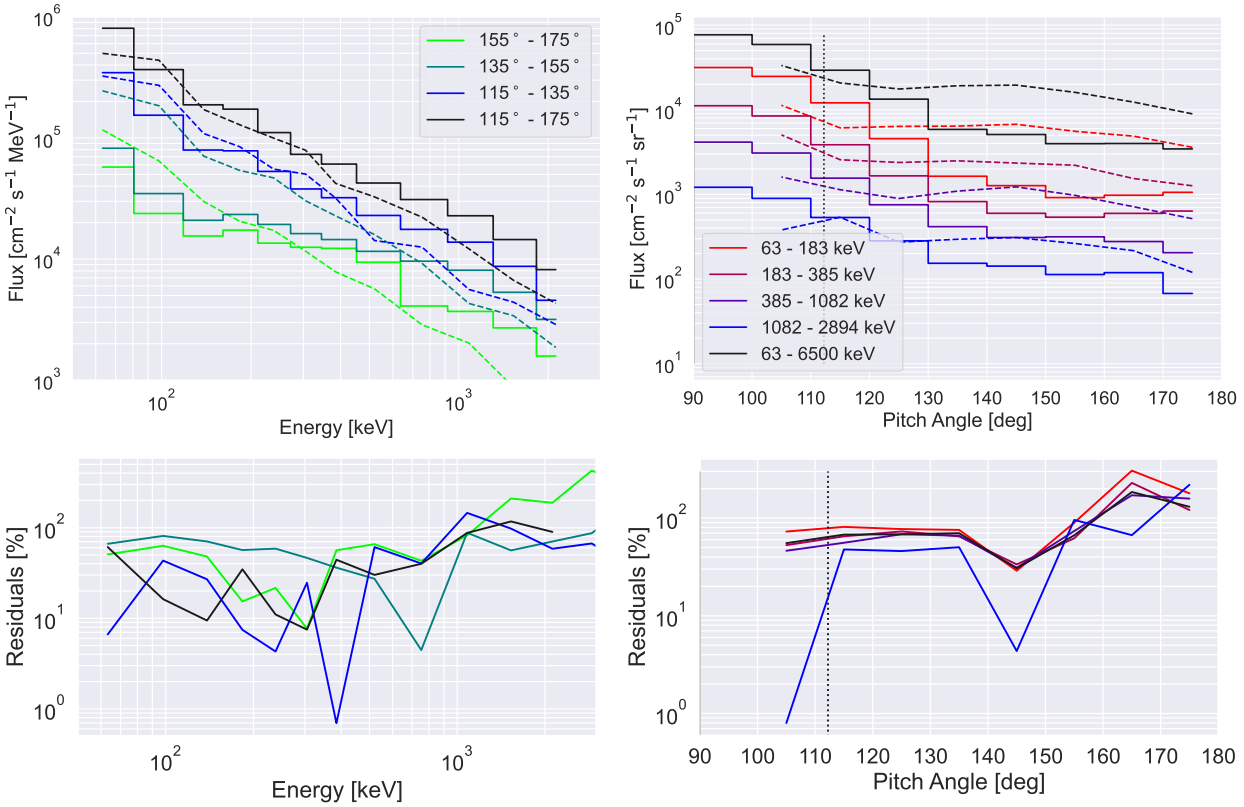

Figure 5.20: The top row shows the anti-loss cone portion of the 144 event-averaged ELFIN data from Figure 5.18 (solid lines) and a 2D surface fit (dashed lines) to the data, where the left plot is an integration of the 2D data over pitch angle to show the energy spectra and the right plot is an integration over the energy dimension to show pitch angle distributions. The various series in the left plot are using 20° bin sizes and the black line is the integral over the entire pitch angle dimension. Similarly, the right plot shows varying energy bin size and the black line is the integral over the entire energy range. The bottom row of plots show the residuals between the data and the surface fit per data series.

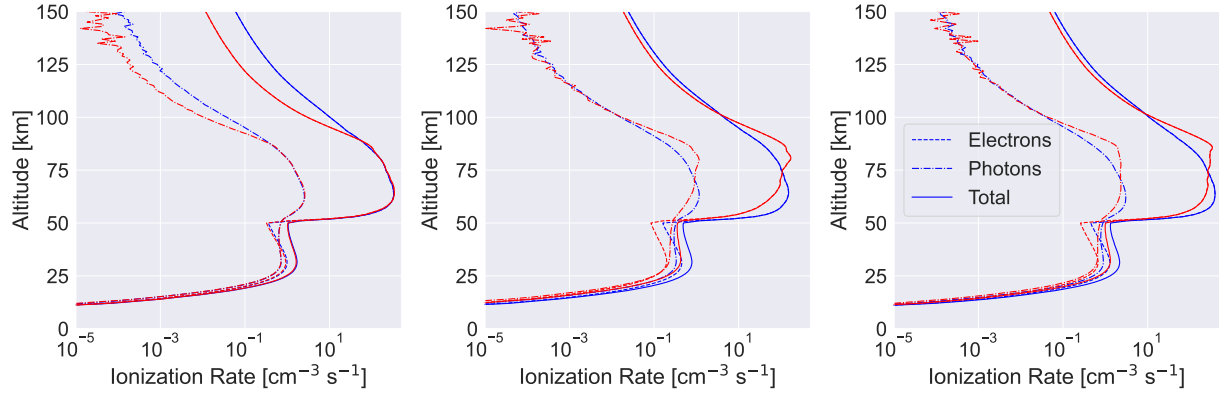

Figure 5.21: Ionization profiles inverted from ELFIN electron-pitch angle spectral measurements, using methods 1 and 2. The left plot here corresponds to the top row in Figure 5.18, the middle to the middle, and right panel to the bottom row.

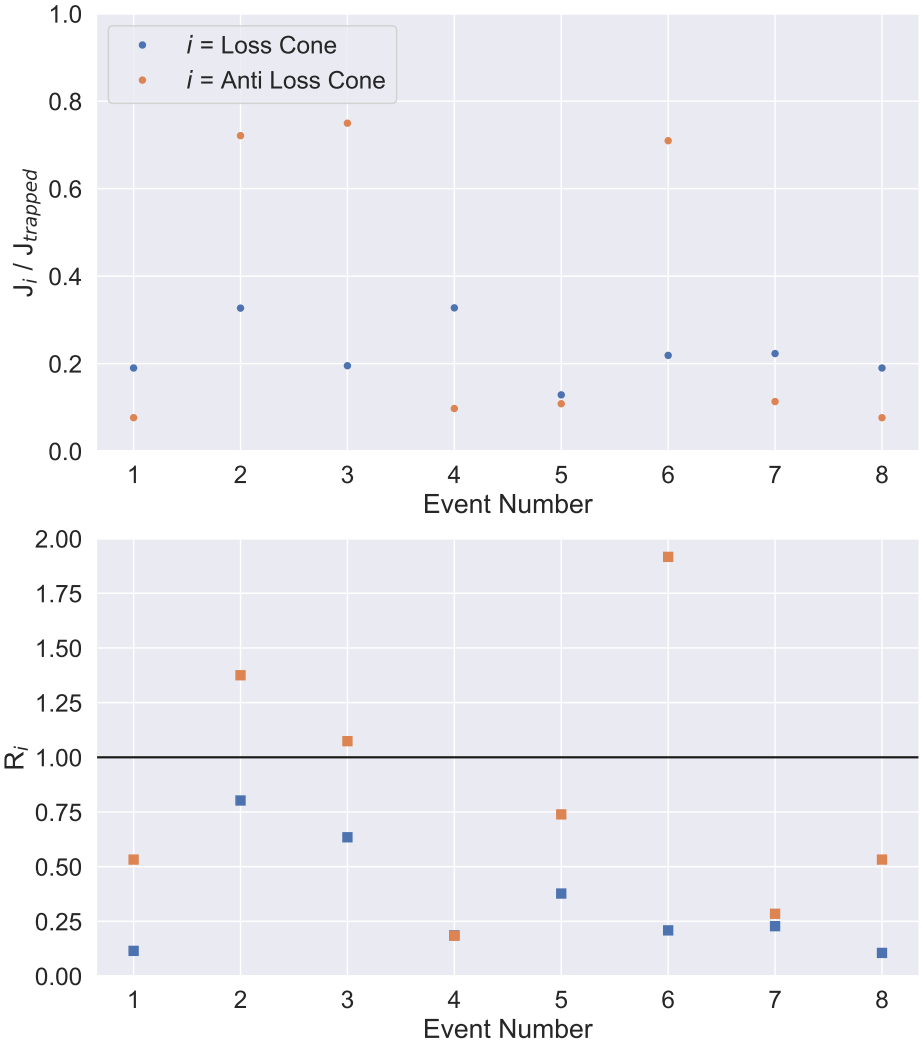

Figure 5.22: (Top) The loss cone-to-trapped (blue) and anti-loss cone-to-trapped (orange) ratios for the 8 ELFIN events studied in Berland, Marshall, and Capannolo (2023). (Bottom) The R-statistic for inversion performance for 8 EMIC wave-driven precipitation cases, with unity (exact reproduction) denote with a line.

Chapter 6

Energetic Particle Precipitation at Jupiter

The search for universal processes in magnetospheric physics takes us to Jupiter. By expanding beyond Earth, we can highlight the importance of studying processes that are unique to Earth's magnetosphere versus processes that occur at all magnetized bodies in the universe. Is the protection from charged particles and radiation at ground level that Earth's magnetosphere and ionosphere have provided a universal property of magnetospheres?

For the loss process of energetic particle precipitation at Jupiter, the open questions are similar to those at Earth: what is the contribution to atmospheric energy input by EPP versus solar inputs? How do acceleration processes in the magnetosphere affect magnetospheric plasma populations and atmospheric constituents seasonally and climatologically? In this chapter, an EPP model at Jupiter is described along with simulation results using that model, and X-ray signal characteristics are calculated and discussed as they pertain to the Comprehensive Observations of Magnetospheric Particles Acceleration, Sources, and Sinks (COMPASS) concept study for a future Jupiter-orbiting space mission.

6.1 Introduction to EPP at Jupiter

In contrast to Earth, where the dominant source of charged particles is the solar wind and ionospheric outflow, the primary source of plasma at Jupiter is from Io's volcanic emissions. These emissions are comprised mostly of SO_2 molecules, which are ejected from the surface of the moon and escape its rarefied atmosphere, where they disassociate into sulfur and oxygen atoms (Mekler

& Eviatar, 1980). These atoms are then ionized into their constituent nuclei and electron(s) by solar photons via photoionization, and by radiation belt electrons via impact ionization (Cheng, 1982). Through impact ionization, the high energy electrons of Jupiter's radiation belt can ionize atoms more than once, creating high charge state sulfur and oxygen ions, e.g. to $q = +9$, i.e. nine unbound electrons are produced per atom (Clark, Mauk, Paranicas, Kollmann, & Smith, 2016) and highly-charged positive ions such as O^{8+} (XX etc). Once singly or multiply ionized, the charged particles are subject to electromagnetic forces from the magnetosphere and are accelerated by a combination of radial diffusion, plasma wave interactions, and electric field-aligned systems and currents (Birmingham, Hess, Northrop, Baxter, & Lojko, 1974; D. N. Baker & Goertz, 1976; Gurnett, Kurth, & Scarf, 1979; B. H. Mauk et al., 2020).

A balance of magnetic and centrifugal forces form the Io plasma torus at a distance of approximately 6 R_j (Jupiter radii $R_J \approx$ 70,000 km $\approx$ 10 R_{Earth}), and an interchange instability occurs that causes turbulence and wave generation that links the Io plasma torus to the resistive auroral regions of Jupiter's atmosphere through Alfvén plasma waves, thereby closing Jupiter's magnetospheric current system (Shemansky, 1980; Siscoe et al., 1981; Sulaiman et al., 2020).

The effects of wave acceleration in the Jovian magnetosphere system are enhanced by the strong magnetic field (the magnetic dipole moment is approximately 10,000 times stronger than Earth's), which causes electrons to routinely reach 10s – 100s MeV kinetic energies and ions to reach GeV/nucleon kinetic energies (Scarf, 1976; Saur et al., 2018; Elliott et al., 2018), at least an order of magnitude more energetic than Earth's radiation belts. Since the magnetosphere of Jupiter is so large (100s $R_J \approx$ 1000s R_{Earth}), and due to the distance from the sun, the magnetopause remains far beyond the outer boundary of the radiation belts; thus, charged particles are not sufficiently lost outside the system via magnetopause shadowing, and therefore the dominant loss mechanisms are through precipitation to the atmosphere and charged particle collisions with the moons (Simpson & McKibben, 1976; Horanyi et al., 1988; Bell & Armstrong, 1986).

Both of these loss processes affect both the plasma population and the target of their collisions. EPP at Jupiter results in photon emissions that range from infrared wavelengths, driven by

collisional and Joule heating of the atmosphere, to X-ray and gamma-ray wavelengths, where high energy processes including bremsstrahlung generate both characteristic and continuous emissions.

6.2 X-ray Sources at Jupiter

By observing X-rays generated from energetic processes at Jupiter, it is possible to remotely study Jupiter's magnetosphere, precipitation processes, and other aspects of planetary science such as moon composition. Figure 6.1 shows a variety of X-ray science targets at Jupiter, including auroral X-rays, diffuse emissions from inverse Compton scattering, and particle induced X-ray emissions (PIXE) from Jupiter's moons.

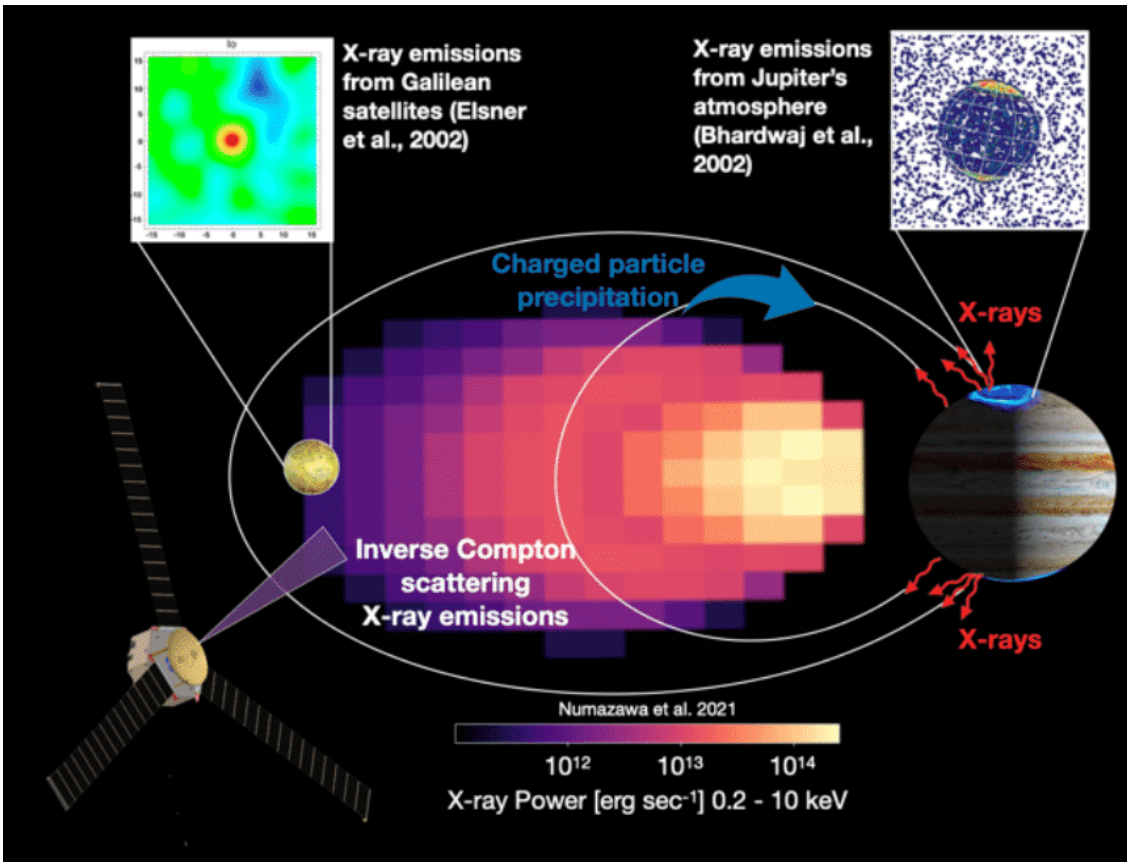

Figure 6.1: Sources of X-ray emission from the Jovian system, showing X-ray emissions from charged particle collisions with moons, inverse Compton scattering from solar optical photons energized by Jupiter's ultra-relativistic electrons, and auroral X-rays from electron and heavy ion precipitation Figure from Clark et al. (2023).

Another important emission that is common at Jupiter is heavy ion charge exchange. The charge exchange collision is the process in which a high energy ion transits in the vicinity of a neutral atom and an electron is transferred from the neutral to the ion, either neutralizing the ion or lowering the ion's charge state (Rapp & Francis, 1962). The excess energy from the captured electron once it reaches its ground state in its specific electron shell is released as an X-ray photon. For heavy ions in Jupiter's magnetosphere, namely highly ionized oxygen and sulfur, charge exchange occurs with neutral constituent both in Jupiter's upper atmosphere and in the Io plasma torus. The characteristic emissions are in the 100s eV – 2 keV range and are specific to the species and charge state transition of the ion (Cravens et al., 1995). Charge exchange spectroscopy can be used as a plasma diagnostic to probe the extent of EPP and magnetospheric loss that is occurring from the ion portion of the population (Isler, 1994). Additionally, if the ion is a singly ionized species, such as a proton, then after charge exchange the ion can become an energetic neutral atom (ENA) (Gruntman, 1997). Observations of ENAs can also be used a plasma diagnostic, e.g. to study charge exchange and ionization in Europa's neutral gas torus (B. Mauk, Mitchell, Krimigis, Roelof, & Paranicas, 2003).

In addition to charged particle losses to the atmosphere, charged particles can be lost via collisions with the Galilean moons of Jupiter, which orbit within the Jovian magnetosphere. Charged particle collisions with moons can be used to probe the surface composition of Jupiter's moons through the spectrum of their bremsstrahlung and particle-induced X-ray emissions (PIXE) (e.g. R. Elsner et al., 2005; Nulsen et al., 2020), which has spectral characteristic unique to the materials in the moons' regolith.

A diffuse X-ray emission is generated from the radiation belts themselves. This emission is unlike the synchrotron radio emission from the ultra-relativisitic electrons in Jupiter's strong magnetic field; the X-ray generation mechanism arises from photon interactions with high energy electrons. This process is known as inverse Compton scattering, which occurs when Compton collisions between ultra-relativistic electrons (10s MeV) and low energy photons ($\sim$eV) accelerate the photons to X-ray energies (Jones, 1968). This process causes a diffuse X-ray emission from the

vicinity of Jupiter, a few R_J to either side within the ecliptic plane, corresponding to the inner part of the electron radiation belt (Ezoe et al., 2010; Numazawa et al., 2021b). This process does not occur at Earth due to the lower electron energies present, but is well-studied in extra-galactic magnetized objects such as active galactic nuclei and around pulsars (Moskalenko & Strong, 2000).

The science target for comparison between Earth and Jupiter relevant to this work is EPP. There are many acceleration mechanisms shared between the two systems and some unique to Jupiter. For instance, at Jupiter, strong, quasi-static electric fields accelerate charged particles up to MeV energies, which subsequently precipitate into the atmosphere. At Earth, on the other hand, auroral electrons are rarely accelerated above 30 keV (Clark et al., 2020; Østgaard et al., 2001). A large variety of X-ray observations of electron and heavy ion precipitation have been made of Jupiter (e.g. Branduardi-Raymont et al., 2004; R. F. Elsner et al., 2005; Branduardi-Raymont et al., 2008; Dunn et al., 2017)) arguably more than at Earth, so a study of Jovian X-rays can shed light on the process of X-ray production at Earth. A study by Mori et al. (2022) performs an inversion between remote X-ray observations of electron bremsstrahlung with in-situ measurements of charged particle spectra with an atmospheric forward model, similarly to the studies performed in Chapter 5 of this work.

Figure 6.2 shows a background-subtracted X-ray lightcurve from a Jupiter observation by XMM-Newton when the Juno spacecraft was 110 R_J away from Jupiter. The lightcurve is shifted in time to account for the speed-of-light transit time, and the electron and proton fluxes are shown as time series. This figure shows that electron and proton flux enhancement at higher energies and X-ray power from Jupiter are temporally correlated, even at the farthest reaches of Jupiter's magnetosphere. The power is calculated using a similar formulation to Branduardi-Raymont et al. (2008):

$$P = \int_{E_1}^{E_2} 2\pi \ (4.4 \text{ AU})^2 \ f(E) \ dE \tag{6.1}$$

where $f(E)$ is the differential X-ray flux observed between energies E_1 and E_2 at 4.4 AU, which is the Jupiter-Earth distance at the time of this observation. These studies show that X-ray

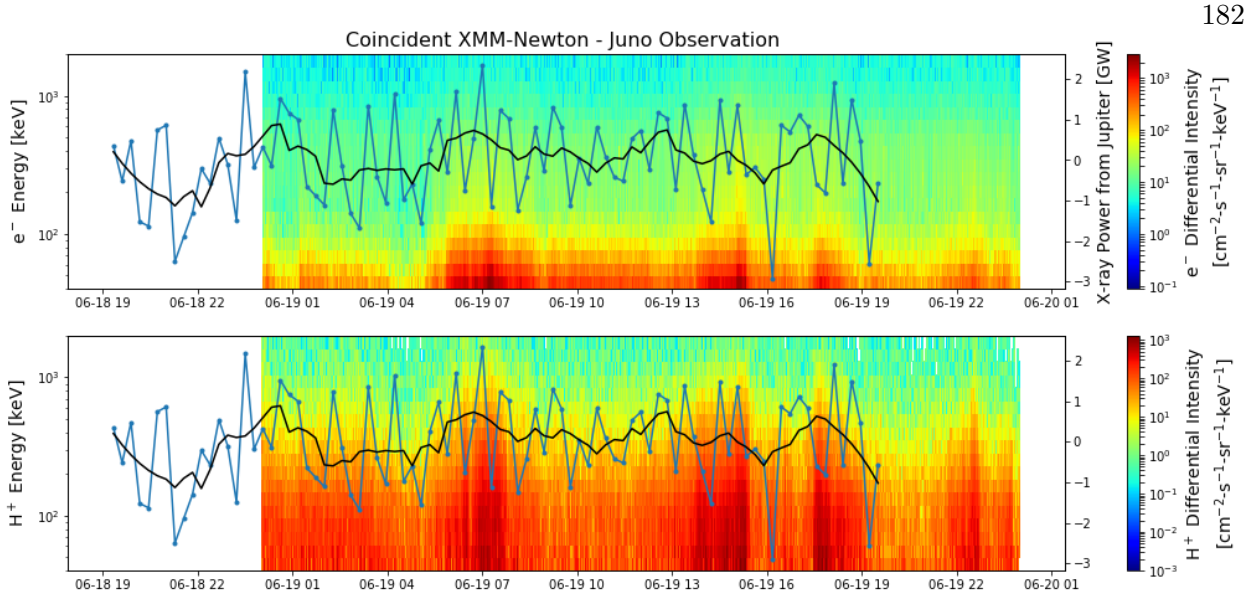

Figure 6.2: (Black line) XMM-Newton X-ray Observatory background-subtracted and smoothed X-ray lightcurve (smoothed from the instrument counts shown in blue), converted to power in the X-ray band from Jupiter and shifted to account for the Jupiter-Earth transit time overplotted with Juno electron and proton differential intensity. Note the correlation in charged particle flux enhancement with X-ray power.

observations can be a powerful diagnostic tool to remotely probe the magnetospheric acceleration and loss processes occurring of Jupiter. In Section 6.3, the EPP model described in Chapter 5 is modified to be used at Jupiter in order to study Jovian X-ray emissions from EPP.

6.3 EPP Model Extension to Jupiter

The EPP model described in Chapter 5 is comprised of the GEANT4 framework, which serves as the physics solver and geometry handler, combined with an atmospheric model and a magnetic field model. In order to adapt the usage of this model for Jovian precipitation, atmospheric and magnetic field intensity models are chosen that describe the Jovian environment. The energy range of electrons at Jupiter is encompassed by the simulation physics list chosen for terrestrial precipitation electron energies. Additionally, the energy range of initial conditions, including parameterizations of characteristic energies from spectral distributions, is increased to correspond with the higher-energy electrons at Jupiter. Figure 6.3 shows the difference in the atmospheric

density profile versus altitude at Earth and Jupiter. Note that the loss cone definition is based on the altitude at which the atmospheric density has increased to the point where electrons are more likely to precipitate than to escape, although in Chapter 5 we show that that definition does not account for energy and pitch angle dependencies. The atmospheric mass density at 100 km at Earth is reached at ∼350 km above the one bar pressure surface at Jupiter, implying the loss cone altitude should be calculated at this altitude at Jupiter.

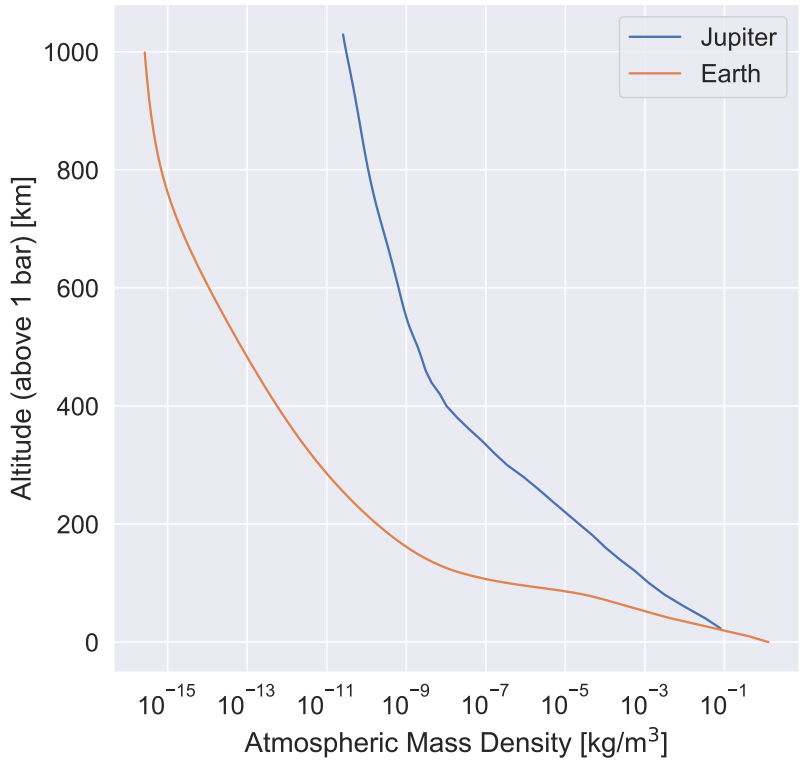

Figure 6.3: Comparative atmospheric density profiles between Earth and Jupiter, showing a "knee" in the profiles where the rate of change of mass density with decreasing altitude increases sharply at approximately 100 km at Earth and 400 km at Jupiter. Of note, the major constituents in the most dense part of the atmosphere at Earth are oxygen and nitrogen versus Jupiter where its hydrogen and helium.

The Jovian atmosphere model chosen is based on Galileo spacecraft probe measurements as it descended into Jupiter's atmosphere (Seiff et al., 1996, 1998). Figure 6.4 shows the atmospheric state and composition of Jupiter's atmosphere from 0 to 1000 km altitude, where the altitude is referenced to the one bar pressure level. The atmospheric scattering targets for EPP are determined

by the atmospheric composition: Jupiter's upper atmosphere is comprised of approximately 90% molecular hydrogen (H_2) and 10% helium, as well as small percentages of ammonia, sulfur, methane, and other trace solar elements (Lindal et al., 1981; Atreya, Mahaffy, Niemann, Wong, & Owen, 2003).

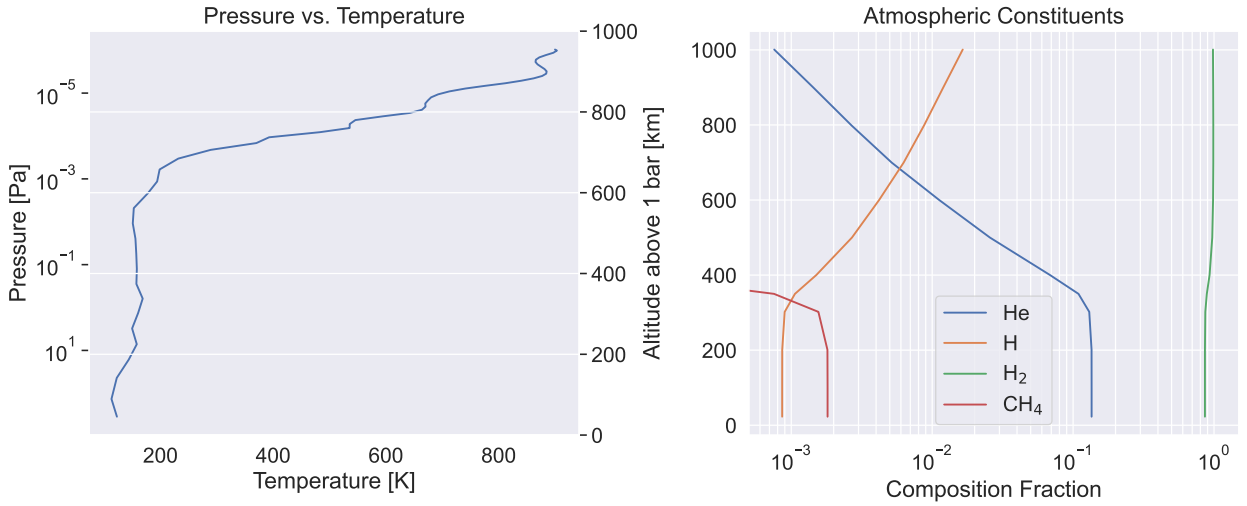

Figure 6.4: Jovian atmospheric state and composition model from Galileo probe in-situ data detailed in Seiff et al. (1996). The constituents in the upper atmosphere are primarily hydrogen and helium gas, and atomic hydrogen. Methane gas and other organics become more prominent below 400 km near the cloud-tops of Jupiter.

The magnetic field model chosen is the VIP4/VIPAL model from S. Hess, Bonfond, Zarka, and Grodent (2011) and is plotted for Jovian surface values in Figure 6.6. This field model primarily characterizes the more complicated magnetic field structure away from Jupiter's surface shown in Figure 6.5 and is similar to a dipole model near the Jovian surface. The electron energy range and distribution characteristic energies are selected from B. H. Mauk et al. (2017). Maxwellian energy distributions of the form

$$f(E) = \frac{1}{E_0^2}\, E\, e^{-E/E_0} \tag{6.2}$$

and monoenergetic beams are simulated through the Jovian atmosphere. Electrons with this form of Maxwellian distribution can be randomly generated to obtain a sample E_s drawn from the distribution described by the characteristic energy E_0 by inverting the cumulative distribution

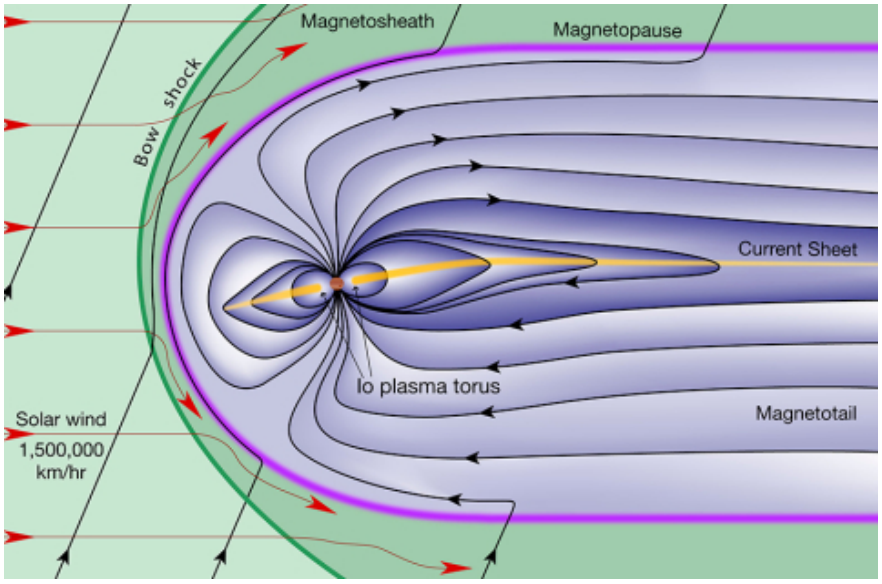

Figure 6.5: Illustration of the Jovian magnetosphere model, showing the solar wind interacting with the bow shock, Io plasma torus, and stretched magnetic field-lines trailing the planet. Figure made by Fran Bagenal and Steve Bartlett.

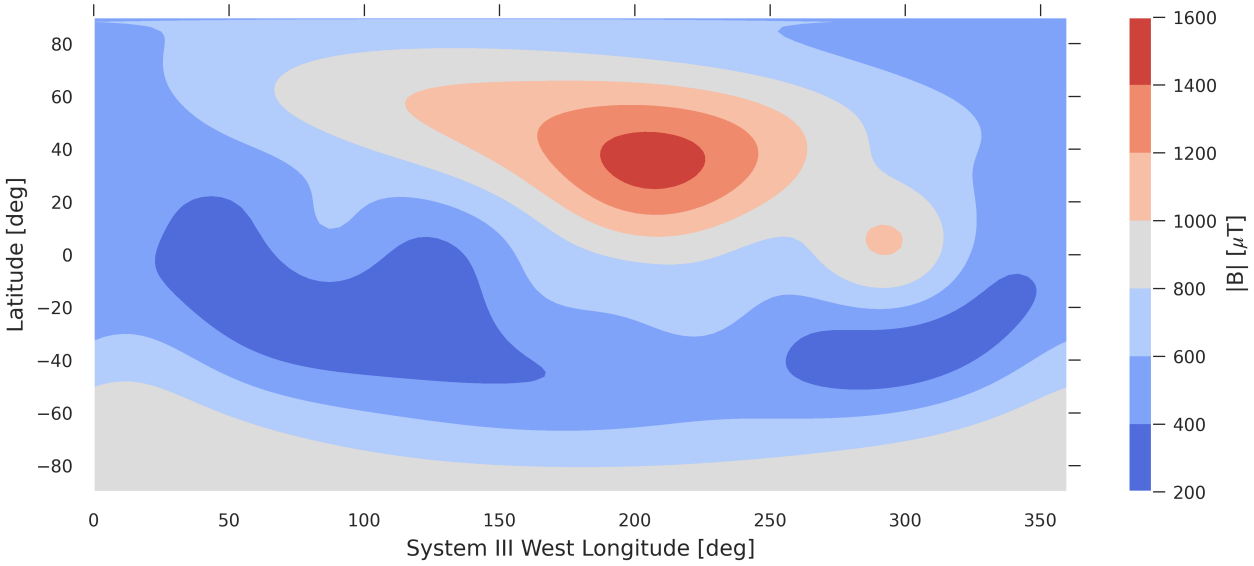

Figure 6.6: Surface magnetic field intensity in System III coordinates from S. Hess et al. (2011), showing the "Great Blue Spot" of weaker magnetic field strength where Jovian disk photon emission from precipitation are enhanced.

function $F(E)$:

$$F(E) = 1 - (1 + E/E_0)e^{-E/E_0} \tag{6.3}$$

and drawing the sample

$$E_s = \mathbb{R}\left[-E_0\left(1 + W_{-1}(U\ e^{-1})\right)\right] \tag{6.4}$$

where W_{-1} is the -1 branch of the Lambert-W function, U is a random number drawn from a uniform random distribution between $[0, 1]$, and $\mathbb{R}$ is the real operator (Corless, Gonnet, Hare, Jeffrey, & Knuth, 1996).

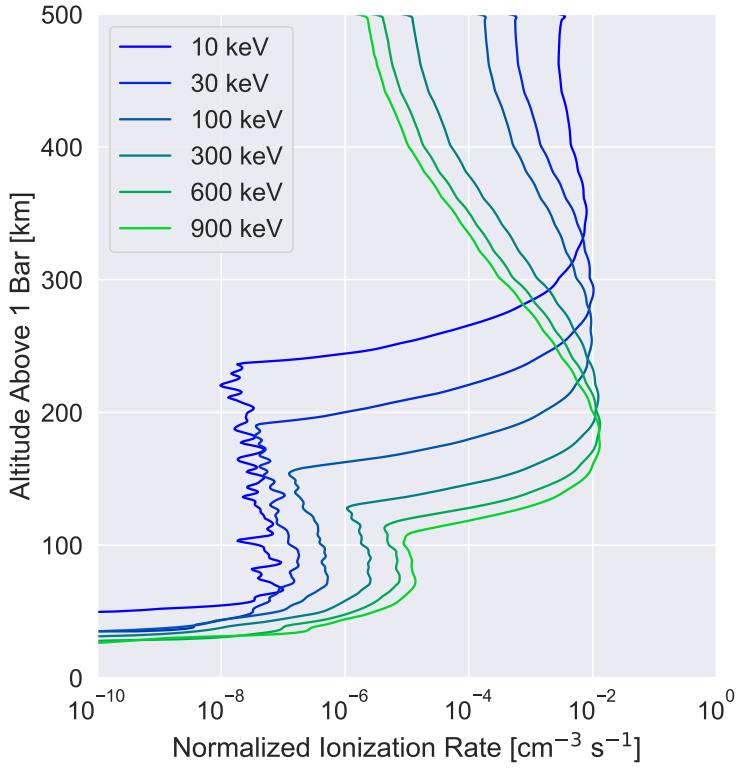

Figure 6.7: Normalized ionization rate profiles generated from exponential energy, sine pitch angle distribution, electron inputs. The profiles are normalized such that each ionization rate profile integrates to unity.

With these input distributions, the modified Geant4 Jupiter precipitation is run and we extract ionization rate profiles versus altitude, X-ray spectra and emission rates, etc. for the purpose of studying EPP at Jupiter. An example of ionization rate profiles are shown in Figure 6.7 over a range of folding energies spanning 10 keV – 0.9 MeV. The X-ray spectra that result from simulating exponential electron energy distributions for characteristic energies within the range of 10 keV to 500 keV are shown in Figure 6.8. A comparison between the X-ray spectra generated

from exponential and Maxwellian distributions energy electron distributions is shown in Figure 6.9.

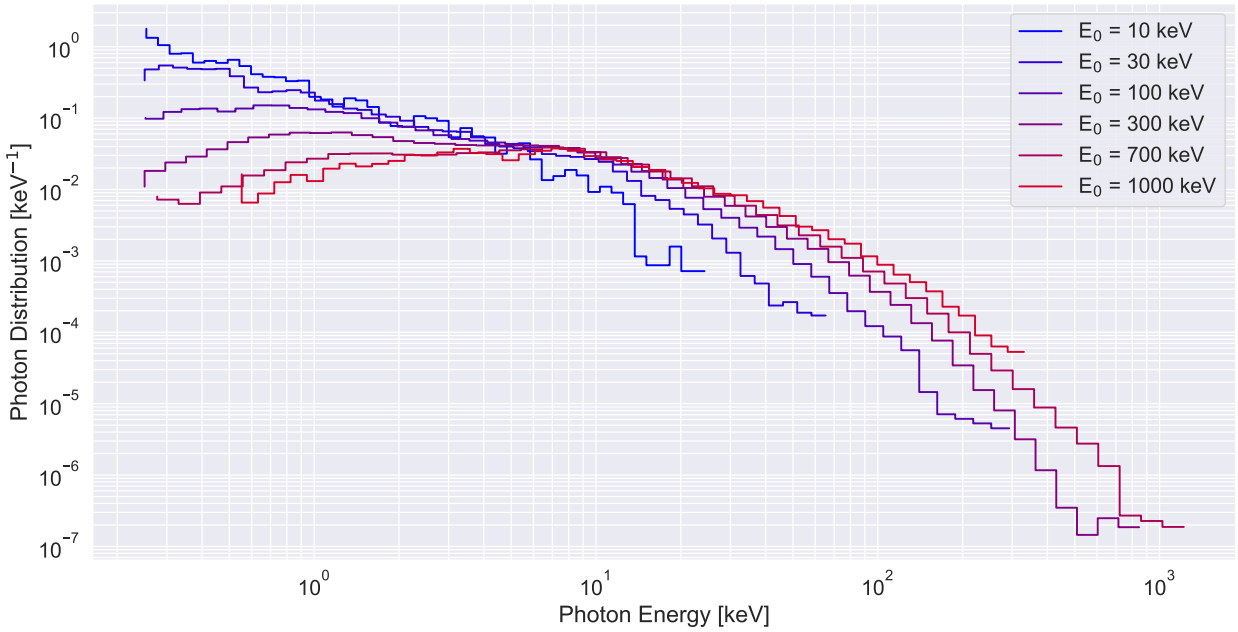

Figure 6.8: Geant4 modeling results of normalized bremsstrahlung X-ray spectra that escapes Jupiter's atmosphere from energetic electron precipitation, varying the input electron spectra characteristic energy for an exponential energy, sine pitch angle distribution. Note the "knee" energy of ∼6 keV where the spectra pivot about as the input electron energy increases.

This model does not consider the characteristic emission from heavy ion charge exchange that dominate the X-ray signal below 2 keV; the simulation of these emissions is usually performed by separate models that simulate hot, collisional plasmas. In Figure 6.8 the X-ray spectra are normalized to integrate to unity, and there are a variety of interesting identifiable features. The energy of peak flux, or "pivot point" at lower precipitating electron energies of the X-ray distribution is at ∼6 keV, almost exactly a factor of 10 lower than that of Earth's, which occurs at 60 keV. This energy is a function of the atmospheric composition, and thus the difference is due to the fact that Earth's atmosphere is primarily nitrogen and oxygen ($Z_{Earth} = 7 - 8$) while Jupiter's atmosphere is primarily hydrogen and helium ($Z_{Jupiter} = 1 - 2$). Thus we find that $(Z_{Earth}/Z_{Jupiter})^2 \approx 10$, and we know that the bremsstrahlung spectral dependence is proportional to Z^2.

The total bremsstrahlung efficiency is calculated in Figure 6.10, showing the efficiency (brems-

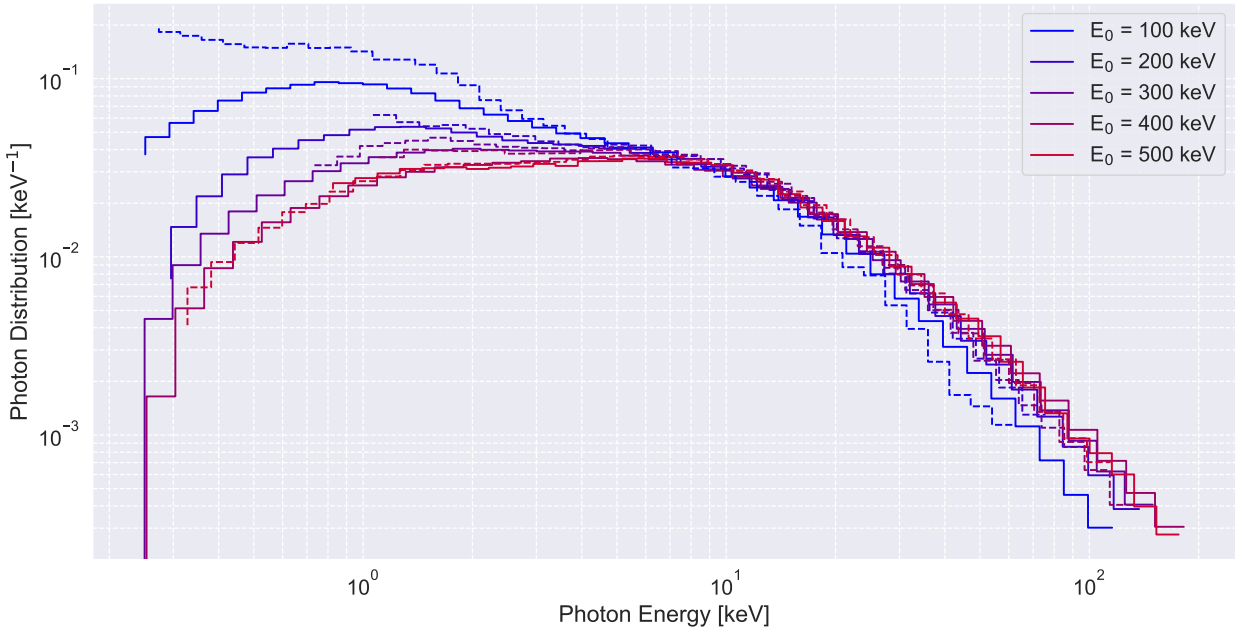

Figure 6.9: Comparison of the X-ray spectra that escapes Jupiter's atmosphere and generated from exponential (dashed lines) and Maxwellian (solid lines) electron energy distributions. The high energy tail matches, which corresponds to the matching high energy tail of input spectra, but the low energy portion of the exponential input distributions has a higher flux than a Maxwellian input.

strahlung photons produced per electron) as a function of exponential folding energy and monoenergetic beam energy. Two power law curves are fit to the bremsstrahlung efficiency versus characteristic energy trend with spectral indices of 1.14 and 1.25 for monoenergetic and exponential distributions, respectively. The exponential distribution randomly samples significantly more high energy electrons, which is the cause of the order of magnitude higher efficiency for exponential energy inputs versus monoenergetic.

Figure 6.11 shows the descent of the altitude of peak ionization rate with increasing folding energy from an exponential energy distribution. The peak bremsstrahlung production is correlated with peak ionization rate, so this quantity can be used to account for the optical depth at which photons are produced, and therefore the fraction of the flux that is extinguished as the photons leave the atmosphere.

These results can be used to characterize X-ray observations of Jupiter and to study how precipitation affects the upper atmosphere of Jupiter. The X-ray spectral results are used in the

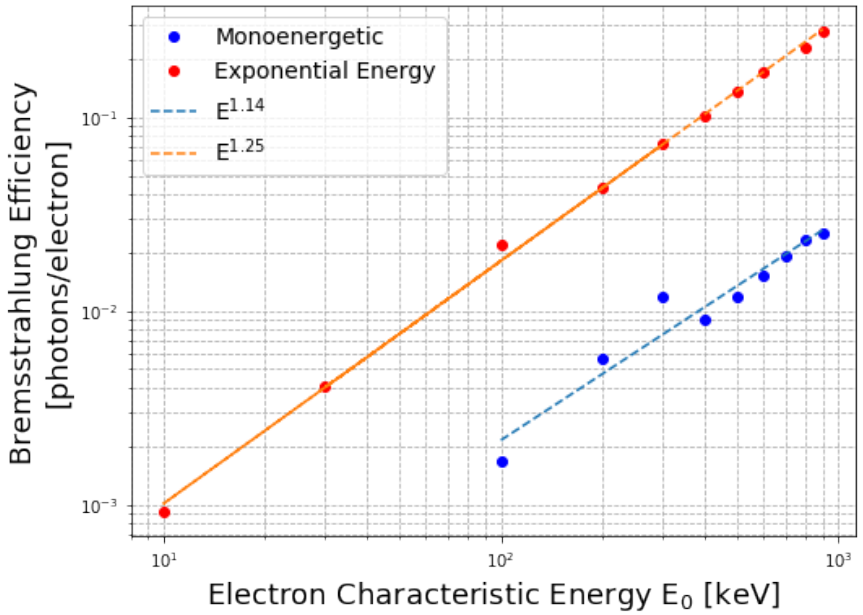

Figure 6.10: Geant4-modeled Jovian bremsstrahlung photon production efficiency versus electron distribution characteristic energy and monoenergetic beam energy. The blue and red series refers to the input electron spectral distribution, and power law distributions are fit to the efficiency.

next section in comparison with older models of auroral X-rays produced at Jupiter in order to aid the design of the COMPASS mission.

6.4 COMPASS Concept Mission X-ray Imager Design

The COMPASS (Comprehensive Observation of Magnetospheric Particle Acceleration, Sources and Sinks) mission is a NASA-funded Heliophysics Mission Concept Study (HMCS) proposing a mixed in-situ and remote sensing mission to Jupiter (Clark et al., 2023; Dunn et al., 2023; Kollmann et al., 2022; Turner et al., 2022). The PI institution is the Johns Hopkins University Applied Physics Laboratory (JHU/APL) leading the mission and spacecraft engineering design. The remote sensing portion is achieved by the inclusion of an X-ray imaging spectrometer to observe a variety of X-ray generation mechanisms that occur in the Jovian magnetosphere, and relate them to the sources, sinks, and acceleration of charged particles.

AXIS is chosen as the heritage instrument on which the COMPASS X-ray Imager (XRI)

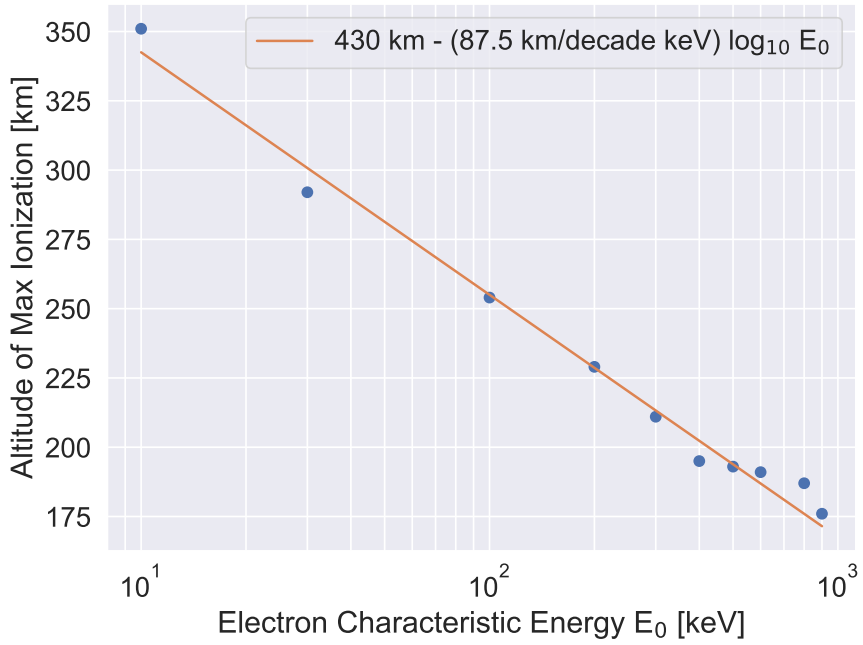

Figure 6.11: A plot of the altitude of peak ionization from an electron exponential energy, sine pitch angle distribution input with folding energy E_0. Altitude here is above the 1 bar pressure surface. A logarithmic fit is performed to show the slope of the line is -87.5 km/decade keV with increasing folding energy.

instrument is based, and as such a variety of sources are analyzed in order to modify and confirm the instrument sizing choices made for the COMPASS XRI. The primary difference between AXIS and the XRI instrument designed for Jupiter is in detector selection and the amount of shielding necessary to mitigate the intense radiation environment of Jupiter.

The following X-ray generation mechanisms were investigated in-depth for this concept study: i) EPP, from both the auroral zone and the Jovian disk; ii) inverse Compton scattering (ICS), which involves solar photons scattering off the ultra-relativistic electrons in the radiation belts, which can convert IR-vis-UV band photons to X-ray energies (Ezoe et al., 2010; Numazawa et al., 2021b); iii) charged particle losses to Jupiter's moons, which emit photons from the PIXE and electron bremsstrahlung processes from charged particle impacts with Jupiter's Galilean moons (Nulsen et al., 2020; R. Elsner et al., 2005); and iv) a variety of scattering interactions including electron-electron, electron-ion, and electron-neutral bremsstrahlung scattering and charge exchange of the

constituents in Io's plasma and neutral torii. Figure 6.12 shows the ICS emissions imaged from Earth with the Suzaku X-ray telescope.

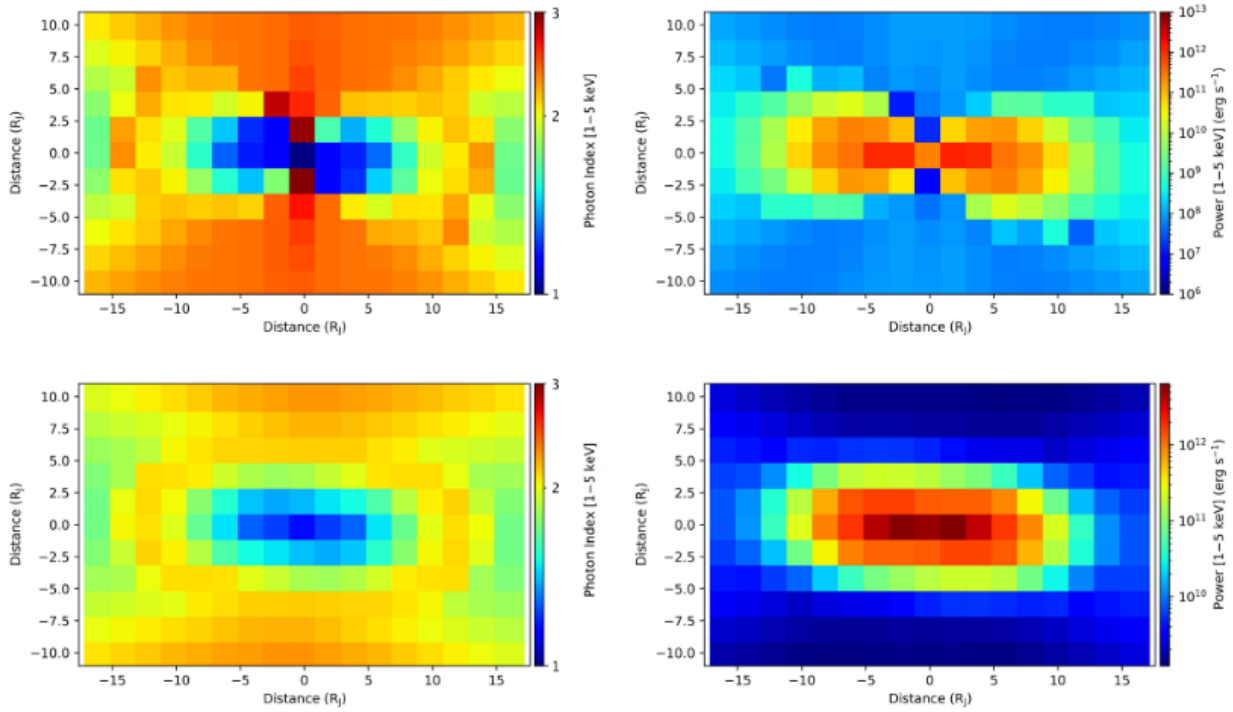

Figure 6.12: Figure from Numazawa et al. (2021b), showing the extent of the ICS emissions from Jupiter's radiation belt. The left column shows the spectral indices of a fit to the observation, and the right column shows integrated X-ray power between 1 – 5 keV for two observations (top and bottom rows).

Figure 6.13 shows a collection of previous X-ray modeling efforts alongside X-ray observations of Jupiter. The precipitation models have their input energy flux adjusted to 10 ergs cm^{-2} s^{-1} in order to compare spectral shape and bremsstrahlung efficiency between models. The X-ray observations were performed by the Einstein X-ray and XMM-Newton observatories from the campaigns of Metzger et al. (1983) and Branduardi-Raymont et al. (2004), respectively. These spectral estimates of auroral bremsstrahlung photons are used to scale the necessary detection characteristics of the XRI instrument and the COMPASS mission, such as detector area and exposure time for example.

Achieving spatial and energy resolution of the X-ray targets mentioned above requires a

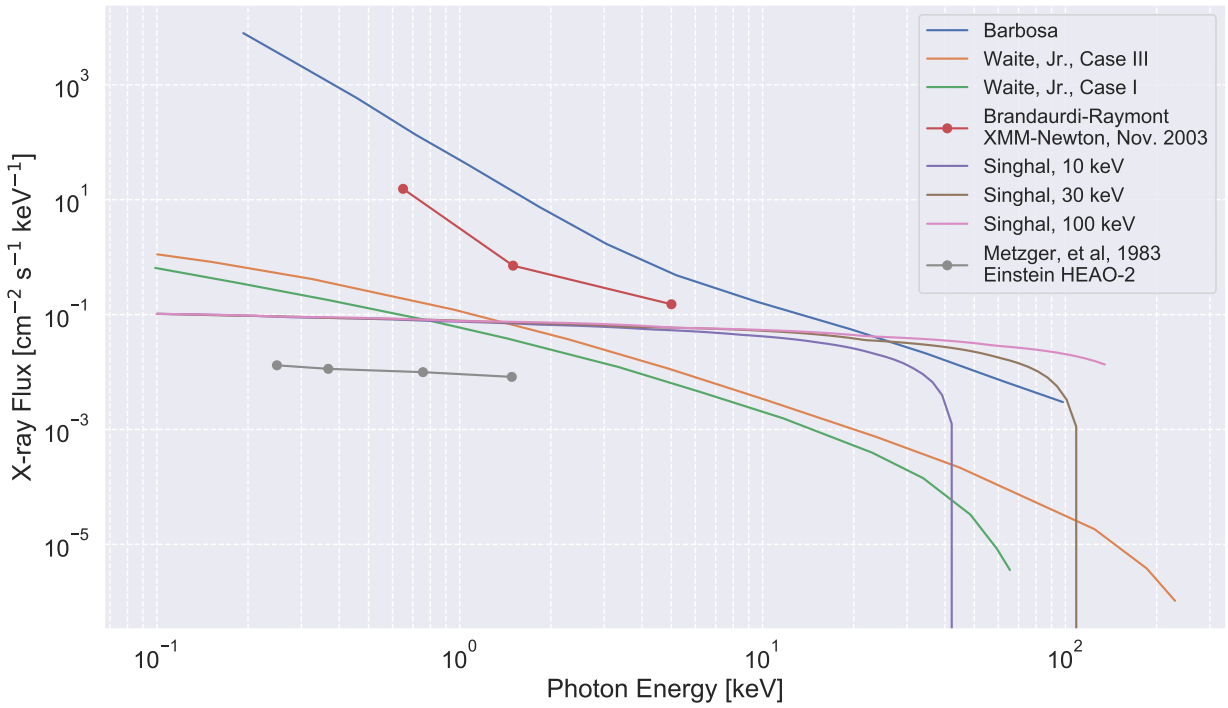

Figure 6.13: A survey of previous Jovian X-ray models and observations, including Waite Jr et al. (1983), Barbosa (1990) and Singhal et al. (1992). The input energy flux is normalized to 10 ergs cm^{-2} s^{-1} for comparison purposes, and this flux is taken as observed from a distance of 10 R$_J$. X-ray observations are performed by the XMM-Newton and HEAO-2 observatories.

lower energy, higher resolution X-ray detector selection and a higher rank optical design than the AXIS instrument. Table 6.1 shows the other heritage instruments studied for the XRI, and their associated aperture/focal techniques, energy resolution, and SWaP (size, weight, and power) properties. The concept study report is published under Clark et al. (2023). The optical properties of the XRI are drawn from the ability to perform the X-ray measurements to answer questions related to various charged particle loss mechanisms.

The field-of-view must be 22°×22° with <1° angular resolution, and must detect photons between 0.2 – 10 keV with better than 100 eV resolution in the range of 0.2 – 2 keV to detect heavy ion charge exchange lines. Observations will primarily be made at altitudes that are between the extrema of the orbit: orbit altitudes range from 1.3 R$_J$ at perijove and 60 – 90 R$_J$ at apojove. In order to achieve this spatial resolution, a detector system with >24 pixels per dimension is needed

that is hardened against radiation. The electronics must also be hardened, likely to a >300 krad dose level, and shielded from radiation in a "vault," much like the electronics of the Juno mission (S. Bolton, Team, et al., 2010). The XRI must have the detection sensitivity and dynamic range to detect the range of signal fluxes shown in Figure 6.13 among substantial background noise. In order to achieve this detection sensitivity, an array of detectors with shared fields-of-view are designed, much like the AXIS instrument, to co-add their integrated images to boost signal statistics. A similar SNR formulation as the one used in Chapter 3 is chosen here; the background flux is derived from the JOSE model of the Jovian magnetosphere (Sicard-Piet, Bourdarie, & Krupp, 2011) combined with a 1D shielding radiation transport model using SPENVIS (Lei et al., 2002).

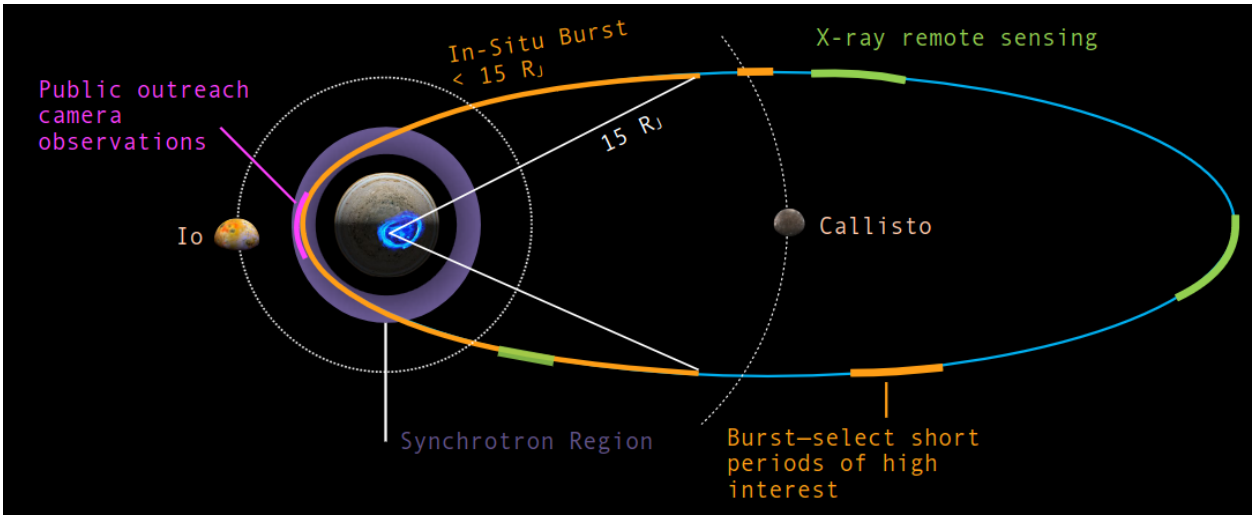

Figure 6.14: The science concept of operations of the COMPASS mission from Clark et al. (2023), showing the operation periods of the XRI to perform remote measurements at 10s R_J versus the in-situ instruments throughout the Jovian magnetosphere.

Two X-ray pointing campaigns are shown in Figure 6.14 and will be performed at altitudes between the two maxima, where the radiation belts, aurora, and Galilean moons can be spatially resolved and imaged simultaneously. Measurements of opportunity can be performed during the Jupiter orbit insertion, such as imaging of charge exchange lines as Jupiter's magnetopause interacts with the heavy ion species of the solar wind. Solar photon albedo from Jupiter in the soft X-ray regime must be removed in order to determine auroral precipitation contributions to the X-ray

signal. This can be performed by estimates made by observations of the Jovian disk concurrent on their own and with other X-ray monitors, e.g. the GOES X-ray monitor (Bornmann et al., 1996) as performed in Bhardwaj et al. (2005).

The XRI instrument is developed to a concept-level design, including size, mass, and power consumption details in order to perform the X-ray spectral imaging measurements necessary to meet the science requirements of the COMPASS mission. An example of an acceptable geometry for the XRI instrument is shown in Figure 6.15. The box-camera design is implemented here with a higher resolution detector and higher rank mask and more shielding to account for the intense radiation environment of the Jovian system.

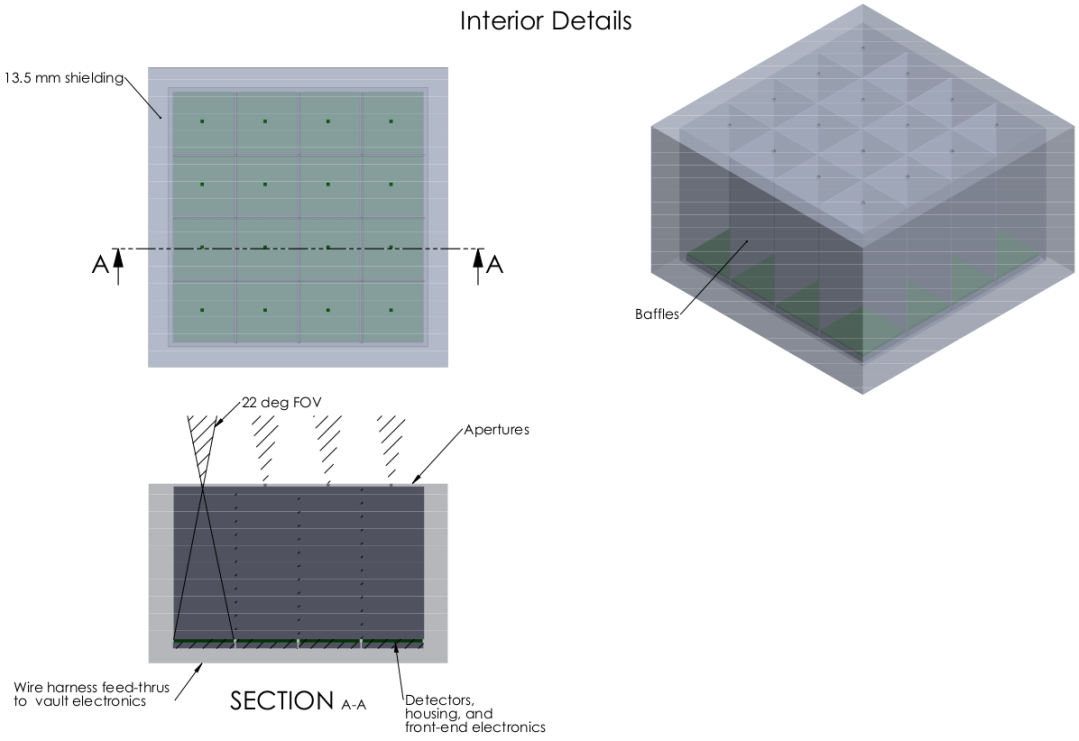

Figure 6.15: Example CAD design of the COMPASS XRI, showing the box camera design, array of co-pointing detectors, radiation shielding, and fields-of-view.

Mission Instrument	**Description**	**Energy**	**SWaP**
BepiColombo MIXS-C MIXS-T	Combination of two X-ray imaging spectrometers **Aperture** MIXS-C: wide FOV (∼10° FOV & resolution) , radial collimator MIXS-T: Wolter type-I telescope (1.1° FOV, 9 arcmin resolution) **Detectors** Silicon Depleted P-channel FET detectors, needs to be cooled to -40°C	**Range** 0.5 – 7.5 keV **Resolution** dE/E =10% (100 eV at 1 keV)	**Power** ∼20 W **Mass** 10.9 kg **Size** MIXS-T: 1.05 m MIXS-C: 0.55 m
SMILE SXI	Wide FOV imager for solar wind CX, uses micropore optics **Detectors** 2 CCDs **Aperture** Lobster eye 15.5° x 26° FOV	**Range** 0.2 – 5 keV **Resolution** dE/E ∼10% (50 eV at 0.5 keV)	**Mass** 26 kg **Size** 30 cm focal length
ASTRO-H SXI	**Detectors** CCD camera	**Range** 0.4 – 12 keV	
POLAR PIXIE	**Detectors** Position-sensitive proportional counting chambers and scintillators **Aperture** Multiple pinhole apertures for varying FOV and spatial resolution with moving plates 21° FOV	**Range** 2 – 60 keV	**Power** 11 W **Mass** 24.5 kg
AEPEX AXIS	**Detectors** Solid-state CZT **Aperture** Tungsten coded apertures and pinhole aperture 90° FOV	**Range** 50 – 250 keV **Resolution** dE/E ∼6.5% (3 keV at 50 keV)	**Power** 15 W **Mass** 7 kg **Size**
JMO JUXTA	Concept instrument from JAXA **Aperture** Wolter type-I telescope	**Range** 0.3 – 2 keV **Resolution** (100 eV at 1 keV)	

Table 6.1: COMPASS XRI Heritage Instrument Trade Study

Chapter 7

Summary and Conclusions

7.1 Summary

This thesis provides an introduction to Earth's magnetosphere and the process of EPP, which couples the magnetosphere, atmosphere, and ionosphere. In Chapter 1, the universality of EPP is touched on to motivate the study of magnetospheres at magnetized bodies beyond Earth, such as Jupiter. Chapter 2 introduces charged particle motion in a magnetic field, and a range of energetic scattering interactions are covered in order to provide context for EPP as well as EPP-generated bremsstrahlung. Fundamental topics such as the loss cone and pitch angle and energy distributions are introduced, which are relevant to the generation of the photons which will serve as the proxy measurement for precipitating electrons, and the focus of much of this work.

The inversion of bremsstrahlung photons in order to estimate precipitating electron characteristics is the topic of the design of the AEPEX CubeSat mission, which aims to quantify the energy input into the atmosphere and the spatial scales of radiation belt electron precipitation. The AXIS instrument onboard the AEPEX mission, which will perform the X-ray spectral and imaging measurements, is described in detail in Chapter 3, in addition to the publication Berland, Marshall, Martin, et al. (2023). The instrument design, estimated signal analysis, and background simulations are performed in order to estimate the SNR of the X-ray measurements to ensure that the science questions are answerable by the AEPEX mission and AXIS instrument.

In order to support the design of the AXIS instrument, the instrument is designed within the GEANT4 radiation transport simulation framework to simulate the charged particle conditions

that induce background on the instrument in the low Earth orbit environment where AXIS will perform its measurements. Additionally, a laboratory experiment was performed using the NASA Goddard Radiation Effects Facility 2 MV electron accelerator to illuminate the instrument in two configurations; this experiment was used to verify the graded-Z shielding electron and photon attenuation capabilities and to validate the predicted background spectra.

The AFIRE instrument, the electron detector from the FIREBIRD-II missions, is briefly reviewed as the second instrument onboard the AEPEX CubeSat. AFIRE will provide in-situ electron spectral measurement with two detectors, which, due to the partially overlapping fields-of-view, enables a coarse estimate of the in-situ pitch angle distribution.

In order to perform the measurements of X-ray spectral images, Chapter 4 describes how the AXIS instrument onboard the AEPEX mission is designed and tested with novel, wide field-of-view coded aperture optics to image extended source regions in the atmosphere. X-ray imaging theory is introduced to provide context for coded aperture imaging, and the algorithmic image reconstruction process is described. Coded aperture mask manufacturing is described and a combination of simulation and laboratory testing is performed in order to validate the design and verify the X-ray spectral imaging performance.

To support the future AEPEX measurements and to provide a deeper understanding of the atmospheric effects of precipitation, Chapter 5 describes how an EPP model is built using GEANT4 that provides high accuracy X-ray spectra and ionization profiles versus altitude from energetic electron inputs. This model improves the latest EPP modeling work using the EPMC code by updating secondary electron and bremsstrahlung production cross sections and by using higher-fidelity numerical methods for charged particle and radiation transport. The model results and an inversion method based on Green's function solutions are described here and in Berland, Marshall, and Capannolo (2023), and verification and validation of the results and inversion methods are performed using three case studies: comparison with ionization profile generated from previous EPP models; an inversion of X-ray production in the stratosphere measured by an atmospheric balloon; and an analysis of spectral pitch angle distributions measured by a spinning, low Earth

orbiting spacecraft.

This precipitation and X-ray transport model is extended beyond Earth in Chapter 6 to study EPP at Jupiter. The input spectra, and therefore the driving acceleration processes, have numerous similarities but also many differences between Earth and Jupiter, which provides a venue to study the universality of particle acceleration processes in planetary magnetospheres. This thesis is concluded by the extension of this work to benefit the COMPASS mission, a concept study of a Jupiter-orbiting spacecraft mission with an X-ray imaging spectrometer. The AXIS instrument design, coded aperture optics, and the EPP modeling work performed here are used to demonstrate the concept design of an X-ray imaging spectrometer capable of performing X-ray measurements in the Jovian system.

7.2 Conclusions and Future Work

This thesis covers the design of a novel, wide field-of-view X-ray imaging spectrometer that is modular and can fit within the CubeSat form factor enables its inclusion on a variety of future missions. The RADICALS mission (I. Mann et al., 2022) looks to implement a version of the AXIS instrument for further observations of EPP bremsstrahlung, and a modified version of the AEPEX mission is being proposed by other institutions to quantify microburst precipitation. Necessary modifications to the AXIS instrument include fast spectral imaging that yield engineering challenges related to software and hardware implementation. Finally, the inclusion of an AXIS-like instrument on board the COMPASS concept mission would allow this design to be used to study heliophysics beyond Earth.

The coded aperture imaging of extended objects and the algorithmic reconstruction of these object distributions under various constraints is the subject of current research. This work will be continued throughout the AEPEX mission lifetime and beyond for follow-on mission opportunities and in order to implement this instrument, or a version of this instrument, on future missions. Coded aperture imaging is currently being explored for imaging charged particle and ENA distributions to expand the scientific purview of this technology (e.g. Reid, Marshall, Blum, & Berland,

2022).

The future measurements of the AEPEX mission will be inverted using the modeling efforts and methods described herein. A large variety and number of combined in-situ electron and remote photon measurements are needed to fully characterize and understand the relationship between precipitation electrons and the subsequent bremsstrahlung photons produced. Key questions include the following: how much information on the precipitation spectrum can be inverted from photon measurements? Can these inversions be performed in all atmospheric types, or is there an advantage to lower atomic number planetary atmospheres, such as the inversion performed at Jupiter in Mori et al. (2022)?

The EPP modeling efforts described by this work can be extended to other planets either by scaling or implementation of that planet's atmospheric profile. For instance, Uranus has a similar hydrogen-helium atmosphere and trapped energetic electron population compared to Jupiter. The first definitive detection of X-rays from Uranus was recently published in Dunn et al. (2021); X-ray spectral measurements can provide immense value to an in-situ or flyby mission to Uranus, and further the Planetary Science Decadal Survey for 2023 – 2033 has selected the study of the Uranian magnetosphere as a high-priority science target (National Academies of Sciences, Engineering, and Medicine and others, 2022). The study of many magnetospheric systems with an energetic population of charged particles can benefit from X-ray spectral measurements.

A major advantage of the CubeSat framework is in its modularity; CubeSats can be designed, built, and launched much more rapidly than larger spacecraft missions, and instruments can be modified to accommodate follow-on missions in similarly short time frames. At the projected launch date of AEPEX, a number of CubeSat missions will be in-orbit that are equipped with particle and wave detection instruments. Synergistic measurements made in conjunction with AEPEX can provide insight into the inter-connected magnetospheric system and can provide immense value for measurements-of-opportunity. Furthermore, a variety of X-ray detection balloon missions are slated to overlap with the lifetime of AEPEX. A variety of other ground-based instrumentation, including ground-based incoherent scatter radar, which can measure the D-region during precipitation events

(Sanchez et al., 2022; Ma et al., 2022), and can be coordinated with AEPEX fly-overs to conduct conjunction science. With the possibility of a no-cost mission extension to AEPEX beyond its nominal 1 year lifetime, the number of these coincident opportunities will increase.

References

Abel, B., & Thorne, R. M. (1999). Modeling energetic electron precipitation near the south atlantic anomaly. Journal of Geophysical Research: Space Physics, 104(A4), 7037–7044.

Accorsi, R. (2001). Design of a near-field coded aperture cameras for high-resolution medical and industrial gamma-ray imaging (Unpublished doctoral dissertation). Massachusetts Institute of Technology.

Accorsi, R., Gasparini, F., & Lanza, R. C. (2001). Optimal coded aperture patterns for improved snr in nuclear medicine imaging. Nuclear Instruments and Methods in Physics Research Section A: Accelerators, Spectrometers, Detectors and Associated Equipment, 474(3), 273–284.

Adams Jr, J. H., Silberberg, R., & Tsao, C. (1981). Cosmic ray effects on microelectronics. part 1. the near-earth particle environment (Tech. Rep.). Naval Research Lab Washington DC.

Agostinelli, S., Allison, J., Amako, K. a., Apostolakis, J., Araujo, H., Arce, P., ... others (2003). Geant4—a simulation toolkit. Nuclear instruments and methods in physics research section A: Accelerators, Spectrometers, Detectors and Associated Equipment, 506(3), 250–303.

Akkurt, I., Gunoglu, K., & Arda, S. (2014). Detection efficiency of nai (tl) detector in 511–1332 kev energy range. Science and Technology of Nuclear Installations, 2014.

Ali, E., & Rogers, D. (2007). Efficiency improvements of x-ray simulations in egsnrc user-codes using bremsstrahlung cross-section enhancement (bcse). Medical physics, 34(6Part1), 2143–2154.

Allison, H. J., & Shprits, Y. Y. (2020). Local heating of radiation belt electrons to ultra-relativistic energies. Nature Communications, 11(1), 4533.

Allison, J., Amako, K., Apostolakis, J., Araujo, H., Dubois, P. A., Asai, M., ... others (2006). Geant4 developments and applications. IEEE Transactions on nuclear science, 53(1), 270–278.

Als-Nielsen, J., & McMorrow, D. (2011). Elements of modern x-ray physics. John Wiley & Sons.

Anderson, B., Shekhar, S., Millan, R., Crew, A., Spence, H., Klumpar, D., ... Turner, D. (2017). Spatial scale and duration of one microburst region on 13 august 2015. Journal of Geophysical Research: Space Physics, 122(6), 5949–5964.

Andersson, M., Verronen, P., Rodger, C., Clilverd, M., & Seppälä, A. (2014). Missing driver in the sun–earth connection from energetic electron precipitation impacts mesospheric ozone. Nature communications, 5(1), 5197.

Angelopoulos, V., Tsai, E., Bingley, L., Shaffer, C., Turner, D., Runov, A., ... others (2020). The elfin mission. Space science reviews, 216, 1–45.

Angot, A. (1897). The aurora borealis (Vol. 77). D. Appleton & Company.

Arnaud, K., Smith, R., & Siemiginowska, A. (2011). Handbook of x-ray astronomy (Vol. 7). Cambridge University Press.

Arnold, S. (1966). Repressing the growth of tin whiskers.

Artamonov, A., Mishev, A., & Usoskin, I. (2016). Atmospheric ionization induced by precipitating electrons: Comparison of crac: Epii model with a parametrization model. Journal of Atmospheric and Solar-Terrestrial Physics, 149, 161–166.

Artemyev, A., Vasiliev, A., Mourenas, D., Agapitov, O., & Krasnoselskikh, V. (2013). Nonlinear electron acceleration by oblique whistler waves: Landau resonance vs. cyclotron resonance. Physics of Plasmas, 20(12), 122901.

Aschenbach, B. (2009). Realization of x-ray telescopes–from design to performance. Experimental Astronomy, 26, 95–109.

Atreya, S., Mahaffy, P., Niemann, H., Wong, M., & Owen, T. (2003). Composition and origin of the atmosphere of jupiter—an update, and implications for the extrasolar giant planets. Planetary and Space Science, 51(2), 105–112.

Atwell, W., Rojdev, K., Aghara, S., & Sriprisan, S. (2013). Mitigating the effects of the space radiation environment: A novel approach of using graded-z materials. In Aiaa space 2013 conference and exposition (p. 5385).

Axford, W. (1964). Viscous interaction between the solar wind and the earth's magnetosphere. Planetary and Space Science, 12(1), 45–53.

Axford, W. I., & Hines, C. O. (1961). A unifying theory of high-latitude geophysical phenomena and geomagnetic storms. Canadian Journal of Physics, 39(10), 1433–1464.

Bagenal, F. (2013). Planetary magnetospheres. Planets, Stars and Stellar Systems. Volume 3: Solar and Stellar Planetary Systems, 251.

Baier, V. N., & Katkov, V. M. (2005). Concept of formation length in radiation theory. Physics reports, 409(5), 261–359.

Bailey, V., & Martyn, D. (1934). Interaction of radio waves. Nature, 133(3354), 218–218.

Baker, D. (1985). Statistical analyses in the study of solar wind-magnetosphere coupling.

Baker, D. (1998). What is space weather? Advances in Space Research, 22(1), 7–16.

Baker, D. (2000). Effects of the sun on the earth's environment. Journal of Atmospheric and Solar-Terrestrial Physics, 62(17-18), 1669–1681.

Baker, D., Daly, E., Daglis, I., Kappenman, J. G., & Panasyuk, M. (2004). Effects of space weather on technology infrastructure. Wiley Online Library.

Baker, D., Jaynes, A., Hoxie, V., Thorne, R., Foster, J., Li, X., ... others (2014). An impenetrable barrier to ultrarelativistic electrons in the van allen radiation belts. Nature, 515(7528), 531–534.

Baker, D., Kanekal, S., Hoxie, V., Henderson, M., Li, X., Spence, H. E., ... others (2013). A long-lived relativistic electron storage ring embedded in earth's outer van allen belt. Science, 340(6129), 186–190.

Baker, D. N. (2000). The occurrence of operational anomalies in spacecraft and their relationship to space weather. IEEE Transactions on Plasma Science, 28(6), 2007–2016.

Baker, D. N., & Goertz, C. (1976). Radial diffusion in jupiter's magnetosphere. Journal of Geophysical Research, 81(28), 5215–5219.

Baker, D. N., Mason, G. M., Figueroa, O., Colon, G., Watzin, J. G., & Aleman, R. M. (1993). An overview of the solar anomalous, and magnetospheric particle explorer (sampex) mission. IEEE Transactions on Geoscience and remote sensing, 31(3), 531–541.

Balan, N., Otsuka, Y., Nishioka, M., Liu, J., & Bailey, G. (2013). Physical mechanisms of the ionospheric storms at equatorial and higher latitudes during the recovery phase of geomagnetic storms. Journal of Geophysical Research: Space Physics, 118(5), 2660–2669.

Barbosa, D. (1990). Bremsstrahlung x rays from jovian auroral electrons. Journal of Geophysical Research: Space Physics, 95(A9), 14969–14976.

Bauer, E. (1994). Low energy electron microscopy. Reports on Progress in Physics, 57(9), 895.
Bearden, J. A. (1967). X-ray wavelengths. Reviews of Modern Physics, 39(1), 78.
Bell, E., & Armstrong, T. (1986). Monte carlo simulation of charged particle impact on the satellites of jupiter and saturn. Journal of Geophysical Research: Space Physics, 91(A2), 1397–1403.
Berger, M., & Seltzer, S. (1972). Bremsstrahlung in the atmosphere. Journal of Atmospheric and Terrestrial Physics, 34(1), 85–108.
Berger, M. J., Coursey, J. S., Zucker, M. A., et al. (1999). Estar, pstar, and astar: computer programs for calculating stopping-power and range tables for electrons, protons, and helium ions (version 1.21).
Berland, G., Marshall, R., & Capannolo, L. (2023). Kinetic modeling of radiation belt electrons with geant4 to study energetic particle precipitation in earth's atmosphere. Earth and Space Sciences.
Berland, G., Marshall, R., Martin, C., Buescher, J., Kohnert, R., Boyajian, S., ... Xu, W. (2023). The atmospheric x-ray imaging spectrometer (axis) instrument: Quantifying energetic particle precipitation through bremsstrahlung x-ray imaging. Review of Scientific Instruments, 94(2), 023103.
Beskin, V. S., Gurevich, A. V., Istomin, Y. N., Istomin, J. N., & Istomin, Y. N. (1993). Physics of the pulsar magnetosphere. Cambridge university press.
Bhardwaj, A., Branduardi-Raymont, G., Elsner, R. F., Gladstone, G. R., Ramsay, G., Rodriguez, P., ... Cravens, T. E. (2005). Solar control on jupiter's equatorial x-ray emissions: 26–29 november 2003 xmm-newton observation. Geophysical Research Letters, 32(3).
Bhardwaj, A., Elsner, R. F., Gladstone, G. R., Cravens, T. E., Lisse, C. M., Dennerl, K., ... others (2007). X-rays from solar system objects. Planetary and Space Science, 55(9), 1135–1189.
Bhardwaj, A., & Gladstone, G. R. (2000). Auroral emissions of the giant planets. Reviews of Geophysics, 38(3), 295–353.
Bhardwaj, A., Gladstone, G. R., Elsner, R. F., Østgaard, N., Waite Jr, J. H., Cravens, T. E., ... Metzger, A. E. (2007). First terrestrial soft x-ray auroral observation by the chandra x-ray observatory. Journal of atmospheric and solar-terrestrial physics, 69(1-2), 179–187.
Bhatia, K., & Lakhina, G. (1980). Drift loss cone instability in the ring current and plasma sheet. Proceedings of the Indian Academy of Sciences-Earth and Planetary Sciences, 89, 99–108.
Bilitza, D., & Reinisch, B. W. (2008). International reference ionosphere 2007: improvements and new parameters. Advances in space research, 42(4), 599–609.
Birmingham, T., Hess, W., Northrop, T., Baxter, R., & Lojko, M. (1974). The electron diffusion coeffcient in jupiter's magnetosphere. Journal of Geophysical Research, 79(1), 87–97.
Blandford, R. D., & Thorne, K. S. (2008). Applications of classical physics. lecture notes, California Institute of Technology, 12.
Blum, L., Bonnell, J., Agapitov, O., Paulson, K., & Kletzing, C. (2017). Emic wave scale size in the inner magnetosphere: Observations from the dual van allen probes. Geophysical Research Letters, 44(3), 1227–1233.
Blum, L., Halford, A., Millan, R., Bonnell, J., Goldstein, J., Usanova, M., ... others (2015). Observations of coincident emic wave activity and duskside energetic electron precipitation on 18–19 january 2013. Geophysical Research Letters, 42(14), 5727–5735.
Blum, L., Remya, B., Denton, M., & Schiller, Q. (2020). Persistent emic wave activity across the nightside inner magnetosphere. Geophysical Research Letters, 47(6), e2020GL087009.
Blum, L. W., & Breneman, A. W. (2020). Observations of radiation belt losses due to cyclotron wave-particle interactions. In The dynamic loss of earth's radiation belts (pp. 49–98). Elsevier.

Blum, L. W., Halford, A., Millan, R., Bonnell, J. W., Goldstein, J., Usanova, M., ... Li, X. (2015). Observations of coincident emic wave activity and duskside energetic electron precipitation on 18–19 january 2013. Geophysical Research Letters, 42(14), 5727-5735. Retrieved from https://agupubs.onlinelibrary.wiley.com/doi/abs/10.1002/2015GL065245 doi: https://doi.org/10.1002/2015GL065245

Blumenthal, G. R., & Gould, R. J. (1970). Bremsstrahlung, synchrotron radiation, and compton scattering of high-energy electrons traversing dilute gases. Reviews of modern Physics, 42(2), 237.

Bolotnikov, A., Camarda, G., Wright, G., & James, R. (2005). Factors limiting the performance of cdznte detectors. IEEE transactions on nuclear science, 52(3), 589–598.

Bolton, S., Team, J. S., et al. (2010). The juno mission. Proceedings of the International Astronomical Union, 6(S269), 92–100.

Bolton, S. J., Levin, S. M., Gulkis, S. L., Klein, M. J., Sault, R. J., Bhattacharya, B., ... Leblanc, Y. (2001). Divine-garrett model and jovian synchrotron emission. Geophysical research letters, 28(5), 907–910.

Bornmann, P. L., Speich, D., Hirman, J., Matheson, L., Grubb, R., Garcia, H. A., & Viereck, R. (1996). Goes x-ray sensor and its use in predicting solar-terrestrial disturbances. In Goes-8 and beyond (Vol. 2812, pp. 291–298).

Borovsky, J. E., Thomsen, M. F., & Elphic, R. C. (1998). The driving of the plasma sheet by the solar wind. Journal of Geophysical Research: Space Physics, 103(A8), 17617–17639.

Bradt, H. V., Ohashi, T., & Pounds, K. A. (1992). X-ray astronomy missions. Annual review of astronomy and astrophysics, 30(1), 391–427.

Bragg, W. H., & Bragg, W. L. (1913). The reflection of x-rays by crystals. Proceedings of the Royal Society of London. Series A, Containing Papers of a Mathematical and Physical Character, 88(605), 428–438.

Branduardi-Raymont, G., Elsner, R., Gladstone, G., Ramsay, G., Rodriguez, P., Soria, R., & Waite, J. (2004). First observation of jupiter by xmm-newton. Astronomy & Astrophysics, 424(1), 331–337.

Branduardi-Raymont, G., Elsner, R. F., Galand, M., Grodent, D., Cravens, T., Ford, P., ... Waite Jr, J. (2008). Spectral morphology of the x-ray emission from jupiter's aurorae. Journal of Geophysical Research: Space Physics, 113(A2).

Brice, N., & Mcdonough, T. R. (1973). Jupiter's radiation belts. Icarus, 18(2), 206–219.

Brice, N. M. (1967). Bulk motion of the magnetosphere. Journal of Geophysical Research, 72(21), 5193–5211.

Brown, J. C., & Emslie, A. G. (1988). Analytic limits on the forms of spectra possible from optically thin collisional bremsstrahlung source models. Astrophysical Journal, Part 1 (ISSN 0004-637X), vol. 331, Aug. 1, 1988, p. 554-564. SERC-supported research., 331, 554–564.

Brussaard, P., & Van de Hulst, H. (1962). Approximation formulas for nonrelativistic bremsstrahlung and average gaunt factors for a maxwellian electron gas. Reviews of Modern Physics, 34(3), 507.

Bučík, R., Kudela, K., Dmitriev, A., Kuznetsov, S., Myagkova, I., & Ryumin, S. (2005). Review of electron fluxes within the local drift loss cone: Measurements on coronas-i. Advances in Space Research, 36(10), 1979–1983.

Bunaciu, A. A., UdriŞTioiu, E. G., & Aboul-Enein, H. Y. (2015). X-ray diffraction: instrumentation and applications. Critical reviews in analytical chemistry, 45(4), 289–299.

Bunkin, F., & Fedorov, M. (1966). Bremsstrahlung in a strong radiation field. Sov. Phys. JETP, 22(4), 844–847.

Burns, C., Turunen, E., Matveinen, H., Ranta, H., & Hargreaves, J. (1991). Chemical modelling of the quiet summer d-and e-regions using eiscat electron density profiles. Journal of atmospheric and terrestrial physics, 53(1-2), 115–134.

Burtis, W., & Helliwell, R. (1976). Magnetospheric chorus: Occurrence patterns and normalized frequency. Planetary and Space Science, 24(11), 1007–1024.

Cannon, P., Angling, M., Barclay, L., Curry, C., Dyer, C., Edwards, R., ... others (2013). Extreme space weather: impacts on engineered systems and infrastructure. Royal Academy of Engineering.

Cannon, T. M., & Fenimore, E. E. (1980). Coded aperture imaging: many holes make light work. Optical Engineering, 19(3), 283–289.

Capannolo, L., Li, W., Ma, Q., Chen, L., Shen, X.-C., Spence, H., ... others (2019). Direct observation of subrelativistic electron precipitation potentially driven by emic waves. Geophysical Research Letters, 46(22), 12711–12721.

Capannolo, L., Li, W., Ma, Q., Shen, X.-C., Angelopoulos, V., Artemyev, A., ... Hanzelka, M. (under review 2023). Electron precipitation observed by elfin using proton precipitation as a proxy for electromagnetic ion cyclotron (emic) waves. Geophysical Research Letters.

Capannolo, L., Li, W., Ma, Q., Shen, X.-C., Zhang, X.-J., Redmon, R., ... others (2019). Energetic electron precipitation: Multievent analysis of its spatial extent during emic wave activity. Journal of Geophysical Research: Space Physics, 124(4), 2466–2483.

Capannolo, L., Li, W., Spence, H., Johnson, A., Shumko, M., Sample, J., & Klumpar, D. (2021). Energetic electron precipitation observed by firebird-ii potentially driven by emic waves: Location, extent, and energy range from a multievent analysis. Geophysical Research Letters, 48(5), e2020GL091564.

Carlson, B. E. (2010). Terrestrial gamma-ray flash production by lightning. Stanford University.

Caroli, E., Stephen, J., Di Cocco, G., Natalucci, L., & Spizzichino, A. (1987). Coded aperture imaging in x-and gamma-ray astronomy. Space Science Reviews, 45, 349–403.

Carson, B. R., Rodger, C. J., & Clilverd, M. A. (2013). Poes satellite observations of emic-wave driven relativistic electron precipitation during 1998–2010. Journal of Geophysical Research: Space Physics, 118(1), 232–243.

Cartwright, J. H., & Piro, O. (1992). The dynamics of runge–kutta methods. International Journal of Bifurcation and Chaos, 2(03), 427–449.

Catenza, J. L. U. (2022). Focusing x-rays using micropore optics (mpo) (Tech. Rep.).

Chapman, S. (1956). The electrical conductivity of the ionosphere: A review. Il Nuovo Cimento (1955-1965), 4(Suppl 4), 1385–1412.

Chase, R., & VanSpeybroeck, L. (1973). Wolter-schwarzschild telescopes for x-ray astronomy. Applied Optics, 12(5), 1042–1044.

Cheng, A. F. (1982). So2 ionization and dissociation in the io plasma torus. Journal of Geophysical Research: Space Physics, 87(A7), 5301–5304.

Churazov, E., Sazonov, S., Sunyaev, R., & Revnivtsev, M. (2008). Earth x-ray albedo for cosmic x-ray background radiation in the 1–1000 kev band. Monthly Notices of the Royal Astronomical Society, 385(2), 719–727.

Churazov, E., Sunyaev, R., Revnivtsev, M., Sazonov, S., Molkov, S., Grebenev, S., ... others (2007). Integral observations of the cosmic x-ray background in the 5–100 kev range via occultation by the earth. Astronomy & Astrophysics, 467(2), 529–540.

Cieślak, M. J., Gamage, K. A., & Glover, R. (2016). Coded-aperture imaging systems: Past, present and future development–a review. Radiation Measurements, 92, 59–71.

Clark, G., Kinnison, J., Kelly, D., Kollmann, P., Li, W., Jaynes, A., ... Furrow, M. (2023, Feb). Comprehensive observations of magnetospheric particle acceleration, sources, and sinks (COMPASS): A mission concept to jupiter's extreme magnetosphere to address fundamental mysteries in heliophysics.
doi: 10.22541/essoar.167751608.84818747/v1

Clark, G., Mauk, B., Kollmann, P., Paranicas, C., Bagenal, F., Allen, R., ... others (2020). Heavy ion charge states in jupiter's polar magnetosphere inferred from auroral megavolt electric potentials. Journal of Geophysical Research: Space Physics, 125(9), e2020JA028052.

Clark, G., Mauk, B., Paranicas, C., Kollmann, P., & Smith, H. (2016). Charge states of energetic oxygen and sulfur ions in jupiter's magnetosphere. Journal of Geophysical Research: Space Physics, 121(3), 2264–2273.

Clilverd, M. A., Rodger, C. J., McCarthy, M., Millan, R., Blum, L. W., Cobbett, N., ... Halford, A. J. (2017). Investigating energetic electron precipitation through combining ground-based and balloon observations. Journal of Geophysical Research: Space Physics, 122(1), 534-546. Retrieved from https://agupubs.onlinelibrary.wiley.com/doi/abs/10.1002/2016JA022812 doi: https://doi.org/10.1002/2016JA022812

Clilverd, M. A., Rodger, C. J., Thomson, N. R., Brundell, J. B., Ulich, T., Lichtenberger, J., ... others (2009). Remote sensing space weather events: Antarctic-arctic radiation-belt (dynamic) deposition-vlf atmospheric research konsortium network. Space Weather, 7(4).

Connerney, J., Timmins, S., Herceg, M., & Joergensen, J. (2020). A jovian magnetodisc model for the juno era. Journal of Geophysical Research: Space Physics, 125(10), e2020JA028138.

Corless, R. M., Gonnet, G. H., Hare, D. E., Jeffrey, D. J., & Knuth, D. E. (1996). On the lambert w function. Advances in Computational mathematics, 5, 329–359.

Cravens, T., Howell, E., Waite Jr, J., & Gladstone, G. (1995). Auroral oxygen precipitation at jupiter. Journal of Geophysical Research: Space Physics, 100(A9), 17153–17161.

Crew, A. B., Spence, H. E., Blake, J. B., Klumpar, D. M., Larsen, B. A., O'Brien, T. P., ... others (2016). First multipoint in situ observations of electron microbursts: Initial results from the nsf firebird ii mission. Journal of Geophysical Research: Space Physics, 121(6), 5272–5283.

Cummer, S. A., Bell, T. F., Inan, U. S., & Chenette, D. (1997). Vlf remote sensing of high-energy auroral particle precipitation. Journal of Geophysical Research: Space Physics, 102(A4), 7477–7484.

Daglis, I. A., Thorne, R. M., Baumjohann, W., & Orsini, S. (1999). The terrestrial ring current: Origin, formation, and decay. Reviews of Geophysics, 37(4), 407–438.

Dai, Y.-H. (2002). Convergence properties of the bfgs algoritm. SIAM Journal on Optimization, 13(3), 693–701.

Davis, G. K. (2007). History of the noaa satellite program. Journal of Applied Remote Sensing, 1(1), 012504.

de Pater, I. (2006). Technical report: Jupiter's synchrotron radiation. Synchrotron Radiation News, 19(5), 12-17. Retrieved from https://doi.org/10.1080/08940880600978689 doi: 10.1080/08940880600978689

Dessler, A. (1959). Effect of magnetic anomaly on particle radiation trapped in geomagnetic field. Journal of Geophysical Research, 64(7), 713–715.

Divine, N., & Garrett, H. B. (1983). Charged particle distributions in jupiter's magnetosphere. Journal of Geophysical Research: Space Physics, 88(A9), 6889-6903. Retrieved from https://agupubs.onlinelibrary.wiley.com/doi/abs/10.1029/JA088iA09p06889 doi: https://doi.org/10.1029/JA088iA09p06889

Dormand, J. R., & Prince, P. J. (1980). A family of embedded runge-kutta formulae. Journal of

computational and applied mathematics, 6(1), 19–26.
Dungey, J. (1963). Loss of van allen electrons due to whistlers. Planetary and Space Science, 11(6), 591–595.
Dunn, W., Berland, G., Roussos, E., Clark, G., Kollmann, P., Turner, D., ... others (2023). Exploring fundamental particle acceleration and loss processes in heliophysics through an orbiting x-ray instrument in the jovian system. arXiv preprint arXiv:2303.02161.
Dunn, W., Branduardi-Raymont, G., Ray, L., Jackman, C., Kraft, R., Elsner, R., ... others (2017). The independent pulsations of jupiter's northern and southern x-ray auroras. Nature Astronomy, 1(11), 758–764.
Dunn, W., Ness, J.-U., Lamy, L., Tremblay, G., Branduardi-Raymont, G., Snios, B., ... Wibisono, A. (2021). A low signal detection of x-rays from uranus. Journal of Geophysical Research: Space Physics, 126(4), e2020JA028739.
Durkee III, R. R. (2006). High-density composites replace lead. Composites in Manufacturing, 22(3), 1–7.
Eather, R. (1967). Auroral proton precipitation and hydrogen emissions. Reviews of Geophysics, 5(3), 207–285.
Edwards, P., & Pawlak, D. (2000). Metop: The space segment for eumetsat's polar system. ESA bulletin, 7–18.
Egorova, T., Rozanov, E., Zubov, V., Manzini, E., Schmutz, W., & Peter, T. (2005). Chemistry-climate model socol: a validation of the present-day climatology.
Eisenberger, P., & Platzman, P. (1970). Compton scattering of x rays from bound electrons. Physical Review A, 2(2), 415.
Ejiri, M. (1978). Trajectory traces of charged particles in the magnetosphere. Journal of Geophysical Research: Space Physics, 83(A10), 4798–4810.
Elliott, S., Gurnett, D., Kurth, W., Mauk, B., Ebert, R., Clark, G., ... Bolton, S. (2018). The acceleration of electrons to high energies over the jovian polar cap via whistler mode wave-particle interactions. Journal of Geophysical Research: Space Physics, 123(9), 7523–7533.
Elsner, R., Ramsey, B., Waite Jr, J., Rehak, P., Johnson, R., Cooper, J., & Swartz, D. (2005). X-ray probes of magnetospheric interactions with jupiter's auroral zones, the galilean satellites, and the io plasma torus. Icarus, 178(2), 417–428.
Elsner, R. F., Lugaz, N., Waite Jr, J., Cravens, T., Gladstone, G., Ford, P., ... others (2005). Simultaneous chandra x ray, hubble space telescope ultraviolet, and ulysses radio observations of jupiter's aurora. Journal of Geophysical Research: Space Physics, 110(A1).
Emmert, J. T., Drob, D. P., Picone, J. M., Siskind, D. E., Jones Jr, M., Mlynczak, M., ... others (2021). Nrlmsis 2.0: A whole-atmosphere empirical model of temperature and neutral species densities. Earth and Space Science, 8(3), e2020EA001321.
Ezoe, Y., Ishikawa, K., Ohashi, T., Miyoshi, Y., Terada, N., Uchiyama, Y., & Negoro, H. (2010). Discovery of diffuse hard x-ray emission around jupiter with suzaku. The Astrophysical Journal Letters, 709(2), L178.
Fabian, A. C. (1994). Cooling flows in clusters of galaxies. Annual Review of Astronomy and Astrophysics, 32(1), 277–318.
Fan, W. C., Drumm, C. R., Roeske, S. B., & Scrivner, G. J. (1996). Shielding considerations for satellite microelectronics. IEEE Transactions on nuclear science, 43(6), 2790–2796.
Fang, X., Randall, C. E., Lummerzheim, D., Solomon, S. C., Mills, M. J., Marsh, D. R., ... Lu, G. (2008). Electron impact ionization: A new parameterization for 100 ev to 1 mev electrons. Journal of Geophysical Research: Space Physics, 113(A9).
Fang, X., Randall, C. E., Lummerzheim, D., Wang, W., Lu, G., Solomon, S. C., & Frahm, R. A.

(2010). Parameterization of monoenergetic electron impact ionization. Geophysical Research Letters, 37(22).

Farley, T. A., & Walt, M. (1971). Source and loss processes of protons of the inner radiation belt. Journal of Geophysical Research, 76(34), 8223–8240.

Feng, I., Lamoureux, M., Pratt, R., & Tseng, H. (1983). Calculation of free-free gaunt factors in hot dense plasmas. Physical Review A, 27(6), 3209.

Fenimore, E. E., & Cannon, T. M. (1978). Coded aperture imaging with uniformly redundant arrays. Applied optics, 17(3), 337–347.

Ferrari, A., Sala, P. R., Fasso, A., Ranft, J., Siegen, U., et al. (2005). Fluka: a multi-particle transport code (Tech. Rep.). Stanford Linear Accelerator Center (SLAC).

Flaud, J.-M., Piccolo, C., Carli, B., Perrin, A., Coudert, L., Teffo, J., & Brown, L. (2003). Molecular line parameters for the mipas (michelson interferometer for passive atmospheric sounding) experiment. Optika Atmosfery i Okeana, 16(1), 194–205.

Foster, J., Holt, J. M., Musgrove, R., & Evans, D. (1986). Ionospheric convection associated with discrete levels of particle precipitation. Geophysical Research Letters, 13(7), 656–659.

Fox, N., & Burch, J. L. (2014). The van allen probes mission. Springer Science & Business Media.

Frahm, R., Winningham, J., Sharber, J., Link, R., Crowley, G., Gaines, E., ... Potemra, T. (1997). The diffuse aurora: A significant source of ionization in the middle atmosphere. Journal of Geophysical Research: Atmospheres, 102(D23), 28203–28214.

Frank, L., & Ackerson, K. (1971). Observations of charged particle precipitation into the auroral zone. Journal of Geophysical Research, 76(16), 3612–3643.

Freden, S. C., & White, R. S. (1960). Particle fluxes in the inner radiation belt. Journal of Geophysical Research, 65(5), 1377–1383.

Fujimoto, M., Baumjohann, W., Kabin, K., Nakamura, R., Slavin, J., Terada, N., & Zelenyi, L. (2008). Hermean magnetosphere-solar wind interaction. Mercury, 347–368.

Funke, B., Baumgaertner, A., Calisto, M., Egorova, T., Jackman, C. H., Kieser, J., ... others (2011). Composition changes after the" halloween" solar proton event: the high energy particle precipitation in the atmosphere (heppa) model versus mipas data intercomparison study. Atmospheric Chemistry and Physics, 11(17), 9089–9139.

Galand, M., & Richmond, A. D. (2001). Ionospheric electrical conductances produced by auroral proton precipitation. Journal of Geophysical Research: Space Physics, 106(A1), 117–125.

Gasdia, F., & Marshall, R. A. (2023). A method for imaging energetic particle precipitation with subionospheric vlf signals. Earth and Space Science, 10(1), e2022EA002460.

Giorgetta, M. A., Manzini, E., Roeckner, E., Esch, M., & Bengtsson, L. (2006, Aug 15). Climatology and forcing of the quasi-biennial oscillation in the maecham5 model. Journal of Climate, 19(16), 3882-3897,3899-3901. Retrieved from `https://colorado.idm.oclc.org/login?url=https://search-proquest-com.colorado.idm.oclc.org/docview/222889849?accountid=14503` (Copyright - Copyright American Meteorological Society Aug 15, 2006; Document feature - Tables; ; Graphs; Equations; Last updated - 2017-11-11)

Glukhov, V., Pasko, V., & Inan, U. (1992). Relaxation of transient lower ionospheric disturbances caused by lightning-whistler-induced electron precipitation bursts. Journal of Geophysical Research: Space Physics, 97(A11), 16971–16979.

Gombosi, T., Baker, D., Balogh, A., Erickson, P., Huba, J., & Lanzerotti, L. (2017). Anthropogenic space weather. Space Science Reviews, 212(3), 985–1039.

Gonzalez, W. D., Tsurutani, B. T., & Clúa de Gonzalez, A. L. (1999). Interplanetary origin of geomagnetic storms. Space Science Reviews, 88(3-4), 529–562.

Gottesman, S. R. (2007). Coded apertures: past, present, and future application and design. In Adaptive coded aperture imaging and non-imaging sensors (Vol. 6714, pp. 21–31).

Gottesman, S. R., & Fenimore, E. E. (1989). New family of binary arrays for coded aperture imaging. Applied optics, 28(20), 4344–4352.

Gruber, D., Matteson, J., Peterson, L., & Jung, G. (1999). The spectrum of diffuse cosmic hard x-rays measured with heao 1. The Astrophysical Journal, 520(1), 124.

Gruntman, M. (1997). Energetic neutral atom imaging of space plasmas. Review of Scientific Instruments, 68(10), 3617–3656.

Gupta, M. (2010). Calculation of radiation length in materials (Tech. Rep.).

Gurnett, D. A., Kurth, W., & Scarf, F. (1979). Auroral hiss observed near the io plasma torus. Nature, 280(5725), 767–770.

Hammersley, A., Ponman, T., & Skinner, G. (1992). Reconstruction of images from a coded-aperture box camera. Nuclear Instruments and Methods in Physics Research Section A: Accelerators, Spectrometers, Detectors and Associated Equipment, 311(3), 585–594.

Hasinger, G. (1996). The extragalactic x-ray and gamma-ray background. Astronomy and Astrophysics Supplement Series, 120, 607–614.

Hays, P., Jones, R., & Rees, M. (1973). Auroral heating and the composition of the neutral atmosphere. Planetary and Space Science, 21(4), 559–573.

Hendricks, J. S. (2003). Mcnpx version 2.5. c (Tech. Rep.). Los Alamos National Laboratory.

Hess, S., Bonfond, B., Zarka, P., & Grodent, D. (2011). Model of the jovian magnetic field topology constrained by the io auroral emissions. Journal of Geophysical Research: Space Physics, 116(A5).

Hess, W., Birmingham, T., & Mead, G. (1974). Absorption of trapped particles by jupiter's moons. Journal of Geophysical Research, 79(19), 2877–2880.

Hill, T., & Reiff, P. (1977). Evidence of magnetospheric cusp proton acceleration by magnetic merging at the dayside magnetopause. Journal of Geophysical Research, 82(25), 3623–3628.

Hoffmeyer, R. E., Bündgen, P., & Thakkar, A. J. (1998). Cross sections for x-ray and high-energy electron scattering by small molecules. Journal of Physics B: Atomic, Molecular and Optical Physics, 31(16), 3675.

Högbom, J. (1974). Aperture synthesis with a non-regular distribution of interferometer baselines. Astronomy and Astrophysics Supplement, Vol. 15, p. 417, 15, 417.

Holt, L. A. (2013). Energetic particle precipitation in the atmosphere: Northern hemisphere variability and transport. (Unpublished doctoral dissertation). University of Colorado Boulder.

Holt, L. A., Randall, C. E., Peck, E. D., Marsh, D. R., Smith, A. K., & Harvey, V. L. (2013a). The influence of major sudden stratospheric warming and elevated stratopause events on the effects of energetic particle precipitation in waccm. Journal of Geophysical Research: Atmospheres, 118(20), 11–636.

Holt, L. A., Randall, C. E., Peck, E. D., Marsh, D. R., Smith, A. K., & Harvey, V. L. (2013b). The influence of major sudden stratospheric warming and elevated stratopause events on the effects of energetic particle precipitation in waccm. Journal of Geophysical Research: Atmospheres, 118(20), 11,636-11,646. Retrieved from `https://agupubs.onlinelibrary.wiley.com/doi/abs/10.1002/2013JD020294` doi: 10.1002/2013JD020294

Horanyi, M., Cravens, T., & Waite Jr, J. (1988). The precipitation of energetic heavy ions into the upper atmosphere of jupiter. Journal of Geophysical Research: Space Physics, 93(A7), 7251–7271.

Horne, R. B., Lam, M. M., & Green, J. C. (2009). Energetic electron precipitation from the outer radiation belt during geomagnetic storms. Geophysical Research Letters, 36(19).

Horne, R. B., Thorne, R. M., Glauert, S. A., Douglas Menietti, J., Shprits, Y. Y., & Gurnett, D. A. (2008). Gyro-resonant electron acceleration at jupiter. Nature Physics, 4(4), 301–304.

Hospodarsky, G., Sigsbee, K., Leisner, J., Menietti, J., Kurth, W., Gurnett, D., ... Santolík, O. (2012). Plasma wave observations at earth, jupiter, and saturn. Dynamics of the Earth's radiation belts and inner magnetosphere, 199, 415–430.

Hubbell, J. H., & Seltzer, S. M. (1995). Tables of x-ray mass attenuation coefficients and mass energy-absorption coefficients 1 kev to 20 mev for elements z= 1 to 92 and 48 additional substances of dosimetric interest (Tech. Rep.). National Inst. of Standards and Technology-PL, Gaithersburg, MD (United ....

Imhof, W., Kilner, J., & Reagan, J. (1985). Morphological study of energetic electron precipitation events using the satellite bremsstrahlung x ray technique. Journal of Geophysical Research: Space Physics, 90(A2), 1543–1552.

Imhof, W., Nakano, G., Johnson, R., & Reagan, J. (1974). Satellite observations of bremsstrahlung from widespread energetic electron precipitation events. Journal of Geophysical Research, 79(4), 565–574.

Imhof, W., Spear, K., Hamilton, J., Higgins, B., Murphy, M., Pronko, J., ... others (1995). The polar ionospheric x-ray imaging experiment (pixie). Space Science Reviews, 71(1), 385–408.

Isler, R. (1994). An overview of charge-exchange spectroscopy as a plasma diagnostic. Plasma Physics and Controlled Fusion, 36(2), 171.

Ivantchenko, A. V., Ivanchenko, V. N., Molina, J.-M. Q., & Incerti, S. L. (2012). Geant4 hadronic physics for space radiation environment. International journal of radiation biology, 88(1-2), 171–175.

Jackson, J. (2021). Classical electrodynamics third edition.

Jackson, J. D. (2007). Electrodynamics. The Optics Encyclopedia: Basic Foundations and Practical Applications.

Jakosky, B., Brain, D., Chaffin, M., Curry, S., Deighan, J., Grebowsky, J., ... Zurek, R. (2018). Loss of the martian atmosphere to space: Present-day loss rates determined from maven observations and integrated loss through time. Icarus, 315, 146-157. Retrieved from `https://www.sciencedirect.com/science/article/pii/S0019103517306917` doi: https://doi.org/10.1016/j.icarus.2018.05.030

Johnson, A., Shumko, M., Griffith, B., Klumpar, D. M., Sample, J., Springer, L., ... others (2020). The firebird-ii cubesat mission: Focused investigations of relativistic electron burst intensity, range, and dynamics. Review of Scientific Instruments, 91(3), 034503.

Johnson, A., Shumko, M., Sample, J., Griffith, B., Klumpar, D., Spence, H., & Blake, J. B. (2021). The energy spectra of electron microbursts between 200 kev and 1 mev. Journal of Geophysical Research: Space Physics, 126(11), e2021JA029709.

Johnstone, A. (1978). Pulsating aurora. Nature, 274(5667), 119–126.

Jones, F. C. (1968). Calculated spectrum of inverse-compton-scattered photons. Physical Review, 167(5), 1159.

Judge, P., Kleint, L., Uitenbroek, H., Rempel, M., Suematsu, Y., & Tsuneta, S. (2015). Photon mean free paths, scattering, and ever-increasing telescope resolution. Solar Physics, 290, 979–996.

Kao, M. M., Mioduszewski, A. J., Villadsen, J., & Shkolnik, E. L. (2023). Resolved imaging confirms a radiation belt around an ultracool dwarf. Nature, 1–3.

Kawamura, M., Sakanoi, T., Fukizawa, M., Miyoshi, Y., Hosokawa, K., Tsuchiya, F., ...

Brändström, U. (2021). Simultaneous pulsating aurora and microburst observations with ground-based fast auroral imagers and cubesat firebird-ii. Geophysical Research Letters, 48(18), e2021GL094494. Retrieved from https://agupubs.onlinelibrary.wiley.com/doi/abs/10.1029/2021GL094494 (e2021GL094494 2021GL094494) doi: https://doi.org/10.1029/2021GL094494

Kawrakow, I., Rogers, D., & Walters, B. (2004). Large efficiency improvements in beamnrc using directional bremsstrahlung splitting: directional bremsstrahlung splitting. Medical physics, 31(10), 2883–2898.

Kellman, P., & McVeigh, E. R. (2005). Image reconstruction in snr units: a general method for snr measurement. Magnetic resonance in medicine, 54(6), 1439–1447.

Kennel, C. F. (1969). Consequences of a magnetospheric plasma. Reviews of Geophysics, 7(1-2), 379–419.

Kennel, C. F., & Petschek, H. (1966). Limit on stably trapped particle fluxes. Journal of Geophysical Research, 71(1), 1–28.

Kersten, K., Cattell, C., Breneman, A., Goetz, K., Kellogg, P., Wygant, J., ... Roth, I. (2011). Observation of relativistic electron microbursts in conjunction with intense radiation belt whistler-mode waves. Geophysical Research Letters, 38(8).

Khazanov, G., Robinson, R., Zesta, E., Sibeck, D., Chu, M., & Grubbs, G. (2018). Impact of precipitating electrons and magnetosphere-ionosphere coupling processes on ionospheric conductance. Space Weather, 16(7), 829–837.

Khodachenko, M. L., Ribas, I., Lammer, H., Grießmeier, J.-M., Leitner, M., Selsis, F., ... Rucker, H. O. (2007). Coronal mass ejection (cme) activity of low mass m stars as an important factor for the habitability of terrestrial exoplanets. i. cme impact on expected magnetospheres of earth-like exoplanets in close-in habitable zones. Astrobiology, 7(1), 167-184. Retrieved from https://doi.org/10.1089/ast.2006.0127 (PMID: 17407406) doi: 10.1089/ast.2006.0127

King, M. A., Doherty, P. W., Schwinger, R. B., & Penney, B. C. (1983). A wiener filter for nuclear medicine images. Medical physics, 10(6), 876–880.

Kivelson, M. G., & Bagenal, F. (2014). Chapter 7 - planetary magnetospheres. In T. Spohn, D. Breuer, & T. V. Johnson (Eds.), Encyclopedia of the solar system (third edition) (Third Edition ed., p. 137-157). Boston: Elsevier. Retrieved from https://www.sciencedirect.com/science/article/pii/B9780124158450000074 doi: https://doi.org/10.1016/B978-0-12-415845-0.00007-4

Kivelson, M. G., & Russell, C. T. (1995). Introduction to space physics. Cambridge University Press.

Klein, O., & Nishina, Y. (1928). The scattering of light by free electrons according to dirac's new relativistic dynamics. Nature, 122(3072), 398–399.

Knödlseder, J., Jean, P., Lonjou, V., Weidenspointner, G., Guessoum, N., Gillard, W., ... others (2005). The all-sky distribution of 511 kev electron-positron annihilation emission. Astronomy & Astrophysics, 441(2), 513–532.

Koch, H., & Motz, J. (1959). Bremsstrahlung cross-section formulas and related data. Reviews of modern physics, 31(4), 920.

Köhn, C., & Ebert, U. (2014). Angular distribution of bremsstrahlung photons and of positrons for calculations of terrestrial gamma-ray flashes and positron beams. Atmospheric Research, 135, 432–465.

Kollmann, P., Clark, G. B., Li, W., Jaynes, A. N., Blum, L. W., Marshall, R. A., ... others (2022). Heliophysics at the solar system's most powerful particle accelerator: the compass mission to jupiter. In Agu fall meeting abstracts (Vol. 2022, pp. SM22E–1956).

Kollmann, P., Roussos, E., Paranicas, C., Woodfield, E. E., Mauk, B., Clark, G., ... Vandegriff, J. (2018). Electron acceleration to mev energies at jupiter and saturn. Journal of Geophysical Research: Space Physics, 123(11), 9110–9129.

Koons, H., Edgar, B., & Vampola, A. (1981). Precipitation of inner zone electrons by whistler mode waves from the vlf transmitters ums and nwc. Journal of Geophysical Research: Space Physics, 86(A2), 640–648.

Kouker, W., Langbein, I., Reddmann, T., & Ruhnke, R. (1999). The karlsruhe simulation model of the middle atmosphere (kasima). Forschungszentrum Karlsruhe, Germany, Version, 2.

Krajewska, K., Vélez, F. C., & Kamiński, J. (2015). Generalized klein-nishina formula. Physical Review A, 91(6), 062106.

Krause, L. H. (1998). The interaction of relativistic electron beams with the near-earth space environment. University of Michigan.

Krivonos, R., Tsygankov, S., Lutovinov, A., Revnivtsev, M., Churazov, E., & Sunyaev, R. (2012). Integral/ibis nine-year galactic hard x-ray survey. Astronomy & Astrophysics, 545, A27.

Krivonos, R., Tsygankov, S., Revnivtsev, M., Grebenev, S., Churazov, E., & Sunyaev, R. (2010). Integral/ibis 7-year all-sky hard x-ray survey-ii. catalog of sources. Astronomy & Astrophysics, 523, A61.

Kruse, P. (2005). The photon detection process. Optical and Infrared Detectors, 5–69.

Lagoutte, D., Brochot, J., De Carvalho, D., Elie, F., Harivelo, F., Hobara, Y., ... others (2006). The demeter science mission centre. Planetary and Space Science, 54(5), 428–440.

Lampton, M., Margon, B., & Bowyer, S. (1976). Parameter estimation in x-ray astronomy. Astrophysical Journal, vol. 208, Aug. 15, 1976, pt. 1, p. 177-190., 208, 177–190.

Langmuir, I. (1915). The melting-point of tungsten. Physical Review, 6(2), 138.

Laundal, K., & Østgaard, N. (2009). Asymmetric auroral intensities in the earth's northern and southern hemispheres. Nature, 460(7254), 491–493.

Lee, B.-Z., & Lee, D. (1998). Spontaneous growth mechanism of tin whiskers. Acta Materialia, 46(10), 3701–3714.

Lehtinen, N. G., Bell, T. F., & Inan, U. S. (1999). Monte carlo simulation of runaway mev electron breakdown with application to red sprites and terrestrial gamma ray flashes. Journal of Geophysical Research: Space Physics, 104(A11), 24699–24712.

Lei, F., Truscott, R., Dyer, C., Quaghebeur, B., Heynderickx, D., Nieminen, R., ... Daly, E. (2002). Mulassis: A geant4-based multilayered shielding simulation tool. IEEE Transactions on Nuclear Science, 49(6), 2788–2793.

Lemaire, J. (1975). The mechanisms of formation of the plasmapause.

Lemaire, J. F., & Gringauz, K. I. (1998). The earth's plasmasphere.

Li, W., & Hudson, M. (2019). Earth's van allen radiation belts: From discovery to the van allen probes era. Journal of Geophysical Research: Space Physics, 124(11), 8319–8351.

Li, W., Ni, B., Thorne, R., Bortnik, J., Green, J., Kletzing, C., ... Hospodarsky, G. (2013). Constructing the global distribution of chorus wave intensity using measurements of electrons by the poes satellites and waves by the van allen probes. Geophysical Research Letters, 40(17), 4526–4532.

Li, X., Selesnick, R., Schiller, Q., Zhang, K., Zhao, H., Baker, D. N., & Temerin, M. A. (2017). Measurement of electrons from albedo neutron decay and neutron density in near-earth space. Nature, 552(7685), 382–385.

Li, X., & Temerin, M. A. (2001). The electron radiation belt. Space Science Reviews, 95(1-2), 569–580.

Liang, X., Min, J., Chen, J., Wang, D., Li, H., Wang, Y., ... Zhang, J. (2012). Metal/semiconductor contacts for schottky and photoconductive cdznte detector. Physics Procedia, 32, 545–550.

Lindal, G. F., Wood, G., Levy, G., Anderson, J., Sweetnam, D., Hotz, H., ... others (1981). The atmosphere of jupiter: An analysis of the voyager radio occultation measurements. Journal of Geophysical Research: Space Physics, 86(A10), 8721–8727.

Liu, H.-L., Bardeen, C. G., Foster, B. T., Lauritzen, P., Liu, J., Lu, G., ... Wang, W. (2018a). Development and validation of the whole atmosphere community climate model with thermosphere and ionosphere extension (waccm-x 2.0). Journal of Advances in Modeling Earth Systems, 10(2), 381-402. Retrieved from https://agupubs.onlinelibrary.wiley.com/doi/abs/10.1002/2017MS001232 doi: 10.1002/2017MS001232

Liu, H.-L., Bardeen, C. G., Foster, B. T., Lauritzen, P., Liu, J., Lu, G., ... others (2018b). Development and validation of the whole atmosphere community climate model with thermosphere and ionosphere extension (waccm-x 2.0). Journal of Advances in Modeling Earth Systems, 10(2), 381–402.

Long, M., Ni, B., Cao, X., Gu, X., Kollmann, P., Luo, Q., ... Shprits, Y. Y. (2022). Losses of radiation belt energetic particles by encounters with four of the inner moons of jupiter. Journal of Geophysical Research: Planets, 127(2), e2021JE007050.

Longden, N., Denton, M. H., & Honary, F. (2008). Particle precipitation during icme-driven and cir-driven geomagnetic storms. Journal of Geophysical Research: Space Physics, 113(A6).

Lönnblad, L. (1994). Clhep—a project for designing a c++ class library for high energy physics. Computer Physics Communications, 84(1-3), 307–316.

Looper, M. D., Blake, J. B., & Mewaldt, R. A. (2005). Response of the inner radiation belt to the violent sun-earth connection events of october–november 2003. Geophysical Research Letters, 32(3). Retrieved from https://agupubs.onlinelibrary.wiley.com/doi/abs/10.1029/2004GL021502 doi: 10.1029/2004GL021502

Lorence Jr, L., Morel, J., & Valdez, G. (1989). Physics guide to cepxs: a multigroup coupled electron-photon cross-section generating code (Tech. Rep.). Sandia National Lab.(SNL-NM), Albuquerque, NM (United States).

Lotz, W. (1967). An empirical formula for the electron-impact ionization cross-section. Zeitschrift für Physik, 206(2), 205–211.

Lund, M., & Jevremovic, T. (2019). Enhanced geant4 monte carlo simulations of the space radiation effects on the international space station and apollo missions using high-performance computing environment. Acta Astronautica, 165, 219–228.

Luo, Q., & Melrose, D. (2007a). Pulsar radiation belts and transient radio emission. Monthly Notices of the Royal Astronomical Society, 378(4), 1481–1490.

Luo, Q., & Melrose, D. (2007b, 06). Pulsar radiation belts and transient radio emission. Monthly Notices of the Royal Astronomical Society, 378(4), 1481-1490. Retrieved from https://doi.org/10.1111/j.1365-2966.2007.11889.x doi: 10.1111/j.1365-2966.2007.11889.x

Lutz, G. (2006). Silicon drift and pixel devices for x-ray imaging and spectroscopy. Journal of synchrotron radiation, 13(2), 99–109.

Lyons, L. (1997). Magnetospheric processes leading to precipitation. Space Science Reviews, 80(1-2), 109–132.

Lyons, L. R., & Thorne, R. M. (1973). Equilibrium structure of radiation belt electrons. Journal of Geophysical Research, 78(13), 2142–2149.

Ma, Q., Xu, W., Sanchez, E. R., Marshall, R. A., Bortnik, J., Reyes, P. M., ... others (2022). Analysis of electron precipitation and ionospheric density enhancements due to hiss using incoherent scatter radar and arase observations. Journal of Geophysical Research: Space

Physics, 127(8), e2022JA030545.
Madej, J. (1989). The effects of compton scattering in x-ray spectra. Astrophysical Journal, Part 1 (ISSN 0004-637X), vol. 339, April 1, 1989, p. 386-396., 339, 386–396.
Mann, I., Ward, W. E., Cully, C., Connors, M., Rankin, R., Zee, R. E., ... others (2022). The radiation impacts on climate and atmospheric loss satellite (radicals) mission. 44th COSPAR Scientific Assembly. Held 16-24 July, 44, 735.
Mann, I. R., Ozeke, L., Murphy, K. R., Claudepierre, S. G., Turner, D. L., Baker, D. N., ... others (2016). Explaining the dynamics of the ultra-relativistic third van allen radiation belt. Nature Physics, 12(10), 978–983.
Mannucci, A., Tsurutani, B., Iijima, B., Komjathy, A., Saito, A., Gonzalez, W., ... Skoug, R. (2005). Dayside global ionospheric response to the major interplanetary events of october 29–30, 2003 "halloween storms". Geophysical Research Letters, 32(12).
Marcia, R. F., Harmany, Z. T., & Willett, R. M. (2009). Compressive coded aperture imaging. In Computational imaging vii (Vol. 7246, pp. 106–118).
Mark, T. (1982). Fundamental aspects of electron impact ionization. International Journal of Mass Spectrometry and Ion Physics, 45, 125–145.
Märk, T. D., & Dunn, G. H. (2013). Electron impact ionization. Springer Science & Business Media.
Marshall, R., & Bortnik, J. (2018). Pitch angle dependence of energetic electron precipitation: Energy deposition, backscatter, and the bounce loss cone. Journal of Geophysical Research: Space Physics, 123(3), 2412–2423.
Marshall, R. A., & Cully, C. M. (2020). Atmospheric effects and signatures of high-energy electron precipitation. In The dynamic loss of earth's radiation belts (pp. 199–255). Elsevier.
Marshall, R. A., Newsome, R., Lehtinen, N., Lavassar, N., & Inan, U. (2010). Optical signatures of radiation belt electron precipitation induced by ground-based vlf transmitters. Journal of Geophysical Research: Space Physics, 115(A8).
Marshall, R. A., Xu, W., Woods, T., Cully, C., Jaynes, A., Randall, C., ... others (2020). The aepex mission: Imaging energetic particle precipitation in the atmosphere through its bremsstrahlung x-ray signatures. Advances in Space Research.
Martinello, M. (2012). Coded aperture imaging (Unpublished doctoral dissertation). Heriot-Watt University Edinburgh, Scotland.
Mauk, B., Fox, N. J., Kanekal, S., Kessel, R., Sibeck, D., & Ukhorskiy, a. A. (2012). Science objectives and rationale for the radiation belt storm probes mission. The Van Allen Probes Mission, 3–27.
Mauk, B., Mitchell, D., Krimigis, S., Roelof, E., & Paranicas, C. (2003). Energetic neutral atoms from a trans-europa gas torus at jupiter. Nature, 421(6926), 920–922.
Mauk, B. H., Clark, G., Gladstone, G. R., Kotsiaros, S., Adriani, A., Allegrini, F., ... others (2020). Energetic particles and acceleration regions over jupiter's polar cap and main aurora: A broad overview. Journal of Geophysical Research: Space Physics, 125(3), e2019JA027699.
Mauk, B. H., Haggerty, D., Paranicas, C., Clark, G., Kollmann, P., Rymer, A., ... others (2017). Discrete and broadband electron acceleration in jupiter's powerful aurora. Nature, 549(7670), 66–69.
Mayaud, P. (1978). The annual and daily variations of the dst index. Geophysical Journal International, 55(1), 193–201.
Mekler, Y., & Eviatar, A. (1980). Time analysis of volcanic activity on io by means of plasma observations. Journal of Geophysical Research: Space Physics, 85(A3), 1307–1310.
Metzger, A. E., Gilman, D. A., Luthey, J. L., Hurley, K. C., Schnopper, H. W., Seward, F. D., &

Sullivan, J. D. (1983). The detection of x rays from jupiter. Journal of Geophysical Research: Space Physics, 88(A10), 7731–7741.

Millan, R., McCarthy, M., Sample, J., Smith, D., Thompson, L., McGaw, D., ... others (2013). The balloon array for rbsp relativistic electron losses (barrel). Space Science Reviews, 179(1-4), 503–530.

Millan, R., & Thorne, R. (2007). Review of radiation belt relativistic electron losses. Journal of Atmospheric and Solar-Terrestrial Physics, 69(3), 362–377.

Mironova, I. A., Aplin, K. L., Arnold, F., Bazilevskaya, G. A., Harrison, R. G., Krivolutsky, A. A., ... Usoskin, I. G. (2015). Energetic particle influence on the earth's atmosphere. Space science reviews, 194, 1–96.

Moderski, R., Sikora, M., Coppi, P. S., & Aharonian, F. (2005). Klein—nishina effects in the spectra of non-thermal sources immersed in external radiation fields. Monthly Notices of the Royal Astronomical Society, 363(3), 954–966.

Mori, K., Hailey, C., Bridges, G., Mandel, S., Garvin, A., Grefenstette, B., ... others (2022). Observation and origin of non-thermal hard x-rays from jupiter. Nature Astronomy, 1–7.

Moskalenko, I. V., & Strong, A. W. (2000). Anisotropic inverse compton scattering in the galaxy. The Astrophysical Journal, 528(1), 357.

Motz, J., Olsen, H. A., & Koch, H. (1969). Pair production by photons. Reviews of Modern Physics, 41(4), 581.

Mould, R. F. (1995). The early history of x-ray diagnosis with emphasis on the contributions of physics 1895-1915. Physics in Medicine & Biology, 40(11), 1741.

Mutz, J.-L., Bonnet, O., Fairbend, R., Schyns, E., & Seguy, J. (2007). Micro-pore optics: from planetary x-rays to industrial market. In Quantum sensing and nanophotonic devices iv (Vol. 6479, pp. 64–71).

Narita, Y. (2017). Wave analysis methods for space plasma experiment. Nonlinear Processes in Geophysics, 24(2), 203–214.

National Academies of Sciences, Engineering, and Medicine and others. (2022). Origins, worlds, and life: A decadal strategy for planetary science and astrobiology 2023-2032.

Nénon, Q., Sicard, A., Kollmann, P., Garrett, H., Sauer, S., & Paranicas, C. (2018). A physical model of the proton radiation belts of jupiter inside europa's orbit. Journal of Geophysical Research: Space Physics, 123(5), 3512–3532.

Newell, P., Sotirelis, T., & Wing, S. (2009). Diffuse, monoenergetic, and broadband aurora: The global precipitation budget. Journal of Geophysical Research: Space Physics, 114(A9).

Ni, B., Thorne, R. M., Zhang, X., Bortnik, J., Pu, Z., Xie, L., ... others (2016). Origins of the earth's diffuse auroral precipitation. Space Science Reviews, 200, 205–259.

Nishida, A. (1966). Formation of plasmapause, or magnetospheric plasma knee, by the combined action of magnetospheric convection and plasma escape from the tail. Journal of Geophysical Research, 71(23), 5669–5679.

Nishimura, Y., Bortnik, J., Li, W., Thorne, R. M., Lyons, L. R., Angelopoulos, V., ... others (2010). Identifying the driver of pulsating aurora. science, 330(6000), 81–84.

Northrop, T. G. (1961). The guiding center approximation to charged particle motion. Annals of Physics, 15(1), 79–101.

Northrop, T. G. (1963). Adiabatic charged-particle motion. Reviews of Geophysics, 1(3), 283–304.

Nulsen, S., Kraft, R., Germain, G., Dunn, W., Tremblay, G., Beegle, L., ... others (2020). X-ray emission from jupiter's galilean moons: A tool for determining their surface composition and particle environment. The Astrophysical Journal, 895(2), 79.

Numazawa, M., Ezoe, Y., Ohashi, T., Ishikawa, K., Miyoshi, Y., Shiota, D., ... Branduardi-

Raymont, G. (2021a). Suzaku observations of jovian diffuse hard x-ray emission. Publications of the Astronomical Society of Japan.

Numazawa, M., Ezoe, Y., Ohashi, T., Ishikawa, K., Miyoshi, Y., Shiota, D., ... Branduardi-Raymont, G. (2021b, 06). Suzaku observations of Jovian diffuse hard X-ray emission. Publications of the Astronomical Society of Japan, 73(4), 894-911. Retrieved from https://doi.org/10.1093/pasj/psab053 doi: 10.1093/pasj/psab053

Nymmik, R., Panasyuk, M., Pervaja, T., & Suslov, A. (1992). A model of galactic cosmic ray fluxes. International Journal of Radiation Applications and Instrumentation. Part D. Nuclear Tracks and Radiation Measurements, 20(3), 427–429.

Obayashi, T., & Hakura, Y. (1960a). Enhanced ionization in the polar ionosphere associated with geomagnetic storms. Journal of Atmospheric and Terrestrial Physics, 18(2), 101-122. Retrieved from https://www.sciencedirect.com/science/article/pii/0021916960900829 doi: https://doi.org/10.1016/0021-9169(60)90082-9

Obayashi, T., & Hakura, Y. (1960b). Enhanced ionization in the polar ionosphere associated with geomagnetic storms. Journal of Atmospheric and Terrestrial Physics, 18(2-3), 101–122.

O'Brien, T. P., & McPherron, R. L. (2000). An empirical phase space analysis of ring current dynamics: Solar wind control of injection and decay. Journal of Geophysical Research: Space Physics, 105(A4), 7707–7719.

Omura, Y., Hsieh, Y.-K., Foster, J. C., Erickson, P. J., Kletzing, C. A., & Baker, D. N. (2019). Cyclotron acceleration of relativistic electrons through landau resonance with obliquely propagating whistler-mode chorus emissions. Journal of Geophysical Research: Space Physics, 124(4), 2795–2810.

O'Neill, P. M. (2010). Badhwar–o'neill 2010 galactic cosmic ray flux model—revised. IEEE Transactions on Nuclear Science, 57(6), 3148–3153.

Østgaard, N., Stadsnes, J., Aarsnes, K., Søraas, F., Måseide, K., Smith, M., & Sharber, J. (1998). Simultaneous measurements of x-rays and electrons during a pulsating aurora. Annales Geophysicae, 16(2), 148–160. Retrieved from https://angeo.copernicus.org/articles/16/148/1998/ doi: 10.1007/s00585-998-0148-0

Østgaard, N., Stadsnes, J., Bjordal, J., Germany, G., Vondrak, R., Parks, G., ... Pronko, J. (2001). Auroral electron distributions derived from combined uv and x-ray emissions. Journal of Geophysical Research: Space Physics, 106(A11), 26081–26089.

O'Donoghue, D. (1995). High speed ccd photometry. Open Astronomy, 4(4), 519–526.

Patrick, M. R. (2022). Measuring energetic electron precipitation using high altitude balloons and x-ray spectroscopy.

Peterson, L. E. (1975). Instrumental technique in x-ray astronomy. Annual review of astronomy and astrophysics, 13(1), 423–509.

Petrinec, S., McKenzie, D., Imhof, W., Mobilia, J., & Chenette, D. (2000). Studies of x-ray observations from pixie. Journal of Atmospheric and Solar-Terrestrial Physics, 62(10), 875–888.

Pettit, J., Randall, C., Peck, E., Marsh, D., van de Kamp, M., Fang, X., ... Funke, B. (2019). Atmospheric effects of > 30-kev energetic electron precipitation in the southern hemisphere winter during 2003. Journal of Geophysical Research: Space Physics, 124(10), 8138–8153.

Pettit, J. M., Randall, C. E., Peck, E. D., & Harvey, V. L. (2021). A new meped-based precipitating electron data set. Journal of Geophysical Research: Space Physics, 126(12), e2021JA029667.

Picone, J., Hedin, A., Drob, D. P., & Aikin, A. (2002). NRLMSISE-00 empirical model of the atmosphere: Statistical comparisons and scientific issues. Journal of Geophysical Research: Space Physics, 107(A12), SIA–15.

Prangé, R., Rego, D., Southwood, D., Zarka, P., Miller, S., & Ip, W. (1996). Rapid energy dissipation and variability of the lo–jupiter electrodynamic circuit. Nature, 379(6563), 323–325.

Pratt, R., Ron, A., & Tseng, H. (1973). Atomic photoelectric effect above 10 kev. Reviews of Modern physics, 45(2), 273.

Press, W. H., & Teukolsky, S. A. (1990). Savitzky-golay smoothing filters. Computers in Physics, 4(6), 669–672.

Randall, C., Harvey, V., Manney, G., Orsolini, Y., Codrescu, M., Sioris, C., ... others (2005). Stratospheric effects of energetic particle precipitation in 2003–2004. Geophysical Research Letters, 32(5).

Randall, C., Harvey, V., Singleton, C., Bailey, S., Bernath, P., Codrescu, M., ... Russell III, J. (2007). Energetic particle precipitation effects on the southern hemisphere stratosphere in 1992–2005. Journal of Geophysical Research: Atmospheres, 112(D8).

Randall, C., Harvey, V., Singleton, C., Bernath, P., Boone, C., & Kozyra, J. (2006). Enhanced nox in 2006 linked to strong upper stratospheric arctic vortex. Geophysical Research Letters, 33(18).

Randall, C., Harvey, V. L., Siskind, D., France, J., Bernath, P., Boone, C., & Walker, K. (2009). Nox descent in the arctic middle atmosphere in early 2009. Geophysical Research Letters, 36(18).

Randall, C. E., Harvey, V. L., Holt, L. A., Marsh, D. R., Kinnison, D., Funke, B., & Bernath, P. F. (2015). Simulation of energetic particle precipitation effects during the 2003–2004 arctic winter. Journal of Geophysical Research: Space Physics, 120(6), 5035–5048.

Ranieri, M., Badiali, M., Cardini, D., Emanuele, A., & Auriemma, G. (1981). Coded aperture telescopes for hard x-ray astronomy. Journal of the British Interplanetary Society, 34, 135–138.

Rapp, D., & Francis, W. E. (1962). Charge exchange between gaseous ions and atoms. The Journal of Chemical Physics, 37(11), 2631–2645.

Reagan, J., Meyerott, R., Evans, J., Imhof, W., & Joiner, R. (1983). The effects of energetic particle precipitation on the atmospheric electric circuit. Journal of Geophysical Research: Oceans, 88(C6), 3869–3878.

Rees, M. H. (1989). Physics and chemistry of the upper atmosphere. Cambridge University Press.

Reeves, G., Spence, H. E., Henderson, M., Morley, S., Friedel, R., Funsten, H., ... others (2013). Electron acceleration in the heart of the van allen radiation belts. Science, 341(6149), 991–994.

Reid, R., Marshall, R. A., Blum, L. W., & Berland, G. (2022). Pitch-angle resolved measurements of energetic electrons using coded aperture imaging. In Agu fall meeting abstracts (Vol. 2022, pp. SH52F–1517).

Reiff, P., Hill, T., & Burch, J. (1977). Solar wind plasma injection at the dayside magnetospheric cusp. Journal of Geophysical Research, 82(4), 479–491.

Ridley, A., Gombosi, T. I., & DeZeeuw, D. (2004). Ionospheric control of the magnetosphere: Conductance. In Annales geophysicae (Vol. 22, pp. 567–584).

Ripoll, J.-F., Claudepierre, S. G., Ukhorskiy, A. Y., Colpitts, C., Li, X., Fennell, J. F., & Crabtree, C. (2020). Particle dynamics in the earth's radiation belts: Review of current research and open questions. Journal of Geophysical Research: Space Physics, 125(5), e2019JA026735. Retrieved from https://agupubs.onlinelibrary.wiley.com/doi/abs/10.1029/2019JA026735 (e2019JA026735 2019JA026735) doi: https://doi.org/10.1029/2019JA026735

Robinson, R., Vondrak, R., Miller, K., Dabbs, T., & Hardy, D. (1987). On calculating ionospheric conductances from the flux and energy of precipitating electrons. Journal of Geophysical Research: Space Physics, 92(A3), 2565–2569.

Roble, R., & Ridley, E. (1987). An auroral model for the ncar thermospheric general circulation model (tgcm).

Rodger, C. J., Clilverd, M. A., Green, J. C., & Lam, M. M. (2010). Use of poes sem-2 observations to examine radiation belt dynamics and energetic electron precipitation into the atmosphere. Journal of Geophysical Research: Space Physics, 115(A4).

Rodger, C. J., Clilverd, M. A., Thomson, N. R., Gamble, R. J., Seppälä, A., Turunen, E., ... Berthelier, J.-J. (2007). Radiation belt electron precipitation into the atmosphere: Recovery from a geomagnetic storm. Journal of Geophysical Research: Space Physics, 112(A11).

Rodger, C. J., Kavanagh, A. J., Clilverd, M. A., & Marple, S. R. (2013). Comparison between poes energetic electron precipitation observations and riometer absorptions: Implications for determining true precipitation fluxes. Journal of Geophysical Research: Space Physics, 118(12), 7810-7821. Retrieved from https://agupubs.onlinelibrary.wiley.com/doi/abs/10.1002/2013JA019439 doi: https://doi.org/10.1002/2013JA019439

Rodger, C. J., McCormick, R. J., & Clilverd, M. A. (2004). Testing the importance of precipitation loss mechanisms in the inner radiation belt. Geophysical research letters, 31(10).

Rostoker, G. (1972). Geomagnetic indices. Reviews of Geophysics, 10(4), 935–950.

Roussos, E., & Kollmann, P. (2021). The radiation belts of jupiter and saturn. Magnetospheres in the solar system, 499–514.

Royrvik, O., & Davis, T. (1977). Pulsating aurora: Local and global morphology. Journal of Geophysical Research, 82(29), 4720–4740.

Russell, C. (1993). Planetary magnetospheres. Reports on Progress in Physics, 56(6), 687.

Sanchez, E. R., Ma, Q., Xu, W., Marshall, R. A., Bortnik, J., Reyes, P., ... Kaeppler, S. (2022). A test of energetic particle precipitation models using simultaneous incoherent scatter radar and van allen probes observations. Journal of Geophysical Research: Space Physics, 127(8), e2021JA030179.

Saur, J., Janser, S., Schreiner, A., Clark, G., Mauk, B. H., Kollmann, P., ... Kotsiaros, S. (2018). Wave-particle interaction of alfvén waves in jupiter's magnetosphere: Auroral and magnetospheric particle acceleration. Journal of Geophysical Research: Space Physics, 123(11), 9560–9573.

Sazonov, S., Churazov, E., Sunyaev, R., & Revnivtsev, M. (2007, 05). Hard X-ray emission of the Earth's atmosphere: Monte Carlo simulations. Monthly Notices of the Royal Astronomical Society, 377(4), 1726-1736. Retrieved from https://doi.org/10.1111/j.1365-2966.2007.11746.x doi: 10.1111/j.1365-2966.2007.11746.x

Scarf, F. (1976). Plasma physics and wave-particle interactions at jupiter. In Iau colloq. 30: Jupiter: Studies of the interior, atmosp here, magnetosphere and satellites (pp. 870–895).

Schmidt, H., Brasseur, G. P., Charron, M., Manzini, E., Giorgetta, M. A., Diehl, T., ... Walters, S. (2006). The hammonia chemistry climate model: Sensitivity of the mesopause region to the 11-year solar cycle and co2 doubling. Journal of Climate, 19(16), 3903-3931. Retrieved from https://doi.org/10.1175/JCLI3829.1 doi: 10.1175/JCLI3829.1

Seiff, A., Kirk, D. B., Knight, T. C., Mihalov, J. D., Blanchard, R. C., Young, R. E., ... others (1996). Structure of the atmosphere of jupiter: Galileo probe measurements. Science, 272(5263), 844–845.

Seiff, A., Kirk, D. B., Knight, T. C., Young, R. E., Mihalov, J. D., Young, L. A., ... Atkinson, D. (1998). Thermal structure of jupiter's atmosphere near the edge of a 5-μm hot spot in the

north equatorial belt. Journal of Geophysical Research: Planets, 103(E10), 22857–22889.
Selesnick, R., Baker, D., Jaynes, A., Li, X., Kanekal, S., Hudson, M., & Kress, B. (2014). Observations of the inner radiation belt: Crand and trapped solar protons. Journal of Geophysical Research: Space Physics, 119(8), 6541–6552.
Selesnick, R., & Blake, J. (1997). Dynamics of the outer radiation belt. Geophysical research letters, 24(11), 1347–1350.
Selesnick, R. S., Looper, M. D., & Albert, J. M. (2004). Low-altitude distribution of radiation belt electrons. Journal of Geophysical Research: Space Physics, 109(A11). Retrieved from https://agupubs.onlinelibrary.wiley.com/doi/abs/10.1029/2004JA010611 doi: https://doi.org/10.1029/2004JA010611
Seltzer, S. M. (1996). Tables and graphs of photon mass attenuation coefficients and mass energy-absorption coefficients for photon energies 1 kev to 20 mev for elements z= 1 to 92. The X-Ray Attenuation and Absorption for Materials of Dosimetric Interest Database.
Seltzer, S. M., & Berger, M. J. (1986). Bremsstrahlung energy spectra from electrons with kinetic energy 1 kev–10 gev incident on screened nuclei and orbital electrons of neutral atoms with z= 1–100. Atomic data and nuclear data tables, 35(3), 345–418.
Seppälä, A., Clilverd, M. A., Beharrell, M. J., Rodger, C. J., Verronen, P., Andersson, M., & Newnham, D. (2015). Substorm-induced energetic electron precipitation: Impact on atmospheric chemistry. Geophysical Research Letters, 42(19), 8172–8176.
Seppälä, A., Douma, E., Rodger, C., Verronen, P., Clilverd, M. A., & Bortnik, J. (2018). Relativistic electron microburst events: Modeling the atmospheric impact. Geophysical Research Letters, 45(2), 1141–1147.
Sergeev, V., Sazhina, E., Tsyganenko, N., Lundblad, J., & Søraas, F. (1983). Pitch-angle scattering of energetic protons in the magnetotail current sheet as the dominant source of their isotropic precipitation into the nightside ionosphere. Planetary and Space Science, 31(10), 1147–1155.
Sharber, J., Frahm, R., Winningham, J., Biard, J., Lummerzheim, D., Rees, M., ... Imhof, W. (1993). Observations of the uars particle environment monitor and computation of ionization rates in the middle and upper atmosphere during a geomagnetic storm. Geophysical research letters, 20(12), 1319–1322.
Shemansky, D. (1980). Mass-loading and diffusion-loss rates of the io plasma torus. Astrophysical Journal, Part 1, vol. 242, Dec. 15, 1980, p. 1266-1277., 242, 1266–1277.
Shprits, Y., Menietti, J., Gu, X., Kim, K.-C., & Horne, R. (2012). Gyroresonant interactions between the radiation belt electrons and whistler mode chorus waves in the radiation environments of earth, jupiter, and saturn: A comparative study. Journal of Geophysical Research: Space Physics, 117(A11).
Shprits, Y., Thorne, R., Horne, R., Glauert, S., Cartwright, M., Russell, C., ... Kanekal, S. (2006). Acceleration mechanism responsible for the formation of the new radiation belt during the 2003 halloween solar storm. Geophysical Research Letters, 33(5).
Shprits, Y. Y., Menietti, J. D., Drozdov, A. Y., Horne, R. B., Woodfield, E. E., Groene, J. B., ... others (2018). Strong whistler mode waves observed in the vicinity of jupiter's moons. Nature communications, 9(1), 3131.
Shumko, M., Gallardo-Lacourt, B., Halford, A. J., Liang, J., Blum, L. W., Donovan, E., ... Spanswick, E. (2021). A strong correlation between relativistic electron microbursts and patchy aurora. Geophysical Research Letters, 48(18), e2021GL094696.
Shumko, M., Johnson, A. T., Sample, J. G., Griffith, B. A., Turner, D. L., O'Brien, T. P., ... Claudepierre, S. G. (2020). Electron microburst size distribution derived with aerocube-6. Journal of Geophysical Research: Space Physics, 125(3), e2019JA027651.

Shumko, M., Sample, J., Johnson, A., Blake, B., Crew, A., Spence, H., ... Handley, M. (2018). Microburst scale size derived from multiple bounces of a microburst simultaneously observed with the firebird-ii cubesats. Geophysical Research Letters, 45(17), 8811–8818.

Sicard-Piet, A., Bourdarie, S., & Krupp, N. (2011). Jose: A new jovian specification environment model. IEEE Transactions on Nuclear Science, 58(3), 923–931.

Sihver, L., Barghouty, F., & Falconer, D. (2021). Space radiation risk reduction through prediction, detection and protection. In 2021 ieee aerospace conference (50100) (pp. 1–10).

Simms, L. M., Jernigan, J. G., Malphrus, B. K., McNeil, R., Brown, K. Z., Rose, T. G., ... others (2012). Cxbn: a blueprint for an improved measurement of the cosmological x-ray background. In Hard x-ray, gamma-ray, and neutron detector physics xiv (Vol. 8507, pp. 171–182).

Simpson, J., & McKibben, R. (1976). Dynamics of the jovian magnetosphere and energetic particle radiation. In Iau colloq. 30: Jupiter: Studies of the interior, atmosp here, magnetosphere and satellites (pp. 738–766).

Singhal, R., Chakravarty, S., Bhardwaj, A., & Prasad, B. (1992). Energetic electron precipitation in jupiter's upper atmosphere. Journal of Geophysical Research: Planets, 97(E11), 18245–18256.

Sinnhuber, M., Nieder, H., & Wieters, N. (2012). Energetic particle precipitation and the chemistry of the mesosphere/lower thermosphere. Surveys in Geophysics, 33(6), 1281–1334.

Siscoe, G., Eviatar, A., Thorne, R., Richardson, J., Bagenal, F., & Sullivan, J. (1981). Ring current impoundment of the io plasma torus. Journal of Geophysical Research: Space Physics, 86(A10), 8480–8484.

Sivadas, N., Semeter, J., Nishimura, Y., & Mrak, S. (2019). Optical signatures of the outer radiation belt boundary. Geophysical Research Letters, 46(15), 8588–8596.

Skinner, G. K. (1984). Imaging with coded-aperture masks. Nuclear Instruments and Methods in Physics Research, 221(1), 33–40.

Smith, B. A., Soderblom, L. A., Johnson, T. V., Ingersoll, A. P., Collins, S. A., Shoemaker, E. M., ... others (1979). The jupiter system through the eyes of voyager 1. Science, 204(4396), 951–972.

Smith, E., Davis Jr, L., Jones, D., Coleman Jr, P., Colburn, D., Dyal, P., ... Frandsen, A. (1974). The planetary magnetic field and magnetosphere of jupiter: Pioneer 10. Journal of Geophysical Research, 79(25), 3501–3513.

Smith, F. (1999). Industrial applications of x-ray diffraction. CRC press.

Sonwalkar, V. S., & Inan, U. S. (1989). Lightning as an embryonic source of vlf hiss. Journal of Geophysical Research: Space Physics, 94(A6), 6986–6994.

Sousa, A. P. (2018). Global and seasonal effects of lightning-induced electron precipitation. Stanford University.

Southwood, D., & Wolf, R. (1978). An assessment of the role of precipitation in magnetospheric convection. Journal of Geophysical Research: Space Physics, 83(A11), 5227–5232.

Stenzel, R. (1976). Whistler wave propagation in a large magnetoplasma. The physics of fluids, 19(6), 857–864.

Stephen, J. (1991). Techniques of coded aperture imaging for gamma-ray astronomy. Advances in Space Research, 11(8), 407–418.

Stern, D. P. (1983). The origins of birkeland currents. Reviews of geophysics, 21(1), 125–138.

Strangeway, R., Russell, C. T., Carlson, C., McFadden, J., Ergun, R., Temerin, M., ... Moore, T. (2000). Cusp field-aligned currents and ion outflows. Journal of Geophysical Research: Space Physics, 105(A9), 21129–21141.

Strazzulla, G., Brucato, J., Cimino, G., Leto, G., & Spinella, F. (1995). Interaction of solar wind ions with planetary surfaces. Advances in Space Research, 15(10), 13–17.

Sulaiman, A., Hospodarsky, G., Elliott, S., Kurth, W., Gurnett, D., Imai, M., ... others (2020). Wave-particle interactions associated with io's auroral footprint: Evidence of alfvén, ion cyclotron, and whistler modes. Geophysical Research Letters, 47(22), e2020GL088432.

Sumner, T., Rochester, G., & Hall, G. (1988). Silicon drift chambers for x-ray astronomy. Nuclear Instruments and Methods in Physics Research Section A: Accelerators, Spectrometers, Detectors and Associated Equipment, 273(2-3), 701–705.

Swift, D. W. (1981). Mechanisms for auroral precipitation: A review. Reviews of Geophysics, 19(1), 185–211.

Tao, X., & Bortnik, J. (2010). Nonlinear interactions between relativistic radiation belt electrons and oblique whistler mode waves. Nonlinear Processes in Geophysics, 17(5), 599–604.

Thibeault, S. A., Fay, C. C., Lowther, S. E., Earle, K. D., Sauti, G., Kang, J. H., ... McMullen, A. M. (2012). Radiation shielding materials containing hydrogen, boron, and nitrogen: Systematic computational and experimental study (Tech. Rep.).

Thorne, R. M. (1980). The importance of energetic particle precipitation on the chemical composition of the middle atmosphere. Pure and applied geophysics, 118, 128–151.

Thorne, R. M. (2010). Radiation belt dynamics: The importance of wave-particle interactions. Geophysical Research Letters, 37(22).

Tiwari, M., & Varma, P. (1993). Drift wave instability with loss-cone distribution function—particle aspect analysis. Planetary and space science, 41(3), 199–207.

Treumann, R. A., Baumjohann, W., & Balogh, A. (2014). The strongest magnetic fields in the universe: how strong can they become? Frontiers in Physics, 2, 59.

Tseng, H., & Pratt, R. (1971). Exact screened calculations of atomic-field bremsstrahlung. Physical Review A, 3(1), 100.

Tsurutani, B. T., Lakhina, G. S., & Verkhoglyadova, O. P. (2013). Energetic electron (¿ 10 kev) microburst precipitation,˜ 5–15 s x-ray pulsations, chorus, and wave-particle interactions: A review. Journal of Geophysical Research: Space Physics, 118(5), 2296–2312.

Tsurutani, B. T., Southwood, D. J., Smith, E. J., & Balogh, A. (1993). A survey of low frequency waves at jupiter: The ulysses encounter. Journal of Geophysical Research: Space Physics, 98(A12), 21203–21216.

Turner, D., Angelopoulos, V., Li, W., Bortnik, J., Ni, B., Ma, Q., ... others (2014). Competing source and loss mechanisms due to wave-particle interactions in earth's outer radiation belt during the 30 september to 3 october 2012 geomagnetic storm. Journal of Geophysical Research: Space Physics, 119(3), 1960–1979.

Turner, D., O'Brien, P., Kraft, R., Hospodarsky, G., Looper, M., Smith, H. T., ... others (2022). Comprehensive observations of magnetospheric particle acceleration, sources, and sinks (compass): A dedicated jovian radiation belt mission to unlock the secrets of the solar system's greatest particle accelerator. 44th COSPAR Scientific Assembly. Held 16-24 July, 44, 1672.

Tverskoy, B. (1969). Main mechanisms in the formation of the earth's radiation belts. Reviews of Geophysics, 7(1-2), 219–231.

Van Allen, J. A. (1959). The geomagnetically trapped corpuscular radiation. Journal of Geophysical Research, 64(11), 1683–1689.

Verronen, P., Andersson, M., Marsh, D., Kovács, T., & Plane, J. (2016). Waccm-d—whole atmosphere community climate model with d-region ion chemistry. Journal of Advances in Modeling Earth Systems, 8(2), 954–975.

Vette, J. I. (1991). The ae-8 trapped electron model environment (Vol. 91) (No. 24). National Space Science Data Center (NSSDC), World Data Center A for Rockets ....

Voss, H., & Smith, L. (1980). Global zones of energetic particle precipitation. Journal of Atmospheric and Terrestrial Physics, 42(3), 227–239.

Wagner, R. F., & Brown, D. G. (1985). Unified snr analysis of medical imaging systems. Physics in Medicine & Biology, 30(6), 489.

Waite Jr, J., Cravens, T., Kozyra, J., Nagy, A., Atreya, S., & Chen, R. (1983). Electron precipitation and related aeronomy of the jovian thermosphere and ionosphere. Journal of Geophysical Research: Space Physics, 88(A8), 6143–6163.

Walt, M. (1996). Source and loss processes for radiation belt particles. Radiation Belts: Models and Standards, 97, 1–13.

Watanabe, K. (1958). Ultraviolet absorption processes in the upper atmosphere. Advances in geophysics, 5, 153–221.

Weisskopf, M. C., Tananbaum, H. D., Van Speybroeck, L. P., & O'Dell, S. L. (2000). Chandra x-ray observatory (cxo): overview. X-Ray Optics, Instruments, and Missions III, 4012, 2–16.

Werner, W. (1977). Imaging properties of wolter i type x-ray telescopes. Applied optics, 16(3), 764–773.

West, H., Buck, R., & Walton, J. (1972). Shadowing of electron azimuthal-drift motions near the noon magnetopause. Nature Physical Science, 240(97), 6–7.

White, D., Jones, C., & Forman, W. (1997). An investigation of cooling flows and general cluster properties from an x-ray image deprojection analysis of 207 clusters of galaxies. Monthly Notices of the Royal Astronomical Society, 292(2), 419–467.

Whittaker, I. C., Gamble, R. J., Rodger, C. J., Clilverd, M. A., & Sauvaud, J.-A. (2013). Determining the spectra of radiation belt electron losses: Fitting demeter electron flux observations for typical and storm times. Journal of Geophysical Research: Space Physics, 118(12), 7611–7623.

Willingale, R., Sims, M., & Turner, M. (1984). Advanced deconvolution techniques for coded aperture imaging. Nuclear Instruments and Methods in Physics Research, 221(1), 60–66.

Winningham, J., Sharber, J., Frahm, R., Burch, J., Eaker, N., Black, R., ... others (1993). The uars particle environment monitor. Journal of Geophysical Research: Atmospheres, 98(D6), 10649–10666.

Wolf, R. A. (1975). Ionosphere-magnetosphere coupling. Space Science Reviews, 17(2-4), 537–562.

Wong, W., Alozy, J., Ballabriga, R., Campbell, M., Kremastiotis, I., Llopart, X., ... Turecek, D. (2020). Introducing timepix2, a frame-based pixel detector readout asic measuring energy deposition and arrival time. Radiation Measurements, 131, 106230.

Woodger, L., Halford, A., Millan, R., McCarthy, M., Smith, D., Bowers, G., ... Liang, X. (2015). A summary of the barrel campaigns: Technique for studying electron precipitation. Journal of Geophysical Research: Space Physics, 120(6), 4922–4935.

Xu, W., & Marshall, R. A. (2019). Characteristics of energetic electron precipitation estimated from simulated bremsstrahlung x-ray distributions. Journal of Geophysical Research: Space Physics, 124(4), 2831–2843.

Xu, W., Marshall, R. A., Fang, X., Turunen, E., & Kero, A. (2018). On the effects of bremsstrahlung radiation during energetic electron precipitation. Geophysical Research Letters, 45(2), 1167-1176. Retrieved from `https://agupubs.onlinelibrary.wiley.com/doi/abs/10.1002/2017GL076510` doi: https://doi.org/10.1002/2017GL076510

Xu, W., Marshall, R. A., & Tobiska, W. K. (2021). A method for calculating atmospheric radiation produced by relativistic electron precipitation. Space Weather, 19(12), e2021SW002735.

Xu, W., Marshall, R. A., Tyssøy, H. N., & Fang, X. (2020). A generalized method for calculating atmospheric ionization by energetic electron precipitation. Journal of Geophysical Research: Space Physics, 125(11), e2020JA028482.

Yang, D., & Bayazitoglu, Y. (2020). Polymer composites as radiation shield against galactic cosmic rays. Journal of Thermophysics and Heat Transfer, 34(2), 457–464.

Yau, A., Peterson, W., & Shelley, E. (1988). Quantitative parametrization of energetic ionospheric ion outflow. Modeling magnetospheric plasma, 44, 211–217.

Zawdie, K. A., Drob, D. P., Siskind, D. E., & Coker, C. (2017). Calculating the absorption of hf radio waves in the ionosphere. Radio Science, 52(6), 767-783. doi: 10.1002/2017RS006256

Zeitlin, C. (2021). Space radiation shielding. Handbook of Bioastronautics, 353–375.

Zhang, X.-J., Angelopoulos, V., Mourenas, D., Artemyev, A., Tsai, E., & Wilkins, C. (2022). Characteristics of electron microburst precipitation based on high-resolution elfin measurements. Journal of Geophysical Research: Space Physics, 127(5), e2022JA030509.

Zhang, Y., Ross, A. W., & Fink, M. (1991). High-energy electron scattering study of molecular hydrogen. Physical Review A, 43(7), 3548.

Appendix A

Bremsstrahlung Implementations

From Koch and Motz (1959), the differential bremsstrahlung spectrum produced from a classical approach can be written as the radiation produced from n_e electrons passing through the Coulomb field of n_i ions:

$$4\pi\ j_\nu = \frac{\pi^3 Z^2 q^6 n_e n_i}{c^3 m_e^2} \int_\nu^\infty \frac{f(\nu)}{\nu} d\nu \int_{b_{min}}^{b_{max}} \frac{db}{b} \tag{A.1}$$

integrating over photon frequency ν and impact parameter b, given the scattering target's atomic number Z, to obtain the omnidirection flux j_ν. The differential cross section in energy, integrated over solid angle and in units of cm^2 keV^{-1}, is then

$$\sigma(\hbar\omega, E) = \frac{\sigma_0 Z^2}{\hbar\omega E}\ \ln \frac{1+\sqrt{1-\hbar\omega/E}}{1-\sqrt{1-\hbar\omega/E}} \tag{A.2}$$

which is the non-relativistic Bethe-Heitler bremsstrahlung cross section, where photon energy is $\hbar\omega$, electron energy is E, and $\sigma_0 = 7.9 \times 10^{-25}$ cm^2-keV, under the condition of $\hbar\omega < E$ and $\gamma \sim 1$ (the non-relativistic case). This is perhaps the simplest bremsstrahlung cross section formalism since added complexity is needed when b_{min} gets small which represents the electron approaching sufficiently close to the scattering target nucleus where a wave-like description of the electron is needed. This formalism also breaks down when electron or photon energies become relativistic, or when differential solid angle and photon emission direction are included.

Repeated from Chapter 2, a more complete description of the bremsstrahlung cross section comes from treating both the electron with a wave function. However, this formulation still is not full description of bremsstrahlung, as electronic screening, i.e. the influence of the target nucleus

bound electron shells screening the charge of the nuclei, is not included here. The Bethe-Heitler cross section under the first Born approximation is

$$\frac{d\sigma}{d(\hbar\omega)\ d\Omega_k\ d\Omega_p} = Z^2\ \alpha\ \left(\frac{r_0}{2\pi}\right)^2\ \ (1-F(q,Z))^2\ \ \frac{1}{\hbar\omega}\frac{1}{q^4}\frac{p}{p_0}\left\{\frac{p^2\ \sin^2\theta}{(E-p\cos\theta)^2}(4E_0^2-q^2)+\right.$$

$$\frac{p_0^2\ \sin^2\theta_0}{(E_0-p_0\cos\theta_0)^2}(4E^2-q^2) - \frac{2pp_0\ \sin\theta\sin\theta_0\cos\phi(4EE_0-q^2)}{(E-p\cos\theta)(E_0-p_0\cos\theta_0)}+$$

$$\left.\frac{2(\hbar\omega)^2(p^2\sin^2\theta+p_0^2\sin^2\theta_0-2pp_0\sin\theta\sin\theta_0\cos\phi)}{(E-p\cos\theta)(E_0-p_0\cos\theta_0)}\right\} \quad \text{(A.3)}$$

where $F(q,Z)$ is an atomic form factor, and the total momentum transferred to the nucleus q is defined as

$$q^2 = p^2+p_0^2+(\hbar\omega)^2-2p_0\hbar\omega\cos\theta_0+2p\hbar\omega\cos\theta-2p_0p(\cos\theta\cos\theta_0+\sin\theta\sin\theta_0\cos\phi) \quad \text{(A.4)}$$

where $\alpha \approx 1/137$ is the fine structure constant, r_0 is the classical electron radius, p_0 and p are initial and final momentum of the electron, E_0 and E are the initial and final electron energies respectively, θ_0 and θ are incident and final in-plane electron angles with respect to the photon emission direction, and ϕ determines the rotation of the plane of emission. This equation is in canonical units (e.g. momentum in units of m_0c) such that photon energy and electron momentum are directly comparable.

We would like to quantitatively check the validity of the GEANT4 numerical implementation of the bremsstrahlung cross section. We can integrate the double differential cross section given in Köhn and Ebert (2014) in photon frequency ω and in photon emission angle θ with respect to the incident electron plane at electron kinetic energy E_e that more describes the bremsstrahlung cross section:

$$\sigma_{Tot}(E_e) = \int\int \frac{1}{\hbar}\frac{d\sigma}{d\omega\ d\theta}(E_e)\ \sin(\theta)\ d\theta\ dE \quad \text{(A.5)}$$

where $\hbar$ is the reduced Planck's constant that converts photon frequency to energy and σ_{Tot} is the integrated cross section at electron energy E_e for all incident angles and photon energies in m^2.

A classical scattering experiment can be performed to estimate the frequency of bremsstrahlung photon productions by integrating the number density of scattering targets in the column

$$\mathcal{L} = \sigma_{Tot}(E_e) \int_{\infty}^{0} n(h)\ ds \tag{A.6}$$

where $\mathcal{L}$ is the luminosity or event rate of bremsstrahlung in units of photons/electron, n is the number density of scattering targets in m^{-3}, and ds is the linear path length travelled by the electron through the density n gas at altitude h. The path length s is a function of electron pitch angle and magnetic field inclination angle, so we'll take an approximation of it as $ds = dh\ \sec(I)\ F(E, \alpha)$, where I is the magnetic dip angle and $F(E, \alpha)$ is a energy- and pitch angle-dependent modifier that accounts for the additional path length travelled by an electron's helical motion.

This calculation is performed for the three profiles in Figure 5.15 at 100 keV, 1 MeV, and 10 MeV and the double differential cross sections $d\omega/(dE\ d\theta)$ shown in Figure A.1.

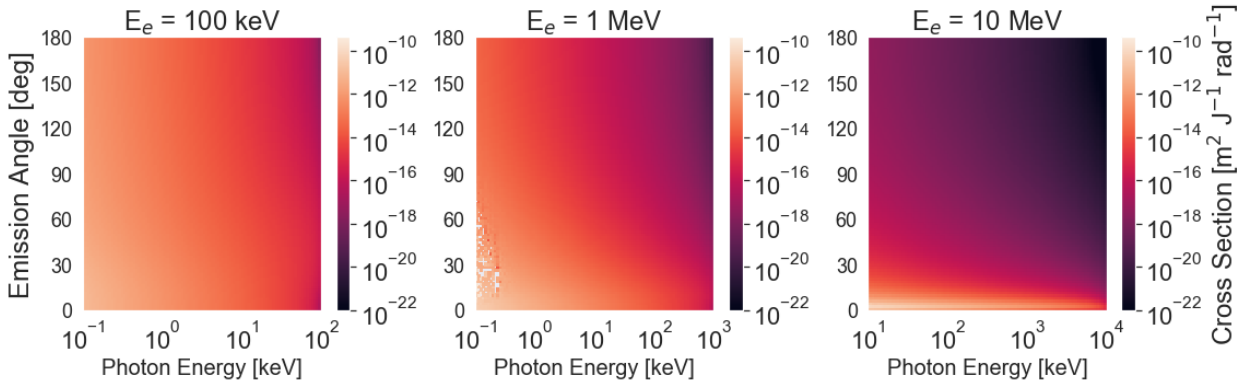

Figure A.1: Bremsstrahlung differential cross section that describes the photon generation likelihood given photon emission angle and energy at three incident electron energies. Note that the forward beaming behavior becomes more pronounced at higher incident electron energies.

Appendix B

Simulation Flux Normalization Integral

In order to contextualize our results, we must perform the following calculation to find the ratio of simulated particles to "real" particles. That is to say, when we chose a number of particles to simulate in Geant4, how does that correspond to the actual number of electrons that would be incident on the spacecraft per second? The simplest 3D case would be an isotropic distribution in a spherical simulations surface, which we calculate at the end to check this work. Here, we take a sine pitch angle distribution (in cylindrical coordinates) and project that distribution onto a spherical simulation surface. We let the background magnetic field be in the +Z direction, and assume azimuthal symmetry in our distribution. We take the following integral over the simulation surface and the target distribution to find the Monte Carlo equivalent particles rate:

$$\frac{\Delta N}{\Delta t} = -\Delta\Omega_s \left(f\left(\hat{k}_s\right) \hat{k}_s \right) \cdot \left(\Delta A_d \hat{k}_d \right) \left[\hat{k}_s \cdot \hat{k}_d < 0 \right] \tag{B.1}$$

$$\frac{\Delta N}{\Delta t} = -\int_D dA_d \int_{S_s} d\Omega_s f\left(\hat{k}_s\right) \hat{k}_s \cdot \hat{k}_d \left[\hat{k}_s \cdot \hat{k}_d < 0 \right] \tag{B.2}$$

We notate the simulation boundary surface D and unit normal to the distribution surface $\hat{k}_d$, and our source distribution S with unit direction vector $\hat{k}_s$, and $f_0 = |f(\hat{k}_s)\ \hat{k}_s|$ is our nominal flux, in this case 10^5 cm^{-2} s^{-1} sr^{-1} integrated over the entire energy range $[0, \infty)$. Terms in brackets are the indicator function, i.e. 1 when the term within brackets is true and 0 otherwise, which enforces inward particle directionality. Our simulations surface is a sphere with radius R which we'll treat in terms of area later. Our source geometry however is better suited to cylindrical coordinates, and we'll write the outward surface normal for the curved sides of a cylinder (we'll later see that the

sine pitch angle distribution goes to 0 at ±Z so we do not need to treat the top and bottom of the cylinder):

$$\hat{k}_s = \langle \cos(\theta_s)\ ,\ \ \sin(\theta_s)\ ,\ 0 \rangle \tag{B.3}$$

Our simulation surface is the typical spherical area element, $dA_d = r\ d\Omega_d = r\sin(\theta_d) d\phi_d\ r d\theta_d$,

$$\frac{1}{f_0}\frac{\Delta N}{\Delta t} = -R^2 \int_D d\Omega_d \int_{S_s} d\Omega_s f\left(\hat{k}_s\right) \hat{k}_s \cdot \hat{k}_d \left[\hat{k}_s \cdot \hat{k}_d < 0\right] \tag{B.4}$$

We'll now introduce our sine pitch angle probability distribution function in a cylindrical coordinate system with polar angle θ_s, parameterized by our loss cone angle θ_{LC}:

$$f(\theta_s) = f_0 \sin(\theta_s) \quad , \quad \theta_s \in [0, \pi] \tag{B.5}$$

where $1/f_0 \int f(\theta_s) d\theta_s$ is unity on the domain of θ_s. We'll later find that the domain is truncated to $[0, \pi/2]$ via the indicator function. We can now substituting these unit normals and our sine pitch angle distribution to produce

$$\frac{1}{f_0}\frac{\Delta N}{\Delta t} = -R^2 \int_D d\Omega_d \int_{S_s} d\Omega_s\ \sin(\theta_s)\ \langle \cos(\theta_s), \sin(\theta_s), 0 \rangle \cdot \hat{k}_d \left[\langle \cos(\theta_s), \sin(\theta_s), 0 \rangle \cdot \hat{k}_d < 0\right] \tag{B.6}$$

The normal element $\hat{k}_d$ here is in spherical coordinates, which we can write as

$$\hat{k}_d = \langle \sin(\theta_d)\cos(\phi_d),\ \ \sin(\theta_d)\sin(\phi_d),\ \ \cos(\theta_d) \rangle \tag{B.7}$$

Since our problem is azimuthally symmetric, we can ignore variation terms in ϕ_d. Substituting this element and performing the inner product yields

$$\begin{gathered} \tfrac{1}{f_0}\tfrac{\Delta N}{\Delta t} = -R^2 \textstyle\int_D d\Omega_d \int_{S_s} d\Omega_s\ \sin(\theta_s)\ \langle \cos(\theta_s), \sin(\theta_s), 0 \rangle \cdot \langle \sin(\theta_d),\ \ \sin(\theta_d),\ 0 \rangle \\ [\langle \cos(\theta_s), \sin(\theta_s), 0 \rangle \cdot \langle \sin(\theta_d),\ \ \sin(\theta_d),\ 0 \rangle < 0] \end{gathered} \tag{B.8}$$

which becomes

$$\begin{gathered} \tfrac{1}{f_0}\tfrac{\Delta N}{\Delta t} = -R^2 \textstyle\int_D d\Omega_d \int_{S_s} d\Omega_s\ \sin^2(\theta_s)\ (\cos(\theta_d) + \sin(\theta_d)) \\ [\sin(\theta_s)(\cos(\theta_d) + \sin(\theta_d)) < 0] \end{gathered} \tag{B.9}$$

Now we'll break out the solid angle integration into an appropriate coordinate system, in this case we'll again chose a spherical system, which will introduce an additional factor of $sin(\theta_s)$ to account for the annulus size formed at a given polar angle:

$$\frac{1}{f_0}\frac{\Delta N}{\Delta t} = -R^2 \int_0^{2\pi} d\phi_s \int_0^{\pi} d\theta_d \int_0^{2\pi} d\phi_s \int_0^{\pi} d\theta_s \ \sin^3(\theta_s)\sin(\theta_d) \ (\cos(\theta_d)+\sin(\theta_d)) \\ [\sin(\theta_s)(\cos(\theta_d)+\sin(\theta_d)) < 0] \tag{B.10}$$

We're almost there! The integral is computed with 20 Monte Carlo simulations using 10^7 evaluation points each (see Figure B.1) and is found to be $\mathcal{I} = -5.65 \pm 0.1\%$. Therefore, the Monte Carlo flux normalization factor N_{real}/N_{sim} can be calculated. The simulation starts particles on a sphere of radius $R = 25\ cm$ and input flux of $f_0 = 10^5\ cm^{-2}s^{-1}sr^{-1}$, so we have

$$\frac{1}{f_0}\frac{\Delta N_{real}}{\Delta t} = -R^2\mathcal{I} = 3.5 \times 10^3\ cm^2 sr \tag{B.11}$$

$$\frac{\Delta N_{real}}{\Delta t} = (10^5\ cm^{-2}s^{-1}sr^{-1})(3.5 \times 10^3\ cm^2 sr) = 3.5 \times 10^8\ s^{-1} \tag{B.12}$$

which indicates the actual number of electrons that would pass through a 25 cm sphere, given a sine pitch angle distribution. The simulation uses $N_{sim} = 10^8$ electrons such that the ratio that the background electron hit results need to be modified by is

$$\frac{\Delta N_{real}/\Delta t}{\Delta N_{sim}/\Delta t} = \frac{N_{real}}{N_{sim}} = \frac{3.5 \times 10^8}{10^8} = 3.5 \tag{B.13}$$

We can check this equation is true as it must be bounded from above by the isotropic case. Starting again with

$$\frac{\Delta N}{\Delta t} = -\int_D dA_d \int_{S_s} d\Omega_s f\left(\hat{k}_s\right)\hat{k}_s \cdot \hat{k}_d \left[\hat{k}_s \cdot \hat{k}_d < 0\right] \tag{B.14}$$

and assuming $f(\hat{k}_s) = f_0$, we can write

$$\frac{1}{f_0}\frac{\Delta N}{\Delta t} = -\Delta A_d \int_0^{2\pi} d\phi_s \int_0^{\pi} d\theta_s \sin(\theta_s)\cos(\theta_s)[\cos(\theta_s) < 0] \tag{B.15}$$

$$\frac{1}{f_0}\frac{\Delta N}{\Delta t} = -\Delta A_d\ (2\pi) \int_{\pi/2}^{\pi} d\theta_s \sin(\theta_s)\cos(\theta_s) = -\Delta A_d\ (2\pi)(-1/2) \tag{B.16}$$

$$\frac{1}{f_0}\frac{\Delta N}{\Delta t} = \Delta A_d \pi \tag{B.17}$$

We'll tile a sphere with our area elements such that $\Delta A_d = 4\pi R^2$,

$$\frac{\Delta N}{\Delta t} = 4\pi^2 R^2 f_0 \tag{B.18}$$

and for the same case as above, $R = 25$ cm and $f_0 = 10^5$ cm^{-2} s^{-1} sr^{-1} we have

$$\frac{\Delta N}{\Delta t} = (2.5 \times 10^4\ cm^2 sr)(10^5\ cm^{-2} s^{-1} sr^{-1}) = 2.5 \times 10^9\ s^{-1} \tag{B.19}$$

So for $N_{sim} = 10^8$, we would have the Monte Carlo factor $N_{real}/N_{sim} = 25$, which is indeed above our sine pitch angle distribution case. Calculations like this are standard practice in normalizing results from Monte Carlo, but a special thanks to Michael McCarthy for guidance on this calculation! E.g., a similar calculation is performed using Geant4 spacecraft background radiation results in (Lund & Jevremovic, 2019).

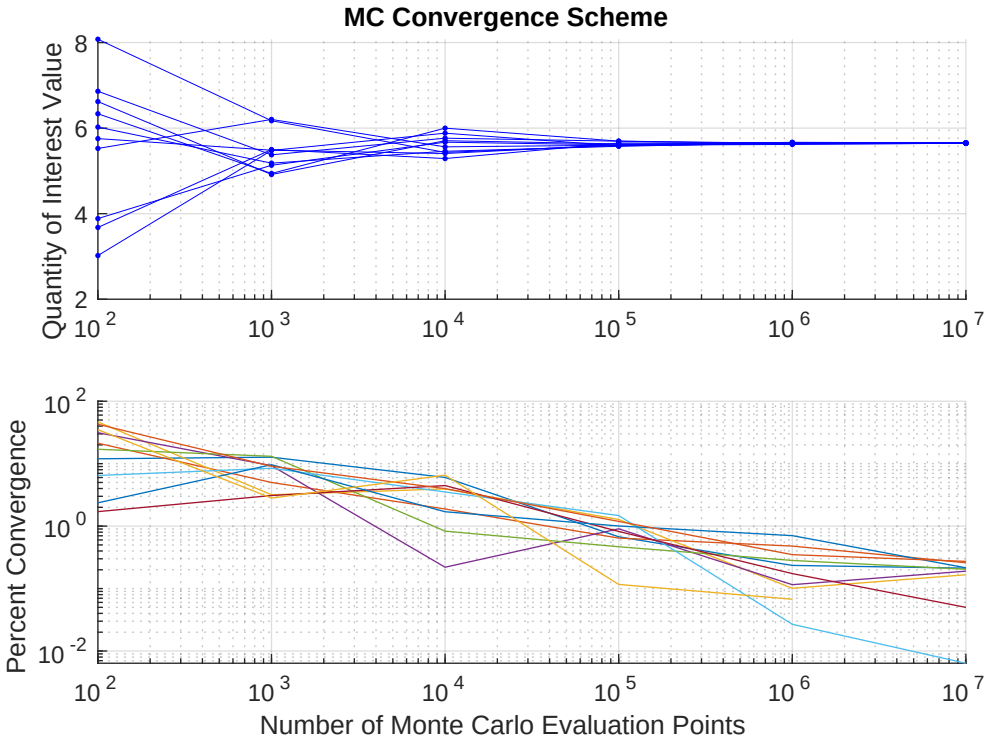

Figure B.1: Monte Carlo convergence plot of the first 10 solutions to the integral $\mathcal{I}$. The lower plot refers to the relative convergence to the average value obtained at 10^7 evaluation points.

Appendix C

AXIS Coded Aperture Deconvolution Algorithm

Listing C.1: Python coded aperture deconvolution method

```
import numpy as np
from scipy.ndimage import zoom

def fft_conv(rawImage, decoder):
    # Stack an empty row and column onto the detector image
    # in order to have an integer multiple of the decoding mask
    rawImage = np.hstack([rawImage, np.zeros([16, 1])])
    rawImage = np.vstack([rawImage, np.zeros([1, 17])])

    # scipy.ndimage.zoom used here to upscale image 2x
    resizedImage = zoom(rawImage, 2)

    # Fourier space multiplication
    image = np.real(np.fft.ifft2( np.fft.fft2(resizedImage) * \
                                  np.fft.fft2(np.rot90(decoder, 2)) ))
    # Set minimum value to 0
    image += np.abs(np.min(image))
```

```
    # Shift to by half of image length after convolution to recenter
    return shift(image, int(len(image)/2)+1, int(len(image)/2)+1)


def shift(m, hs, vs):
    '''
    m: input image
    hs: horizontal shift
    vs: vertical shift
    Adapted to Python from the Matlab version in Accorsi, 2001
    '''
    # Get original image size
    rm,cm = np.shape(m)

    # Shift each quadrant by amount [hs, vs]
    return np.block([[m[rm-vs:rm, cm-hs:cm], m[rm-vs:rm, 0:cm-hs]],
                     [m[0:rm-vs,cm-hs:cm], m[0:rm-vs,0:cm-hs]]])
```

Appendix D

Calculation of Inverse Compton Scattering X-ray Signal at Jupiter

This appendix describes a recalculation and reanalysis of the inverse Compton scattering (ICS) interaction between solar photons and ultra-relativistic electrons in Jupiter's radiation belt that was originally performed in Numazawa et al. (2021a), but the calculation was not explicitly published. This reanalysis was performed in order to inform the COMPASS X-ray science goals which involved estimating the signal strength and spectrum of various X-ray targets. Code to plot and evaluate this calculation can be found at `https://www.github.com/GrantBerland/InverseComptonScattering`.

Our starting point is the power spectral density of the Sun, assuming blackbody radiation:

$$S_\lambda = \frac{2\pi c^2 h}{\lambda^5} \frac{1}{e^{hc/\lambda kT} - 1} \ \ [W/m^2/nm] \tag{D.1}$$

and we'll impose that the integration of S_λ over wavelength must be equal to the total spectral irradiance at Earth:

$$I_{Sun,\ Earth} = \int_\lambda S_\lambda \ d\lambda = 1360.8 \ W/m^2 \tag{D.2}$$

We use the following relationship to scale the solar photon intensity I_{Sun} from Earth to Jupiter:

$$I_{Sun}(r_{Jupiter}) = I_{Sun}(r_{Earth}) \cdot \left(\frac{1 \ AU}{5 \ AU} \right)^2 \tag{D.3}$$

We are interested in the individual photons at each wavelength, so we divide by the energy per photon, $E = hc/\lambda$ [J/photon]:

$$N_\lambda = S_\lambda \cdot \frac{\lambda}{hc} \ \ [photons/m^2/s/nm] \tag{D.4}$$

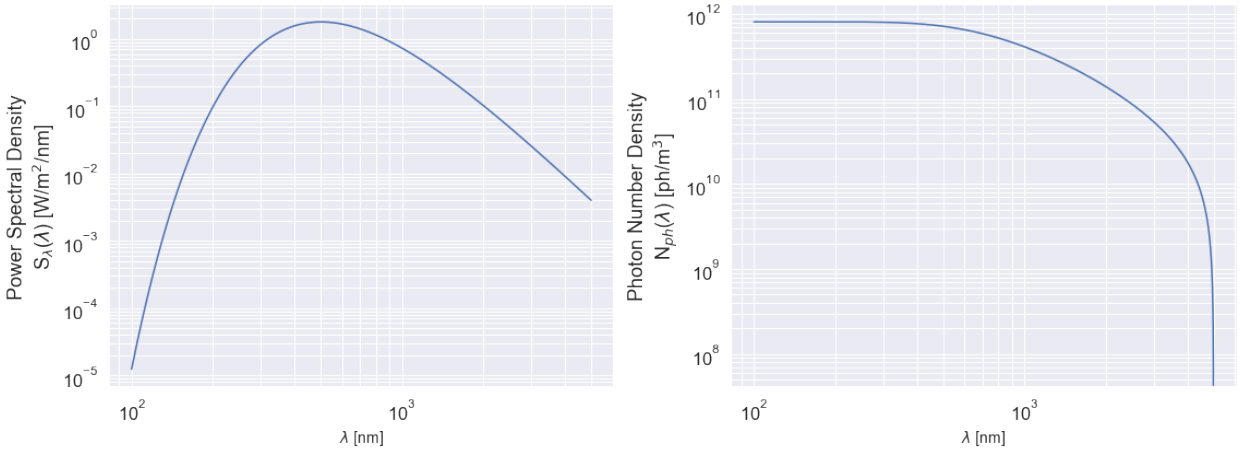

Figure D.1: (Left) The solar blackbody photon spectrum at Earth. (Right) The photon number density disribution versus energy at Jupiter.

And integrate over infinitesmal wavelength bins $d\lambda$ to obtain the continuum number of photons at each wavelength:

$$N = \int_{\lambda'}^{\infty} N_\lambda \cdot \ d\lambda = \int_{\lambda'}^{\infty} S_\lambda \cdot \frac{\lambda}{hc} \cdot \ d\lambda \quad [photons/m^2 - s] \tag{D.5}$$

To get the volumetric number density of photons at Jupiter, we assume that in 1 second the photons (which at 5 AU are a parallel beam from an infinitely far point source) transit a box the size of $\Delta x = c\Delta t = 3 \times 10^8 \ m$, where Δt is unity. We'll then divide by the box side length and multiply by the duration of unity to obtain

$$N_{ph} = \Delta t \cdot \frac{1}{c\Delta t} N = \frac{1}{c} N \quad [photons/m^3] \tag{D.6}$$

Figure D.1 shows the solar blackbody spectrum at Earth and the photon density distribution versus energy at Jupiter. From Blumenthal and Gould (1970) the differential cross section for photon production from inverse Compton scattering (i.e. Compton scattering in the high-energy electron limit) is

$$\frac{dN_{\gamma,e}}{dtd\epsilon} = \frac{\pi r_0^2 c}{2\gamma^4} \frac{N(\epsilon_0)d\epsilon_0}{\epsilon_0^2} \left(2\epsilon \ ln \frac{\epsilon}{4\gamma^2\epsilon_0} + \epsilon + 4\gamma^2\epsilon_0 - \frac{\epsilon^2}{4\gamma^2\epsilon_0} \right) \tag{D.7}$$

where the very first term becomes

$$\frac{\pi r_0^2 c}{2\gamma^4} = \frac{3\sigma_T c}{16\gamma^4} \tag{D.8}$$

by substituting the Thomson cross section in place of the classical electron radius, r_0, where ϵ_0 is the incident photon energy in$[J]$, ϵ_1 is the scattered photon energy in $[J]$, $N(\nu_0)$ is the incident photon field number density in $[photons/m^3]$, γ is the electron relativistic factor, and $\sigma_T = 8/3\ \pi r_0^2 = 6.6524 \times 10^{-25}\ \text{cm}^2 = 6.6524 \times 10^{-29}\ \text{m}^2$ is the Thomson cross section. The photon spectra for optical and UV photons scattering from an ultra-relativistic electron popluation is shown in Figure D.2. NB: this spectral integration assumes the Thomson cross section for electrons is valid, that is

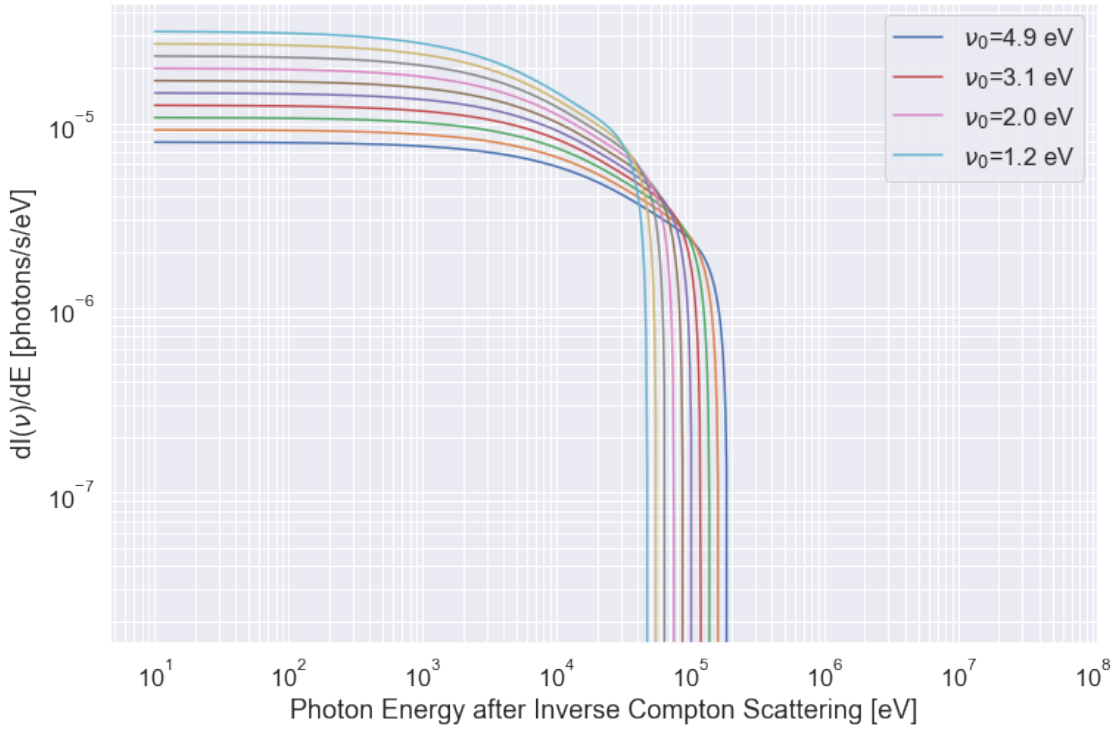

Figure D.2: The photon spectral distribution after scattering between discrete photon wavelengths and 50 MeV electrons using the Thomson scattering cross section.

to say the photon energy after the first Lorentz boost:

$$\gamma\ \epsilon_0 \ll mc^2 = 511\ keV/c^2$$

and if the above condition is true, the final photon energy in the lab frame gains another factor of γ such that the final energy is $\epsilon_1 = \gamma^2\ \epsilon_0$. Averaged over all solid angles, the average

energy after scattering is then

$$\langle \epsilon_1 \rangle = \frac{4}{3}\gamma^2 \, \epsilon_0$$

If we instead use the Klein-Nishina cross section in place of the Thomson cross section, we obtain a result that is true for both the Thomson scattering regime and for higher photon energies:

$$\frac{dN_{\gamma,e}}{dtdE_1} = \frac{3\sigma_T(mc^2)}{4\gamma}\frac{c\, n(\epsilon)d\epsilon}{\epsilon}\left[2q \; ln \; q + (1+2q)(1-q) + \frac{1}{2}\frac{(\Gamma_e q)^2}{1+\Gamma_e q}(1-q)\right] \tag{D.9}$$

where we are writing the scattered photon energy in terms of the initial electron energy

$$\epsilon_1 = \gamma mc^2 E_1 \tag{D.10}$$

and we have the terms

$$\Gamma_e = \frac{4\epsilon\gamma}{mc^2} \;, \quad q = \frac{E_1}{\Gamma_e(1-E_1)} \tag{D.11}$$

where this expression is valid for all Γ_e (where $\Gamma_e \ll 1 \implies$ Thomson scattering), under the assumption that we have high-energy electrons; $\gamma \gg 1$. Figure D.3 shows the photon spectrum formed when the solar blackbody spectrum scatters with monoenergetic electron populations.

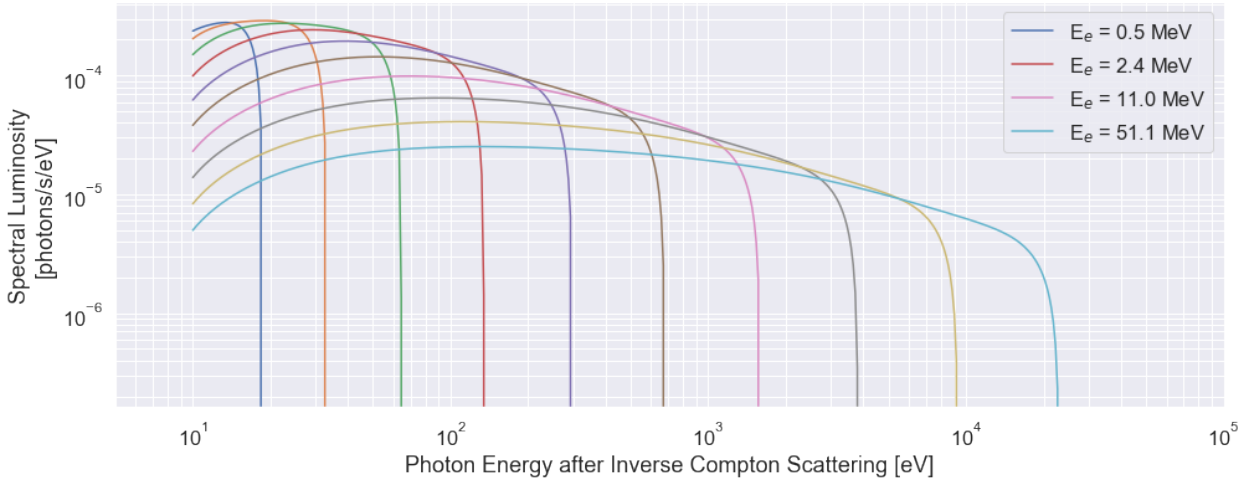

Figure D.3: The solar blackbody photon spectrum after scattering with an electron population that has discrete kinetic energies.

In order to combine the photon spectrum with an electron spectrum, we can write, again

from Blumenthal and Gould (1970):

$$\frac{dN_{Tot}}{dtd\epsilon_1} = \int\int dN_e \frac{dN_{\gamma,e}}{dtd\epsilon_1} \tag{D.12}$$

we'll chose integration over electron gamma factor, i.e. $dN_e = N_e(\gamma)d\gamma$, and use our spectrum from above,

$$\frac{dN_{Tot}}{dtd\epsilon_1} = \int\int N_e(\gamma)d\gamma \ \frac{dN_{\gamma,e}}{dtd\epsilon_1} \tag{D.13}$$

where below we present Jupiter's electron spectra as a function of L-shell and electron γ. We implement the Jovian electron distribution from Divine and Garrett (1983), which is shown plotted over L-shell and electron energy in Figure D.4. The resulting diffuse photon emissions, integrated

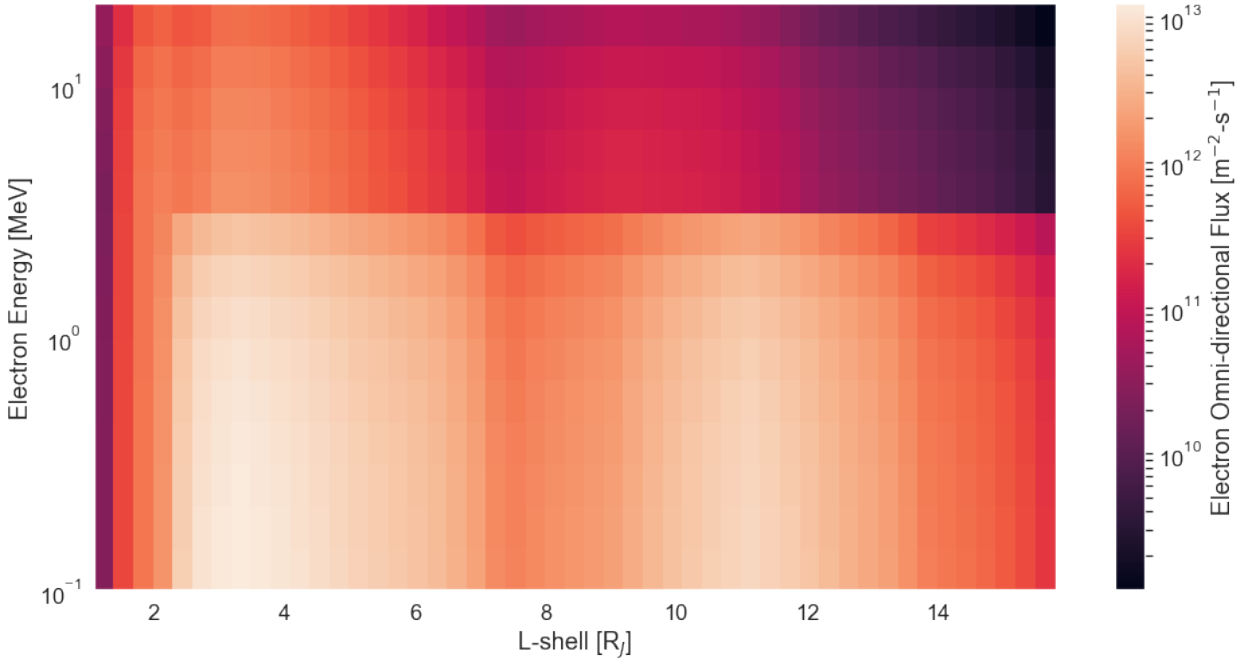

Figure D.4: Jovian radiation belt electron model from Divine and Garrett (1983).

between 0.2 – 10 keV and mapped spatially from L-shell to 2D coordinates is shown in Figure D.5.

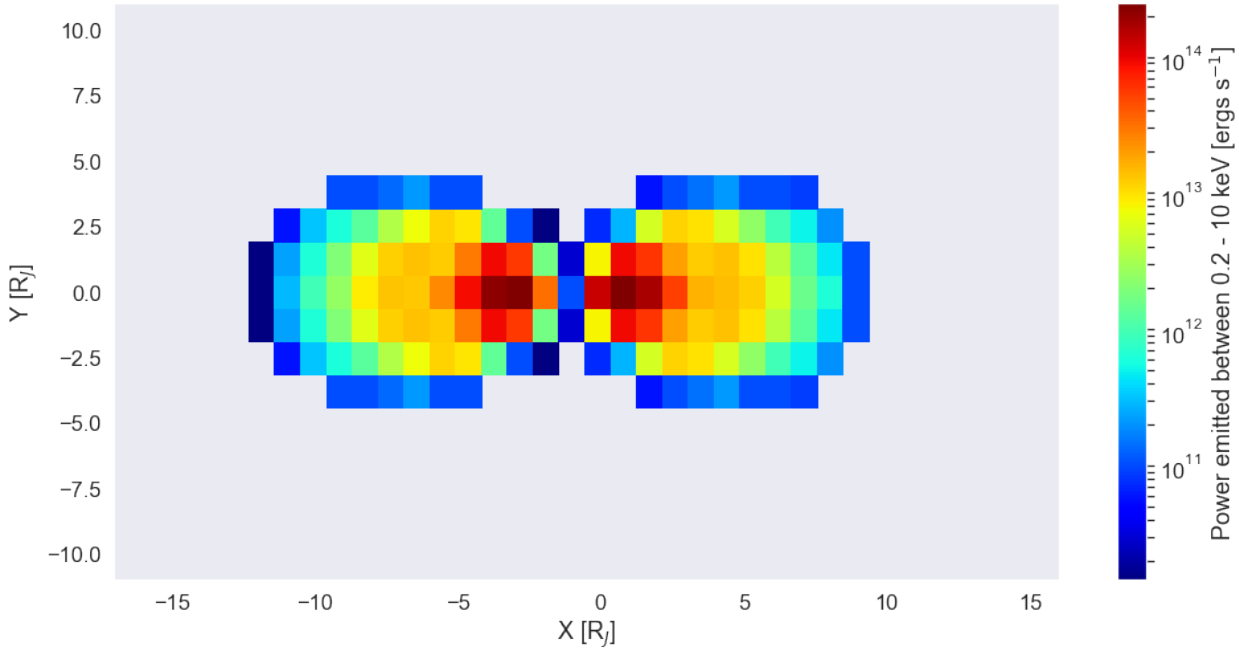

Figure D.5: Estimate of spectral power between 0.2 – 10 keV from inverse Compton scattering between solar photons and Jupiter's radiation belt.